Accurate Quantitative and Dynamic PET Imaging with the *pheno*PET Scanner for Plant Studies

Dissertation zur Erlangung des Grades eines Doktors der Naturwissenschaften

von

Carsten Hinz,
aus Jülich

vorgelegt der

Fakultät für Mathematik und Naturwissenschaften,
Bergischen Universität Wuppertal (BUW)

im November 2021

angefertigt im

Institut für Bio- und Geowissenschaften: Pflanzenwissenschaften (IBG-2),
Forschungszentrums Jülich

bei

Erstgutachter: Prof. Dr. Markus Axer
Zweitgutachter: Prof. Dr. Wolfgang Wagner
Weitere Mitglieder der Prüfungskommission:
Prof. Dr. Reinhard Hentschke
Prof. Dr. Dirk Lützenkirchen-Hecht
Tag der mündlichen Prüfung: 10. März 2022

Betreuungskomitee:
Dr. Ralf Metzner,
Dr. Daniel Pflugfelder,
Dr. Jürgen Scheins,
Dr. Matthias Streun,
Prof. em. Dr. Uwe Pietrzyk

The PhD thesis can be quoted as follows:

urn:nbn:de:hbz:468-20220512-102306-4
[http://nbn-resolving.de/urn/resolver.pl?urn=urn%3Anbn%3Ade%3Ahbz%3A468-20220512-102306-4]

DOI: 10.25926/tqj1-fs08
[https://doi.org/10.25926/tqj1-fs08]

“You cannot hope to build a better world without improving the individuals. To that end each of us must work for his own improvement, and at the same time share a general responsibility for all humanity, our particular duty being to aid those to whom we think we can be most useful.”

Marie Curie

Zusammenfassung

Der Einsatz von Radiotracern und Positronen-Emissions-Tomographie (PET) erlaubt die dynamische 3D-Beobachtung von Transport- und Allokationsprozessen in lebenden Organismen. Dies ist im medizinischen Bereich vor allem in klinischen und präklinischen Studien weit verbreitet. In den letzten Jahrzehnten haben verschiedene Forschergruppen aber auch mit der Anwendung von PET in den Pflanzenwissenschaften begonnen. Hier ist ein Fokus die Messung des Transportes und der Verteilung von Photoassimilaten, welche über die Aufnahme von $[^{11}C]CO_2$ durch die Pflanze markiert werden, im Spross und dem Wurzelsystem der Pflanze. Im Forschungszentrum Jülich wurde mit dem *pheno*PET-System bereits die zweite Generation eines PET-Scanners, speziell für die Messung von Pflanzen entwickelt, größtenteils im Rahmen des Bundesministerium für Bildung und Forschung (BMBF) Projekts „Deutsches Pflanzen Phänotypisierungsnetzwerk (DPPN)“. *pheno*PET bietet gegenüber der ersten Generation ein erweitertes Messvolumen für die Arbeit mit größeren und älteren Pflanzen, sowie einen höhere Empfindlichkeit für den Tracer und einen größeren dynamischen Messbereich für die Tracersignale. *pheno*PET nutzt aktuelle digitale Silizium-Photomultiplier (Digital Photon Counters (DPCs), Philips). Die DPCs sind an Kristalle aus dem anorganischen Szintillator Lutetium-Yttriumoxyorthosilicat (LYSO) gekoppelt und in horizontalen Ringen zur Messung eines Sichtfeldes mit einer Höhen von 200 mm und einem Durchmesser von 180 mm organisiert. Die Rekonstruktion der Bilder wird mit dem iterativen Algorithmus Ordinary-Poisson-Maximum-Likelihood-Expectation-Maximization des Softwarepaketes PET Reconstruction Software Toolkit (PRESTO) durchgeführt.

Für den Vergleich des Transportes und der Verteilung von Photoassimilaten zwischen verschiedenen Pflanzen werden quantitative Bilder benötigt. Die Voraussetzung dafür ist ein zuverlässiger und nachvollziehbarer Betrieb des *pheno*PET. Diese Doktorarbeit hat unter anderem zur Charakterisierung und der Überwachung des Betriebs beigetragen, was zu verschiedenen Verbesserungen der Firmware und der Datenauswertung der Rohdaten des *pheno*PET geführt hat. Besondere Bedeutung für diese Arbeit hat ein dynamisches und kontrolliertes Auslassen von Datenpaketen, sobald die DPCs mehr Daten messen als über die USB 3.0-Schnittstelle auf die Festplatten geschrieben werden können. In dieser Arbeit wurde der Algorithmus zur Identifikation von Koinzidenzen umgestellt auf einen Multikoinzidenzfenster Algorithmus mit einem Koinzidenzfenster von 2,5 ns. Das Energiefenster für *Singles*, einzelne Photonen, liegt unverändert zwischen 348 keV und 652 keV.

Kern dieser Dissertation ist die Implementierung der notwendigen Korrekturen für die Rekonstruktion quantitativer Bilder. Diese korrigieren folgende Fehlerquellen: Zufällige Koinzidenzen, statische Sensitivitäten, dynamische Zählratenverluste sowie Abschwächung und Streuung von Annihilationphotonen. Zufällige Koinzidenzen werden über ein verzögertes Koinzidenzfenster bestimmt; dies wurde für den neuen Algorithmus angepasst. Diese zufälligen Koinzidenzen werde an einen bestehenden Algorithmus zur Varianzreduktion weitergegeben. Eine Komponenten basierte Normalisierung wurde implementiert, um die unterschiedlichen statischen Sensitivitäten aller Paare von Detektorkristallen im Sichtfeld zu korrigieren. Die Zählratenkorrekturen berücksichtigen das kontrollierte Verwerfen von Daten und die Totzeit der Detektormodule. Zudem wird ein „Pile-up“-Effekt korrigiert.

Zwei weitere Korrekturen, die vom gemessenen Objekt abhängen sind notwendig. Als Erstes wird die Abschwächung von Annihilationsphotonen, zum Beispiel durch den Topf, die Erde und die Pflanze, mit einer Transmissionsmessung einer rotierende ^{68}Ge-Stabquelle bestimmt. Die Rekonstruktion nutzt einen iterativen Algorithmus (Maximum Likelihood for Transmission Reconstruction (MLTR)). Als Zweites werden gestreute Koinzidenzen mit einer

Monte Carlo Simulation für die Transmissions- und Emissionsrekonstruktion abgeschätzt.

Zusammenfassend erlauben die präsentierten Korrekturen quantitative Pflanzenmessungen mit *pheno*PET. In einem Zylinderphantom von der Größe eines typischen Pflanzentopfes können Aktivitäten von bis zu 100 MBq mit einer zeitlichen Stabilität von 2 % bei einer Ortsauflösung von bis zu 1,6 mm für ^{18}F gemessen werden. In radialen und axialen Profilen werden systematische Abweichungen von unter 2,5 % beobachtet. Die genutzten Schwächungskarten liegen maximal um 6,5 % unter dem erwarteten Wert und zeigen weder radiale noch axiale Abhängigkeiten. Für ein Phantom, welches das ganze Messvolumen ausfüllt, werden größere radiale und axiale Abhängigkeiten sowohl in den Transmissions- als auch in den Emissionsbildern beobachtet. Diese sollten reduziert werden durch weitere Untersuchungen. Die Kalibrationsfaktoren aus beiden Messungen stimmen gut überein.

Abstract

Radioactive isotopes are widely used as tracers in medicine and biology for non-invasive imaging. Positron Emission Tomography (PET) provides dynamic 3D imaging of several tracers and is widely applied for imaging in clinical and preclinical studies. In the last 20 years plant research has become another field of application. Here one focus is the investigation of the transport and allocation of photo assimilates within shoot and root systems, which are labeled by uptake of $[^{11}C]CO_2$ of the plant. We developed a second generation PET system dedicated for plant research called *pheno*PET within the German Plant Phenotyping Network. *pheno*PET makes use of state-of-the-art digital Silicon photomultipliers (Digital Photon Counters (DPCs), Philips). These DPCs are equipped with lutetium-yttrium oxyorthosilicate (LYSO) scintillators and are organized in horizontal rings forming a Field-of-View (FOV) of 180 mm diameter and 200 mm height. The image reconstruction is performed with Ordinary Poisson Maximum Likelihood Expectation-Maximization (OP-MLEM) provided by PET Reconstruction Software Toolkit (PRESTO).

For the comparison of the transport and the allocation of photo assimilates quantitative images are required. The prerequisite is a reliable and well understood operation of *pheno*PET. This thesis contributes to the characterisation and monitoring of *pheno*PET which leads to several improvements of its firmware and the associated data processing. The most important improvement is the implementation of a dynamic and controlled data dropping as soon as the data rate of the DPCs exceeds the band width of the USB 3.0 interface, which is used for the data transfer to disc. In the scope of this work a multi-window coincidence sorter with a coincidence window of 2.5 ns is implemented. The energy window accepts events between 348 keV and 652 keV.

To achieve quantitative tracer measurements, several data corrections have been implemented. *Random* coincidences are obtained with a delayed coincidence window, which has been adopted for the new coincidence sorter. These randoms are fed to a variance reduction algorithm. A newly introduced component-based normalization corrects for different sensitivities of the Lines-of-Response (LOR) across the FOV. Count rate corrections are applied for the controlled dropping of data and the dead time of modules. In addition a pile-up effect is corrected.

Two additional corrections are required depending on the imaged object. First, the attenuation of annihilation photons by e.g. the pot, soil and plant are obtained from transmission measurements with a rotating ^{68}Ge rod source. These data are reconstructed with an iterative reconstruction (Maximum Likelihood for Transmission Reconstruction (MLTR)). Second, *scattered* coincidences are estimated with a Monte Carlo simulation for the transmission and the emission reconstruction.

In summary, the applied corrections allow quantitative measurements of plants using *pheno*PET. In a cylinder phantom of the size of a typical plant pot, activities up to 100 MBq can be measured with a stability of 2 % over $9\,t_{1/2}$ at a spatial resolution of up to 1.6 mm with ^{18}F. Radial and axial profiles of the cylinder show a bias below 2.5 %. The applied attenuation maps are 6.5 % below the expected value and show neither an axial nor a radial bias. A larger phantom, covering the full FOV, shows larger radial and axial bias in the attenuation maps and in the emission images. Those should be alleviated by further investigations. Calibration measurements with both phantoms show a good agreement.

Contents

Chapter 1

Introduction

Plants are the primary source of food and feed for animals as well as building material and raw material for other products. Therefore a detailed understanding of plants and their cultivation is important to improve sustainability and productivity. Plant sciences cover a large variety of topics from practical applications like bioeconomy, which combines bio based production and recycling to improve industrial and agricultural productivity, down to basic research, which aims to understand plant function and their response to environmental changes.

Plants need to cope with external conditions like stress as they are not able to move away. Therefore, the acquisition of dynamic information on the growth and the function of a plant organ or structure through non-invasive measurements are required. The results of these measurements allow a classification of individual plants with slightly different genetic make-up, due to their response to certain environmental conditions e.g. drought. This approach is called phenotyping and an overview of different methods is given in [1]. Among the most in-depth or deep-phenotyping approaches are those studying in-plant resource allocation in response to environmental conditions.

One approach for non-invasive dynamic investigation of plant resource allocation is the use of radioactive isotopes. The isotope ^{11}C, for example, is taken up by plants as $[^{11}\mathrm{C}]\mathrm{CO}_2$ and transformed into photo assimilates during photosynthesis. The flow and allocation of these photo assimilates can then be measured from outside the plant using the β^+ decay of ^{11}C. This β^+ is stopped in the surrounding matter and annihilates with an electron into a pair of back-to-back emitted photons which can be measured outside of the plant. Already in 1963, Moorby studied the flow of photo assimilates and its dependency on light with ^{11}C with individual scintillation counters [2]. Single detectors can determine the transport between two points. In 1997 the PETIS system was set up to measure the coincidence of the two photons [3]. PETIS consists of two position sensitive detector heads. This allows a 2D projection of decay distribution. In 2003 PETIS was used to study the photosynthesis within a leaf with $[^{11}\mathrm{C}]\mathrm{CO}_2$. The third option for the investigation is Positron Emission Tomography (PET). PET allows *in vivo* 3D measurements of the photo assimilates in the root system (e.g. [4]) or the shoot (e.g. [5]). Here, individual below ground structures like organs or root tips can be resolved.

In 2015 Hubeau and Steppe pointed out the potential of $[^{11}\mathrm{C}]\mathrm{CO}_2$ and PET for the investigation of flow in phloem and xylem, the two transport systems within plants [6]. Furthermore, there are a number of other short lived radiotracers, that have been applied in plant science. For example ^{15}O can be used to study the uptake of water [7]. An alternative approach is to dilute ^{18}F in the water like in the first experiments with PETIS [3]. A glucose analogue labeled with ^{18}F allows the tracking of sugar [8]. In [9], PETIS is used to investigate the uptake of ammonium labeled with ^{13}N. The application of ammonium is a main fertilizer to improve plant growth and yield [10]. In [11] ^{52}Fe is used to investigate the transport and allocation of iron. These examples demonstrate the potential of radiotracers to answer questions in plant science.

For the acquisition of tracer distributions in 3D, a PET system is required. An option that is easily available is to use clinical PET scanners, e.g. [5, 12], or preclinical scanners, e.g. [13, 14, 15]. Several groups have developed PET scanners dedicated to plant research, e.g. [16, 17, 18]. The main difference for the measurement of plants is a vertical opening instead of a horizontal one used for lab animals or patients. Furthermore, these scanners are often placed in a climate chamber to control the environmental conditions appropriately for plant growth and physiology.

The development of plant dedicated systems profits from the progress achieved in preclinical and clinical scanners. In Jülich, the plant dedicated system PlanTIS was set up with modules developed for the preclinical ClearPET system [19]. The investigations focused on the uptake and transport of $[^{11}C]CO_2$ [4, 20].

*pheno*PET is the second generation system in Jülich and developed within Deutsches Pflanzen Phänotypisierungsnetzwerk (DPPN), a project founded by the Bundesministerium für Bildung und Forschung (BMBF). The aim of *pheno*PET is to provide a larger Field-of-View (FOV) and a higher sensitivity than PlanTIS. Therefore, a full detector ring was constructed in contrast to the eight rotating detector cassettes of PlanTIS. *pheno*PET is located in a climate chamber for environmental monitoring and control and close to a cyclotron dedicated for plant research. The current experiments in Jülich focus on the interactions of plant roots with beneficial microorganisms. The latest results are obtained with PlanTIS [21]. In addition a similar research question is investigated with *pheno*PET [22]. Both experiments are designed for the analysis of qualitative images and require a reproducible operation of the PET scanner.

Radiotracers were commonly used to quantify the flow velocity and allocation in plants. Different approaches are summarized in [23]. The analysis of the flow velocity with PET can be done without fully quantitative images, e.g. [15]. Bühler et al. developed a model to obtain flow and transport velocities as well as the allocation of tracer from quantitative *pheno*PET data [24, 25]. Furthermore, the qualitative interpretation of bias free images is much easier. This is especially true if the experiment is analyzed without a full understanding of the underlying physics of the decay and interactions of photons with matter or measurement processes in the detector.

My aim is the reconstruction of quantitative images of plants measured by *pheno*PET. The quantification includes a number of corrections, which are related to the system itself or to the measured plant. In the case of imaging the root system, the growth medium, like soil or hydroponics, causes attenuation and scatter, which requires major corrections. The result of my work will be images with a bias free visualization of spatial tracer distribution as well as an accurate dynamic behavior for different activity concentrations. This requires a detailed understanding of *pheno*PET with respect to the hardware, the measurement software and the image reconstruction. The characterization of the system is crucial for the implementation of corrections to obtain quantitative images. This detailed understanding reveals possible limits and opportunities of *pheno*PET for measurements of plants.

In this thesis, the acquisition of quantitative images with *pheno*PET will be presented in detail together with current limitations and ideas for further improvement. Chapter 2 starts with the theoretical background and explains the required effects that need to be corrected. The first section of Chapter 2 deals with special requirements for the measurement of plants and consequences for a PET system. Chapter 3 presents the setup of *pheno*PET and the software used for operation and image reconstruction. Further details on the reconstruction algorithm and the data correction model are introduced. Chapter 4 discusses the coincidence sorter. Here, different sorting strategies are investigated for *pheno*PET. This is followed by the investigation of a count-rate-depending correction in Chapter 5. In Chapter 6 the normalization is investigated. This focuses on the correction of different detection efficiencies and deviation from the model used for the reconstruction. The correction of attenuation and *scattered* coincidences is presented in Chapter 7. The achieved quantification for the reconstruction is investigated in Chapter 8. Here, the spatial and temporal accuracy of *pheno*PET will be demonstrated. The outlook and discussion of further improvements will be discussed in the final Chapter 9.

Chapter 2

Theoretical Background

2.1 Radiotracers in Plant Biology

Radioactive isotopes are applied in plant science for the investigation of dynamic processes. In particular, the flow and the allocation of the isotopes are of interest. Water can be investigated with ^{15}O [7], recently allocated carbon with ^{11}C [4] and nitrogen with ^{13}N [9]. In the following section a brief overview on the long-distance transport systems in plants is given. Afterwards the aspects of the experimental design for Positron Emission Tomography (PET) measurements of plants are discussed as well as their consequences for the operation of the PET system.

2.1.1 Transport System of Plants

The long-distance transport system of plants for nutrient and water has two major parts phloem and xylem. Here I give a brief summary. More information on the transport processes can be found for example in [26]. The phloem transports carbohydrates like photo assimilates and an additional number of solutes, like organic acids or amino acids. In the phloem a mass flow is generated by hydrostatic pressure. For example a leaf is a source for photo assimilates. Here new molecules are loaded into the phloem. At sink locations, like growing roots and growing leaves, the photo assimilates are unloaded. The second system, xylem, is mainly responsible for the transport of water. In addition, ions like iron and calcium are transported. The water transport is for example driven by the evaporation of water in the leaves during photosynthesis.

For the understanding of PET measurements of plants basic knowledge of anatomy of the transport system is important. The phloem and xylem consists of a number of different cells. Those are typically arranged in bundles, which are called vascular bundles. The vascular bundles can be found at different positions within the cross section of a stem mostly depending on the plant taxonomy, a classification of the plants. In monocotyledon species such as sorghum the vascular bundles are distributed over the hole cross section, see for example [27]. In contrast in dicotyledonous species like pea on the other hand the vascular bundles are arranged in the stem in a ring close to the surface of the stem (see for example [28]).

2.1.2 PET Measurements of Plants

In this section a general overview on the experimental approach in plant science is given. In particular, consequences for PET measurements of plants are described. Those have two important categories: Interactions of environmental parameters with the PET system and the experimental design to answer biological questions.

Plant science investigates the response of a plant to a treatment. Therefore a control group of plants is required, which is not treated. This results in at least two groups of plants that need to be measured. In their review on phenotyping, Fiorani and Schurr [1] point out that an experiment needs to be designed to study a single aspect. Thus, all environmental conditions need to be monitored or even better be fully controlled. Therefore, a climate chamber is a valuable addition to answer many research questions. A possible treatment might be an increased temperature or dynamic variations of the temperature. Wang et al. report a dependency of their PET system on the temperature within the climate chamber [16].

Another possible environmental parameter interfering with a PET measurement is humidity. Those interactions have to be considered in the experimental design and the analysis.

Fiorani and Schurr point out that an experimental design needs to be optimized for a specific research question. On the one hand an invasive application of radiotracers through a cut is possible [13, 15]. On the other hand a non-invasive application is possible through the uptake by the roots or the leaves. Roots can take up water or solutions [3, 9]. For plants grown in hydroponics, this can easily be achieved by replacing the growth fluid. The experimental focus at the Institute of Bio- and Geosciences: Plant Sciences (IBG-2) is [^{11}C]CO$_2$, which is applied with a gas tight cuvette, either to the complete shoot [4] or a single leaf [5, 29]. The cuvette allows a monitoring of the gas exchange, which requires tubes as connection. For the setup of a PET measurements those tubes need to be considered.

A further aspect needs to be considered: A possible damage caused by ionizing radiation. A number of studies investigated short and long term damage in plants, (e.g. [30, 31]). In recent years the damage on growth due to monitoring with X-ray Computer Tomography (CT) scans has been addressed for example by Blaser et al. [32]. Blaser et al. found a dependency on the plant species and encouraged to quote the dose applied to the pot during scans. For PET the applied dose is considered to be smaller. But a problem might arise as tracer is directly transported to sinks like a growing root or leaves. Blaser et al. point out that the effect of radiation can be addressed with a number of control plants, that are treated similarly but not exposed to the radiation. During a destructive harvest a possible effect can be measured. In the worst case, this doubles the required number of plant groups which need to be grown and harvested.

The experimental protocol developed for PlanTIS, the first generation system at the IBG-2, aims to investigate the flow and the allocation of photo assimilates. After labeling the plant, the cuvette is flushed to remove free [^{11}C]CO$_2$. The PET measurements typically run for two hours. The dynamic reconstruction uses a frame length of five minutes. This results in only two to four measurements per day. For a measurement week, a number of plants is grown and only a few are measured with PET. The other plants are backup and increase the statistical relevance for other measurements like the harvest or Magnetic Resonance Imaging (MRI). Those data provide a control on potential radiation damage. An approach to increase the throughput of PET is to acquire incomplete data sets. Therefore the measurements need to be focused on crucial points of the signal as presented in [25]. This also includes the necessity of an optimization of the measurement protocol, like the relevant time points along the measurement and the required duration.

For the routine application of PET experiments a good knowledge of the detector system is necessary. For the data acquisition challenges might arise from the environmental conditions. The number of grown and harvested plants for PET studies is rather small compared to other experiments in plant science. The low number of measurements per day presents a challenge. Therefore, a sufficiently large number of measurements for a statistical analysis is time consuming. The benefit of these efforts are non-invasive measurements of flow and allocation. The dynamic measurements in 3D are unique, as the decay of the tracer allows subsequent measurements of the same plant, which are not influenced by previous measurements.

2.2 Radioactive Decay

Radioactive decay is a process within a nucleus that transforms an unstable parent nucleus into a daughter nucleus. This daughter nucleus might either be stable or unstable. An unstable nucleus will decay further until a stable nucleus is reached. During radioactive decay bonding energy of the parent nucleus is set free. The resulting particles carry away this energy.

The main two decays are called α-decay and β-decay. In addition, γ-decay can occur as a follow up after one of these two decays. In the following, a short reminder on the occurring nuclear conversions is given. Afterwards some statistical properties of a radioactive decay are discussed. More detailed discussions of the different decays can be found in [33, 34, 35]. Further details on the physical process are presented in [36, 37].

α-Decay During an α-decay a helium nucleus is emitted by a parent nucleus X with the nucleon number N, the sum of neutrons and protons, and the charge number Z into a daughter nucleus Y

$$^{\mathrm{N}}_{\mathrm{Z}}\mathrm{X} \longrightarrow {}^{\mathrm{N-4}}_{\mathrm{Z-2}}\mathrm{Y} + {}^{4}_{2}\mathrm{He}^{2+} + 2\mathrm{e}^{-}.$$

The resulting helium nucleus is referred to as an α-particle. This decay only contains two bodies. Therefore the α-particle leaves with a discrete amount of energy and momentum. The daughter nucleus is left with the recoil for momentum conservation. A mother nucleus can also decay via different branches of α decays, leaving an excited daughter nucleus. Here, the α of each branch has a discrete energy value.

β-Decay The β decay can be separated into two cases, β^-- and β^+-decay. In a β^--decay a neutron is transformed into a proton and an electron and during a β^+-decay a proton is transformed into a neutron and a positron. The processes can therefore be written with the parent nucleus $^{\mathrm{N}}_{\mathrm{Z}}\mathrm{X}$ and the daughter nucleus Y like

$$\begin{aligned} \beta^-: \quad & ^{\mathrm{N}}_{\mathrm{Z}}\mathrm{X} \longrightarrow {}_{\mathrm{Z+1}}^{\mathrm{N}}\mathrm{Y} + \mathrm{e}^- + \bar{\nu}_{\mathrm{e}} \\ \beta^+: \quad & ^{\mathrm{N}}_{\mathrm{Z}}\mathrm{X} \longrightarrow {}_{\mathrm{Z\text{-}1}}^{\mathrm{N}}\mathrm{Y} + \mathrm{e}^+ + \nu_{\mathrm{e}}. \end{aligned}$$

The ν_e and $\bar{\nu}_e$ are an electron neutrino and electron antineutrino, respectively. Those neutrinos are not detected in PET. The kinetic energy of the β-particle is not a discrete number because there are three decay particles. The energy spectrum depends on the decaying nucleus and can be described by the maximum kinetic energy of the β-particles [38].

Electron capture is a different process that competes with the β^+-decay for the conversion of neutrons into protons. In an electron capture a proton and an electron are converted into a neutron

$$^{\mathrm{N}}_{\mathrm{Z}}\mathrm{X} + \mathrm{e}^- \longrightarrow {}_{\mathrm{Z-1}}^{\mathrm{N}}\mathrm{Y} + \nu_{\mathrm{e}}.$$

As the electron needs to come close to the nucleus this process is more likely for large nuclei.

γ-Decay The γ-decay is the emission of a photon from an excited nucleus, that was left after a α- or β-decay. The energy of the photons has discrete values depending on the decay. An excited nucleus can emit several photons with different probabilities. After a γ-decay the nucleus can still remain in an excited state resulting in a subsequent γ-decay.

2.2.1 Statistical Properties

The decay of each unstable nucleus is an independent quantum mechanical process. Therefore the decay of an individual nucleus cannot be predicted. Furthermore, the decay of a nucleus does not depend on any outer condition like the temperature. For a sample containing a radioactive isotope, the number of decays per time $A(t)$ is given by

$$A(t) = A_0 \cdot \exp(-\lambda \cdot t) \tag{2.1}$$

with the activity at a time point $A(t = 0) = A_0$ and the decay constant λ. This constant describes the probability for any of the nuclei decaying in a given time interval. The number of expected decays r within a time interval from t_1 to t_2 can than be obtained by an integration of Equation (2.1). The probability of n decaying nuclei is than given by a Poisson distribution

$$P(n) = \frac{r^n}{n!} \exp(-r) \,. \tag{2.2}$$

In such a time interval between t_1 and t_2, the probability $p(\Delta t)$ for a time differences Δt between two decays follows an exponential distribution

$$p(\Delta t) = \frac{1}{a} \exp(-a\Delta t)$$

with the the average decay rate $a = r/(t_2 - t_1)$.

The Poisson distribution of observed decays and the distribution of time difference between two decays are also valid for the measurement of a sample. This measurement can be restricted to only one direction e.g. with a small detector. More information on the statistical details are presented in [37].

The standard deviation of a Poisson distribution is given by $\sigma = \sqrt{r}$. For a specific measurement of n events the standard deviation can be assumed to be $\sqrt{n}$ [35].

The Poisson distribution is approximated with a Gaussian distribution with increasing r with the side condition of $\sigma = \sqrt{r}$

$$p(n) = \frac{1}{\sqrt{2\pi\sigma^2}} \exp\left(-\frac{(n-r)^2}{2\sigma^2}\right) = \frac{1}{\sqrt{2\pi r}} \exp\left(-\frac{(n-r)^2}{2r}\right) .$$

This approximation is suitable for $r \geq 10$. The remaining differences decrease for large r. The approximation with a Gaussian distribution is especially useful for fitting and the propagation of uncertainties.

2.3 Interaction of Particles with Matter

Charged particles and photons (γ) interact with matter during their passage. In the following section the interaction of electrons and positrons is briefly presented. Afterwards the interactions of γ with matter is discussed. The processes focus on the energy range and other aspects important for this thesis. More details can be found [33, 39].

2.3.1 Interaction of Positrons and Electrons with Matter

Charged particles undergo electromagnetic interactions with matter. For electrons and positrons these interactions are divided into collisions and radiation interactions.

Collisions include the ionization and excitation of electrons of the matter by the passing electron or positron. In each collision the incoming particle changes its direction.

An ionization electron undergoes further collisions, including ionization if it has a sufficient kinetic energy, until it is finally absorbed. Excited electrons transfer their energy either into molecular vibration or lead to the emission of light.

The energy loss per path length divided by the density is called stopping power and presented for two materials in Figure 2.1. The stopping power and energy loses are dominated by collisions for the given energies. The main difference between the water and lutetium-yttrium oxyorthosilicate (LYSO) is the density. This increases the energy loss in the denser LYSO and therefore decreases the electron range.

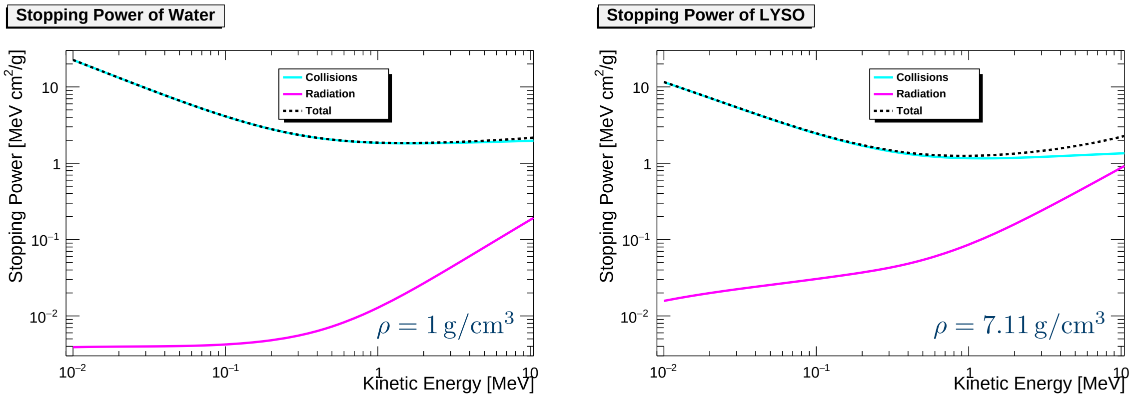

Figure 2.1: Stopping power for electrons and positrons in water and LYSO, which is used for the detector crystals. The data are obtained from the ESTAR database [40].

Radiation losses or bremsstrahlung are caused by the acceleration of the electrons in the coulomb field of atomic nuclei. This acceleration leads to a change of the direction and an emission of photons. As visible in Figure 2.1, radiation losses only play a minor role in PET with positron energies below 2 MeV, compare Section 2.4.

Annihilation is an additional process relevant for positrons. A positron with a low kinetic energy annihilates with a electron into two photons, each with an energy of $E = m_e \cdot \mathrm{c}^2 = 511\,\mathrm{keV}$. In the center-of-mass system of the electron-positron pair the two photons are emitted back to back. Due to the remaining momentum of this pair the emission angle has an uncertainty with a Full Width at Half Maximum (FWHM) of about 0.5° in the laboratory system [33].

A positron and an electron can also form a meta stable state called positronium. A small fraction of this positronium in human tissue ($<0.5\,\%$) decays into three photons [41]. This decay is typically ignored in PET imaging [42].

2.3.2 Photons in Matter

The signal in Positron Emission Tomography (PET) is provided by the two photons produced during the annihilation of an electron-positron pair. The photons need to leave the object and need to be detected by the scanner. Humans or plants in soil mainly consist of organic material, which behaves similarly to water. The detector consists of anorganic crystal LYSO. The probability for the different interactions of photons with these two materials are presented in Figure 2.2. The presented mass attenuation coefficient includes the effect of the chemical composition into the probabilities. A measure for the probability of a process between a photon and a single atom is the so called cross section σ, given as an area per atom (cm^2/atom). The relation between those two quantities are discussed later in Section 2.3.3.

Photoelectric effect The photoelectric effect is the absorption of a photon by an electron of an atom. This atom is ionized, while the electron leaves with the kinetic energy of

$$E_{kin} = E_\gamma - E_B$$

where E_B is the binding energy required for the ionization. The different electron shells have different binding energies which result in the steps visible in Figure 2.2b. The nucleus is left excited, which leads to the emission of a so called Auger electron or the emission of photons.

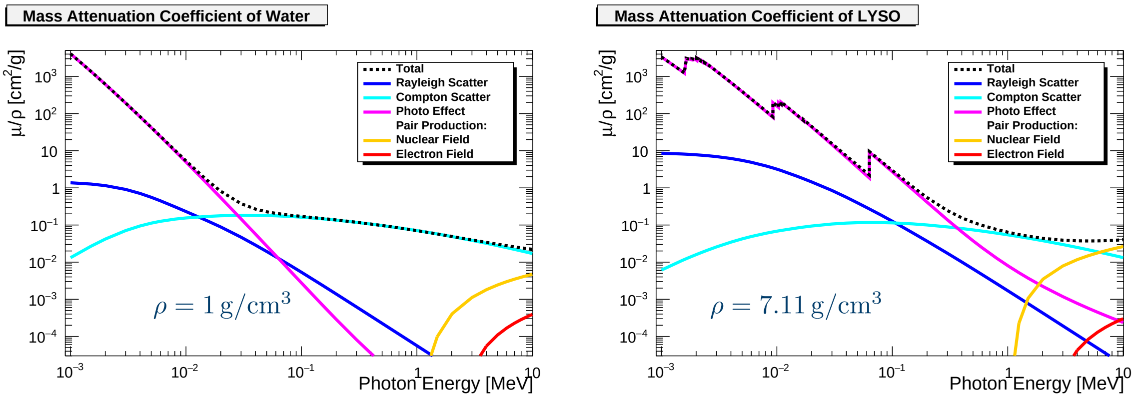

(a) Water.

(b) Inorganic detector crystals (LYSO).

Figure 2.2: Mass Attenuation coefficients (μ/ρ) of photons. For water Compton scattering is the dominant interaction for 511 keV photons. In LYSO photoelectric effect and Compton scattering have similar probabilities. The data are taken from the XCOM database [43].

Compton scattering is the scattering between a photon and an electron. The electron leaves the atom with a fraction of the photon's energy. Compton scattering is the dominant process for 511 keV photons in matter. Even within the crystals it is more likely than the photoelectric effect, as visible in Figure 2.2.

The differential cross section gives the probability for a scattering angle θ_c and can be calculated for free electron at rest with the Klein-Nishina formula

$$\frac{d\sigma}{d\Omega} = Zr_0^2 \left(\frac{1}{1+\alpha(1-\cos\theta_c)}\right)^2 \left(\frac{1+\cos^2\theta_c}{2}\right) \left(1 + \frac{\alpha^2(1-\cos\theta_c)^2}{(1+\cos^2\theta_c)\left[1+\alpha(1-\cos\theta_c)\right]}\right)$$

with $\alpha = E_\gamma/(m_e c^2)$ and the classical electron radius r_0 [39]. The energy of the photon after the scattering is given by

$$E_\gamma^{sc}(\theta_c) = E_0 \cdot \frac{m_e c^2}{m_e c^2 + E_0 \cdot (1-\cos(\theta_c))}.$$

Rayleigh scattering occurs between a photon and a complete atom. The direction of the photon is changed without an energy transfer. The probability of Rayleigh scattering is over two orders of magnitude below Compton scattering or the photoelectric effect. Therefore the influence on PET is negligible.

Pair production is the splitting of a photon into an electron and a positron. This requires an energy of at least $2m_e c^2 = 1022\,\text{keV}$. Furthermore pair production requires the presence of the coulomb field either of a nucleus or electrons. For PET measurements the effect does not play a role.

2.3.3 Attenuation of Photons

A narrow photon beam passing through matter is attenuated due to the above presented interactions. The intensity $I(\Delta l)$ after a distance Δl of material is given by Lambert Beer's law

$$I(\Delta l) = I_0 \exp\left(-\mu \cdot \Delta l\right)$$

with the linear attenuation coefficient μ, which depends on the material. The remaining photons from the initial intensity I_0 did not undergo any reaction. The linear attenuation is given by

$$\mu = \mu_{mass} \cdot \rho$$

with the density of the material and the mass attenuation coefficient presented in Figure 2.2. The μ_{mass} depends on the cross sections and the chemical composition. For a composition with N elements, with number of atoms $n_{a,i}$ and the mass m_i of one atom, the total μ_{mass} is given by

$$\mu_{mass} = \sum_i^N \frac{n_{a,i} \cdot m_i}{m_a} \mu_{mass,i} = \frac{1}{m_a} \sum_i^N \sigma_i$$

with the cross section of each element i with mass m_i and the mass of the composition $m_a = \sum_i^N n_{a,i} m_i$, see [39, 44].

2.4 Isotopes for Quantification and Radiotracers for Experiments with Plants

A large variety of elements undergo a β^+-decay and can be used as tracer in PET experiments, see for example [33, 45]. The experimental focus within the IBG-2 is ^{11}C that is applied as [^{11}C]CO$_2$ to plants. Due to its short half life of about 20 min, ^{11}C needs to be produced close to the PET.

There are further isotopes, which can be applied in PET measurements of plants, like ^{18}F, ^{13}N and ^{15}O, e.g. [3, 9]. The handling of the latter two isotopes can be challenging due to their short halt life $T_{1/2}$ of about 9.97 min and 2.03 min, respectively [33]. This is especially true if a further chemical synthesis is required to produce molecules for a study. Besides ^{11}C, further isotopes are used for the characterization and quantification of *pheno*PET. Their properties are summarised in Table 2.1.

For the production of short lived radiotracers cyclotrons are common particle accelerators. A cyclotron uses a constant magnetic field and an alternating electrical field between two D-shaped electrodes for the acceleration of protons on a spiral path [33]. These protons are produced by the ionization of hydrogen. The proton beam is directed to a specific target depending on the desired isotope. ^{11}C can be produced in a gas target with the reaction

$$^{14}\mathrm{N} + \mathrm{p} \longrightarrow {}^{15}\mathrm{O} \longrightarrow {}^{11}\mathrm{C} + \alpha.$$

The presence of oxygen in the target leads to the formation of [^{11}C]CO$_2$, which is taken up by the plant.

Within the scope of this project ^{18}F is used for calibration measurements due to its larger half life. The production process is

$$^{18}\mathrm{O} + \mathrm{p} \longrightarrow {}^{19}\mathrm{F} \longrightarrow {}^{18}\mathrm{F} + \mathrm{n}$$

with the oxygen provided in a liquid target as H$_2$[^{18}O]O. Therefore, the resulting sample is ^{18}F diluted in water, which is quite easy to handle for the filling of phantoms.

The last β^+ source is ^{68}Ge with a half life of 270.8 d. It decays via electron capture into ^{68}Ga, which has a half life of only 68 min. The isotopes have reached an equilibrium state, which results in a effective half life of 270.8 d for the ^{68}Ga. About 3.38 % of the decays of a ^{68}Ga are followed by one or more γ-decays with different energies. In most of the cases an energy of 1077 keV is emitted. A full list can be found in [49].

Table 2.1: Radioactive isotopes and their decay modes relevant for this thesis. The energy values for β-decays are end points of the spectrum. For γ-decays, the energy is given if it is relevant for this work. EC denotes electron capture.

Isotope	Daughter	Decays (E_{max})	Probability	Half Life	Ref.
^{11}C	^{11}B	β^+(960.5 keV)	99.75 %	20.361 min	[46]
		EC	0.25 %		
^{18}F	^{18}O	β^+(633.9 keV)	96.86 %	109.734 min	[47]
		EC	3.14 %		
^{68}Ge	^{68}Ga	EC	100 %	270.8 d	[48]
^{68}Ga	^{68}Zn	β^+(1899.1 keV)	87.68 %	67.83 min	[49]
		β^+(821.7 keV) + γ (various)	1.2 %		
		EC	8.94 %		
		EC + γ (various)	2.18 %		
^{176}Lu	^{176}Hf	β^-(593.2 keV)+γ(306 keV) +γ(201 keV)+γ(88 keV)	99.61 %	3.76×10^{10} year	[50]
		β^-(192.3 keV)+γ(401 keV) +γ(306 keV)+γ(201 keV) +γ(88 keV)	0.39 %		
		(most proper decay chains, probabilities of γ differ from β^- decay)			

The last isotope is ^{176}Lu, which is part of the detector crystals. ^{176}Lu has a β^--decay with three subsequent γ-decays. The second decay is also an β^--decay with a additional γ with an energy of 401 keV. Several combinations of a β^- and a γ result in an event with an energy deposit close to 511 keV. Those events cannot be distinguished from a 511 keV γ from an electron-positron annihilation. A more important feature is the extremely long half life, see Table 2.1. This results in a constant radiation source, which is background and also used for experiments.

2.5 Detector Working Principles

The measurement of annihilation photons in *pheno*PET is done with the inorganic scintillator LYSO read out with Silicon photomultipliers (SiPM). The scintillator converts the 511 keV photons into visible light, which is then measured by the SiPMs. In addition, the SiPMs digitize the results.

In the following section the scintillation process is briefly discussed. The concept of a SiPM and its operation are explained. *pheno*PET uses a so called Digital Photon Counter (DPC), which includes the digitization of the signals. Their properties and operation are presented in Section 3.2.1.

2.5.1 Inorganic Scintillator

In the scope of this work scintillation is the conversion of an energy deposition within the crystal into visible light. The exact mechanisms of the scintillation process depend on the material. Therefore I focus on a model relevant for LYSO, which is doped with cerium. This is an inorganic scintillator and the cerium works as a so called activator. The explanation is based on the educational model presented in [39]. More detailed discussions of the process and the underlying mechanisms can be found in [51].

In general, inorganic scintillators are semiconductors or insulators. These materials feature a band structure for electrons, which can be simplified with a valence and a conducting band. In the valence band, electrons are bound to the crystal lattice and in the conduction band they are allowed to move freely. There is a gap between the two bands with forbidden states. An activator is typically a positive charge doping that introduces energy states within the band gab. The band structure and states are illustrated in Figure 2.3 together with the scintillation process.

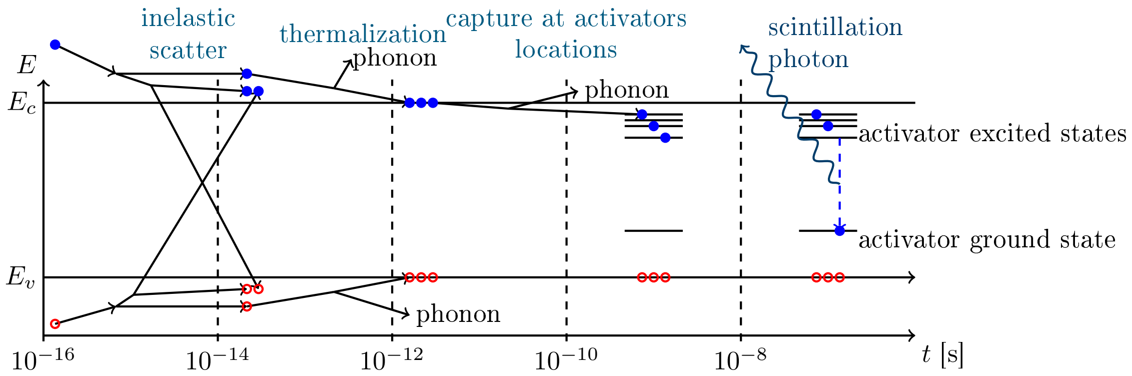

Figure 2.3: Scintillation process in inorganic scintillator. E_v is the upper boundary of the valence band and E_c the lower bound of the conduction band. Blue dots are electrons and red circles are holes. Phonons are oscillation or vibration states of the crystal lattice. This figure is based on the Figure 8.6 in [39] and simplified from Figure 4.3 in [51].

An ionizing particle passing through the crystal deposits energy within the crystal and therefore excites electrons from the valence to the conducting band. These leave holes in the valence band. Electrons and holes transfer their kinetic energy until they reach the lower boundary of the conduction band and the upper boundary of the valence band, respectively. The excited electrons first create additional electron-hole pairs. Afterwards, during the so called thermalization, energy is transferred to the crystal lattice as vibration or oscillation.

The recombination of electrons and holes occurs mainly at the activator centers, in this case cerium. The electrons are trapped in excited states of the Ce atoms. The emission of the scintillation light results from the decay to the ground state of Ce. The stability of these excited states defines the decay time of the scintillation light. Ce-based scintillators have a decay time of about 40 ns [52] and are therefore fast compared to other inorganic scintillators (see [39, 51]). The Ce emits photons in the visible spectrum [52].

It has to be noted that LYSO is not a specific material but covers a wide range of different crystals ($\mathrm{Lu_{2(1-x)}Y_{2x}SiO_5}$) with different fractions x of yttrium. The properties of these crystals differ, see e.g. [53]. In general, a higher fraction of Y reduces the light output and the density. A lower light output reduces the energy and timing resolution. In addition, a higher density increases the probability of measuring an incoming photon by either the photoelectric effect or multiple Compton scattering events. Below 200 keV the light output of LYSO to photons is not linear [54]. For 511 keV photons the response can be taken as linear.

2.5.2 Silicon Photo Multipliers

The scintillation light is detected with so called Silicon photomultipliers (SiPM). This detector consists of an array from hundred to several thousand individual cells. Each cell is an avalanche photodiode operated in Geiger mode. More information can be found in [39, 55].

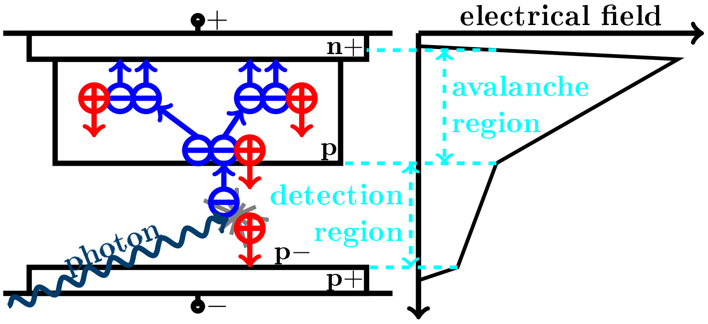

Figure 2.4: Sketch of an avalanche photodiode and its operation. The right part illustrates the electrical field. The layer thickness is not to scale. Adopted from [39, 55].

An avalanche photodiode is a semiconductor that converts the incoming light into an electrical signal. The detection and amplification process requires a doping of regions with electron acceptors (p) and electron donors (n) forming a p-n junction. Here, a p+ and n+ denote a high doping concentration and a p− denotes a lower acceptor concentration. An example structure is presented in Figure 2.4. At a p-n junction free electrons recombine with holes in the lattice forming a depletion zone without free charge carriers. A reverse voltage is applied to the photodiode and enlarges the size of the depletion zone. In the large depleted region or detection zone an optical photon creates an electron-hole pair. Those are pulled towards the electrodes. The electrons enter the avalanche region with a high electrical field, that is created by the doping atoms left in place after depleting their electrons and holes. In the avalanche region a large number of electron-hole pairs is created.

The cells of a SiPM are operated with a bias voltage close to the breakdown voltage. Therefore, the diode becomes conductive as the avalanche can sustain itself for a detected event. The breakdown voltage and the amplification depend on the temperature [56, 57]. Therefore the chance of the breakdown of a cell decreases for increasing temperature. This is explained with the increased scattering between electrons and phonons of the crystal lattice [55, 56]. A typical compensation of this dependency is the adjustment of the bias voltage to keep the gain and therefore the detection efficiency constant [58, 59].

The discharge of a single cell is quite fast and allows a good time resolution. But single cells can also break down by chance due to an electron-hole pair created by thermal excitation. These events are called dark counts. Philips reports a dark count rate below 140 kHz/mm^2 at 20 °C, which doubles every 7.5 K [60]. They observed most of the dark counts from only a few cells, which are already deactivated for the presented numbers. These dark counts can cause dead time effects.

The available number of individual cells results in a saturation effect. Each cell can only be triggered once and a second photon will not be detected until the avalanche is quenched. Philips recommends to correct the number of triggered cells n_{trigg}

$$n_{corr} = N \cdot \ln\left(n_{trigg}/N\right)$$

with the number of possible cells N and the actual number of photons n_{corr} [61]. The number of triggered cells is used as an information on the deposited energy.

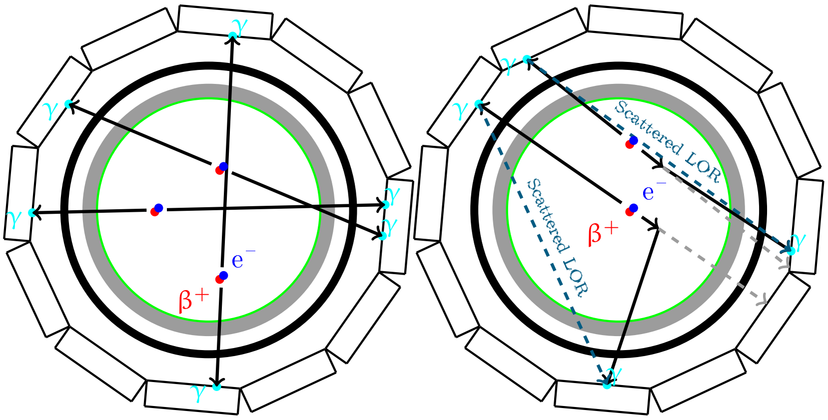

(a) *True* coincidences.

(b) *Scattered* coincidences.

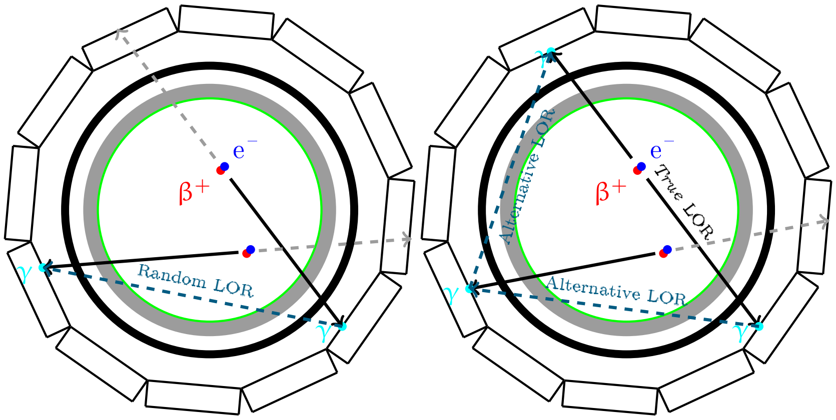

(c) Random coincidence.

(d) *Multiple* coincidence.

Figure 2.5: Examples for coincidences occurring in PET. A ring of twelve modules confines a Field of View (FOV, gray) which contains an object (white with green boarder). Measured photons are marked with black arrows and a cyan dot. Photons not being measured at the correct position are gray dashed arrows.

2.6 Coincidence Detection and Classification

PET measurements are based on the identification of the pairs of photons that originate from an annihilation of a positron with an electron. The two photons travel through the object and might be detected as so called *singles* by a detector crystal. The identification of simultaneous events is done with a coincidence method e.g. [62]. Therefore, either a circuit is implemented on the hardware level or within the analysis software. These programs are called coincidence sorter and the implementations for *pheno*PET is discussed in Chapter 4. Independent of the approach two *singles* are required to be measured within a timing window, called coincidence window, and have an energy depositions in the detectors within a certain energy window. Further selection is done with the position of both crystals. The resulting coincidences are called *prompt* coincidences (*prompts*). *Prompts* can be further separated into *true*, *random*, or *scattered* coincidences. These categories depend on the physical process occurring during the passage of the photons from the annihilation to the detectors. Examples for these categories are presented in Figure 2.5.

2.6.1 True Coincidences

True coincidences (Figure 2.5a) originate from an actual annihilation of a positron and an electron. Both photons do not undergo any interaction with the measured object. *Trues* contain the information required for the reconstruction of the activity distribution.

2.6.2 Scattered Coincidences

In a *scattered* coincidence at least one of the photons emitted by the annihilation underwent Compton scattering. Two examples for Compton scattering with the measured object is given in Figure 2.5b. Most of the interactions cause a low scattering angle and therefore the photon only loses a small amount of energy.

Another possibility is Compton scattering within a detector crystal. Here, subsequent interactions can lead to the deposition of the full energy in the scanner these events cannot be distinguished from photoelectric effect. This inter crystal scattering can also lead to the identification of a wrong crystal for this *single*. The photon can also leave the crystal with its remaining energy after a Compton scattering.

Scattered coincidences do no longer contain a position information and need to be corrected for quantitative image reconstruction. The similar energy depositions of all these events do not allow a separation on a single event level.

2.6.3 Random Coincidences

The coincidence sorting also detects accidental coincidences, which are called *randoms*. In PET, *randoms* result from two simultaneous decays, where only one photon of each decay is detected, see Figure 2.5c. *Randoms* can not be separated from *trues* on a single event level.

2.6.4 Multiple Coincidences

Two examples for *multiple* coincidences are presented in Figure 2.5d. This category has more than two *singles* within a coincidence window. The most likely scenario is a *true* coincidence with an additional *single* [63]. In general, it is not possible to distinguish which two *singles* are the *true* coincidence. The other possibility corresponds to *random* coincidences. The coincidence sorter of the Monte Carlo simulation toolkit GATE offers a large variety of options to deal with *multiple* coincidences [64]. For *pheno*PET two approaches are compared presented in Section 4.1.2. The performance for these two approaches is investigated through Chapter 4

2.7 Tomographic Image Reconstruction

The tomographic reconstruction of PET measurements is divided in two categories: analytical algorithms and iterative algorithms. In the following a brief description on the most common analytical algorithm is given. Advantages and challenges of the methods are discussed. Afterwards iterative image reconstruction with Maximum Likelihood Expectation-Maximization (MLEM) is discussed. In addition, an overview is given on different models of the system and the measurement process.

2.7.1 Analytical Image Reconstruction

A common analytical algorithm is the filtered backprojection, which is now described briefly for a two dimensional image $f(x, y)$. A more detailed description and discussion can be found in [33].

The measured events are sorted into sets of parallel projections depending on a projection angle Φ and the distance of the projection to the scanner axis r. The resulting data, $p(r, \Phi)$ are Fourier transformed into the spatial frequency space (k space), resulting in $P(k_r, \Phi)$. These $P(k_r, \Phi)$ have the same value as the Fourier transformed image at the same point in the k space. Therefore, a transformation from k_r and Φ into the spatial frequencies in k_x and k_y

is done. This results in the Fourier transform of the original image $F(k_x, k_y)$. The Fourier backprojection of $F(k_x, k_y)$ gives the original image $f(x, y)$. This requires ideal projection data that only contain *true* coincidences and no disturbances like *randoms*.

The filter part of this reconstruction is a modification of the projection in the k-space. Here the filtered image is given by

$$P_{filter}(k_r, \Phi) = H(k_r) \cdot P(k_r, \Phi).$$

The simplest filter is the ramp filter $H(k_r) = |k_r|$. This suppresses low frequencies and amplifies high frequencies.

The analytical reconstruction is computationally fast and relatively easy to implement. As drawback the algorithm assumes perfect data, which should in particular be noise-free. Therefore, the data need to be corrected for a large number of effects like *scattered* and *random* coincidences. This does not allow a precise modelling of the measurement process and is especially difficult for low statistics, i.e. a low number of measured events. A more detailed discussion on the challenges can be found in the literature, e.g. [33].

Filtered back projection is used for example for the characterization of different PET scanners. The majority of reconstructions within the National Electrical Manufacturers Association (NEMA) standard for small animal scanner uses filter backprojection [65].

2.7.2 Iterative Image Reconstruction

The most prominent example for iterative image reconstruction is Maximum Likelihood Expectation-Maximization (MLEM). MLEM reconstruction is designed to take into account the nature of the positron source by modelling the Poisson distribution [66, 67]. The MLEM can be used for emission tomography like Single Positron Emission Computer Tomography (SPECT) (e.g. [68]) and PET as well as for transmission tomography, like CT, as discussed by Lange et al. [66].

The number of expected events in a Line-of-Response (LOR) or sinogram bin i is modelled as the sum of all contributing sources. Each source j, for example a 3D volume called voxel, is modeled according to a Poisson distribution that has a specific contribution to a LOR i. These contributions are given by the system matrix, a set of constants c_{ij}.

A maximum-likelihood approach is used to determine the activity of each source by comparing the number of recorded events in each LOR with the expected events in each LOR by maintaining the Poisson distribution. For the expectation maximization a gradient ascent procedure is used and results in an iterative equation of the form [69]

$$\lambda_j^{(n+1)} = \frac{\lambda_j^{(n)}}{\sum_i^N c_{ij}} \sum_i^N c_{ij} \frac{p_i}{\hat{p}_i^{(n)}} \tag{2.3}$$

with

$\lambda_j^{(n)}$	activity in voxel j after iteration step n
c_{ij}	matrix element of LOR i and voxel j
p_i	*prompts* measured by LOR i
$\hat{p}_i^{(n)}$	expected events for LOR i after iteration n
N	Number of LORs.

A large number of methods for the calculation of the c_{ij} and the $\hat{p}_i^{(n)}$ have been developed. First approaches implemented a correction of the measured data p_i for *randoms* and *scattered* coincidences. For example, in [67] the c_{ij} are calculated as the intersection of a sphere to model the positron range and the Tube-of-Response (TOR) of detector pairs. Yavuz and Fessler [70] investigated the so called “shifted Poisson” model for the reconstruction with precorrected data and compared the bias with other approaches for transmission reconstruction. Lange et al. [66] proposed the addition of *randoms* to the expected counts $\hat{p}_i^{(n)}$ instead of a subtraction from the p_i and adding the attenuation to the c_{ij}. Lange et al. did not include *scattered* coincidences into the c_{ij} due to the complexity. Kadrmas et al. [71] do not correct the measured data but add additional events from *random* or *scattered* coincidences as additive corrections to forward projection, the calculation of the $\hat{p}_i^{(n)}$. A multiplicative factor is added to the denominator of the first term in Equation (2.3). This factor should account for the sensitivities and attenuation of each LOR and the c_{ij} are restricted to the geometrical effects.

In contrast Nuyts et al. [72] added the attenuation as a separate factor to the c_{ij} without any additive corrections. They added an iterative calculation of the attenuation coefficients to the iteration process as well as a *posteriori* information on the attenuation coefficients. They perform a simultaneous fit of attenuation and activity distribution. Benoit et al. [69] use a similar approach but implemented the so called ordinary Poisson model. This does not correct the measured data but includes the different detection efficiencies and the additive corrections into the calculation of the $\hat{p}_i^{(n)}$. Other groups extend the ordinary Poisson approach on Time of Flight (TOF) image reconstruction, e.g. [73]. Here, the TOF and the timing resolution are used to improve the estimation of the position of the decay on the LOR.

Hudson and Larkin [74] achieved an acceleration of the computational speed for MLEM with ordered subsets. The idea is to systematically reduce the number of contributing LOR to a voxel of the image during the calculation. This results in a reduction of the required operations to calculate the next update. As drawback the convergence is no longer guaranteed and the results tend to circle between a number of results equal to the number of subsets [34].

A more detailed discussion on the algorithm applied for *pheno*PET is given in Section 3.5. Here, the forward projection model for the $\hat{p}_i^{(n)}$ and the calculation of the system matrix c_{ij} is presented in more details.

2.7.3 Correction for Quantitative Imaging

The quantitative reconstruction of an image requires the correction of several effects resulting from the analysis software, the system and the object itself. A positron and the annihilation photons interact with the object. The interaction of the positrons is required for the annihilation and influences the spatial resolution. Compton scattering of annihilation photons with the objects disturbs the signal. All scattered photons remove coincidence from the original LOR.This coincidence is attenuated from the original LOR but might still be measured as *scattered* coincidence on a different LOR. These two effects are corrected by the attenuation correction and the scatter correction. For positrons, a correction might be required if positrons can escape the imaged plant. The detectors might be influenced by dead time, which needs to be corrected. The coincidence sorting might also require count rate dependent corrections. A specific correction is the correction of *random* coincidences. The normalization corrects for different sensitivities of LORs to radiation. In the analysis also the radioactive decay during the measurement needs to be considered. One possibility is a decay correction. The last factor is a calibration factor to convert the results of the reconstruction into Becquerel per volume.

All mentioned corrections are required for bias free images, which allow an easy interpretation of the results. In the following sections a brief description into all these corrections is given.

2.7.3.1 Correction of Random Coincidences

A simple example for *random* coincidences is the measurement of a β^+ source with a pair of detectors. Each detector measures a rate of singles events $S_{1/2}$ from this radioactive source. The rate of *randoms* between those two detectors can be calculated as

$$R = 2t_{coin} \cdot S_1 \cdot S_2$$

with the coincidence timing window t_{coin} [37]. This formula shows an important point: *randoms* depend quadratically on the activity within the PET. This relation can be used for the correction of *randoms* (e.g. [75, 76]).

The delayed coincidence approach [33] is a different method to directly measure *randoms* (e.g. [77, 78]). A second coincidence window is established but delayed to ensure that no *true* coincidence are detected. Those randoms are not effected by changes of the activity distribution and correctly model the dead time behavior as pointed out in [34]. The implementation for *pheno*PET is part of the coincidence sorter in Chapter 4. The disadvantage of the delayed coincidence approach is the low statistical precision due to the measurement of a few events per LOR. The noise in the measurement of delayed coincidences can be reduced by variance reduction methods. Byars et al. [79] implemented an iterative calculation to estimate *single* count rates of each crystal from measured delayed coincidences. These rates are used to estimate the expected number of *randoms* per LOR. Methods published earlier estimated the expectation value for the *randoms* in each LOR from *randoms* coincidence rates of detector blocks [80, 81]. The algorithm implemented for *pheno*PET is presented in Section 3.5.3.

2.7.3.2 Normalization

The normalization corrects different detection efficiencies. This means the normalization is the calibration between the measurement model and the acquired data. This requires a separat measurement of a well known activity distribution. MLEM reconstruction requires a model of the PET detector. This model is used to reconstruct the acquired data into an image of the activity distribution within the Field-of-View (FOV). Kinouchi et al. [82] point out that the model of the scanner can include the geometry as well as other aspects, such as the attenuation for a dual layer system. In the end, it is impossible to incorporate all deviations from a regular grid of the scanner into the measurement model. For example, PET Reconstruction Software Toolkit (PRESTO) uses the symmetries of the system to reduce the number of independent elements in the system matrix. Including the possible shifts of a single module would break these symmetries and thus increase the size of the system matrix considerably.

The first PET systems used so called direct normalization. The normalization factors were obtained by a single measurement as the ratio of expected values and measured values. A large amount of data is required to achieve a sufficient precision for 3D PET. Thus, the component base normalization was developed. Several models have been developed, which separate the normalization into geometrical components and crystal efficiencies. The sensitivity of a LOR between crystal i and j is than given by

$$s_{ij}^{norm} = \epsilon_i \cdot \epsilon_j \cdot g_{ij}$$

with a geometrical component g_{ij} and crystal efficiencies ϵ_i [83]. For example the geometrical components result from the position of the LOR within the FOV with respect to the crystals defining it. One example is the work by Badawi et al., where they increased the number of parameters to distinguish different effects like a dependency on the position of the crystal on a detector module [84, 85]. Furthermore, the normalization is split into a static and a dynamic (count rate dependent) component [85]. For *pheno*PET the dynamic components are the count rate corrections, which are dominated by a correction for the data transfer together with the dead time correction.

The calculation of a normalization has evolved from single calculations to the use of iterative algorithms. The latter ones are used to solve more complex models of the measurement process. These models incorporate the Poisson statistics of the measurement and are solved with χ^2 [82] or likelihood approaches [83].

For normalization measurements different sources can be used. Rod sources produce a low amount of *scattered* coincidences but are often rotated outside the FOV to illuminate all LORs. Plane sources also have a low scatter, can illuminate a greater number of LORs at the same time and are located within the FOV. The disadvantage is the necessity to buy and store these specialised sources. Cylinder phantoms have the disadvantage of a large number of *scattered* coincidences and thus require a scatter correction to provide a suitable normalization.

2.7.3.3 Dead Time and Pile-Up

Dead time is a time interval in which a detector cannot measure additional events. In general this results in a reduced count rate compared to the real count rate. The most obvious cause is that a detector is busy processing an event and cannot detect a second event, e.g. when the detector is recharging. A different possibility is the measurement of two simultaneous events that overlap. This process is referred to as pile-up. A second event can arrive in the integration interval of an earlier event. These two events are combined to one event. On the one hand the energy deposition of this combined event can be increased into the window and the event would be accepted. This accepted event might correspond to a real event or be an extra event, without information for the further analysis. On the other hand, the energy deposition can be increased above the energy window. This event is lost as in the case of dead time.

Effects similar to dead time and pile-up can also occur in software. For example the access to write an event to memory can be blocked. A further possibility is the incapability of the analysis to distinguish two events during the clustering.

In [39] two idealized models are distinguished: paralyzable and nonparalyzable dead time. A nonparalyzable detector has a constant or at least maximum duration of dead time. Therefore, the detector is able to record a new event after the dead time. A paralyzable dead time is caused by an extension of the dead time with every new event, without the chance to measure additional events. A nonparalyzable dead time model can be described under the terms of

$$R_{ideal} = \frac{R_{meas}}{1 - \tau R_{meas}}$$

with the ideal and measured event rates R_{ideal} and R_{meas}, respectively. The parameter τ is the dead time caused by each measured event. A paralyzable model can be modeled by

$$R_{meas} = R_{ideal} \exp(-R_{ideal} \cdot \tau).$$

Both dead time models have different maximum possible count rates. Furthermore, both models can be approximated for $R_{ideal} \cdot \tau \ll 1$ with

$$R_{meas} = R_{ideal}(1 - R_{ideal} \cdot \tau).$$

In [86] further dead time models are reviewed. For example a combination of a paralyzable and nonparalyzable dead time model is presented.

2.7.3.4 Attenuation Correction

The attenuation correction deals with the loss of events due to Compton scatter or photoelectric effect within the object. An important feature for PET is the independence of attenuation from the location of the annihilation along the LOR.

Consider a LOR that intersects with a homogeneous object for a distance d and an annihilation at the position a from one of the detectors within the object. The probability for the detection of the coincidence is than given by

$$P_{meas} = \exp(-\mu \cdot (d - a)) \cdot \exp(-\mu \cdot a) = \exp(-\mu(d - a + a)) = \exp(-\mu \cdot d)$$

with the attenuation coefficient μ of the object. In an actual measurement typically μ varies within the object. A voxelized image of the object containing the attenuation coefficient of each voxel is called attenuation map.

A number of different approaches can be used to determine an attenuation correction. For a known object, like a phantom, the attenuation can simply be calculated with Lambert Beers law. This approach was also used to estimated the attenuation of a patient with an average attenuation coefficient [87].

For a combined PET and CT scanner the attenuation correction can be obtained from a CT measurement. This requires a scaling due to the different energy of the photons used by CT [88]. An alternative is the measurement with a source emitting 511 keV photons. One possibility are ring sources that are placed inside the FOV for a transmission measurement [89]. Nowadays, rotating rod source are common [90, 91]. Those sources can be mounted on a retractable holder (e.g. [92]). The data can either be used to calculate the attenuation directly [33, 89] or for the reconstruction of an attenuation map. The reconstruction can for example be done with a maximum likelihood approach [93].

For a PET scanner combined with MRI an alternative approach is presented in [94]. The MRI provides structural information for humans. These data are combined with a template of an attenuation map. The MRI data are used for small adjustments of the structure. The template attenuation map can for example be acquired with a high resolution CT scan.

2.7.3.5 Scatter Correction

A scatter correction is the estimation of the fraction of *scattered* coincidences within the *prompt* coincidences. The distribution of *scattered* coincidences depends on the attenuation of the imaged object and the activity distribution. The attenuation for 511 keV photons in organic matter is dominated by Compton scattering. Therefore, the attenuation coefficients are related to the cross section of Compton scattering.

In early PETs, *scattered* coincidences were reduce by septa that collimate the photons towards the crystals. Modern PET scanners operate in 3D mode without a collimation. Therefore, the correction of *scattered* coincidences is important for an accurate quantification.

A possibility is the estimation of the scatter distribution from *prompts* measured outside of the object. Those prompts are either *random* or *scattered* coincidences. A fit function can be used to extrapolate the number of *scattered* coincidences within the object [95, 96]. This method can model scatter from activity outside of the FOV and requires only a low computation time.

Alternative methods are based on the simulation of the scattering process. The first method is the analytical single scatter simulation (SSS). More precise results are possible with a Monte Carlo simulation of the physical processes. Both simulations rely on the well understood physics of Compton scattering. Their main difficulty is the lack of information regarding the real activity distribution, because the measured distribution needs to be taken into account to estimate the *scattered* coincidences. An iterative application of scatter simulation and reconstruction leads to a more accurate image. The information on the attenuation needs to be provided by one of the methods discussed above as attenuation map.

A SSS is a simulation with a number of simplifications [97, 98, 99]. The majority of scattered photons undergo only one scattering event in the object. For a SSS always one photon of an annihilation is scattered. Furthermore, the SSS does not simulate unscattered coincidences. This reduces the required computation time but also reduces the possible precision. There are extensions of the SSS to include double scatter and therefore the possibility of a second Compton interaction [100].

A Monte Carlo simulation models the tracking of both photons of each annihilation through the imaged object. Afterwards the detection process within the detector can be simulated, which improves the results [101]. Monte Carlo simulations provide an accurate modelling of the physical interactions but suffer from a high computation time. Here, several optimizations are possible to speed up the simulation [102, 103, 104].

All scatter simulations require a scaling of the scatter distribution towards the measured data. Monte Carlo simulations provide estimates for scattered and unscattered events. Therefore, the scaling can be achieved quite easily by a comparison of simulated and measured event numbers. For SSS, the tail fit is a common method. It scales the number of measured and simulated events outside of the object to the same values. Tail fits might become unstable for large objects with only small tails. An alternative is the combination with a short Monte Carlo simulation to determine the scaling factor, which is more robust than a tail fit [105].

2.7.3.6 Correction of Positron Range

A further correction can arise from the positron range before the annihilation of the positron. In plants, positrons can escape before they annihilate due to short distances between the vascular bundle and the surface of the plant. For example Alexoff et al. [13] measured the fraction of positrons escaping from tobacco leaves for different isotopes. For ^{11}C $(64.0 \pm 4.4)\,\%$ of the positrons escaped. On the other hand Karve et al. [5] investigated the flow in sorghum. Specifically, they compared the quantification of the activity concentration with a vial filled with ^{18}F. The vial was placed in the stem of a sorghum plant. They report a deviation of about $10\,\%$ from the reference measurement.

Measurements with position sensitive detector systems of the shoot often focused on the comparison of counts without an absolute calibration [11, 106]. A quantification can be achieved for single detectors as done in [29] for specific organs with lead collimators. An applicable correction for PET measurements is topic of current research. The basic idea is to estimate the annihilation probability from the thickness of the stem or leaves [107, 108]. Scheins et al. proposed a method to measure a 2D image of the positrons leaving a thin structure, like leaves, with the aid of an magnetic field [109]. Converse et al. [15] point out that the analysis of the flow velocity of a bolus does not require a correction of the positron range. These measurements require an arrival time and the spatial distance but not the precise amount of radioactivity.

A quantification of radioactivity below ground in the root system does not require a correction for the positron range. Here, the surrounding soil or water for hydroponics stops the positrons. Thus the positron range is not important for the quantification of the activity concentration. For below ground measurements a larger fraction of photons undergoes Compton scatter. Therefore, the correction of attenuation and *scattered* coincidences are more important.

2.7.3.7 Correction of Radioactive Decay

The reconstruction of PET measurements is done in frames with a defined length. In a frame the number of decays are integrated. For the analysis and interpretation of the data the radioactive decay needs to be considered. One possibility is a frame-based decay correction [33, 34, 110].

The measured events within a frame are integrated for the reconstruction of a static image. Therefore, the number of measured events N_{meas} in the frame, between t_S and $t_S + \Delta t$, from a source, e.g. a voxel, is given by

$$N_{meas}(t_S, t_S + \Delta t) = \int_{t_S}^{t_S+\Delta t} A_{ref} \cdot \exp\left(-\lambda \cdot t\right) dt.$$

Here, λ is the decay constant of the measured isotope. The activity A_{ref} is the activity at the reference time point for t_S. For *pheno*PET this reference is by default the start of the data acquisition. Carrying out the above integration and solving the equation for the activity A_{ref} leads to

$$A_{ref} = \frac{\lambda \cdot \exp\left(\lambda t_S\right)}{1 - \exp\left(-\lambda \cdot \Delta t\right)} \cdot N_{meas}(t_S, t_S + \Delta t).$$

For the image reconstruction a dimensionless correction factor is preferred. Therefore, the number of reference counts is calculated to preserve the unit of measure during the reconstruction

$$N_{ref} = A_{ref} \cdot \Delta t = s^{decay} \cdot N_{meas}(t_S, t_S + \Delta t)$$

with the decay correction factor

$$s^{decay}(t_S, t_S + \Delta t) = \exp\left(\lambda t_S\right) \cdot \frac{\lambda \cdot \Delta t}{1 - \exp\left(-\lambda \cdot \Delta t\right)}. \tag{2.4}$$

The correction factor has two components. The first factor corrects for the decay between two frames. The fraction accounts for the radioactive decay during a frame.

An alternative approach is to incorporate the radioactive decay into the analysis. Bühler et al. incorporate the decay into their model based analysis of long-distance tracer-transport in plants [24, 25]. Bailey et al. point out, that this is more accurate for experiments with short-lived radiotracers [34].

The frame-based decay correction is applied as a global scaling factor. Therefore, it is not required during the image reconstruction. A method can therefore be choosen depending on the actual application.

2.7.3.8 Calibration Factor

The reconstructed emission image is given in an arbitrary unit (a.u.), which is called PRESTO Counts for *pheno*PET. The accurate correction of the effects presented above leads to a proportionality of PRESTO Counts and the actual activity distribution. The calibration factor converts the reconstructed values into a physical units like Becquerel per volume ($\mathrm{Bq\,mL^{-1}}$). It has to be noted that therefore the duration of the image frame needs to be taken into account. In principle a reconstructed image is the integration of the activity over the frame duration. Here, the abbreviation pcps for PRESTO Counts $\mathrm{s^{-1}}$ is used in this thesis.

The calibration factor CF is obtained from the measurement of a source with a well known activity. Typically a homogeneous activity distribution of a large source is measured.

Chapter 3

*pheno*PET Setup

The *pheno*PET system is dedicated to Positron Emission Tomography (PET) measurements of plants and developed within the Deutsches Pflanzen Phänotypisierungsnetzwerk (DPPN) by several institutes of the Forschungszentrum Jülich (FZJ) and Philips Digital Photon Counting (PDPC)[1]. The mechanical construction was done by the Central Institute of Engineering, Electronics and Analytics (ZEA), Engineering and Technology (ZEA-1). The Central Institute of Engineering, Electronics and Analytics (ZEA), Electronic Systems (ZEA-2) and PDPC developed the detector setup and readout. The system itself is described in Section 3.2. The climate chamber and further periphery is described first in Section 3.1. The climate chamber is located close to the cyclotron of the Institute of Bio- and Geosciences: Plant Sciences (IBG-2), which provides ^{11}C as [^{11}C]CO$_2$ for plant measurements.

3.1 General Setup

A picture of the setup in the chamber is given in Figure 3.1a. *pheno*PET is mounted on a custom lifting table, which was designed and mounted by FL Mechanik[2]. The lifting table will allow the measurement of larger plants step by step. A small computer, *phenousb2eth*, is mounted on the lifting table for the data acquisition. The climate chamber is developed by IBG-2 to control and monitor the environmental conditions. The chamber is expected to provide temperatures between 10 °C to 30 °C and variable air humidity, wind force and light intensity. Full operation of the climate chamber is expected in Fall 2021. In addition, the gas exchange system operated at PlanTIS [111] will be moved to the climate chamber. This

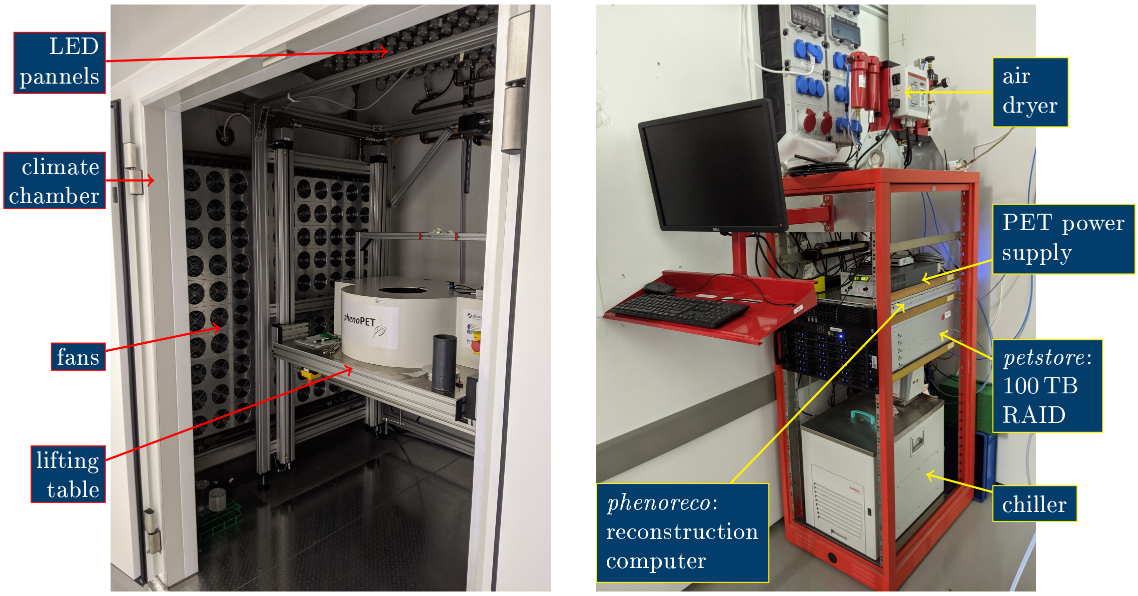

(a) *pheno*PET in climate chamber.

(b) Rack outside of climate chamber.

Figure 3.1: Setup of *pheno*PET on lifting table and additional hardware outside of the climate chamber.

---

[1] Philips GmbH Innovative Technologies. Philips Digital Photon Counting. Pauwelsstraße 17. D-52074 Aachen

[2] FL Mechanik GmbH & Co.KG: Sankt-Jöris-Str. 36, D-52477 Alsdorf

system monitors the gas exchange and controls the application of [^{11}C]CO$_2$ to the leaves of a plant in a cuvette.

Outside of the chamber the rack shown in Figure 3.1b houses the computers and infrastructure for *pheno*PET. The *petstore* is a redundant array of independent disks (RAID) and provides 100 TB to store measured raw data and all data created during the analysis and reconstruction. The *phenoreco* computer is dedicated for the analysis and reconstruction of the measured data. Each of these computers has a Random-Access Memory (RAM) of 128 GB. The *phenoreco* has two Central Processing Units (CPUs) of type Intel® Xeon® CPU E5-2670 v3 2.30 GHz, which results in 24 cores and 48 threads due to Intel® Hyper-Threading. The *petstore* has two CPUs of type Intel® Xeon® CPU E5-2630 v3 2.40 GHz, resulting in 16 cores and 32 threads. For a fast data access a direct 10 Gbit ethernet connection is used. During a measurement the data are written to the *petstore* over ethernet. A second RAID, *petstore2*, with 200 TB has been added. A small computer, *phenorun*, is placed in the rack to control the measurements. In addition the power supply for the *pheno*PET is located here. The chiller provides a liquid cooling for a constant temperature within the detector. An air dryer is used to ensure a low dew point of air blown into the *pheno*PET system to prevent condensation of water.

3.2 Detector Setup

The *pheno*PET [112, 113] system is covered by a white plastic hull made of extruded polystyrene (XPS) that protects the housing beneath it. Inside the plant port an aluminum cylinder is included for additional protection. In Figure 3.2 a view on the components inside the hull is given.

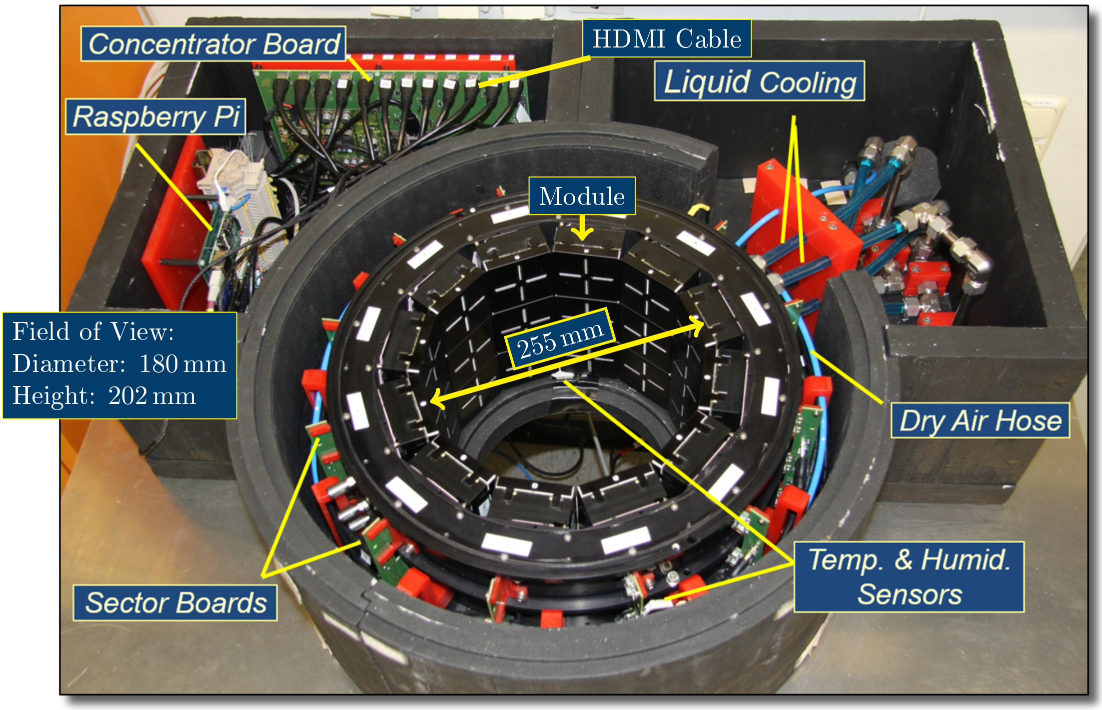

Figure 3.2: *pheno*PET without the white plastic hull and with the XPS isolation on top removed. Original image by Matthias Streun presented in [114].

A Raspberry Pi computer[3], called *phenoPi*, monitors several parameters and provides emergency shutdowns. Additionally, *phenoPi* controls the power supply and the cooler and can be controlled itself remotely via intranet. It measures the air temperature, dew point and light intensity inside the *pheno*PET system. In case of light inside the system or a dew point too close to the air temperature, *phenoPi* performs an emergency shut down of the power supply. This emergency shut down should prevent damage of the modules and the electronics. The sensors of the *phenoPi* are attached to the support structure of the modules. Also, the liquid cooling system and the dry air tubes are attached to these structures.

The photons are detected by 36 modules which are connected to 12 so called sector boards. Each sector board contains three modules, which are aligned vertically. The detector modules, which are described in more detail in Section 3.2.1, have a maximum distance of 255 mm. The plant port has a total diameter of 200 mm. The Field-of-View (FOV) for plant measurements has a maximum diameter of 180 mm and a height of 202 mm, which is defined by the height of a sector.

On the left side the Concentrator Board (CCB) is located. It manages the communication with the *phenorun* outside of the climate chamber over USB 2 and the data transfer. More details can be found in Section 3.2.2.

3.2.1 Digital Photon Counter and Crystal Matrix

The detector modules were developed in cooperation between the ZEA-2 and PDPC. A module consists of an array of 2×2 Digital Photon Counters (DPCs) of type DPC3200-22-44 [60]. A DPC or *tile* consists of an array of 8×8 separate Silicon photomultiplier (SiPM), called *pixels* (Figure 3.3a). Each *pixel* contains 3200 individual cells.

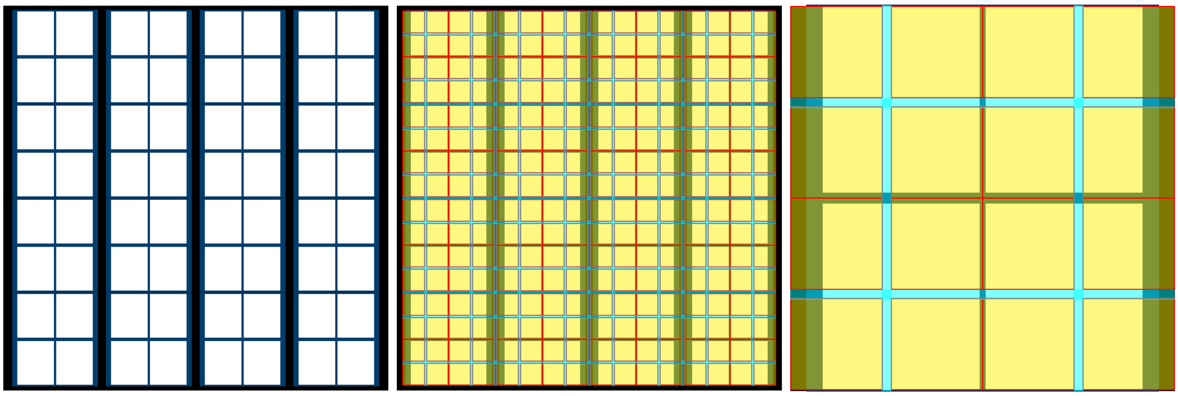

(a) Layout of DPC (b) DPC with crystal matrix. (c) Single *die* with crystal matrix.

Figure 3.3: Layout of a DPC (black, a) and a crystal matrix (b). A *die* (blue, c) contains four *pixels* (white) which are coupled to crystals (yellow). The crystals are coupled by transparent (red lines) or reflective (cyan lines) to their neighbors. The underlying circuit board is drawn in black.

One crystal matrix is attached to each *tile* (Figure 3.3b). This matrix matches 16 crystals to an array of 2×2 *pixels* (Figure 3.3c). For an identification of individual crystals, these are coupled with transparent and reflective contact faces to their neighbours as presented in Figure 3.3. The crystals consist of lutetium-yttrium oxyorthosilicate (LYSO) with a yttrium fraction of 10 % and Cerium and Calcium doping. The crystal matrices were produced by

---

[3] Raspberry Pi Foundation, 37 Hills Rd, Cambridge CB2 1NF, United Kingdom

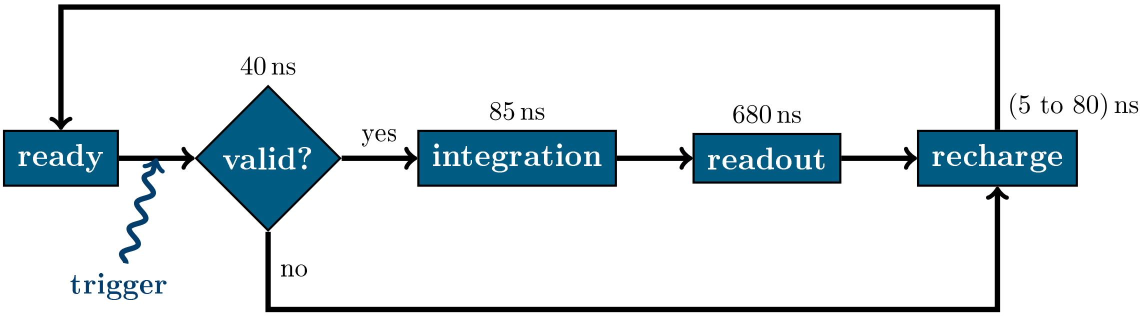

Figure 3.4: Trigger and processing of an event by a *die*. Image taken from [61] and adopted with the settings of *pheno*PET.

Crystal Photonics Inc[4] and each crystal has a dimension of 1.85 mm × 1.85 mm × 10 mm. The two *tiles* on one module result in 32 crystals per side. Therefore, the three rings of modules form 96 crystal rings. Each crystal ring has 384 crystals due to the twelve modules per ring.

The bias voltage of the DPC is set 0.5 V below the breakdown voltage of each *tile*. The breakdown voltage is measured for each *tile* individually. A temperature sensor on each *tile* is used to account for the temperature dependency of the breakdown voltage, whenever the bias voltage is set. This applies the calibration factor of +20 mV/°C provided by Phillips [61]. To ensure the same temperature during the configuration of the modules, the bias voltage is set after a measurement of at least 30 min without a radioactive source in the FOV.

The DPCs collect data in frames with a length of 327.68 µs. The recording of an event is presented in Figure 3.4, which can be adjusted with a large variety of settings (see [61, 115]). Hereinafter, the settings used for *pheno*PET are described.

A so called *die* is the smallest processing unit with an own field-programmable gate array (FPGA). A *die* consists of an array of 2 × 2 *pixels*. An event has to pass a trigger and a validation stage. Therefore, each *pixel* is divided into 2 × 2 subpixel. The so called trigger scheme 2 is used which requires two subpixel to have at least one cell breakdown. The validation uses the $0x00$ scheme within 40 ns. This validation schema divides the rows of cells of each subpixel into eight groups and requires at least one cell discharge in each group. If one of the subpixels is validated, the *pixel* is validated. A validated event initiates the readout of all four *pixels*. The detection time of this hit is given by the earliest triggered *pixel*. The time to digital converter (TDC) uses a 24 bit clock within the package. This results in a bin width of about 19.5 ps. The energy information is given by the number of cells triggered on each *pixel* within a 85 ns integration interval.

Measurements are performed in the so called "corrected mode". Here, the "skew correction" implemented by Phillips is applied and the data are provided in chronological order. The skew results from timing differences within the processing and analysis of each *die* and runtime differences of the clock signal. The skew occurs between different modules and the different *dies* on each module. Matthias Streun developed a method to measure those skews from the intrinsic radiation of the crystals [116], which is used for *pheno*PET.

Each module has two memory blocks of 16 kB each. The first block is filled with new events while the second block is transmitted. As soon as the memory of a single package exceeds the memory of one block, both blocks are used to record events. Afterwards no events are recorded until the current package is transmitted. These packages are called overlong packages. The acquisition of new events starts with the next frame cycle. The *tiles* and *dies* also have two memory blocks to store events before those are transmitted to the next level of the detector, i.e.

---

[4] Crystal Photonics, Inc., 5525 Benchmark Lane, Sanford, Florida 32773.

the module and *tile*, respectively. Therefore, similar behaviors are implemented to overcome memory limitations. But those limit the detector performance only for even higher count rates and are not yet important for *pheno*PET.

The packages transmitted by each module contain a header with additional information, e.g. the temperatures and the frame number. The temperature values are acquired from the four sensors, located on the *tiles*, and a fifth sensor located on the module. The frame number is a wrapping 8 bit counter that is increased for each data package, i.e. whenever the 327.68 µs are started for a new frame.

3.2.2 Concentrator Board

The data packages recorded by all modules are transferred to the Concentrator Board (CCB) [113, 117]. Therefore, each sector board is connected with a High Definition Multimedia Interface (HDMI) cable to the CCB. One line of this cable is used to distribute the 200 MHz system clock to all detector modules. The data transfer of each module is done over one line and thus has a maximum speed of 50 MB s^{-1} due to double data rate transfer. The CCB sorts the transmitted packages into a frame and adds an additional header. Those frames are transferred over USB 3.0 to the *phenousb2eth* computer with up to 375 MB s^{-1}. Here, a program called *phenostore* writes the data stream to disc of the *petstore* computer via ethernet.

The maximum data transfer to the CCB can theoretically reach 1800 MB s^{-1} and is much higher than the possible band width of the USB 3.0. Therefore, the so called frame dropping is implemented on the CCB. The CCB reduces the data transfer by dropping complete frames i.e. not transmitting them. The amount of dropped frames is adopted dynamically to the current data rate, which is proportional to the number of events. Furthermore, the CCB does not transmit overlong packages sent from the modules because the change of the data format is not yet implemented. This limits the dynamic range.

In order to ensure a stable data transfer the phase shift between clock and data signal of each module is measured and corrected by individual delay settings.

The sensitivity of the detectors is dependent on temperature. To achieve stable measurement conditions a warm up mode has been implemented. Here, the CCB performs a measurement without writing the data to disc. The warm up mode is started after all parameters have been set. In addition *pheno*PET is automatically switched back into warm up mode after each measurement.

3.3 *pheno*PET Operation

The operation of *pheno*PET requires further software running on different computers. Their main task and relevant features are discussed below. Several basic programs are operated in the shell. For routine operations a Graphical User Interface (GUI) and macros are provided to simplify the start up. An overview on the computers running the different programs and specific connections is given in Figure 3.5.

3.3.1 *phenostore*

The *phenostore* program runs on *phenousb2eth* within the climate chamber. Its main task is to write measured data to the RAIDs (*petstore* and *petstore2*) over 10 Gbit ethernet connections. An output directory needs to be given and the operation can be monitored by information printed to a shell. The names of the output files are defined by the date-time pattern *pet_yyyy-mm-dd_hh-mm-ss.dat*.

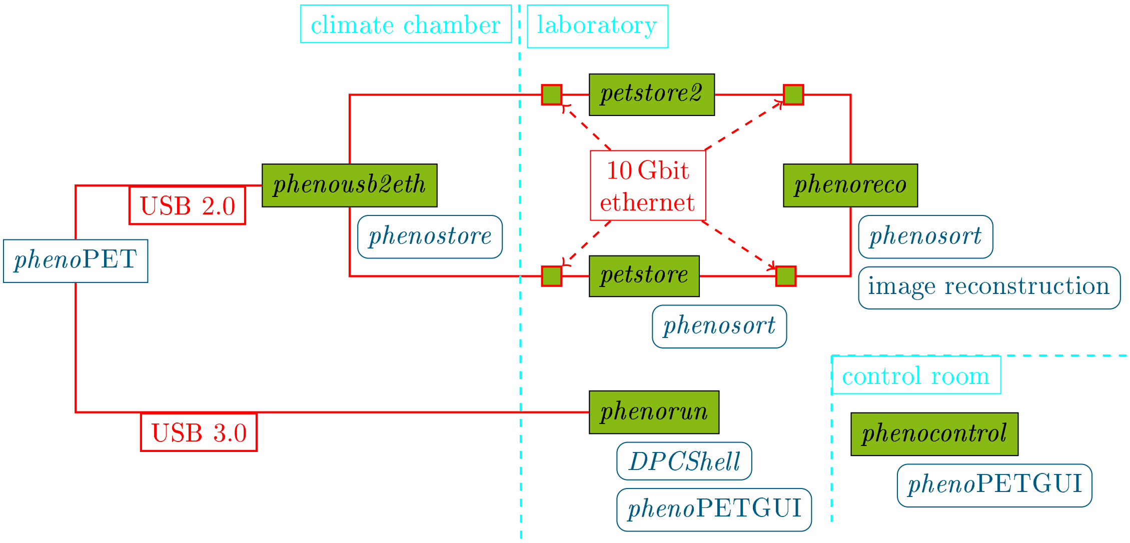

Figure 3.5: Overview on the computers and important connections. The software executed on the different computers is given. All computers are connected over the intranet ($100\,\mathrm{Mbit\,s^{-1}}$). Doubly mentioned programs can be executed on either one of the computers.

3.3.2 *DPCShell*

The control of *pheno*PET is provided by the so called *DPCShell* [117]. This is a command line program initially developed by PDPC. During the construction of *pheno*PET, PDPC and the ZEA-2 adopted the software to support all 36 modules of *pheno*PET. The adaptation and development for *pheno*PET is continued by the ZEA-2. Besides the execution of measurements the complete configuration of the DPCs is done with the *DPCShell*.

The *DPCShell* has the option to execute macros. These can combine configuration commands with measurements and even other macros. One macro is used to start *pheno*PET and initialize all detector parameters to default values.

As already discussed in Section 3.2.1 all measurements are done in corrected mode. Thus, all further software is not able to process other data formats.

3.3.3 Graphical User Interface

The Graphical User Interface (GUI) [118] gathers and displays information from different programs and offers a limited control of the *DPCShell*. The GUI is operated from the control room while it communicates over ethernet with the different programs. The *DPCShell* is contacted to start a measurement with a given duration. Any measurement requires a duration and an output directory. The configuration of *pheno*PET by the GUI is limited to the execution of the initialization macro with the default parameters.

Each measurement is written to its own directory. The GUI provides templates, which support the creation of file and directory names according to the convention of *pheno*PET. A daily run number and the date of the measurement can be used and are updated automatically. In addition, the measurement duration in seconds can be added to these names. The measurements are sorted in a directory structure consisting of three main categories: plant measurements, quality assurance measurements and test measurements. Within these three categories measurements are sorted in directories for the radioactive sources. In the end, each measurement date forms a directory containing the directories of each run. A run directory usually starts with a run number for an easy access and ends with the measurement duration.

The GUI announces the directory name to the *phenostore* program. The measurement setup can be saved to a configuration file and can be loaded for a further measurement.

The GUI also provides online monitoring of the current temperatures measured by the modules. A warning is given if the temperature was not stable within the last 30 min. Furthermore, the data rates and number of recorded and missing packages can be displayed. In addition the available disc space on the *petstore* is displayed.

In order to support the work a macro with a link on the desktop is established. This macro starts the *phenostore* and *DPCShell* programs on the different computers. It is ensured that programs are only executed once. Afterwards the GUI is started.

3.3.4 Improvements due to the Redesign of the Firmware

The above presented software differs from previous publications [112, 113, 117] due to the redesign of the CCB firmware. The extensive use of *pheno*PET during this thesis led to several observations of unstable or unintended behavior. An extensive search revealed several issues within the firmware but also some hardware issues. In the end, not all problems could be solved or identified in an adequate amount of time. Thus, a new firmware version was developed from scratch by the ZEA-2.

A few features were improved. For example, the first implementation of frame dropping only implemented the dropping of every other frame, as soon as the data transfer exceeds the maximum data transfer. This resulted in an increase of the maximum measurable activity. Furthermore, unused code was removed. For example, the previous concepts included the possibility of coincidence sorting by the firmware of the CCB for a further data rate compression.

The firmware rework was also used to split the control of *pheno*PET (*DPCShell*) and the writing of data (*phenostore*) into two programs. Previously, both tasks were handled by the *DPCShell*.

3.4 Data Organization and Preparation for Image Reconstruction

The recorded raw data are sorted into the folder structure (Section 3.3.3). All further processing steps are saved in the measurement directory. As a first step, the *phenosort* program combines the hits measured by the detectors to clusters originating from one particle. This also leads to a reduction of the total amount of data. The next steps are coincidence sorting and afterwards the reconstruction of images.

Before the different processing steps are discussed in more detail a general overview on the data structures are given. The next section starts with the summary of the different software packages forming the analysis and reconstruction framework.

3.4.1 Software Framework

The software toolkit for the analysis and reconstruction of *pheno*PET measurements is based on the PET Reconstruction Software Toolkit (PRESTO) and ROOT. In addition, MeVisLab is used for visualization and for the analysis of biological experiments. The main features used for this work are briefly presented in the following section.

3.4.1.1 ROOT

The analysis framework ROOT [119] is used in the version 5.34/36. ROOT is used for data analysis and visualization. For example, one and two dimensional histograms and graphs can be used for visualization and fitting. These objects and all other ROOT classes can be saved in a binary file format.

A main feature of ROOT is the integration of CINT, a C++ interpreter. CINT can load custom libraries and execute macros. Afterwards, the user can work with a command line and GUIs provided by ROOT, like the *TCanvas* and *TBrowser* for visualization.

3.4.1.2 PET Reconstruction Software Toolkit (PRESTO)

The software for the image reconstruction and analysis of *pheno*PET data is based on PRESTO version 3.01 [120, 121, 122]. PRESTO provides the reconstruction algorithm and especially the calculation of the system matrix c_{ij}. Therefore, classes for the handling of symmetries as well as measured and reconstructed data are provided. Further classes allow geometrical calculations in 3D. PRESTO allows the storage of the system matrix in RAM and an efficient access of the data for a fast calculation.

Furthermore, PRESTO provides the option to add own modules and classes to the toolkit. These classes can use the implemented interfaces. For example, a base class is available, which provides an interface for reading and writing of inherited classes to disc. In addition, a large set of macros for the preprocessor of the compiler are provided. For example, a fast access to the logging class of PRESTO is provided. The output can be printed to the shell or a log file. Two other aspects are quite convenient: Setup and starting of multi-threaded functions and the creation of exceptions.

In addition, PRESTO provides a class for the creation of configuration files called *VariableList*. This class allows the reading and interpretation of strings, bools, integers and floating point numbers. For strings a nesting of up to 19 parameters is possible. The nested parameters can be of any type.

The PRESTO libraries are also compiled for CINT. Here, an access on the visualization of geometrical objects from PRESTO or measured data are available.

3.4.1.3 Libraries for Quantitative Image Reconstruction

In 2018, after about one and a half years of work, the update to the PRESTO version 3.01 was installed for *pheno*PET. This update provided access to the development tools of PRESTO and allowed the creation of new modules.

In the meantime a collection of libraries called *phenoPETQuantification* has been developed. These contain functions and classes for the analysis and visualization of data with ROOT. This analysis focuses on the coincidence sorting and the analysis of count rate corrections. The libraries are also compiled for CINT and can be combined with PRESTO.

3.4.1.4 MeVisLab

MeVisLab (version 2.8.1, MeVis Medical Solutions AG[5]) is a program for the analysis and visualization of medical imaging data. MeVisLab uses a GUI for visual programming. Here, predefined modules can be combined with user-developed modules. The analysis of biological experiments is done with tools developed by IBG-2. In the scope of this thesis MeVisLab is used for the visualization of reconstructed images in 3D.

---

[5] MeVis Medical Solutions AG: Caroline-Herschel-Str. 1, D-28359 Bremen, Germany

3.4.2 Configuration Files

As already discussed in Section 3.3.3 the GUI creates a directory hierarchy to store the measurements. The further analysis steps extend the content of these directories with their results and configuration files containing the used parameters. In this section an overview of the configuration files created and used during the analysis and reconstruction of a plant measurement is presented.

The *phenosort* program creates a file with all parameters used in the analysis and a summary of the results in an easy readable text file. The further analysis steps rely on the classes from *phenoPETQuantification* and PRESTO.

The global configuration file defines the directory hierarchy and file names for general data required for all image reconstructions. This covers all calibrations and corrections as well as the precomputed system matrix and all further basic structures.

The measurement configuration file is created by the coincidence sorter and documents the applied parameters. Here, also the file names of the out put like *single* head curves and the coincidence file are defined as well as the names for reconstructed images. All names contain the parameters applied during the analysis for a secure access of specific data.

Handling of corrections for the image reconstruction is done with a class called phenoPETCorrectionLoader. This handles the loading of corrections during an image reconstruction by a unique identifiers, which is defined during the creation of a correction. Here, the parameters of the analysis and for the image reconstruction are used to identify the specific set of correction factors. This is restricted to parameters potentially influencing a specific correction. A separate handling is required for the attenuation and scatter correction, as they depend on the measured plant or phantom.

Dynamic image reconstruction is configured in a separate file. Here, the frame length and the start time of the first frame as well as the end time are provided. A shift of the start of a following frame different from the frame length can be defined. Furthermore, the identifiers for all corrections are defined. This last file should allow a user an easy configuration of a reconstruction.

3.4.3 Structure of List Mode Files and Event Structure

Single photon candidates and coincidences are saved in a list mode format. These files also contain packages with information on the recorded data packages and a timestamp. The file structure is presented in Table 3.1.

Table 3.1: List mode data structure. The frame data are repeated for the complete measurement duration. The content of the frame data is presented in Table 3.2.

Information	Comment
Absolute timestamp	Optional, as unix time format.
frame Data	Data of first frame
frame Data	Data of second frame
...	repetition of frame data
frame Data	Data of last frame

Table 3.2: Structure of frame data in list mode files. Files contain either *singles* or coincidences (*prompts* and *randoms*). The content of the packages is summarized in Table 3.3.

Package Type	Comment
Event Data	first *single* or coincidence
Event Data	second *single* or coincidence
...	repetition *singles* or coincidences in chronological order
Event Data	last *single* or coincidence of this frame
module status	Information on modules with valid raw data packages
Over long package status	Optional package. Containing information on all modules with overlong raw data package
Relative timestamp	timestamp in ms relative to start of measurement. Calculated from frame data. Only available if a given minimum amount of time has passed, typically 1 s.

In Table 3.2 the structure of the frame data are presented. Each package is 8 B long, from which 7 B are used for data and 1 B is used as identifier. Possible identifiers for events are *single*, *prompt* or *random*. The two types of status packages and the two different timestamps also have separate identifiers. The absolute timestamp contains a unix timestamp and its identifier. The details of all packages found in the frame data are presented in Table 3.3. Energy values are always provided with a resolution of 4 keV[6]. Position information are provided as a module number and a crystal number on this module.

Table 3.3: Structure and information provided by different data packages, which are found in a frame. The number of bits show the required memory for each information. The energy values have a resolution of 4 keV[6].

Byte	Content for different package types			
	event		Status package	timestamp
0 (Type)	*single*	*prompt* or *random*	module or over long package	relative timestamp
1	crystal position	crystal position, early *single*	frame number	timestamp relative to start with 1 ms resolution
2			one status bit for each module; bit indicates valid data or an over long package, depending on package type	
3	energy	energy		
4	timestamp with a resolution of 19.5 ps	crystal position, late *single*		
5				
6		energy		
7		time difference (resolution: 19.5 ps)		

3.4.4 Clustering and Calibration

The first processing step is the identification of photon candidates (*singles*) within the data measured by the DPCs. The measured raw data are the hits recorded by the *dies*. The clustering combines all hits on a *tile* based on the timestamps within the time interval called

---

[6] Energy calibration of *pheno*PET does not account for the saturation of SiPM cells, see Section 3.4.4.1.

clustering window. This step is performed by *phenosort*, a program developed by Matthias Streun.

The first clustering window is opened by the first hit on a *tile* in a frame. An open clustering window is closed as soon as a hit after the end of the clustering window is found. This triggers the processing of the finished cluster. Furthermore, a new clustering window is opened. At the end of a frame all remaining clusters are processed. The currently used clustering window has a size of 5 ns.

The resulting cluster has the timestamp of the first hit. The position is calculated on the *die* with the highest number of triggered cells [123]. The x and y positions on this *die* are calculated as weighted mean from the four *pixel* values. Those positions are assigned to a crystal on the *die*. Therefore, a calibration to identify the different crystals is obtained from a flood map, which is histogram with the x and y positions of each cluster on a *tile*. An example flood map with the crystal separation is shown in Figure 3.6a.

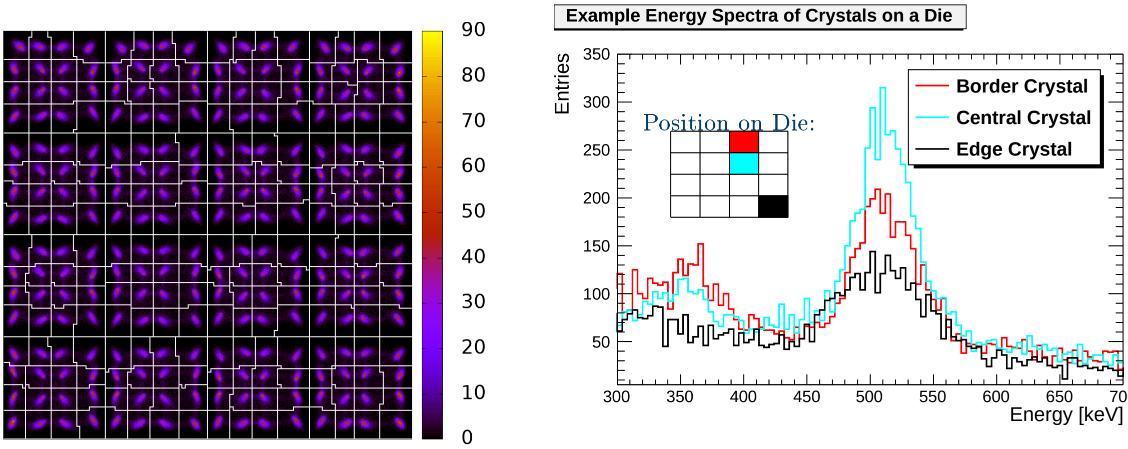

(a) Flood map.

(b) Energy Spectra of three crystals from the top left die.

Figure 3.6: Flood map and energy spectra from a 300 s measurement with a rotating rod source. The flood map illustrates the crystal separation of *tile* 0 of module 18. The energy spectra show the different count rates depending on the crystal position.

To visualize the energy resolution of the detectors exemplary energy spectra of three crystals are presented in Figure 3.6b. The energy value is calculated by summing up the triggered cells of all hits within the clustering window. Afterwards a linear calibration of the identified crystal is applied. The calibration scales the count value of the photo peak to 511 keV. The position of the photo peak is obtained from a previous measurement that used a simple source and a sufficient number of counts. An overview of the energy resolution for all crystals is given in Figure 3.7. The mean energy resolution is 16.6 % at 511 keV.

The identified *singles* are written to a list mode file of *singles* called *clusters.bin*. The *phenosort* program also calculates the relative timestamps. To reduce the amount of data a energy threshold of 248 keV[7] is applied to the *singles*. An alternative energy window of 248 keV to 752 keV[7] was investigated, e.g. [114]. Here, an increased peak sensitivity is reported with ^{22}Na point source.

---

[7] Energy calibration of *pheno*PET does not account for the saturation of SiPM cells, see Section 3.4.4.1.

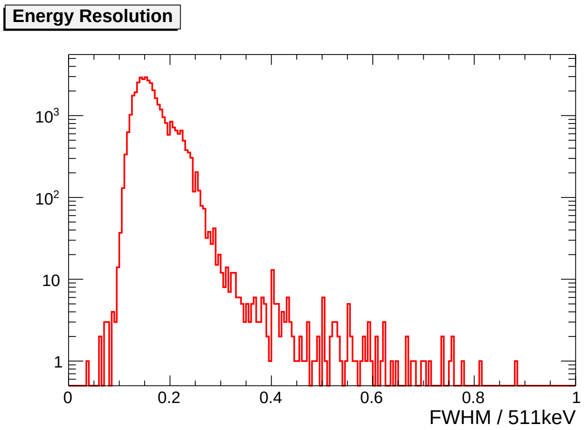

Figure 3.7: Energy resolution as Full Width at Half Maximum (FWHM) of the 511 keV photon peak for all crystals. The mean resolution is 16.6 % and the median resolution is 15.8 %.

3.4.4.1 Saturation Effect in Energy Calibration

It has to be noted that the energy spectra of *pheno*PET cannot directly be compared with other detectors due to the saturation of the cells on the SiPM. This saturation is not taken into account by the calibration. The comparison of a measured spectrum of LYSO and a GATE simulation of LYSO reveals that 349 keV measured by *pheno*PET correspond to about 309 keV without the saturation effect by a comparison of *singles*. The simulation setup is presented later in Section 3.6. In addition, the GATE data were smeared with the mean energy resolution (see Figure 3.7). The resolution for lower energies is calculated according to the inverse square law implemented in GATE [64]

$$FWHM(E) = 17\,\% \cdot \sqrt{511\,\text{keV}} \cdot \sqrt{E}\ .$$

A Gaussian fit to the 306 keV photon peak of the LYSO decay gives the two values above.

The energy values provided by *pheno*PET are biased. Therefore, a comparison between data obtained with *pheno*PET is not effected by the saturation. The comparison with other detector systems is more challenging and requires caution.

3.4.5 Coincidence Sorting

The coincidence sorting aims to identify pairs of *singles* that are within a given timing window and thus most probably originated from the same β^+ decay. The *phenoGateSorter* uses ideas implemented by the OpenGATE collaboration [63]. It behaves like a multiple coincidence window sorter with a *takeAllGood* handling of *multiple* coincidences. Detailed information on the *phenoGateSorter* and the initial coincidence sorter of *phenosort* as well as the reason for the change are presented in Chapter 4.

The default parameters for the coincidence sorter can be modified in the user interface. The following default parameters are used: The *phenoGateSorter* uses an energy window of 348 keV to 652 keV[8] and a coincidence timing window of 2.5 ns. To analyse *random* coincidences, a delayed coincidence method is implemented with a delay of 20 ns. The FOV is restricted to coincidences between a sector and the 11 opposing sectors, which only excludes coincidences between *singles* detected on the same sector.

In Figure 3.8 the timing spectra of a centered plant measurement and a rotating rod source are presented. The centered pot of the plant has a single peak and the rotating rod source has two peaks at about −0.5 ns and 0.5 ns. This indicates that the timing resolution is good enough to observe the Time of Flight (TOF) differences between the two annihilation

---

[8] Energy calibration of *pheno*PET does not account for the saturation of SiPM cells, see Section 3.4.4.1.

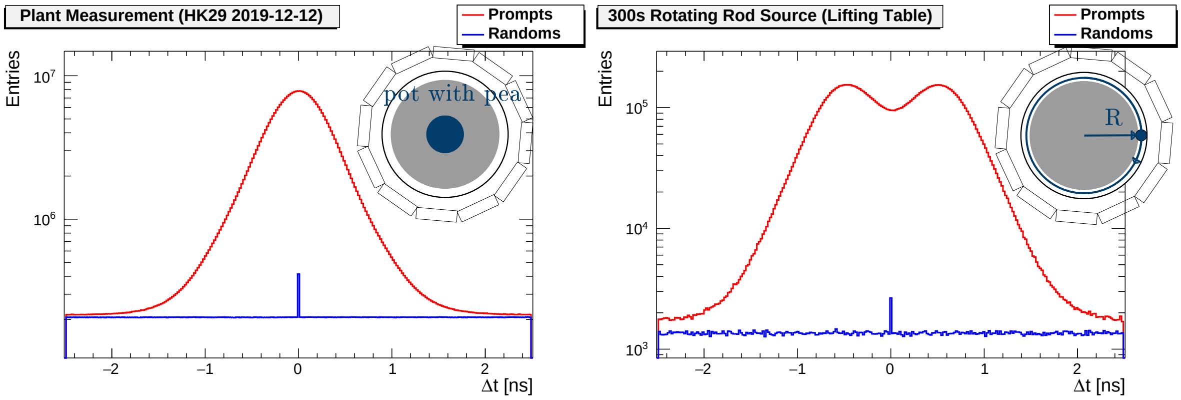

Figure 3.8: Time difference between *singles* forming a coincidence. The pot of the plant measurement was centered in the FOV. [^{11}C]CO$_2$ was applied to the plant and measured for 2 h. The ^{68}Ge rod was rotating two cycles at a radius $R \approx 95.9$ mm. The rotation system mounted to the lifting table is used (see Section 3.7).

photons. The TOF is the time required by a photon from the annihilation to the detector crystal. Therefore, the time difference contains a limited information on the position of the decay. These time difference result from the path length difference between the position of the decay to the crystals detecting the photons. The presented rotating rod source can be approximated with a cylinder shell of the same radius. The path length differences are dominated by the length of intersection between this shell and the Line-of-Response (LOR). They correspond to time differences between 0.26 ns and 0.76 ns with an average of 0.55 ns, which is approximately the position of the peaks. A further reduction of the coincidence window to about 2 ns seems possible. This step will be based on the image quality after all corrections are available.

3.4.6 Control Plots of Measured Data

3.4.6.1 Hit map

A hit map displays the number of events in each crystal. For the visualization the detector is rolled out to a 2D plot. The crystals are identified with their position along the ring and the ring number, i.e. the axial position, starting from the bottom. This results in an array

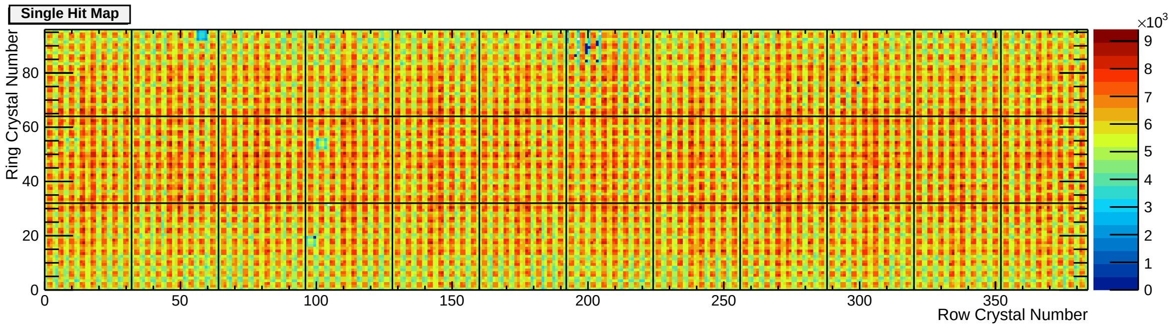

Figure 3.9: Hit map *singles* measured during a 300 s measurement with two full rotations of a rotating ^{68}Ge rod source. The black lines mark the 36 modules, each with 2×2 DPCs resulting in 32×32 crystals.

384×96 due to the twelve sectors and three modules rings. For *singles*, the number of events within an energy range is given in each pixel. For *prompt* or *random* coincidences both crystals contributing to the coincidence are displayed.

An example for a *single* hit map is given in Figure 3.9. The hit map shows a clear pattern on each DPC that correlates to the crystal matrix and the coupling areas between crystals and *pixels* (see Figure 3.3). The crystals with transparent coupling have high counts. The crystals at the boarders of each *die* show lower number. Here, also only a fraction of the crystal is coupled to the *pixel*.

3.4.6.2 Head Curve

Head curves are used to display and analyze the temporal behavior. Therefore, the number of events in a time interval, usually 1 s, are plotted over the acquisition time (see Figure 3.10. The head curves can show *singles*, *prompts* or *randoms* (Figure 3.10a & Figure 3.10b) measured by one module or the sum of all modules. Coincidence head curves use a restricted FOV, by allowing only coincidences between a module and a number of opposing modules. In addition, for coincidences the number of events detected by module combinations can be plotted (Figure 3.10c).

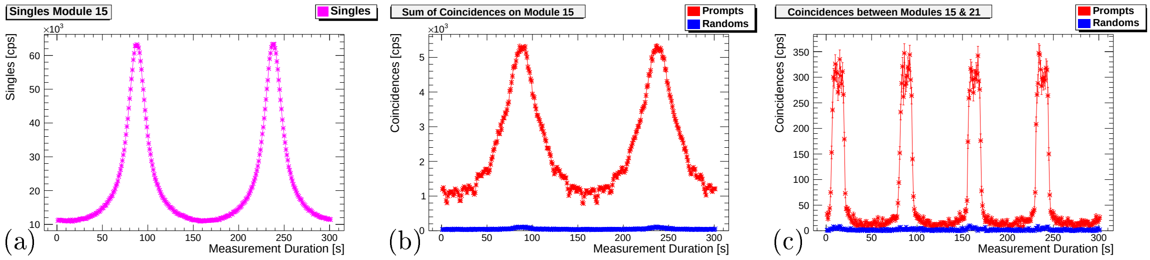

Figure 3.10: Examples for head curves of a rotating rod source. (a) *Singles* detected by module 15. (b) *Prompts* and *randoms* detected by module 15. and any other module. (c) *Prompts* and *randoms* detected by module 15 and 21. The number of *randoms* is low due to the low count rates.

During the coincidence sorting all head curves are created. These curves accept only events within the energy window used for the sorting. Each head curve is created for two cases. The first case contains the raw counts. The counts of the second curve are corrected for missing data due to the frame dropping at high count rates. The correction is described in Section 5.4.1. The default number of opposing modules for coincidences is set to 7. All these head curves are saved as graphs with error bars in ROOT files.

3.4.6.3 Energy and Timing Spectra

The energy of events or time differences between the two *singles* of a coincidence Δt of each event can be displayed as histograms. Energy spectra can include all modules or only entries of a specific module or smaller structure down to a single crystal. The time differences are either given for the complete system or for all events with a specific detector module. It is also possible to fill the time differences between two modules into a histogram. The Δt are the difference between the timestamps of the later *single* and the earlier *single* and thus always positive. For the visualization time differences are displayed as negative if the module number of the first *single* is greater than the module number of the second *single*.

3.5 Image Reconstruction with PET Reconstruction Software Toolkit

The implemented algorithm is Ordinary Poisson Maximum Likelihood Expectation-Maximization (OP-MLEM). The update formula for the next iteration step $n+1$ is given by

$$\lambda_j^{(n+1)} = \frac{\lambda_j^{(n)}}{\sum_i^{N_j} c_{ij} s_i} \sum_i^{N_j} c_{ij} s_i \frac{p_i}{\hat{p}_i^{(n)}} \tag{3.1}$$

with

$\lambda_j^{(n)}$	activity in voxel j after iteration step n
c_{ij}	matrix element of LOR i and voxel j
s_i	sensitivity of LOR i
p_i	*prompts* measured by LOR i
$\hat{p}_i^{(n)}$	expected events for LOR i after iteration n
N_j	Number of LORs passing through voxel j.

The modelling of the measurement process is done with the ordinary Poisson model. Thus, the expected number of events is calculated according to

$$\hat{p}_i^{(n)} = s_i \cdot \left[\sum_j^{N_l} c_{ij} \lambda_j^{(n)} \right] + VRR_i + SE_i. \tag{3.2}$$

The VRR_i are Variance Reduced Randoms and the SE_i is an estimate for the expected number of scatter coincidences. The additive corrections need to be the expectation values and no noisy estimates [71]. Thus, the estimation of the VRR from the noisier delayed coincidences is discussed in Section 3.5.3. The calculation of the scatter estimates is presented in Section 7.2.2 as part of the investigation of scatter and attenuation corrections.

The calculation of the system matrix is discussed in the following Section 3.5.1. The calculation of the s_i is discussed afterwards in Section 3.5.2.

3.5.1 System Matrix

The system matrix defines the contribution of each voxel to the LORs intersecting it. PRESTO uses a polar grid with cylinder shell segments for the reconstruction. Afterwards the images are rebinned to a Cartesian grid.

3.5.1.1 Projection Space of *pheno*PET

The model of *pheno*PET contains the designed positions and dimensions of the detector crystals. Each pair of two crystals defines a LOR. LORs contributing to a FOV are considered by two criteria: the shortest radial distance to the scanner axis and ring difference of the two crystals. For the default FOV the maximum radial distance is 90 mm and a maximum ring difference of 80. This set of LORs is called projection space.

3.5.1.2 Image Space

For the default reconstruction the results are written to Cartesian images with 216 mm × 216 mm × 203 mm. The voxel have a size of 0.9 mm × 0.9 mm × 1 mm. The polar grid in transaxial plane is illustrated in Figure 3.11. The bins have a radial size of 0.9 mm. The transverse size is defined with a constant area in mind. Furthermore, the bin size is adopted by PRESTO to preserve the symmetries. The total number of voxels in this grid is set to the same number as for the Cartesian grid. The voxel size in the axial direction is 1 mm for both grids. After the image reconstruction the voxel values are converted into the Cartesian grid.

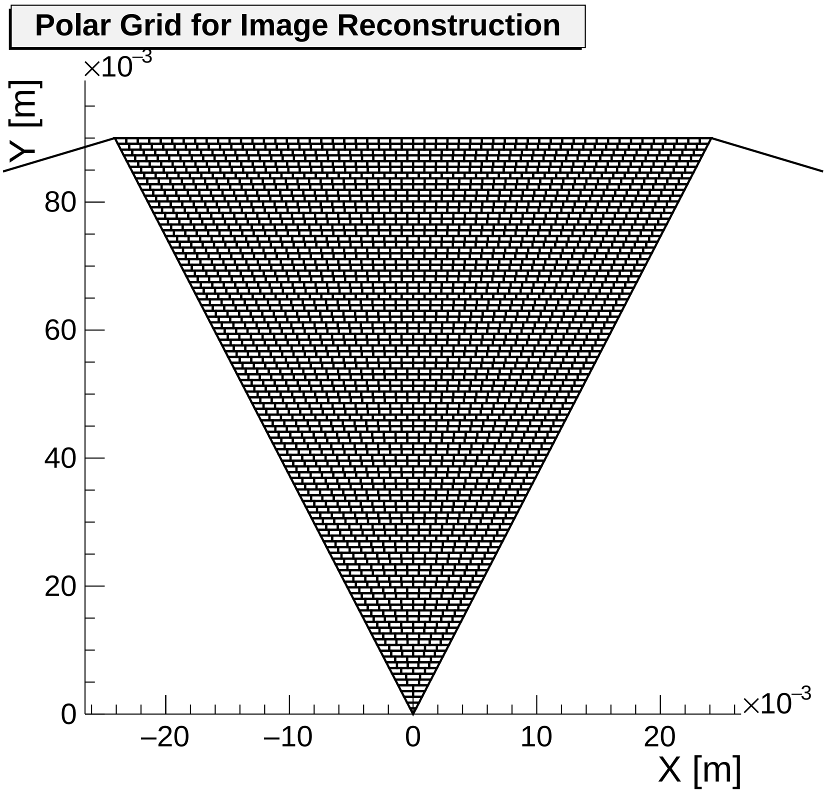

Figure 3.11: Polar grid created by PRESTO for a single sector. The grid is rotated for the further sectors.

3.5.1.3 Symmetries and Calculation of System Matrix

PRESTO reduces the size of the system matrix by utilizing symmetries. The twelve sectors address a rotation symmetry. Furthermore, two flip symmetries are implemented, one within each sector and the second one relative to the center of the scanner at $z = 0\,\mathrm{m}$.

The matrix elements are calculated as the Volume-of-Intersection (VOI) between the Tube-of-Response (TOR), defined by two crystals, and a voxel. Afterwards, the matrix elements are scaled to effective Line-of-Intersection (LOI). This allows an easy comparison to the calculation of line integrals for expectation values [124].

The reconstruction is sped up by sorting the projection data and matrix elements in the RAM. In this way, PRESTO utilizes Single-Instruction-Multiple-Data (SIMD) vectorization [122].

3.5.2 Sensitivity Model

For the ordinary Poisson implementation the detector dynamic response needs to be modelled. For *pheno*PET this is generally done according to

$$s_i^{frame}(t_S, t_E) = s_i^{static} \cdot a_i \cdot s_i^{dyn}(t_S, t_E) \cdot s^{decay}(t_S, t_E) \cdot \frac{t_E - t_S}{CF}$$

The static sensitivity s_i^{static} contains all effects that do not not change during the measurement

$$s_i^{static} = \epsilon_a \cdot \epsilon_b \cdot g_{ab}.$$

This includes the detection efficiencies ϵ_a and ϵ_b of the crystals a and b defining the LOR and the geometric sensitivity $g_i = g_{ab}$. These factors are obtained during the normalization discussed in Chapter 6.

The next factor is the attenuation correction for each LOR a_i. The measurement of the attenuation map is discussed in Section 7.1 and the calculation of the sensitivity in Section 7.1.1.

The dynamic sensitivity s_i^{dyn} corrects for three count-rate-dependent effects. First, the dropping of frames is corrected, $f_i^{frames}(t)$. Afterwards the dead time of each detector module $sDCF_a$ is corrected. In the end, a small global factor remains $coinDCF$. The three dynamic correction factors are defined as expected data over measured data. For the calculation of the s_i^{dyn} is proportional to the inverse of $f_i^{frames}(t)$, $sDCF_a$ and $coinDCF$. The detailed investigation of the count rate corrections are discussed in Chapter 5. The calculation of $s_i^{dyn}(t_S, t_E)$ for a specific image frame is presented in Section 5.2.

The decay correction $s^{decay}(t_S, t_E)$ corrects for the reduction of the activity of the radioactive source between the start of two image frames and during a frame. It is calculated according to Equation (2.4). The final factor does the conversion into an activity concentration in $\mathrm{Bq\,ml^{-1}}$. It consists of the calibration factor, CF, and the duration of the frame $t_E - t_S$. The calculated of CF is presented in Section 7.7 after all corrections have been implemented.

3.5.3 Random Variance Reduction

For *pheno*PET a variance reduction algorithm was already available in PRESTO. This algorithm is based on detector blocks [80, 81]. The number of delayed coincidences per LOR D_i is calculated for each crystal i

$$D_i = \frac{1}{N_i} \sum_{j}^{N_i} d_{ij}$$

with the sorted delayed coincidence d_{ij} between crystal i and j and the number of LORs contributing to the crystal N_i. The number of Variance Reduced Randoms VRR_{ij} is calculated as

$$VRR_{ij} = \alpha \times (D_i \times D_j)\,.$$

The global scaling factor α is required to ensure that the total number of *randoms* does not change, in other words

$$\alpha = \frac{\sum_{ij} d_{ij}}{\sum_{ij} D_i \times D_j}.$$

3.6 Setup for Simulation with OpenGate

A basic simulation with GATE, version 8.0, and GEANT 4 version 10.3.1 is implemented. The simulation is based on a configuration created by Mirjam Lenz and Matthias Streun for a future detector system with the same detector modules. For the simulation of *pheno*PET the crystal matrix was changed from a regular grid to the designed irregular crystal positions. The setup is visualized in Figure 3.12. The extruded polystyrene (XPS) housing, electronics and holding structures are not included. The plant port contains a 2 mm thin aluminum cylinder.

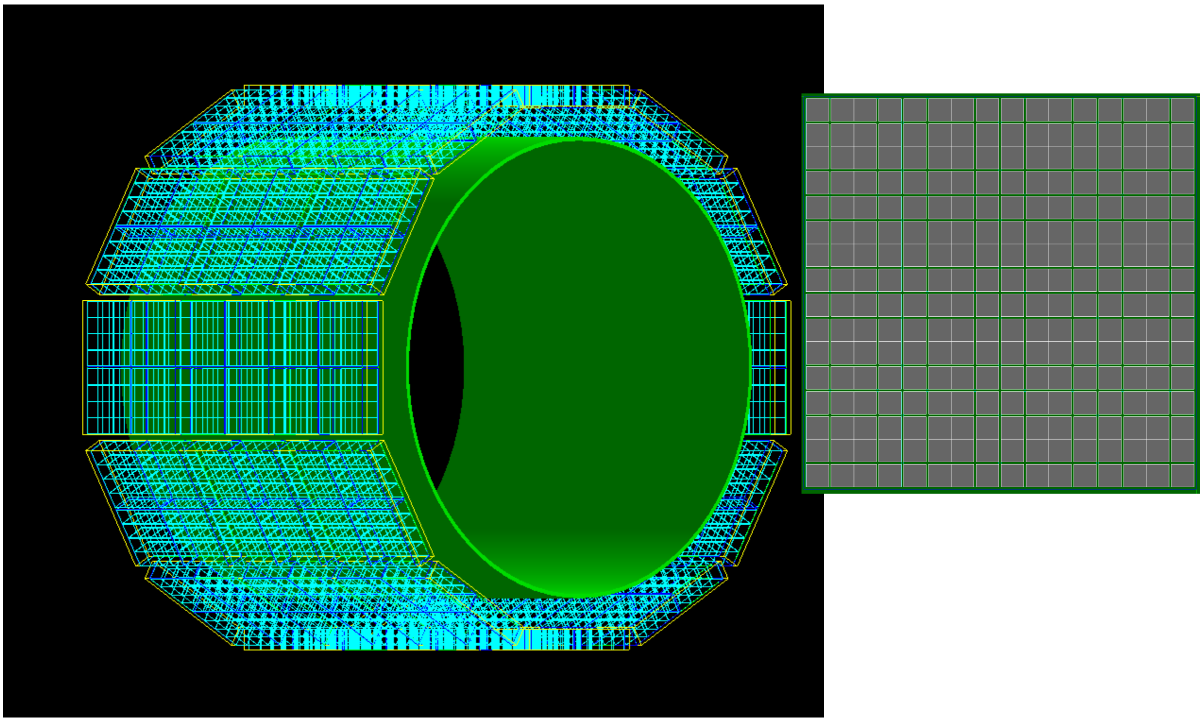

Figure 3.12: GATE implementation of *pheno*PET. The central aluminum cylinder is displayed in green, sectors in yellow, *tiles* in blue and *die* in cyan. The crystals are shown in gray in the visualization of a single *tile*.

The simulation loads the *QGSP_BIC_EMY* physics lists which includes the *emstandard_opt3* model. In addition the *Decay* and *RadioactiveDecay* processes are enabled for the simulation of the ^{176}Lu, which is contained in the LYSO crystals.

A radioactive source is included to simulate the decay of ^{176}Lu within the crystals. The activity in all crystals is estimated from the crystal dimensions of *pheno*PET combined with the density of the crystals and the lutetium fraction. This results in an activity of about 0.356 MBq. In addition, other sources are added as required for individual simulations.

The readout of GATE is configured to add up all energy depositions on a *tile* like the *phenosort* for measured data. The time point of each of these *singles* is the first interaction and the position is calculated by an energy-weighted centroid [64]. The detector simulation does not contain any energy or time resolution.

3.7 Rotation System

The *pheno*PET system needs a measurement of attenuation and a normalization. A rotating rod source was chosen to determine both. In total, three different rotation systems were used. The first system failed after half a year and was replaced with an intermediate solution. This second system was only improvised and not optimized. Thus the orientation was not perfect, as discussed later. The final system is integrated in the lifting table and was designed by FL Mechanik[9]. In this section a short overview on the second and the third system are given.

---

[9] FL Mechanik GmbH & Co.KG: Sankt-Jöris-Str. 36, D-52477 Alsdorf

3.7.1 Setup of Intermediate System

The intermediate system was a rotation table of type DT130-360-SM1 with a Motion Controller Typ - FMC 223, both produced by Feinmess Dresden[10]. It was mounted on a plate and profiles to the frame of the old table. A picture is given in Figure 3.13a. The system was mainly used for test measurements and the monitoring of the system performance. Thus the optimization of the mounting was neglected. The plate at the bottom of the plant port was also required for positioning of plants. Thus biological emission experiments could not be performed during a rotation of the source.

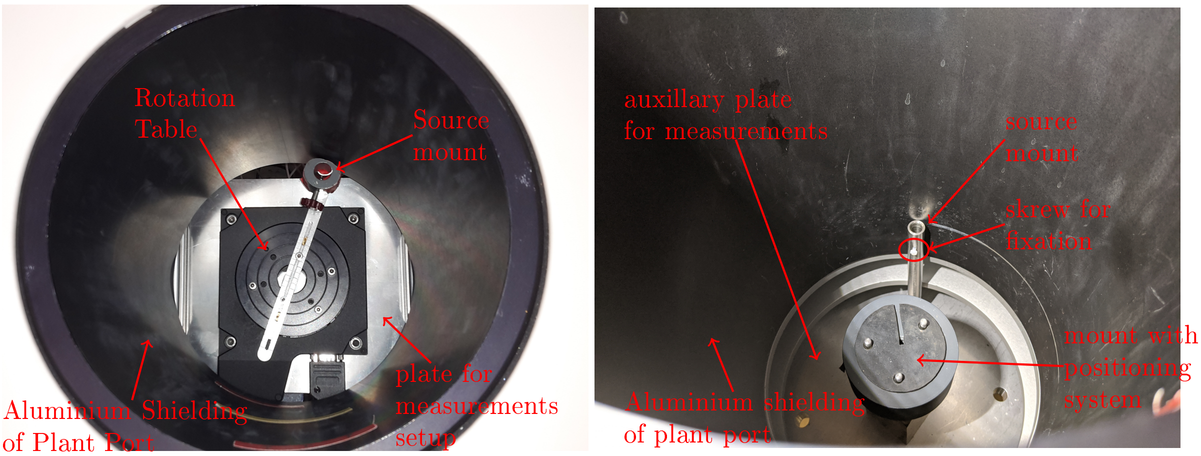

(a) Intermediate rotation system.

(b) Rotation system part of the lifting table.

Figure 3.13: Setup of rotation systems. Images are taken from the top inside the plant port.

A ready to use GUI allows rotation to relative and absolute positions but does not allow endless rotation. The Application Programming Interface (API) provides the possibility of an endless rotation, which was made available in a GUI written by Andreas Fischbach. This GUI lacks a calibration between the internal units and an angular velocity in $^\circ\,\mathrm{s}^{-1}$. A calibration experiment showed a value of 30 interval units is approximately an angular velocity of about $2.35\,^\circ\,\mathrm{s}^{-1}$.

3.7.2 Setup of Rotation System of the Lifting Table

The final rotation system is mounted below the plant port. Only the arm with the source is within the plant port and allows a movement of *pheno*PET along a plant height. The system was designed and mounted by FL Mechanik. The mechanical workshop of the IBG-2 adjusted the system relative to the mounting structures of the modules. A picture of the setup is given in Figure 3.13b.

The control software of the motor has an absolute calibration of the rotation. The user needs to take into account the transmission ratio between the motor and the rotating arm. This ratio decreases the motor velocity of $19.2\,^\circ\,\mathrm{s}^{-1}$ by a factor of 8 to a velocity of the source of $2.4\,^\circ\,\mathrm{s}^{-1}$.

3.7.2.1 Orientation of Rotation Axis

The position of the rotation system mounted at the lifting table is validated with a measurement and analysis developed by Matthias Streun. His analysis determines the height and

---

[10] Feinmess Dreden GmbH: Fritz-Schreiter Straße 32, D-01259 Dresden

orbiting radius of a rotating point source from the data. This source is a acrylic cube with a side length of 10 mm with ^{22}Na smaller than 0.3 mm in the center [65]. The variations of the height are measured to be below 0.1 mm. The radius of the rotation indicates a shift of the rotation axis of about 0.5 mm away from the center of the FOV, which is acceptable for our purposes. More importantly, the measurements require a reproducible setup and not a perfect match between the rotation and the scanner axis.

3.7.3 Confirmation of Orbiting Frequency

To confirm the calibration of the rotation system and for calibration of the intermediate system a method to analyse the rotation velocity from measured data was established. The angular velocity is set close to $2.4\,^\circ\,\mathrm{s}^{-1}$ for measurements which is equal to an orbiting period of 150 s or 2.5 min. This allows an easy determination of the measurement duration with full rotations.

3.7.3.1 Measurement of Orbiting Period

The rotation period is determined by long measurements with a larger number of rotations. The *single*, *prompt* and *random* head curves of a module show clear peaks whenever the source passes. The time difference between those peaks are constant and equal to the rotation period. In the following analysis the *single* head curves are used. The head curves are filled with an integration interval of 1 s for each point and the correction of dropped frames is applied (see Section 5.4.1).

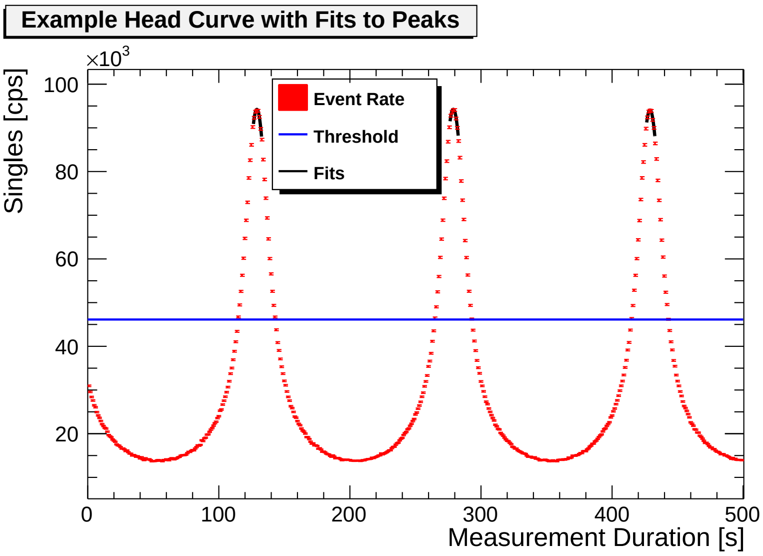

Figure 3.14: Examples on fitting of peak positions to determine the orbiting periods. The blue line represents the threshold for the identification of peak candidates.

The first step is to determine the peak positions, which is illustrated in Figure 3.14. Therefore, the average and standard deviation of all points of the head curve is determined. Peak candidates are defined by a region that is above the average value plus the 70 % of the standard deviation. The exact position of a peak is determined with the fit of a parabola to the peak candidates. A fit interval has a minimum width to exclude small fluctuations around the threshold. A width of 6.25 s is used, which is half the time the source is expected to be in front of each module.

The resulting time points are plotted over the numbers of the peaks. A linear fit is applied. The slope is the orbiting period and the offset results from the starting position of the source.

3.7.3.2 Results and Discussion

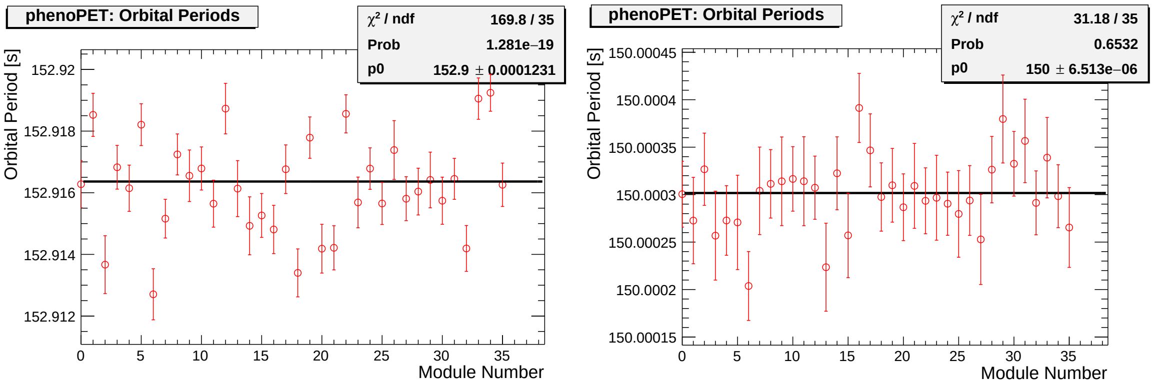

(a) Intermediate rotation system. The measurement duration is 28 800 s or 192 rotations.

(b) Rotation system mounted on lifting table. The measurement duration is 54 000 s or 360 rotations.

Figure 3.15: The rotation periods were obtained for each module from the same scan. A constant is fitted to determine the average. A clear shift is visible for the intermediate system while the newer system match really well with the set value of 150 s.

The resulting orbital periods for each module are given in Figure 3.15. The orbiting period of the intermediate system is about 3 s longer due to the slightly lower velocity. This can result in a significant difference for long measurements and needs to be taken into account. The system mounted on the lifting reports smaller differences. All results differ well below the integration interval for the head curves of 1 s. Thus, the rotation period of 150 s can be assumed to be exact for the setup of further measurements.

Chapter 4

Coincidence Sorting and Delayed Coincidences

Positron Emission Tomography (PET) uses the back-to-back emitted photons of the annihilation to reconstruct an image of the activity distribution. Each single detector only records one of these photons. The coincidence sorter searches the recorded *single* events, which are within the energy window, for pairs of *singles* in coincidence. *Singles* in coincidence need to be within a given time window, the so called coincidence window t_{coin}. Furthermore, the coincidence sorter is also used to estimate the *random* coincidence rates using the delayed coincidence method (see Section 2.7.3.1).

A coincidence sorter with a delayed window algorithm was implemented for *pheno*PET at the start of this work and is referred to as *phenoSorter*. This sorter was developed by the Central Institute of Engineering, Electronics and Analytics (ZEA), Electronic Systems (ZEA-2) before the redesign of the firmware. During the analysis of the increased dynamic range provided by the new firmware, inconsistencies of the *phenoSorter* were detected (see Figure 4.1).

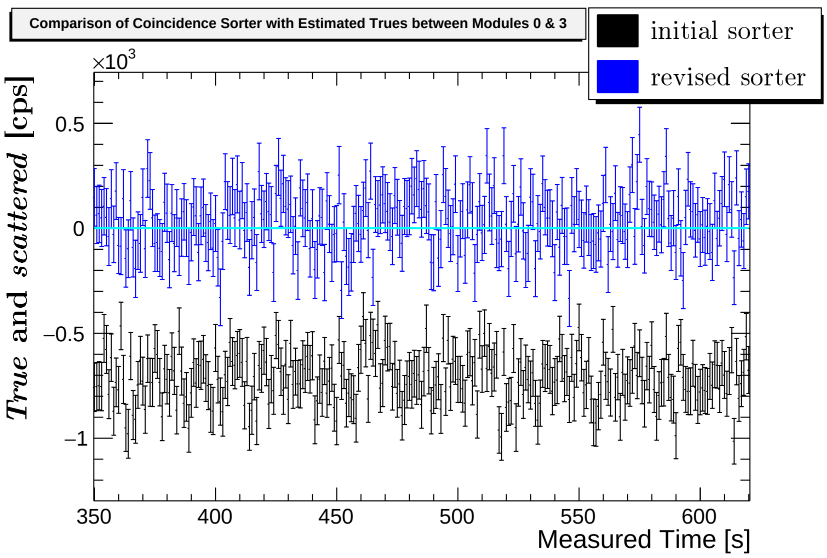

Figure 4.1: *True* and *scattered* coincidences between two outer modules (0 and 3) for a phantom centered in the Field-of-View (FOV) (vial filled with a small disc of about 100 MBq of ^{18}F diluted in water). As no activity is present between the two modules in the lower ring, no *trues* are expected. Using the initial coincidence sorter implementation (*phenoSorter* with *killAll*), estimating the *trues* and *scattered* by subtracting *random* coincidences from the *prompt* coincidences resulted in negative count rates (black points). The revised algorithm (*phenoGateSorter* with *takeAllGood*) presented in this chapter was able to resolve this issue (blue points).

The OpenGate collaboration also observed a mismatch of different coincidence sorter implementations [125] which led to a redesign of their sorter [63]. Based on their ideas an adapted version of this sorter was implemented which is referred to as *phenoGateSorter* in the following chapters where it is compared to the *phenoSorter* of *pheno*PET. Furthermore, a second strategy of handling *multiple* coincidences (*takeAllGood*) was implemented in addition to the existing handling (*killAll*).

In the following chapter the two sorter implementations and the two strategies of handling *multiple* coincidences are described. The resulting four sorting behaviors are characterized with simulated and measured data. This work led to the change of the coincidence sorter to the *phenoGateSorter* with the *takeAllGood* handling of *multiple* coincidences.

4.1 Sorting Algorithms

First the basic concept and general aspects common for both coincidence sorters are discussed. This includes the handling of *multiple* coincidences. Afterwards the two coincidence sorter implemented for *pheno*PET are described.

4.1.1 General Software Structure

The software for coincidence sorting consists of two major parts. The first part reads the *singles* and provides the data structures for storing them. The second part performs the actual sorting and is provided with access to the *singles* by pointers. The same behavior is ensured for measured and simulated data. Separate classes for *singles* and coincidences are used. For simulated data those are extended with additional information the simulation provides like event numbers.

The sorting can be done for one data frame of 327.68 µs after another because the detector setting prevents trigger for 80 ns after the start of a new frame and thus coincidences between two data frames are not possible. Thus the data structure contains a buffer to store the *singles* of one frame.

For each *single* it is checked if it is within the energy window 348 keV to 652 keV[1]. Those *singles* are sorted chronologically. Furthermore, the module status package is used to exclude data from modules which are not trusted like overlong packages.

The sorter gets those presorted and validated data to apply the coincidence sorting on the collection of pointers. This allows to run several sorting processes with only a single data storage.

The coincidence sorter is able to pre-select recorded coincidences by a rough check of the FOV. Coincidences between a module and a number of opposing sectors are taken into account to limit the investigated FOV. A number of 7 opposing sectors means that coincidences between a module and the modules on the opposite sector and the three sectors in each direction of the circle are accepted. The default parameter is 11 opposing sectors accepting all coincidences except of those between modules on same sector. Before the reconstruction the FOV is restricted further. At this point only events on Lines-of-Response (LOR) passing through the desired FOV are accepted.

4.1.2 Handling of Multiple Coincidences

For all sorting algorithms the occurrence of so called *multiple* coincidences (*multiples*) is an issue. Those events have more than two *singles* in a coincidence window. A *multiple* can be treated in different ways. GATE, for example, has implemented many different strategies [64]. For *pheno*PET two strategies are implemented, namely *killAll* and a *takeAllGood*.

The *killAll* handling of *multiples* is the strictest implementation. Here all occurring *multiples* are discarded. This aims for a pure collection of *prompts* with a low number of *randoms*.

The *takeAllGood* handling is the loosest alternative. Here, all *singles* in a coincidence window are combined to coincidences if they fulfill all requirements. Those requirements are

---

[1] Energy calibration of *pheno*PET does not account for the saturation of SiPM cells, see Section 3.4.4.1.

for example the geometric constrains of the FOV to each LOR and the time difference between each pair of *singles*. With this approach all *true* coincidences should be taken into account because *multiple* most often consist of a “real” coincidence, originating from a decay, and an additional *single* event [63]. The downside is an increased number of *random* coincidences.

4.1.3 *phenoSorter*: A Sector Based Coincidence Sorter

The *phenoSorter* was developed by Matthias Streun and briefly presented in [126]. The *phenoSorter* processes the *singles* within a data frame. Those *singles* are sorted chronologically into buffers, one buffer for each of the twelve sectors, see Figure 4.2a. Each sector consists of the three modules on top of each other. The coincidence sorting uses a single timing window as presented in Figure 4.2b. This figure also shows the two implementations of handling of *multiple* coincidences. For each sorting step only the first *single* of each sector is taken into account. Those *singles* within the effective coincidence window are removed from the buffers afterwards. For example in Figure 4.2b, *single* s_2 is not added to *prompt* P_0. Afterwards s_2 opens an own coincidence window. The two multiple coincidences (M_1 & M_2) show the strict suppression of *multiples* for the *killAll* handling, especially for M_2. Here s_8 is over one t_{coin} later than s_6 and discards the *prompt* (s_6, s_7). For the *takeAllGood* this time difference excludes the *prompt* (s_6, s_8). The current applied length of a base coincidence window is $t_{coin} = 2.5\,\mathrm{ns}$. Each coincidence passing the handling of *multiples* needs to fulfill the geometric constrains of opposing modules.

Random coincidences are estimated with a delayed window coincidences approach. Examples for this sorting are given in Figure 4.3b on a second set of *singles* shown in Figure 4.3a. For the delayed coincidences the timestamps of each event is shifted according to the position of the module within its ring. The shift t_{shift} is given by

$$t_{shift} = n_{sector} \times 8 \times t_{coin}$$

with the sector number n_{sector}. Afterwards the same algorithms as for *prompt* coincidences is applied, including the handling of *multiples*. Here, an example is s_6 which is not considered in the coincidence window B_1.

4.1.3.1 Changes and Major Issues

A new implementation of this sorter was developed with the structure discussed in Section 4.1.1. This implementation led to the detection and correction of a few programming errors in both implementations. These issues degraded the functionality of the sorter, especially for high count rates.

Furthermore, the initial sorter only supported the *killAll* handling. The option for the *takeAllGood* handling of *multiples* was included in the new implementation.

Further issues might result from only taking the first *single* of a sector into account for a sorting step. This shadows *singles* recorded by the two other modules and also simultaneous events on the same module detected by one of the other *tiles*. These events cannot contribute to a *multiple* but get the chance to contribute to another coincidence afterwards. This behavior strongly depends on the count rates of each module.

4.1.4 *phenoGateSorter*: Adaptations to the OpenGate Coincidence Sorter

Inspired by the coincidence sorter presented by the OpenGate collaboration a new sorter has been developed taking into account the data structure of *pheno*PET. In addition, ideas from Matthias Streun are used to create a similar behavior.

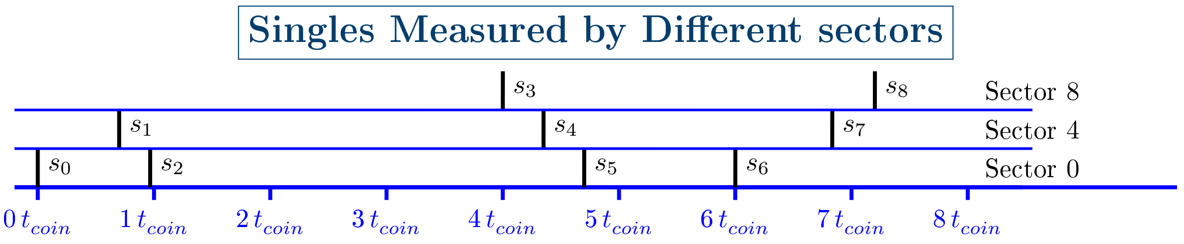

(a) Example of *singles* measured on three sectors. The timing has been chosen to visualize the sorting behavior.

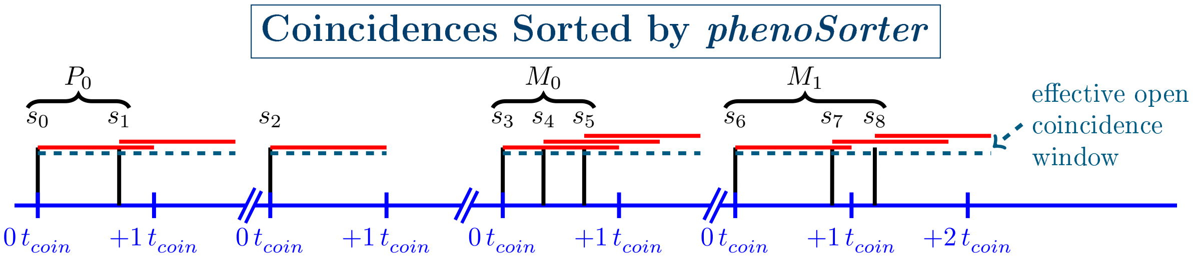

Multiple Coincidence Handling	P_0	M_0	M_1
killAll (initial behavior)	(s_0, s_1)	-	-
takeAllGood	(s_0, s_1)	(s_3, s_4), (s_3, s_5), (s_4, s_5)	(s_6, s_7), (s_7, s_8)

(b) Sorting behavior of the *phenoSorter*. Only the first *single* of a sector is taken into account for a sorting step. Afterwards the earliest sector creates a new coincidence window.

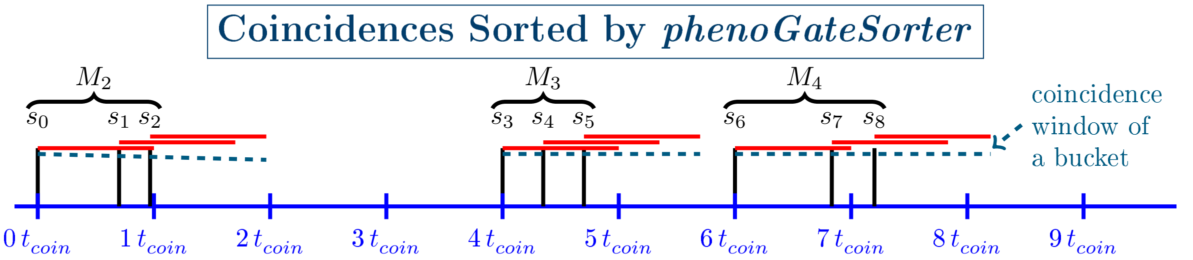

Multiple Coincidence Handling	M_2	M_3	M_4
killAll	-	-	-
takeAllGood	(s_0, s_1), (s_1, s_2)	(s_3, s_4), (s_3, s_5), (s_4, s_5)	(s_6, s_7), (s_7, s_8)

(c) Sorted coincidences obtained from *phenoGateSorter*.

Figure 4.2: Example on sorting and handling of *multiples* for *phenoSorter* and *phenoGateSorter*. The sorted coincidences of both sorters and the results of the handling of *multiples* are shown. The time information is given in multiples of the base coincidence window duration t_{coin}. For both sorters the coincidence window is extended for each additional *single* within an already open coincidence window. The tables present the coincidences taken into account for the reconstruction depending on the handling of *multiple* coincidences. Each of these pairs has to fulfill the geometric constrains of the FOV.

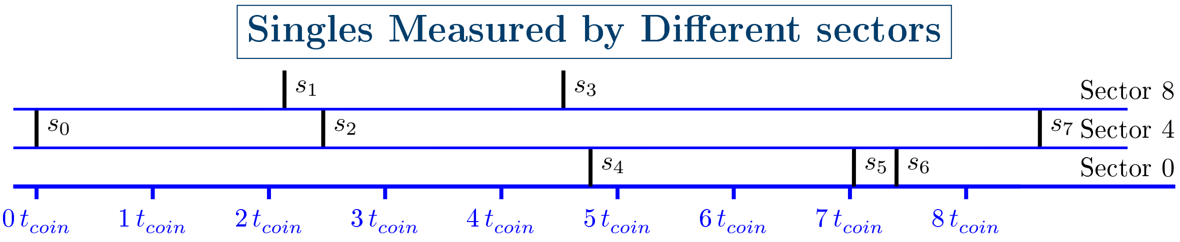

(a) Example of *singles* measured on three sectors. The timing has been chosen to visualize the sorting behavior.

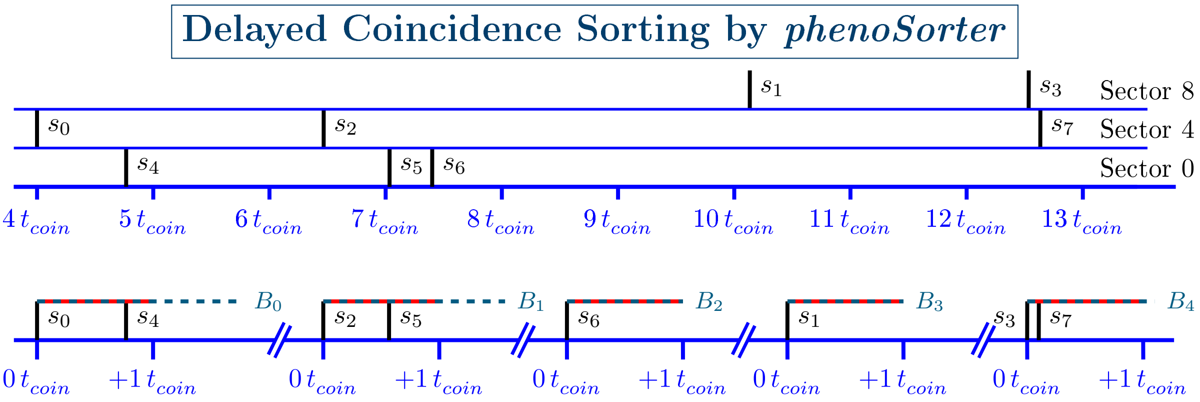

Multiple Coincidence Handling	B_0	B_1	B_2	B_3	B_4
killAll (initial behavior)	(s_0, s_4)	(s_2, s_5)	-	-	(s_3, s_7)
takeAllGood	(s_0, s_4)	(s_2, s_5)	-	-	(s_3, s_7)

(b) Delayed coincidence sorting of the *phenoSorter*. Upper part: Time shifting of *singles*. The shift is reduced from $8\,t_{coin}$ to $1\,t_{coin}$ per sector for the sake of this example. Lower part pairs of coincidences passed to the handling of *multiples*.

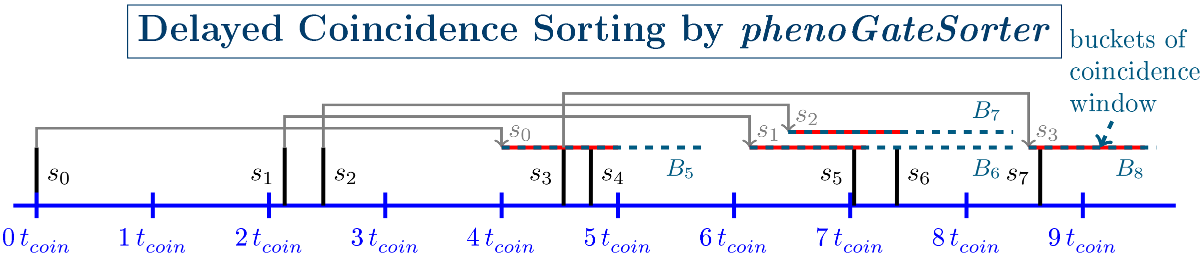

Multiple Coincidence Handling	B_5	B_6	B_7	B_8
killAll	-	(s_1, s_5)	discarded	(s_3, s_7)
takeAllGood	(s_0, s_3), (s_0, s_4)	(s_1, s_5)	(s_2, s_5), (s_2, s_6)	(s_3, s_7)

(c) Sorted coincidences obtained from *phenoGateSorter*. The delay is reduced from $8\,t_{coin}$ to $4\,t_{coin}$ in this example.

Figure 4.3: Examples on delayed coincidence sorting and handling of *multiples* for *phenoSorter* and *phenoGateSorter*. The sorted delayed coincidences of both sorters and the results of the handling of *multiples* are shown. The time information is given in multiples of the base coincidence window duration t_{coin}. For both sorters the coincidence window is extended for each additional *single* within an already open coincidence window. The tables present the delayed coincidences taken into account for the reconstruction depending on the handling of *multiple* coincidences. Each of these pairs has to fulfill the geometric constrains of the FOV.

The Gate coincidence sorter uses a coincidence window class to collect the *singles* within a coincidence window. This class stores the start and end time point of the coincidence window and all *singles* in the window. A shift of the start time point can be added for the delayed coincidence method. New *singles* are added to the coincidence window as long as their timestamp is between the start and end timestamp. Gate allows two major sorting types. A so called single-window sorter allows only one open *prompt* coincidence window at a time. A multi-window sorter allows each *single* to open a coincidence window. Afterwards only coincidences with the single opening the window are allowed.

The coincidence window class within the *phenoGateSorter* is called bucket. In Figure 4.2c the behavior of a bucket for *multiples* is presented (M_2, M_3 and M_4). The first *single* in the frame creates the first bucket. Whenever a new *single* is added the end timestamp is shifted to the timestamp of this new *single* plus the base coincidence window $t_{coin} = 2.5\,\text{ns}$. There is only one open bucket during the sorting of *prompt* coincidences.

When no more *singles* can be added, the bucket is passed to the *multiple* coincidence handling. Afterwards a new bucket is created and *singles* are added until all *singles* within this frame are processed. The last open bucket is handed over to the *multiple* processing as well.

4.1.4.1 Comparison of Coincidence Sorter Type

The *phenoGateSorter* uses only a single-window for *prompts* but is no classic single-window sorter due to the extension of the coincidence window. For the *takeAllGood* handling the combination of all *singles* in the bucket results in a multi-coincidence window sorter behavior due to the extension of the coincidence window. On the other hand for the *killAll* handling the behavior is a stricter single-window sorter, by taking into account *singles* after the last added *single*. An example for this stricter behavior is the *multiple* M_4 in Figure 4.2c.

4.1.4.2 Delayed Coincidence Implementation

The delayed coincidences implementation needs slight adaptations to achieve a behavior similar to the sorter implemented in OpenGate. Here, each *single* opens a new bucket with a start time point shifted by $t_{delay} = 8 \times t_{coin} = 20\,\text{ns}$. The end timestamp of the bucket is extended whenever a *single* is added. Examples for the delayed coincidence sorting wit the two handling of *multiples* are given in Figure 4.3c.

For the *takeAllGood* handling, only coincidences with the initial *single*, which opens the bucket, are taken into account (see B_5 and B_6 in Figure 4.3c). This results in the behavior of a multi-window approach presented by Strydhorst and Buvat [63]. Strydhorst and Buvat also point out that all further pairs are more likely *true* coincidences than further *random* coincidences of three *singles*.

For the *killAll* handling the number of *singles* in the delayed and especially the extended window becomes important to identify *multiple* coincidences. As pointed out above the sorter behaves like a single-window sorter, thus only one coincidence window is allowed. The extension of the end time point results in an unknown duration of the coincidence window of a bucket. Therefore, buckets starting during an open bucket are discarded. On example are the buckets B_6 and B_7 in Figure 4.3c. After B_6 is finished and handed over to the handling of *multiples*, B_7 is discarded because it starts during the timing window of B_6. The same would be true for further buckets starting during B_6.

4.2 Characterization with Simulated Data

For the characterization of the two coincidence sorters and the two handlings of *multiples* a NEMA rat size scatter phantom [65] is simulated with different activities. Therefore the GATE simulation of *pheno*PET is used. Results are compared to Monte Carlo ground truth data.

4.2.1 Method

The aim is to examine the performance of the two algorithms for different count rates and therefore different activity concentrations. Energy or timing resolution are not simulated. The setup of the simulation and the readout is described in Section 3.6. The aluminum shielding of the plant port was not included.

Simulated *singles* are obtained as ROOT files and afterwards handed over to the different coincidence sorters with the different handling of *multiples*. For sorting the timestamps are used to separate the *singles* into data frames similar to the Digital Photon Counter (DPC).

The simulations consist of a source of back-to-back emitted photon pairs with 511 keV each and the ^{176}Lu background from the lutetium-yttrium oxyorthosilicate (LYSO) crystals. The source is a rat size scatter phantom defined for the NEMA standard for small animal PET [65]. This scatter phantom is a polyethylene cylinder with a diameter of 50 mm and a height of 150 mm. The active volume is a water cylinder with a diameter of 3.2 mm at a distance of 17.5 mm to the central scanner axis. For this simulation the translation is done along the x-axis towards a front of a sector. To limit the computation time only a short time interval is simulated. Furthermore, to simulate roughly the same amount of events for each activity level, the measurement duration is decreased for increasing activity. Here, the important aspect are the different time differences between individual decays. The simulation duration and activities are given in Table 4.1.

For the analysis a third sorter is implemented to obtain Monte Carlo truth data, so called *MC-true* coincidences or *MC-trues*. This sorter searches for all pairs of *singles* with the same event ID, in other words if they belong to the same simulated decay. Furthermore, the *singles* need to pass the energy cut and FOV restriction as for the implemented sorter.

The coincidences obtained from *phenoSorter* and *phenoGateSorter* are restricted to a FOV of 7 opposing sectors and checked if they are a *MC-true*. Furthermore, a flag holds the information if the two *singles* forming a coincidence originate from the same source. The data structure of the DPCs is modeled by dividing the *singles* into data frames with a length of 327.68 µs. A further modeling of the detector is not done. Especially the dead time is not modeled. Furthermore, the 80 ns delay after the start of a new data frame before accepting events is not included.

The analysis compares three quantities, that do not depend on the event number in a simulation: purity, detection efficiency and estimation efficiency. The purity is the fraction of *prompts* that are *MC-trues* and the *prompt* coincidences. This corresponds to the fraction of the signal over the signal plus noise. The detection efficiency is the fraction of *MC-trues* in the *prompts* compared to all *MC-trues*. Thus, the detection efficiency describes the ability of a sorter to identify the signal provided by *true* coincidences. The estimation efficiency is the number of *prompts* minus the number of *randoms* over the *MC-trues* and describes the correct estimation of *prompt* and *random* coincidences by the coincidence sorter. For this analysis *scattered* coincidences are counted as *true* as they result from an annihilation.

Table 4.1: Activities and simulation duration for the runs of the GATE simulations. The duration is decreased to reduce the simulation time but keep the number of events similar for all activities.

Activity Range [MBq]			Simulation Duration [ms]
Start	End	Step size	
1	2	1	10 485.76
3	5	1	5242.88
8	15	1	2621.44
16	20	1	1310.72
21	30	1	873.82
31	40	1	655.36
42	50	2	524.288
52	60	2	436.91
62	70	2	374.50
72	80	2	327.68
82	90	2	291.272
92	100	2	262.144
102	110	2	238.32
112	120	2	218.46
122	130	2	201.65
132	140	2	187.25
142	150	2	174.77

4.2.2 Results of NEMA Rat Size Scatter Phantom

In Figure 4.4 the *prompt* and *random* coincidences obtained with the four different sorting approaches are presented. For *prompt* coincidences a clear separation between the handling of *multiples* is visible especially for high count rates. This is expected because the probability for three *singles* in a coincidences window increases. The *prompts* for the *killAll* handling are slightly higher with the *phenoSorter* than with the *phenoGateSorter*. The *randoms* behave differently. The *random* coincidences for the *takeAllGood* handling are quite similar for both sorter. The results for the *killAll* handling differ between the two sorter. Here the *phenoGateSorter* is well below the *phenoSorter*.

The detection efficiencies for the different sorting approaches are presented in Figure 4.5. A clear separation between the two handlings of *multiple* coincidences is visible. Furthermore the *phenoGateSorter* with the *takeAllGood* obtains the best results and detects nearly all Monte Carlo *trues*. On the other hand the same sorter with the *killAll* has the worst detection efficiency. For the *phenoSorter* the *takeAllGood* handling performs a bit worse and the *killAll* a bit better than the same handling with the *phenoGateSorter*.

The purity is given Figure 4.6. The purity is about 10 % better for the *killAll* handling at 150 MBq under these optimal simulated conditions. The *killAll* handling of *multiples* has a lower amount of *randoms* in the *prompt* window which results in this higher purity.

In contrast to the better purity the estimation efficiency of the *phenoSorter* with *killAll* underestimates the number of *true* coincidences by about 35 % at 150 MBq. The full curve is given in Figure 4.7. Both sorters show quite well efficiencies with the *takeAllGood* handling. The *phenoGateSorter* seems to estimate the correct number of *true* coincidences while the *phenoSorter* performs a bit worse. Here the *phenoGateSorter* estimates about 8 % more *true* coincidences than the *phenoSorter*. Both sorters with the *killAll* handling perform worse for

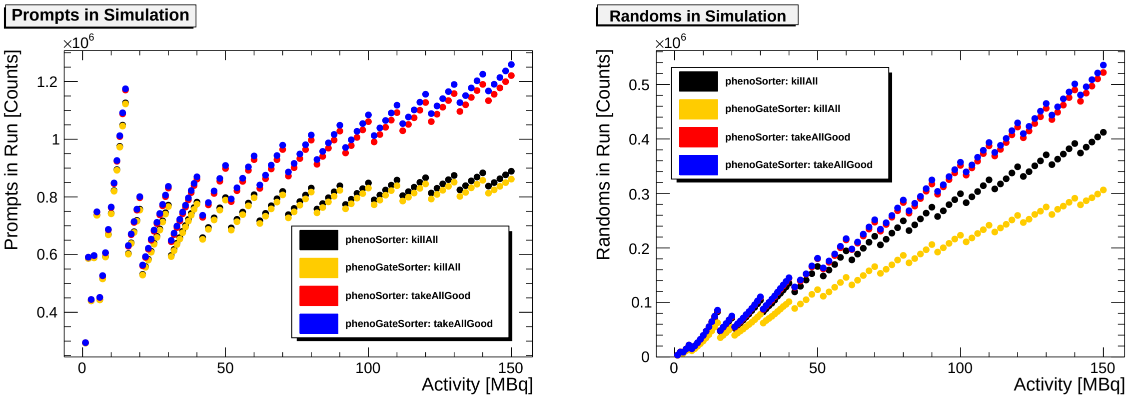

Figure 4.4: Sorted coincidences in each simulation run for the rat size scatter phantom. Different sorter and handlings of *multiples* are color coded. The steps in the count rates result from a reduction of the simulated duration of the measurement (Table 4.1). For *prompt* coincidences differences between the handlings of *multiples* become visible for high activities. For *random* coincidences a difference between the handlings of *multiples* and even for *killAll* between the two sorters are visible.

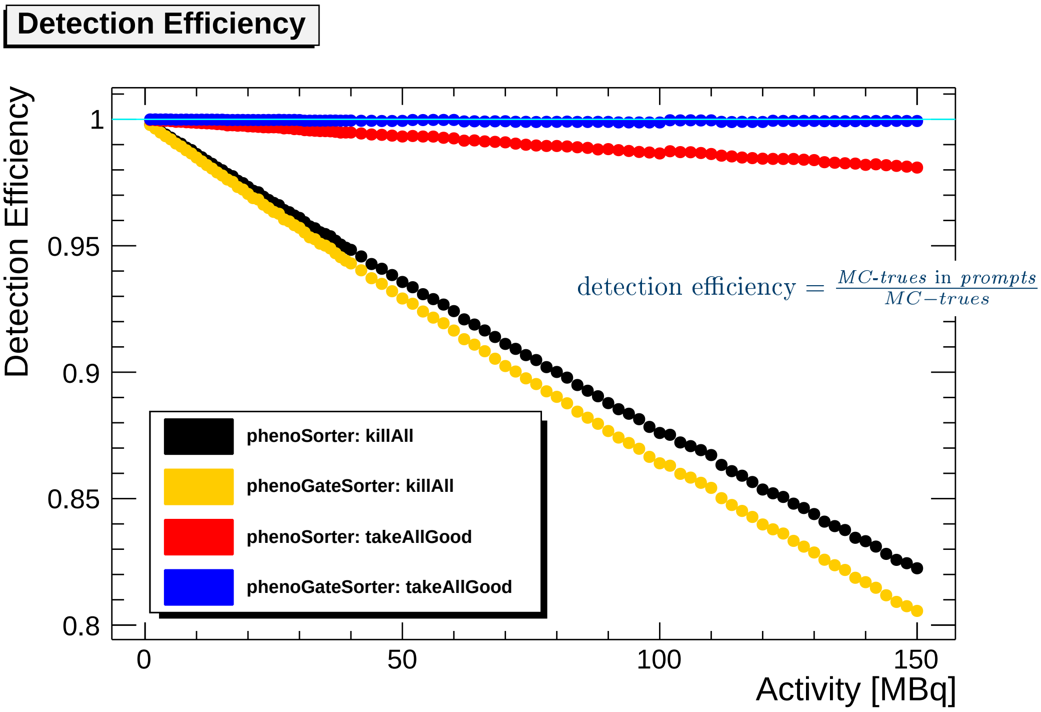

Figure 4.5: Detection efficiencies of rat size NEMA phantom for different sorter and handling of *multiple* coincidences. The cyan line marks an efficiency of 1. The main difference on the efficiency results from the handling of *multiples*.

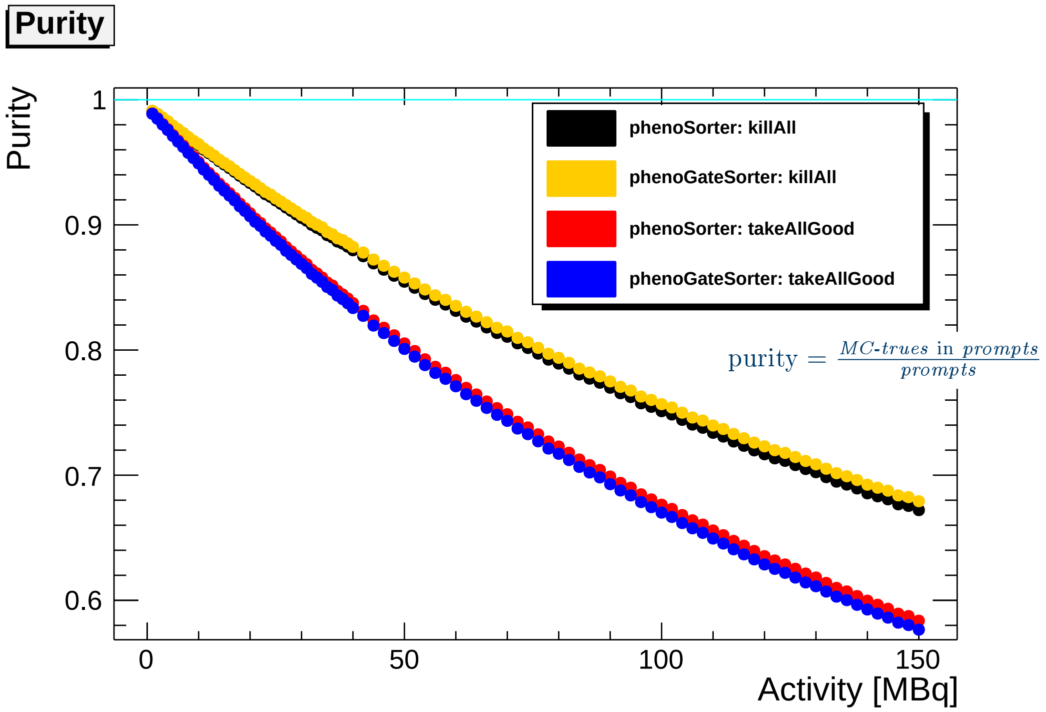

Figure 4.6: Purity of rat size NEMA phantom. The reduced number of *randoms* due to the discarding of all *multiples* is visible for the *killAll* handling.

high count rates.

In conclusion, the four different ways to sort coincidences have been characterized with simulated data and compared with each other. The initial sorter (*phenoSorter* with *killAll*) has the higher purity, which was its designed goal. On the downside it has reduced detection and estimation efficiencies. Therefore, not all *true* coincidences are found by the initial soter and there is a mismatch in the identification of the number of *true* and *scattered* as well as the delay *random* coincidences. Nevertheless a further characterisation with measured data is done because it was the default sorter for the first experiments and has been developed for *pheno*PET. The *phenoGateSorter* with *killAll* performs a bit worse for the detection efficiency but significant better than for the estimation efficiency compared to the *phenoSorter*. The *phenoGateSorter* with *takeAllGood* has a lower purity than the *killAll* handlings but both efficiencies rise to about 100 %. This indicates that nearly all *true* coincidences are found and the number of *randoms* is estimated correctly. The downside is a higher number of *randoms*. Thus it is investigated further with real data. In comparison the *phenoSorter* with *takeAllGood* is always a bit worse than the *phenoGateSorter* with *takeAllGood*. Thus the *phenoSorter* with *takeAllGood* is not investigated with real data. Those small differences might result from the processing in sorting steps with a limited number of *singles* within the *phenoSorter*. Taking into account only the first event of a sector during each sorting step, hides other possible events on a sector. Especially for high count rates this becomes relevant.

4.3 Characterization with a Decay Experiment

With the information from the simulations in mind, the sorting algorithms are now investigated with real data. The following analysis is restricted to only two sorting strategies. The *phenoSorter* with *killAll* is investigated as the initial coincidence sorter. In comparison the

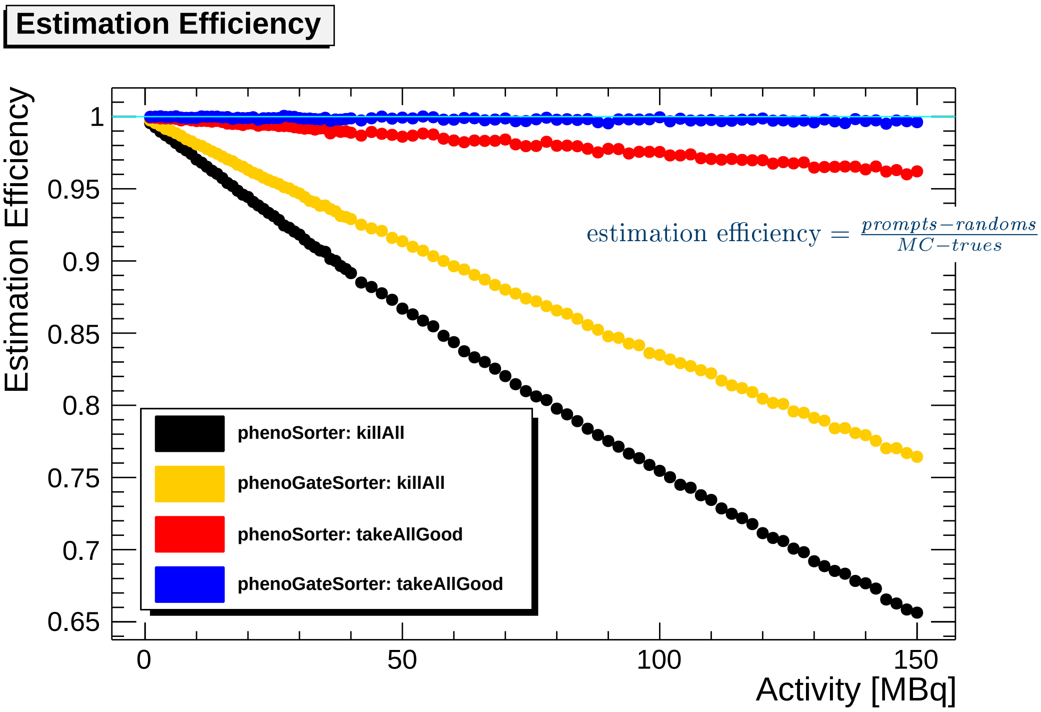

Figure 4.7: Estimation Efficiency for rat size NEMA phantom. The cyan line marks an efficiency of 1. The best results are obtained for *takeAllGood*.

phenoGateSorter with *takeAllGood* is used because it obtained the best efficiencies in the simulation study. Furthermore, [125] states that most commercial PET use this approach.

4.3.1 Measurement Setup

For a decay experiment, an injection vial filled with about 100 MBq ^{18}F diluted in about 1 ml water was measured. The vial has a diameter of 24 mm and a height of 45 mm. The bottom of the vial was placed in the center of the FOV. The decay is observed with a series of measurements. Each measurement has a duration of 300 s. The start of a new measurement takes about 26 s.

4.3.2 Analysis

The recorded raw data was clustered to *singles* and afterwards handed over to the two different coincidence sorter. The number of *prompt* and *random* coincidences detected by each module combination are binned in 300 s intervals and plotted over the measurement time. The uncertainties for each point are calculated by the Poisson statistics and Gaussian error propagation.

The analysis of high count rates requires the correction of dropped and possible missing frames, which is described in Section 5.4.1. In addition, the analysis excludes the complete time region containing overlong packages (see Section 3.2.1).

4.3.3 Results of Decay Experiment

To compare the sorted numbers of coincidences two module combinations are taken into account. The first combination with modules 0 and 3 is in the lower module ring and thus

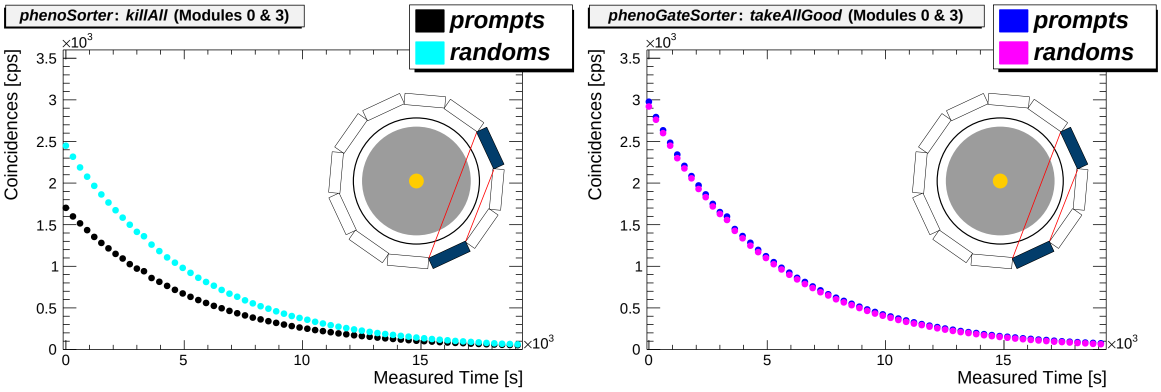

Figure 4.8: Results for a decay experiment with a small vial close to the center of the FOV. The position of the displayed module combination is illustrated in the sketch and in the lower module ring and thus does not observe the radioactive sample. The data shows that the initial coincidence sorter *phenoSorter* with the *killAll* handling estimates a too large number of *randoms* compared to the *prompts*. The other coincidence sorter estimates similar numbers of *prompts* and *randoms*.

well below the vial. The data cannot contain any *true* coincidences. A small number of *scattered* coincidences is possible. Thus *randoms* should dominate the *prompt* coincidences.

In Figure 4.8 the *prompts* and *randoms* for this module combination are presented. For the initial sorter (*phenoSorter* with the *killAll*) the number of delayed *random* coincidences is above the number of *prompt* coincidences for the complete displayed measurement duration. *Prompts* are the sum of *true*, *scattered* and *random* coincidences and therefore the number of *prompts* needs to be larger than the number of delayed *randoms*. This clearly indicates a problem with the coincidence sorting. For the new *phenoGateSorter* with *takeAllGood* the numbers of *prompts* and *randoms* are similar over the complete measurement duration.

The new sorter estimates about 0.5×10^3 cps more *randoms* for the start of the measurement. On the other hand the number of *prompt* coincidences is increased by about 1.25×10^3 cps for the highest activities. Thus the sorting of *prompt* coincidences might be the reason for the differences between the two sorters.

In Figure 4.9 the results of the second combination of modules 16 and 22 is shown. Those modules are facing each other on different sides of the vial. For both coincidence sorters the number of *prompt* coincidences is much larger than the number of *randoms*. The *phenoGateSorter* increases the number of *randoms* by about 1.5×10^3 cps at the start of the measurement. The increase of *prompt* coincidences is about 18×10^3 cps and thus about a factor of 10 higher. These differences between the two sorting strategies decrease during the measurement and converge to similar values for *prompts* and *randoms*. Therefore, the differences between the sorter are count rate dependent.

The measured data shows an improved performance of the *phenoGateSorter* with *takeAllGood* compared to the *phenoSorter* with *killAll*. These improvements are especially important for the high count rates possible due to the new firmware and the correction of dropped frames.

4.4 Comparison of the Different Sorting Strategies

The two implemented coincidence sorters with the two handlings of *multiple* coincidences were investigated first with simulated data and afterwards with measured data. The simulation study showed that the *phenoGateSorter* with a *takeAllGood* handling of *multiples* achieves

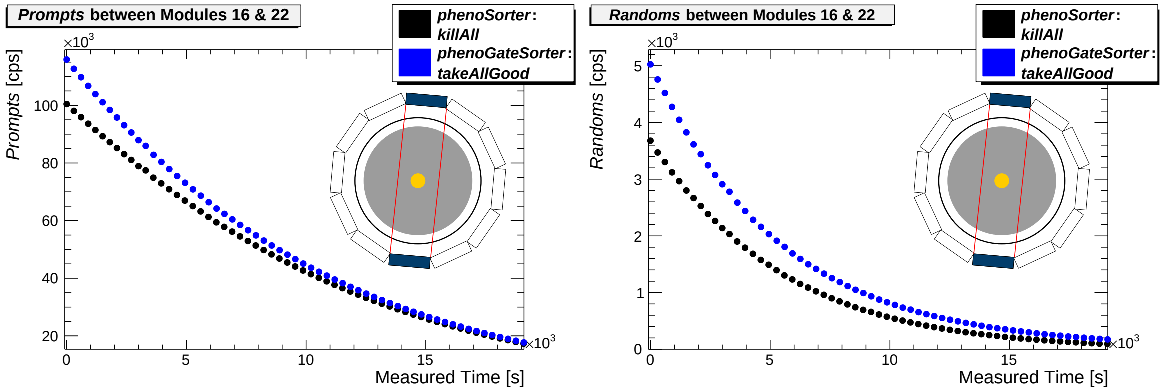

Figure 4.9: *Prompts* and *randoms* between a module combination in the middle module ring. The position of the radioactivity is illustrated in the sketch. The initial coincidence sorter (*phenoSorter* with *killAll*) estimates a smaller number of *prompts* than the revised sorter. The increase for *randoms* is much smaller.

an identification of nearly all *true* coincidences originating from a decay as presented in [63]. The *phenoSorter* with *takeAllGood* does not reach the performance of the *phenoGateSorter* with *takeAllGood*. The number of *random* coincidences can be decreased by applying *killAll* but this decreases the detection efficiency significantly for both sorter. Thus the handling of *multiple* coincidences has a large effect on the identification of *true* coincidences.

The second study compared the *phenoGateSorter* with *takeAllGood* and the *phenoSorter* with *killAll* with a decay experiment of a small disc of radioactivity. The *phenoSorter* with *killAll* shows inconsistencies for modules not observing the sample which could be resolved by the *phenoGateSorter*. For example about 800 cps more coincidences were found in the delayed than in the *prompt* window with the *phenoSorter*, resulting in negative values for the difference of *prompt* and delayed *random* coincidences. Although clearly inconsistent, these 800 cps are small compared to the 100 000 cps *prompts* between two modules observing the sample. More important the *phenoGateSorter* with *takeAllGood*, increases the number of *prompts* and *randoms* for module combinations observing the sample. In the presented combination this increase for *prompts* was a factor of 10 above the increase for *random* coincidences. These differences depend on the count rates. For low count rates the different coincidence sorter and handlings of *multiple* coincidences provide the same results.

The differences observed between the *phenoGateSorter* and *phenoSorter* for the *takeAllGood* handling should result from differences in the design. One aspect here is that the *phenoSorter* only takes the first *single* of a complete sector, that contains three modules, into account. Thus further *singles* are shadowed for the coincidence search. This is especially important for sorting of *multiples*. Another aspect has a further influence the sorting of *random* coincidences. The relative shift of the timestamps results in the creation of independent data. On the other hand the shifts move away all pairs resulting from a real decay. As pointed out in [63] *multiples* are most probably the result of two *singles* from a decay and an additional *single*. Those combinations are no longer modeled correctly during the sorting of *random* coincidences using the *phenoSorter*.

An advantage of the change of the handling of *multiple* coincidences to *takeAllGood* results in a simplification of the further work. For the dead time correction the interaction is restricted to only two modules and not to three or more modules contributing to a *multiple*. Thus a dead time correction becomes easier.

4.5 Possible Improvements and Further Investigations

The behavior of a coincidence sorter always depends on the activity distribution and the amount of activity as pointed out in [125]. Thus a further investigation of other strategies to deal with *multiples* might be useful depending on the biological question. But this is beyond the scope of this work as it also includes a full verification of all corrections for the normalization. Each verification might also require the adaptation of procedures or a new development.

There are further possibilities to improve the speed of the preprocessing of measured data. At the moment the execution of *phenosort*, which analyzes the raw data and performs the clustering, and the coincidence sorter are subsequent. Both programs could be combined to a single tool that can either process raw data or read *singles* from an intermediate file. Furthermore, both programs can be multi-threaded. In addition, the creation of a look up table between timestamps and positions in the coincidence file is done after the sorting. This could be included into the sorting process.

Chapter 5

Count Rate Corrections

Several effects can lead to a bias in the measured count rates and need to be corrected to obtain quantitative Positron Emission Tomography (PET) images. The detector dead time results in the loss of events because the detector is already busy processing another event or getting ready for the next measurement. Those events cannot contribute to the further analysis, leading to an underestimation of the actual count rate. A second effect is pile-up, which means two events are processed as a *single* event. Finally, *pheno*PET can drop frames measured by the Digital Photon Counters (DPCs) to reduce the necessary data bandwidth. Also this controlled reduction of the count rate needs to be corrected. These effects depend on the count rate itself and are becoming more prominent for higher count rates. High count rates can result from a high total amount of radioactivity in the Field-of-View (FOV) or from smaller

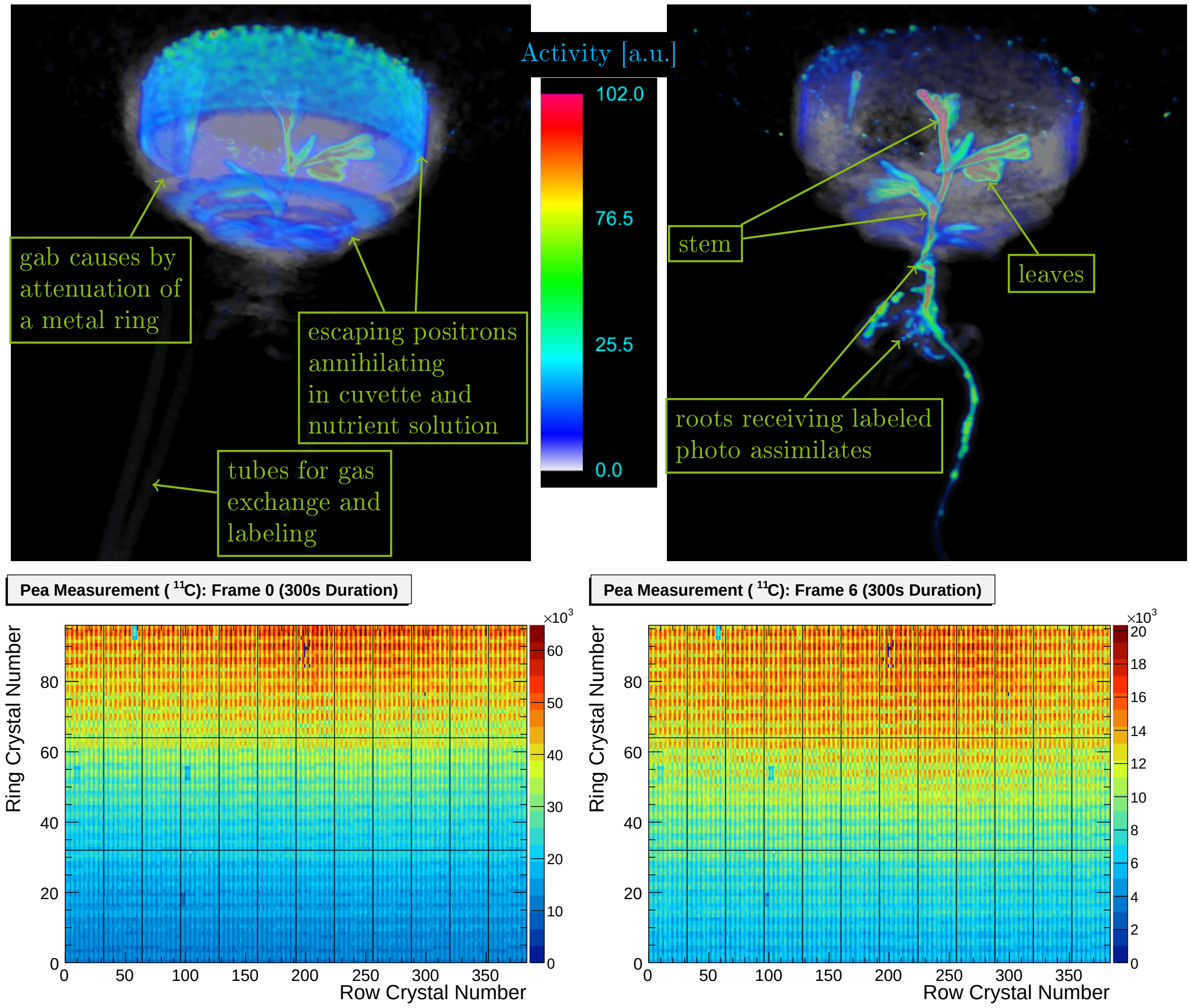

(a) Frame 0.

(b) Frame 6.

Figure 5.1: Two 300 s long frames of a pea plant labeled with $^{11}CO_2$. The images are normalized (Chapter 6). The bottom plots are the hit maps (*single* events) of the frames. The used radioactivity does only cause small dead time effects.

amounts close to the detector modules, thus for the correction the spatial distribution of the activity needs to be taken into account. Count rate effects could be reduced by reducing the total amount of applied radioactivity depending on the experimental requirements. However, the distribution of the tracer depends on the plant and its metabolism and thus cannot be controlled. Furthermore ^{11}C, for example, only has a half life of about 20.361 min [46]. Thus the possible length of study of processes depends on the dynamic range and thus on the ability of *pheno*PET to handle high activities.

Two example image frames of a pea measurement are shown in Figure 5.1 together with the associated hit maps of *singles*. Due to the feeding of the activity into the leaves the shoot has a significant higher signal than the root system. Furthermore, the signal in the root system depends on the depth, which might result from the different amount of roots. Such an activity distribution results in an inhomogeneous distribution of count rates and different dead time effects for the different detector modules of a PET system, demonstrating the importance to apply the count rate corrections on an individual detector basis.

In this chapter, correction models for all aforementioned effects are presented and evaluated. The first results for this analysis were presented on a poster on the 2018 IEEE Medical Imaging Conference (2018 MIC) [126]. In contrast to these data the analysis below uses the new coincidence sorter, *phenoGateSorter*, with *takeAllGood* handling of *multiple* coincidences. The principle analysis procedure has not been changed compared to 2018 MIC but the correction model and the results for single detector modules and the frame dropping is explained in more detail. Furthermore, the dead time due to coincidence sorting is presented. The last step is an investigation of the dead time correction for different positions of activity samples within the FOV.

5.1 Correction Model

The sensitivity is the fraction of recorded events over the number of possible events. For the calculation of the dynamic correction the inverse, called dead time correction factor (DCF), is easier accessible.

For plant measurements we require a model that can deal with inhomogeneous activity distributions. This rules out a single global correction factor. The applied dead time correction model focuses on the correction of the losses between pairs of modules. In the end, a global factor is added to account for a possible global effect of the coincidence sorter.

The individual count rate corrections are multiplicative factors and can be separated into different DCF [39]. Most dead time correction models separate the dead time of each Line-of-Response (LOR) into the dead time of the two crystals defining the LOR [127, 128]. Vicente et al. [129] propose the separation into a correction factor $sDCF_n$ for each detector module n and the factor $coinDCF$ for the coincidence sorting algorithm. Starting from this model, the number of coincidences free of data losses $N_{n,m}^{corr}$ detected by two modules is calculated according to

$$N_{n,m}^{corr} = DCF_{n,m} \cdot N_{n,m}^{raw} = f_{n,m}^{frames} \cdot sDCF_n \cdot sDCF_m \cdot coinDCF \cdot N_{n,m}^{raw} \tag{5.1}$$

with the uncorrected coincidence rate $N_{n,m}^{raw}$ and the dead time correction factor $DCF_{n,m}$. For *pheno*PET the factor $f_{n,m}^{frames}$ has to be introduced to correct for dropped and missed data packages. The calculation of the $sDCF_n$ is discussed in more detail in Section 5.4.2. The $coinDCF$ are investigated and discussed further in Section 5.4.3.

For *single* rates of a module n the corrected count rate is given by

$$N_n^{corr} = f_n^{frames} \cdot sDCF_n \cdot N_n^{raw}. \tag{5.2}$$

The factor f_n^{frames} corrects for the missing packages of module n.

5.2 Application of the Correction Factors in the Iterative Image Reconstruction

For the iterative image reconstruction the Ordinary Poisson Maximum Likelihood Expectation-Maximization (OP-MLEM) requires the sensitivity of each LOR. The sensitivity includes a constant part and a dynamic part as discussed in Section 3.5.2. The dynamic part has to be calculated for each image frame and is defined by the count rate corrections. The sensitivity $s_{n,m}^{dyn}$ is given by the inverse of the $DCF_{n,m}$. The dynamic sensitivity for all LORs between two modules n and m is given by $s_{n,m}^{dyn,mod}$. The sensitivity is the fraction of recorded events over the number of possible events. Therefore, the dynamic sensitivity of an image frame with the start t_S and the end t_E is given by the average the $DCF_{n,m}$ of short correction intervals Δt

$$\begin{aligned} &s_{n,m}^{dyn,mod}(t_S, t_E) \\ &= \frac{1}{t_E - t_S} \sum_{t_0=t_S}^{t_k<t_E} \left(\frac{1}{f_{n,m}^{frames}(t_k)} \cdot \frac{1}{sDCF_n(S_n)} \cdot \frac{1}{sDCF_m(S_m)} \cdot \frac{1}{coinDCF(S_{total})} \cdot \Delta t(t_k) \right) \\ &\qquad \text{with } t_{k+1} = t_k + \Delta t(t_k). \end{aligned}$$

In this expression, the sum represents the time the detector is sensitive and is thus a measure for the number of recordable events and the frame duration $(t_E - t_S)$ is a measure for the number of expected events. The $f_{n,m}^{frames}(t_k)$ are calculated for the same time intervals $\Delta t(t_k)$. The *single* count rate of a module S_n and the total count rate S_{total} are calculated by an integration from t_k to $t_k + \Delta t(t_k)$. Here, a correction of the frame dropping is required. The dependency of Δt on t_k results from the fact that timestamps within the *pheno*PET data are calculated as multiples of the data frame length of 327.68 µs. At the moment this effect is negligible with $\Delta t \approx 1\,\text{s} \gg 327.68\,\mu\text{s}$. In the future shorter correction intervals might be used for shorter image frame durations. A possible application might be the measurement of isotopes with a shorter half life like ^{13}N or even ^{15}O.

5.3 Setup for Determination of Count Rate Corrections

The DCF are obtained from decay experiments with a fillable cylinder of a total height of 163 mm and a diameter of 80 mm. The fillable volume is about 510 ml. The cylinder is filled with water and using a syringe we add a sample of at least 300 MBq of ^{18}F from a vial. A magnetic stirrer mixes the activity to ensure a homogeneous distribution within the cylinder while the activity has been decaying to about 150 MBq, which is close to the maximum count rates *pheno*PET can handle.Before the measurement is started the magnetic stir bar is removed from the cylinder. One measurement with a centered cylinder and one with a cylinder shifted off-center with respect to the FOV are used to determine the DCF.

5.4 Determination of Correction Factors

The measured data are processed with the default parameters for clustering (Section 3.4.4) and coincidence sorting (Section 3.4.5). Furthermore, the data are searched for the last occurrence of an overlong package (see Section 3.2.1). This allows the exclusion of such data.

The head curves for *singles*, *prompt* and *random* coincidences are created. Each point of a head curve contains the events of 1 s. *Prompts* and *randoms* are restricted to the 7 opposing sectors of a module. All head curves are corrected for dropped frames.

5.4.1 Correction of Dropped and Missing Frames

Before further correction factors can be determined, missing and dropped data packages need to be taken into account.We refer to this correction as dropped frames correction. Controlled dropped packages are the dominant effect and described in Section 3.2.2. Missing packages are less likely and result in a frame that lacks at least one of the 36 data packages. The reasons for a missing package remains unknown. Missing packages do not include overlong packages. The required information for each frame are provided by the status packages, see Section 3.4.3.

The number of events within a data package (length: 327.68 µs) is Poisson distributed due to the stochastic nature of a radioactive decay. The average number of events per frame should not change in short time intervals and can be scaled to correct for dropped packages.

The correction factor for a single module f_n^{frames} is given by the number of expected frames over the number of frames, that contain a valid package from module n. The effect of dropped packages on coincidence rates depends on the two involved modules. Therefore, the packages of each frame are checked for all possible module combinations. A valid frame for a combination must contain data of modules n and m. The correction factor $f_{n,m}^{frames}$ is given by the number of expected frames over the number of valid frames for this combination.

It should be noted that the scaling becomes more stable for a larger number of frames. On the other hand the time interval should be short compared to the half life of the radioactive isotope and the velocity of the tracer in the plant. The default interval for this correction is set to 1 s, which includes 3051 or 3052 frames. These different numbers result from the calculation of timestamps at the end of a data frame with its length of 327.68 µs.

5.4.2 Dead Time Analysis of Measured Single Events

The second step is the analysis of the *singles* as a function of time for each module to determine the dead time of the DPCs. The data points of the frame dropping corrected *singles* head curves are averaged within 20 s intervals.

The data loss due to dead time of each module n is determined by the comparsion of expected count rates and the measured counts. For the expectation an exponential decay

$$S_n^{fit}(t) = A_n \exp(-\lambda \cdot t) + b_n \tag{5.3}$$

with the parameters A_n and b_n is fitted to the head curve of module n. The background b is mainly attributed to the ^{176}Lu in the detectors. The decay parameter λ is fixed to $1.053 \times 10^{-4}\,\mathrm{s}^{-1}$ for ^{18}F, which corresponds to a half life of 6.58×10^3 s [130]. The fit relies on data in the low activity region where dead time effects can be neglected. Therefore, several fit regions, which start after the end of the frame dropping, were tested. The decision was based on the behavior between the fit and the data points.

A non-paralyzable dead time model is used (see Section 2.7.3.3 or [39]) because all *dies* on a module operate independently (see Section 3.2.1). Furthermore, the limitations due to available memory on the *dies* are not reached within the dynamic range currently used. Therefore, the ideal *single* count rates, $S_n^{ideal}(t)$ are calculated from Equation (5.3) for each time point of the measurement. The S_n^{ideal} are plotted as a function of the S_n, the measured *singles* per time interval corrected for frame dropping. The dead time model is given by the fit of

$$S_n^{ideal}(S_n) = \frac{\alpha_n \cdot S_n}{1 - S_n \cdot \tau_n} \tag{5.4}$$

to those data with the fit parameters α_n and τ_n, which describes the dead time. These fits exclude the region with overlong packages. Thus the fit range is restricted to a maximum of $S_n = 750 \times 10^3$ cps. The lower bound of the fit is 50×10^3 cps to exclude the points contributing to the exponential fit to the head curves. Furthermore, the data show some features which are excluded from the fit. Those are discussed together with the presentation of the results in the following sections.

The dead time correction factors $sDCF_n$ are obtained from the fit parameters of Equation (5.4) as

$$sDCF_n(S_n) = \frac{S_n^{ideal}(S_n)}{S_n} = \frac{\alpha_n}{1 - S_n \cdot \tau_n}.$$

These factors are required for the image reconstruction or the correction of measured data.

The analysis is done for the head curves of all modules for both measurements presented in Section 5.3. For the dead time correction model one measurement is selected for each module to execute the fit with equation Equation (5.4). This selection is based on the number of excluded data points and the general behavior of the count rates. Therefore the residuals of the fits were examined. As a minor criterion fir this selection the qualities of the fits for the two different measurements are considered.

5.4.3 Dead Time Analysis of Coincidence Count Rates

A first application of the $sDCF_n$ to coincidence head curves revealed only a reduction of the count rate dependent bias. Therefore, a further correction factor is required.

The investigated head curves contain the number of *true* and *scattered* coincidences, which are referred to as *estimated trues* eT. Those are determined as the number of *prompt* coincidences minus the number of *random* coincidences. The *random* coincidences do not undergo any variance reduction because their number per module combination is sufficiently high.

The measured *estimated trues* between two modules $eT_{n,m}^{meas}$ are corrected for count rate losses according to

$$eT_{n,m}^{corr}(t) = sDCF_n(t) \cdot sDCF_m(t) \cdot f_{n,m}^{frames}(t) \cdot eT_{n,m}^{meas}(t).$$

The data points are averaged in 20 s intervals before a fit with an exponential function similar to Equation (5.3) is applied to each head curve of $eT_{n,m}^{corr}(t)$. The same fit region as for the calculation of the $sDCF_n$ is used. A dead time correction factor for each module combination is calculated as

$$coinDCF_{n,m}(t) = \frac{expected}{measured} = \frac{eT_{n,m}^{fit}(t)}{eT_{n,m}^{corr}(t)}.$$

The $eT_{n,m}^{corr}$ and $coinDCF_{n,m}$ are only calculated for coincidences contributing to the FOV with a radius of 90 mm for the reconstruction. This restricts the module combinations to the seven opposing sectors of each module. All $eT_{n,m}^{corr}$ not contributing to this FOV are set to zero.

The global factor implemented in the correction model is calculated from a total head curve of *estimated trues*

$$eT^{corr}(t) = \sum_{n=0}^{n<36} \sum_{m=n+1}^{m<36} eT_{n,m}^{corr}(t)$$

with the sum over all 36 modules of *pheno*PET. The correction factor is than given by

$$coinDCF(t) = \frac{expected}{measured} = \frac{eT^{fit}(t)}{eT^{corr}(t)}.$$

The correction factor $coinDCF$ was motivated as count rate losses caused by the coincidence sorter, which behave similar to the dead time on a detector. The simulations in Section 4.2.2 indicate that the implemented coincidence sorter causes only a minor or no count rate losses. Due to the *takeAllGood* handling of *multiple* coincidences the expectation is that

$$coinDCF = coinDCF_{n,m}$$

for all module combinations contributing to the FOV.

The investigations below present differences between the $coinDCF_{n,m}$. Nevertheless the $coinDCF$ are used for a correction model. A discussion of possible effects contributing to these differences between the $coinDCF_{n,m}$ can be found at the end of this chapter (see Section 5.7).

For the application of the $coinDCF$ to a measurement a non-paralyzable dead time model (see Section 2.7.3.3 or [39]) is used due to the *takeAllGood* handling of *multiple* coincidences. Therefore the $coinDCF$ are plotted over the number of *singles* detected by all modules S_{total} and the function

$$coinDCF(S_{total}) = \frac{\alpha_{coin}}{1 - S_{total} \cdot \tau_{coin}}$$

is fitted with the fit parameters α_{coin} and τ_{coin}. The latter is the dead time associated to the global factor $coinDCF$. Originally the dead time model depends on the measured count rates eT^{corr} and not the *singles*. Therefore, the fit is also done for the $coinDCF(eT^{corr})$ to demonstrate that the usage of the S_{total} gives similar results.

5.5 Resulting Correction Factors

5.5.1 Frame Dropping

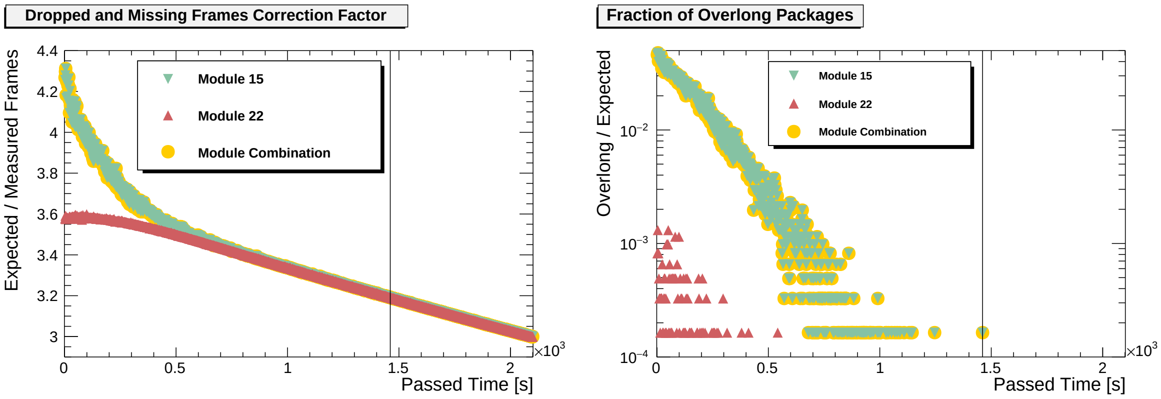

Figure 5.2: Performance of data packages during the decay experiment with the centered cylinder. Left side: Correction factor for dropped and missing frames for modules 15 and 22 and their combination. The fraction of overlong packages during the measurement are presented on the right side. Only the first 35 min of the 15 h long measurement are displayed. The vertical black line marks the last occurrence of an overlong package.

The effect of frame dropping is presented on module 15 and module 22 on the opposite side of the ring. Module 22 is chosen instead of the opposing module for the illustration of a few effects, which are observed for a number of module combinations. Their frame dropping correction factors and the correction factor for their combination are presented in Figure 5.2.

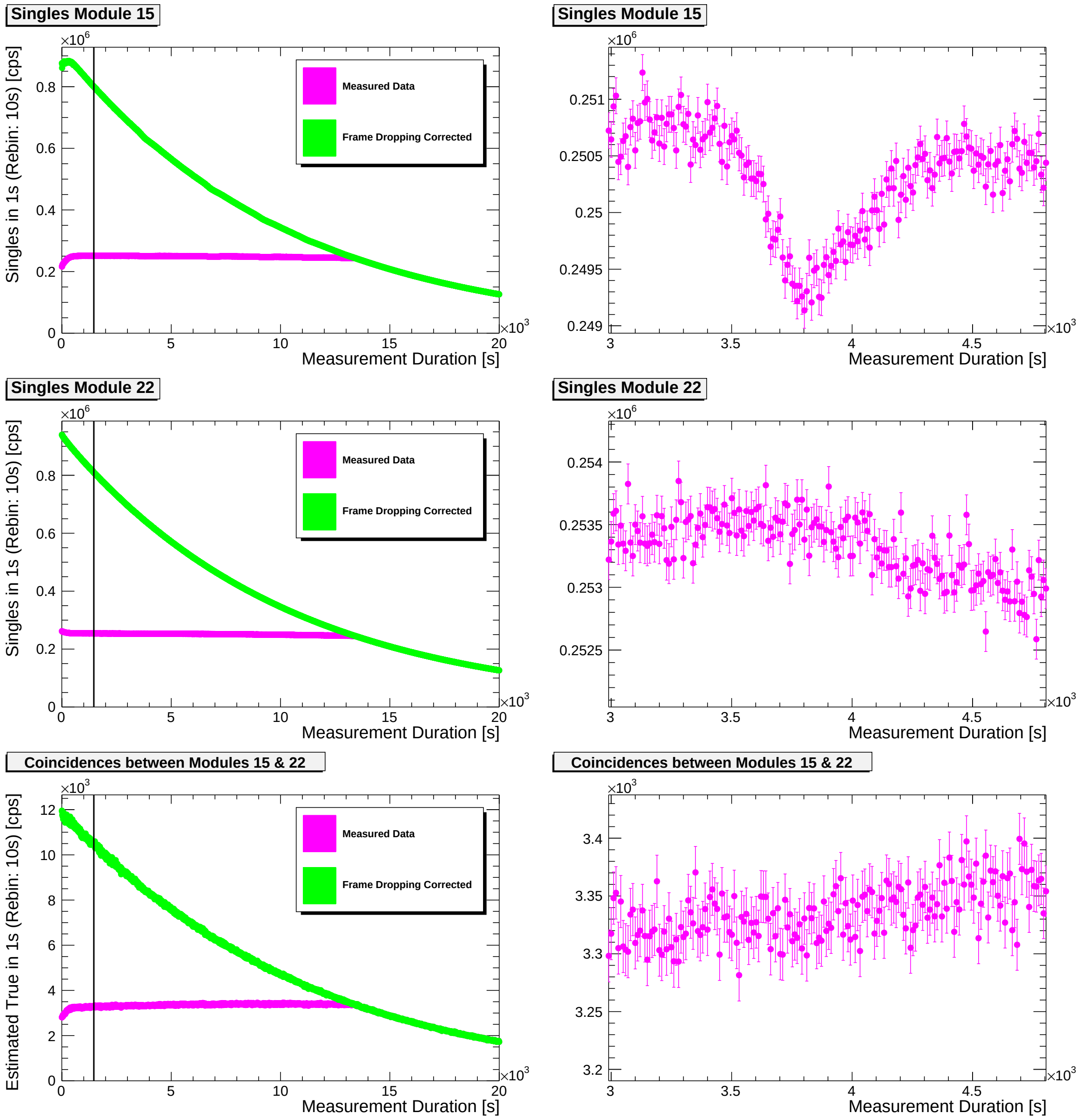

Figure 5.3: Measured *singles* and *estimated trues* with and without the correction of dropped frames. The data result from the centered cylinder already presented in Figure 5.2. The black line marks the last occurrence of an overlong package. The effect of frame dropping and its correction can be observed on the left hand side. The right hand side shows a zoom to a dip of over 1 % for module 15. This dip is not observed by module 22 but a smoother decrease to the end of the zoom is visible. An possible effect on the coincidences seems to be within the statistical variations.

Slightly different correction factors for the two modules and the module combination are visible as long as overlong packages occur. This is expected because module 15 detects a few more hits resulting in a slightly higher data rate. Thus the data buffer within the firmware of module 15 is filled before the buffer of module 22 on the other side of the *pheno*PET. Therefore the firmware of module 15 starts its frame dropping and transmits overlong packages. These overlong packages are discarded by the Concentrator Board (CCB). The newly available band width of the USB 3.0 is used by the CCB to transfer additional data packages of the other modules. This is visible by the lower slope of the correction factors for module 22 at the start of the measurement.

During the further measurement after 2×10^3 s the coordinated frame dropping is the dominant process until the band width is sufficient to transmit all data frames. In this region the correction factors are similar for all modules and all module combinations. This indicates that the coordinated frame dropping by the CCB works and mainly data frames with packages of all modules are transmitted. After 10 h the activity of the ^{18}F is reduced to only 2 %. Here, single modules start to not transmit single packages. A possible explanation might be that these packages would have contained no events.

The effect on the recorded *singles* and *estimated trues* between these two modules is depicted on the left side of Figure 5.3. The *estimated trues* are the difference between *prompt* and *random* coincidences between the two modules. The measured events per time reach a saturation due to the fixed data transfer rate. The *estimated trues* decrease when going to earlier time points due to the increased number of *randoms*. Furthermore the occurrence of overlong packages on module 15 decreases the number of *singles* measured by this module.

The correction scales the measured event rates to numbers, which behave similar to an exponential decay, but are degraded by dead time effects. A few overlong packages result in the dropping of additional packages for this module. If the number of those packages and the number of additional *singles* is not too large, the correction can compensate those drops. For a larger amount of overlong packages the correction does no longer work. This is visible in the first 1×10^3 s for module 15. The event numbers seem to saturate or even decrease closer to the start of the measurement. The correction for module 22 looks fine at this time. A possible effect on the *estimated trues* is not visible due to the large statistical fluctuations. The occurrence of the first overlong packages does not change the result of this correction.

The right hand side of Figure 5.3 shows a decreased number of *singles* for module 15. This is not corrected by the dropped frames correction. Several of these dips can be observed within the *singles* of different modules. The dips furthermore differ in the drop and the duration. Further measurement also showed those drops but at different count rates, different time points and even on different modules. A correlation with the temperature of the modules and the separate *tiles* has been checked but no correlation was visible.

Due to the small decreases in the range of a 1 % to 2 % those dips were not further investigated to achieve a first dead time correction model. Those dips are excluded from the fits of the dead time model to obtain the *DCF*. For the correction of a measurement, these dips can not be distinguished from a biological effect and therefore are not corrected.

5.5.2 Dead Time Correction Factors for *Singles*

In Figure 5.4 the *single* head curves of module 15 and 22 are displayed together with the fit to the low activity region. The extrapolation of the fit to the complete measurement duration is also plotted. The fit region is chosen well after the end of the dominant dead time of the frame dropping. The qualities of the fits are quite good and only very small differences are visible.

The dead time models for modules 15 and 22 are given in Figure 5.5. A fit of the dead time correction model is displayed together with an extrapolation of the fit. In addition the residual graphs and pull distributions of the fits are presented (see Appendix A). The residuals are calculated as the difference of measured and fitted data. The uncertainties on the S_n (x-axis) are transformed into uncertainties on the y-axis via Gaussian error propagation and the fit

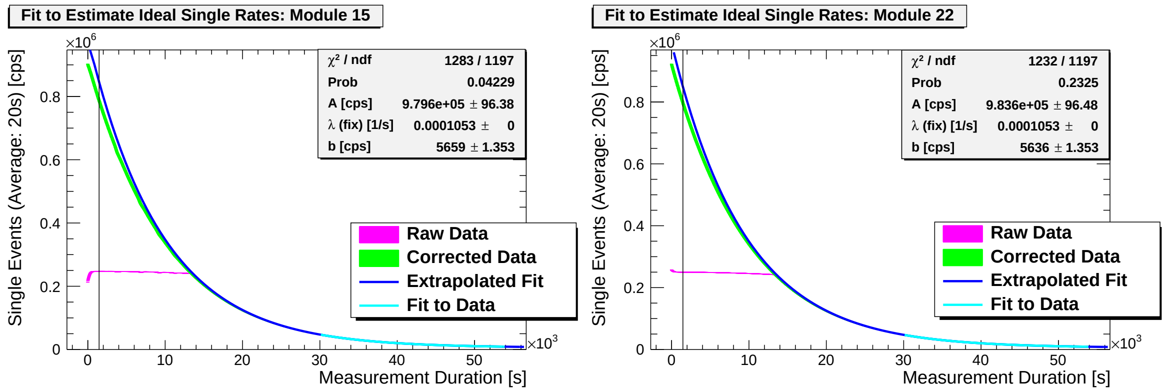

Figure 5.4: *Single* rates of two modules for a cylinder placed close to the center of the FOV. Corrected data are corrected for frame dropping. The plots include the fit to determine the expectation for high count values. The qualities of the fits look good. The vertical black lines mark the last occurrence of overlong packages on module 15. The curves are hidden by the fit towards the end of the measurement.

function. The pulls are the ratio of the residual and the statistical error of the residual.

For module 15, five peaks are excluded from the fit of the dead time model as these residuals show large and systematic deviations in one direction. Those result from the decreased measured data displayed in Figure 5.3 and discussed in Section 5.5.1. For module 22, no peaks are observed and therefore no data are excluded. Both pull distributions fit well to a normal Gaussian shape. This indicates good fit results.

The dead time correction model requires a correction curve for each module. These are taken from two measurements. The probabilities for the fits of all 36 modules are given in Figure 5.6. The probabilities, Figure 5.6a, for the majority of the exponential fits are above 1×10^{-3}. The four fits below 1×10^{-3} (modules 18, 20, 23 and 24) show better probabilities for the not chosen measurement but the obtained $sDCF$ are quite similar. For modules 20 and 23, the fits were chosen due to a larger number of peaks in the $sDCF$. The fits for modules 18 and 24 were selected from the centered cylinder because outside of the fitting range the effect of overlong packages on the $sDCF$ became visible. Nevertheless, the fit region was reduced to minimize a possible effect on the $sDCF$.

The probabilities for the $sDCF$ model fits in Figure 5.6b show good results for most of the fits. For nearly all modules the probability is well above 1×10^{-3}. All fits nicely represent the data for high count rates, even though a few small peaks become visible in the residuals. Further deviations arise for small count rates which are hidden in the large bulk of point below 150×10^3 cps. The comparison of the two measurements does not show a systematic dependency of the qualities of the fits on the measurement.

The two model parameters for the 36 modules are presented in Figure 5.7. The different absolute values, Figure 5.7a, seem to depend on the measurement and are up to 0.0035 below the expected value of 1 for the centered measurement. For the off-center measurements the deviations are smaller, in the order of 0.002 75.

The dead time parameter given by τ in Figure 5.7b are more interesting. Those values show a slight trend depending on the module number and thus the ring number. This effect is relatively small compared to the fluctuations of the modules within each ring and are thus not studied in more details.

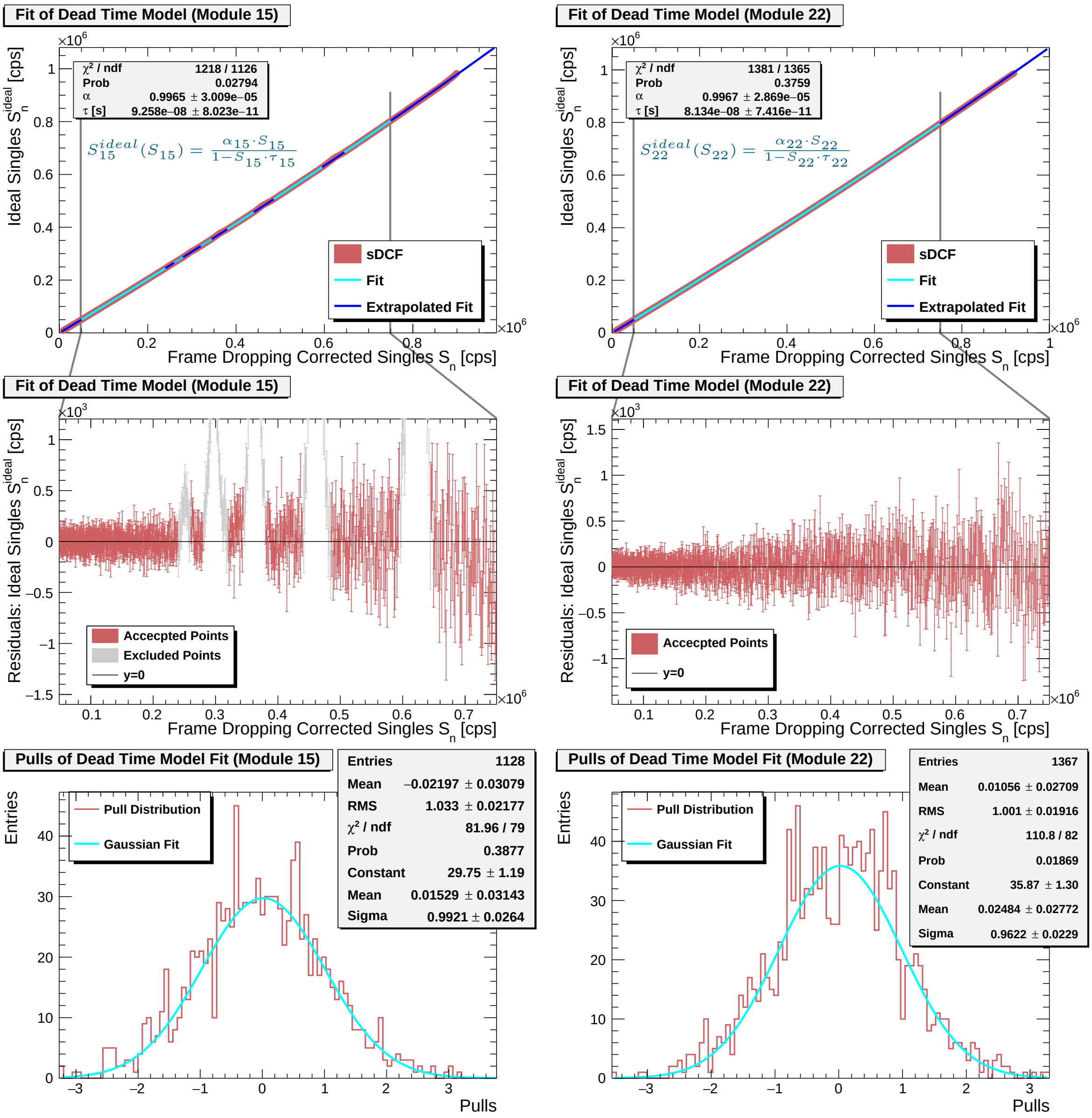

Figure 5.5: Fit of dead time correction model for single dead time correction. The data are still in the linear region of the dead time model. Furthermore, the extrapolation gives good results for the region with the first overlong packages ($S_n > 0.7 \times 10^6$ cps). With a larger amount of overlong packages the S_n no longer matches the S_n^{ideal}. Several points are excluded from the fit for module 15 due the systematic peaks on the residuals.

5.5.2.1 Discussion

The *sDCF* of all modules share the clear linear behavior presented in Figure 5.8 for the two example modules. The *sDCF* are about 1.07 for the end of the fit region at 0.7×10^6 cps. Thus, the system has only minor dead time effects and does not yet reach a saturation for the detection of *singles*. This allows for a further extension of the dynamic range, if the overlong packages can either be handled by the firmware to write them to disc or an appropriate correction can be implemented.

The Vereos PET/CT by Philips Healthcare consists of DPC coupled to lutetium-yttrium

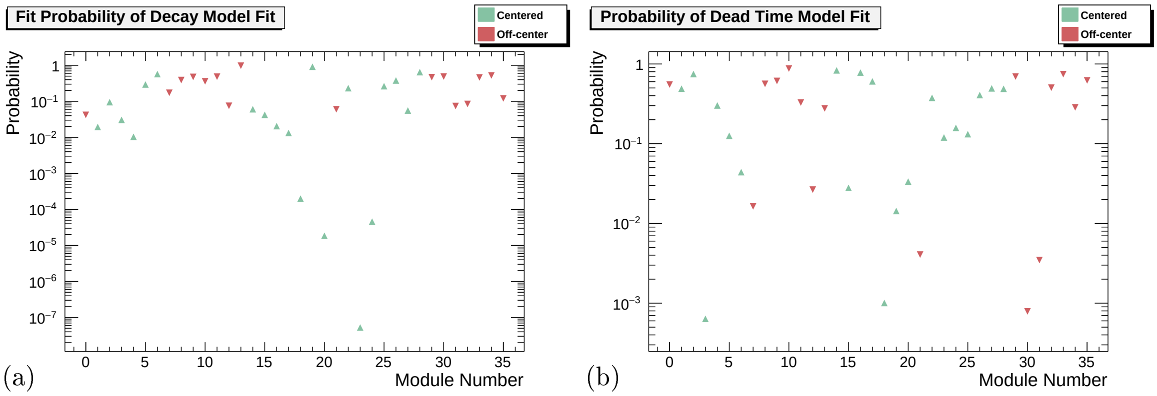

(a) (b)

Figure 5.6: Probabilities for fits of the decay model and the dead time model. Only the quality of the fits of the selected curves are presented. The probabilities are all quite good and no separation between the two measurements is obvious.

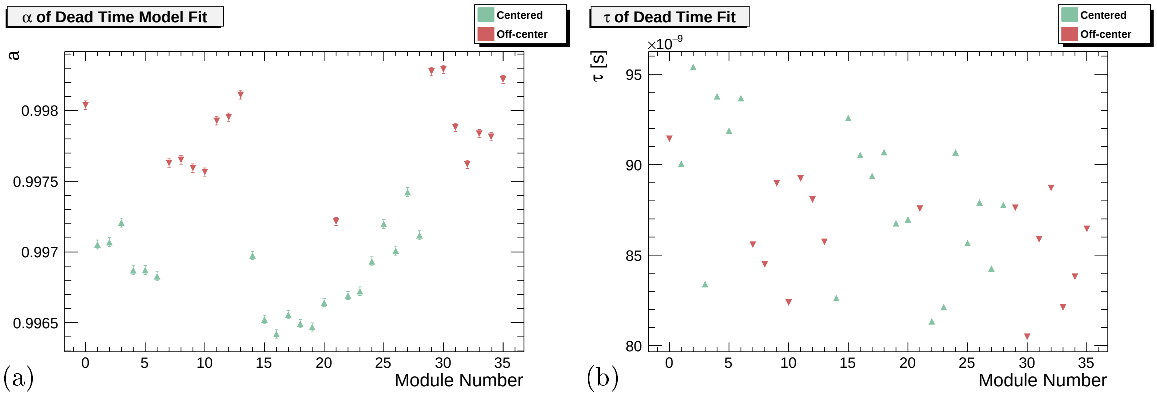

(a) (b)

Figure 5.7: Fit parameters obtained for the dead time model and used to calculate $sDCF$. A similar behavior for all modules is visible. The α indicate the absolute scale for no events and show a separation between the two measurements below 0.2 %. The dead time defined by τ has no separation between the two measurements. The values vary in a range of about 16 % with a mean of 87.4 ns. A slope from low module numbers to higher numbers and thus along the scanner axis could be interpreted.

oxyorthosilicate (LYSO) crystals. Salvadori et al. [131] implemented a GATE simulation and therefore estimated the dead time to 5.9 ns. The dead time for *pheno*PET is much larger with an average of about 87 ns, compare Figure 5.7b. The most reasonable explanation are different settings of the DPC, but the actual parameters within the Vereos PET remain unknown. For example *pheno*PET uses a validation interval of 45 ns. In addition, the recharge process does take 5 ns to 80 ns [61]. These might explain the larger dead time. In contrast to the non-paralyzable dead time model applied in this work Salvadori et al. used a paralyzable dead time model. The results presented above show that the dead time behaves linearly (see Figure 5.8). A linear approximation is valid for both dead time models [39]. Therefore, the choice of the dead time model does not influence the result.

Casey et al. [127] as well as Bai et al. [128] separated the dead time in different components. A main issue is the mispositioning of events on the position sensitive Photo Multiplier Tube (PMT) due to pile-up. This effect should be much smaller for *pheno*PET because the position is computed only on the *die* with the highest count values. Furthermore, *dies* are much smaller than PMTs.

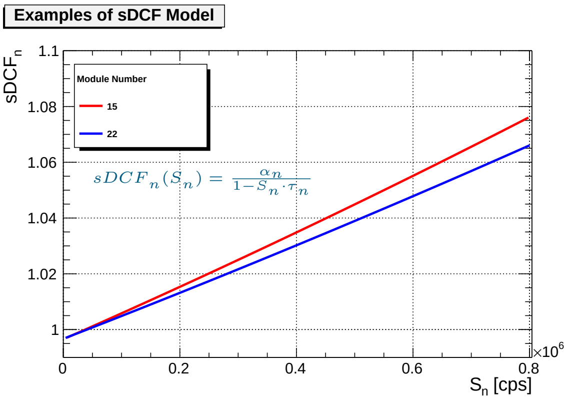

Figure 5.8: $sDCF_n(S_n)$ model for two modules. The linear behavior is observed for all modules. Models are obtained from the fits in Figure 5.5.

5.5.3 Coincidence Dead Time Correction Factors for Module Combinations

The comparison of the $coinDCF_{n,m}$ focuses exemplarily on four module combinations observing different parts of the cylinder. The combinations of module 22 with 14, 15, and 16

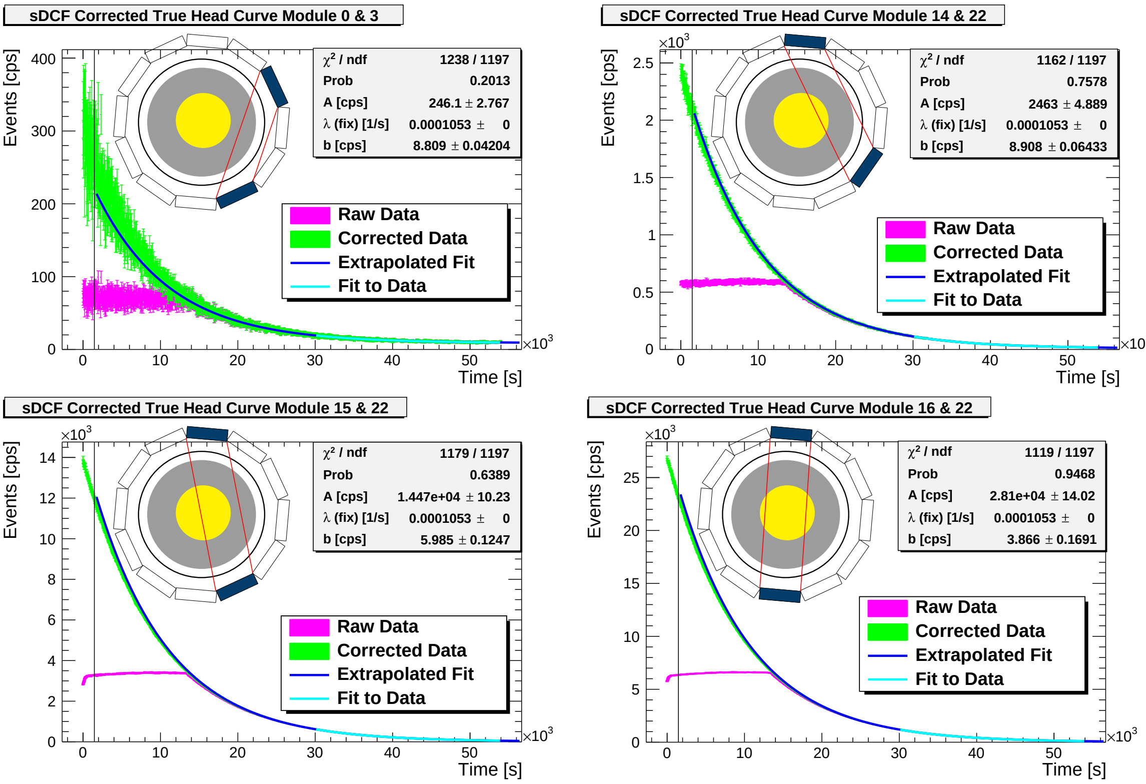

Figure 5.9: Fit for dead time analysis for four module combinations. The *pheno*PET sketches show the channel observed by the given module combination. The *estimated trues* are the difference of the *prompt* and *random* coincidences. Module combination 0 and 3 observes only a few *scattered* coincidences while the other modules observed larger fractions of the cylinder filled with ^{18}F. The active volume of the cylinder is presented in yellow. The vertical black line marks the occurrence of the last overlong package. The qualities of the fits are quite good and indicate only a small correction. Towards the end of the measurement the fit hides the measured values.

belong to the middle ring and observe the cylinder. In contrast, the combination of modules 0 and 3 is in the bottom ring and does only observe additional *scattered* coincidences. The fit to the *estimated trues* for these four combinations are given in Figure 5.9. As expected, the head curves show quite different count rates depending on the module combination and the amount of observed radioactivity. The qualities for the exponential fits are good and indicate a good match between the model and the data.

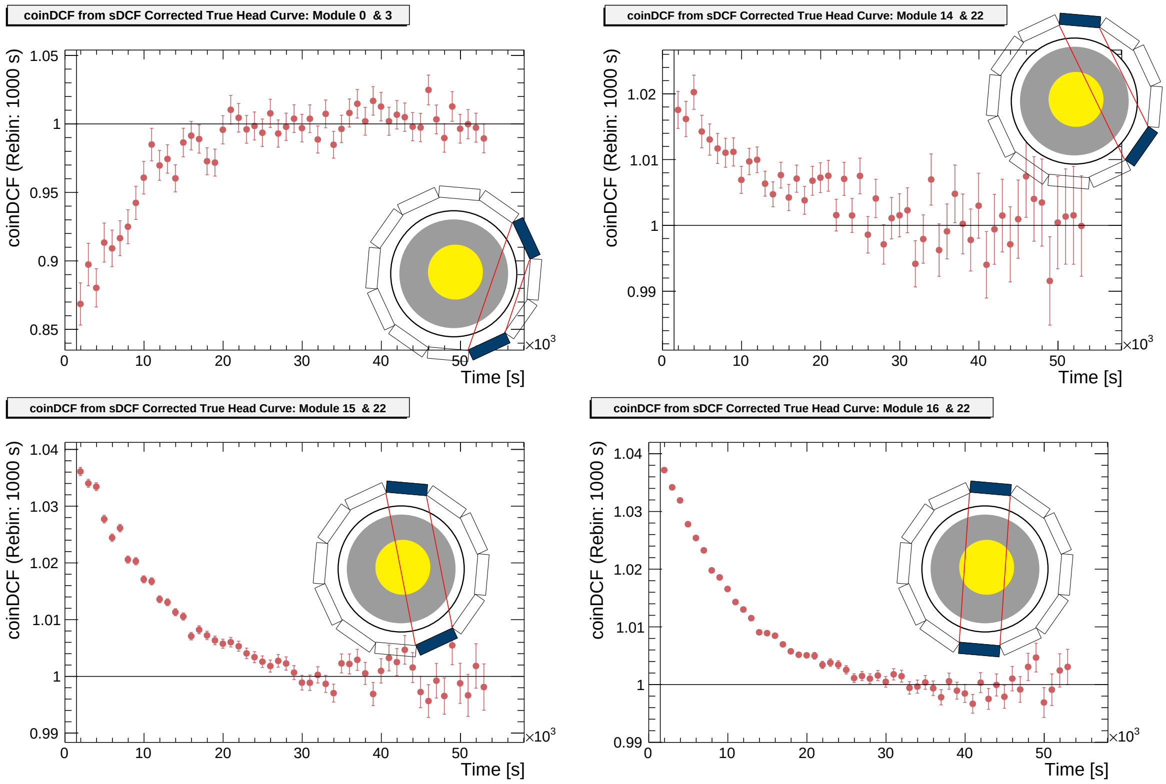

Figure 5.10: $coinDCF_{n,m}$ for four module combinations. The *pheno*PET sketches show the channel observed by the given module combination. The active volume is marked in yellow. The module combinations have quite different results depending on the amount of radioactivity they observe. The vertical black line marks the occurrence of the last overlong package.

The resulting $coinDCF_{n,m}$ are plotted over the measurement duration in Figure 5.10. Module combination 0 and 3 observes up to 15 % more events than expected for the highest activities. In contrast, the other module combinations lack less than 5 % of events. Here further differences for the three combinations with module 22 are visible. A higher amount of radioactivity, resulting from a higher part of the cylinder being measured by the two modules, leads to higher losses. It is important to note that the missing 15 % for modules 0 and 3 are only a small number of events compared to the other module combinations because the absolute event numbers are about two orders of magnitude smaller.

The presented results show that the $coinDCF_{n,m}$ differ between the module combinations. On the other hand the analysis of module combinations is also not sufficient. For example the combinations of module 22 with 15 and 16 have a similar $coinDCF_{n,m}$ of about 1.04, but the count rates differ by a factor of 2. This illustrates that the $coinDCF_{n,m}$ do not only depend on the count rates. The presented examples indicate that the $coinDCF_{n,m}$ depend on the portion of the tube between the two modules filled with radioactive material. The corresponding correction is done with the global $coinDCF$, presented in the next section. The dependency on the individual module combination results in a small bias.

5.5.4 Coincidence Dead Time Correction Factor of Total Head Curve

The head curve of the total number of *estimated true* coincidences $eT^{corr}(\mathrm{t})$ is presented in Figure 5.11. The correction of $sDCF$ shows an improvement towards the expected count rates obtained from the fit to the low count rate region. The resulting $coinDCF$ are given in Figure 5.12 and plotted over the total number of *singles* corrected for dropped frames.

A non-paralyzable dead time model is fitted to the $coinDCF(S_{total})$ and $coinDCF(eT^{corr})$, while the most prominent peaks within the data were excluded. The residuals show a systematic deviation from $y = 0$. The residuals behave like a parabola with its peak close to the center of the fit. The points close to the start and the end of the fit region are below zero. Thus the non-paralyzable dead time model does not describe the data. On the other hand, the fits only differ between 0.1 % and 0.2 % from the obtained values. This can be translated directly into a bias compared to the head curve. Therefore the fitted functions are a suitable approximation.

Figure 5.11: Total head curve of *estimated true* coincidences with correction of dropped packages and detector dead time $sDCF$. The vertical black line represents the last occurring overlong package. The fit is applied to the dead time corrected data. Small losses for high count values are visible. Towards the end of the measurement the fit hides the measured values.

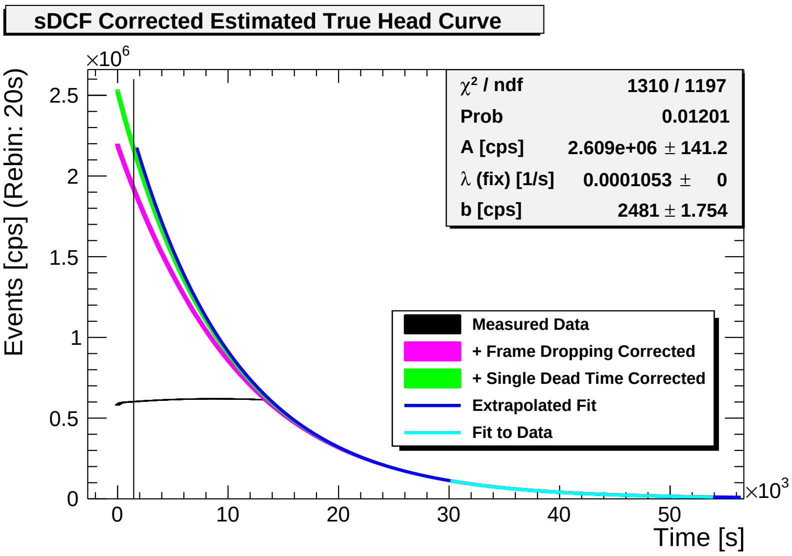

The presented approximation does not model the differences between module combinations observed in Section 5.5.3. Here, the $coinDCF_{n,m}$ in Figure 5.10 indicates a dependence on the position of the phantom, which could translate into a bias on the image. The $coinDCF$ are close to $coinDCF_{15,22}$ and $coinDCF_{16,22}$ with a difference of below 1 % for the highest corrected count rates of 12×10^3 cps and 25×10^3 cps, respectively (see Figure 5.9). Thus these module combinations dominate the $coinDCF$ in contrast to the other two presented combinations. These show a bias of about 2 % at 2×10^3 cps and -18 % at 200 cps for the combination of module 14 with 22 and 0 with 3, respectively. Therefore, a bias on module combinations with low count rates is expected. These differences between the various module combinations might be a reason for the mismatch between the dead time model fits and the data.

The quality of the fit to the $coinDCF(eT^{corr})$ and the quality of the fit to the $coinDCF(S_{total})$ in Figure 5.12 are quite bad. It has to be noted that the covariance between the $coinDCF$ on the y-axis and the S_{total} or eT^{corr} on the x-axis are not considered during the fit. The covariance would lead to larger uncertainties during the fit and therefore improve the quality

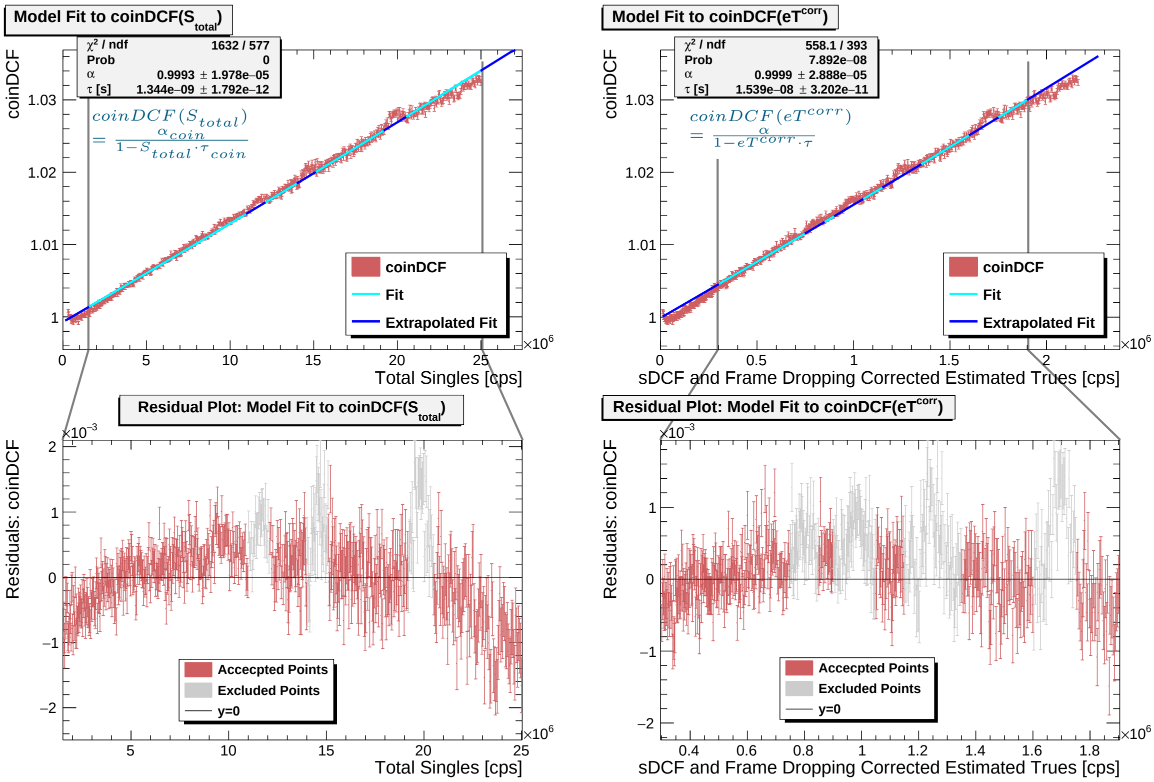

Figure 5.12: Fit of a non-paralyzable dead time model to the obtained *coinDCF*. The three largest peaks of the *coinDCF* were excluded. The residuals show a somehow quadratic behavior. Thus the model does not describe the data in an adequate manner.

of the fit. A consideration of the covariance would not reduce the systematic deviations between the models and the data points. For the $sDCF_n$ first fits gave the same fit parameters, even though the covariance was not considered during the fit. Therefore, the addition of the covariances to the fit procedure is omitted for the *coinDCF*.

The theoretical dead time model depends on the eT^{corr} and not the S_{total} but both curves deliver models with similar deviations from the data as presented in Figure 5.12. The S_{total} can be calculated quite easily during the sorting of coincidences in the projection space for the reconstruction because the S_n are already required for the calculation of the $sDCF_n$. A calculation of head curves corrected for the $sDCF_n$ requires additional computational effort and is therefore not implemented yet.

5.6 Validation of Dead Time Correction Factors and Investigation of Position Dependence

The acquired dead time correction model is validated in this section. During the analysis $sDCF_n$ are calculated from one of the two measurements presented in Section 5.3. The same is true for the *coinDCF*. Therefore, the second measurement can be used for validation. In addition, a third measurement with the same homogeneous cylinder phantom located in the center of the FOV was acquired.

For the $sDCF_n$ four additional measurements are available, which were already presented at the 2018 MIC [126]. Each measurement is done with a small vial at a different radial position. These measurements are used for the validation of the $sDCF_n$. Furthermore, these data illustrate only a small position dependency of the $sDCF_n$.

5.6.1 Comparison of Dead Time Correction Factors of Modules

The comparison of the dead time correction factors of the modules $sDCF$ has two goals. The first is to prove that the above presented factors still hold for a different measurement. The vial data allow the investigation of a possible dependency of the $sDCF$ on the position of a small sample. The results indicate the precision of the calculated $sDCF$ and indicate a small bias for high activity sources close to the edge of the FOV.

5.6.1.1 Measurement Setup of ^{18}F Vial

The vial experiment consists of four measurements with vials containing ^{18}F. The ^{18}F is diluted in about 0.5 ml to 1 ml water. The vial has a diameter of 24 mm and a height of 45 mm. For each measurement the vial is placed at one of the positions presented in Figure 5.13. The vial is placed in a small beaker, which is fixated with adhesive tape. The amount of radioactivity within each vial is measured with a Curie-Meter right after the production in the cyclotron. In Figure 5.13 the maximum activity, that could be measured without the occurrence of overlong packages, is given.

These vial measurements were acquired with an intermediate firmware version. Therefore, the measurements were divided in a series of 300 s long measurements. As soon as an overlong package occurred on a module, the data transfer was stopped by the CCB for the current running measurement but the measurement was not aborted. The next measurement then starts, saving data until it is complete or an overlong package occures.

It has to be noted that 10 of the total 1028 acquired short measurements failed and stopped data acquisition during operation in the absence of overlong packages. The data of this measurement series were already presented at the 2018 MIC [126].

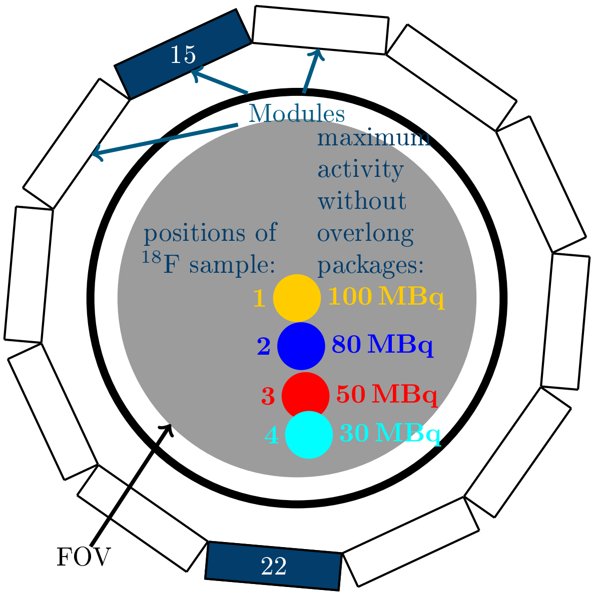

Figure 5.13: Measurement positions and maximum measured activities. The sample is kept on the same height (axial position) within the middle ring. The activities at each position are limited by the occurrence of overlong packages measured by any module.

5.6.1.2 Analysis

The seven measurements are analysed in the same way. For the analysis the procedure presented in Section 5.4.2 is adopted. The *singles* measured by each module are used to create *single* head curves. An exponential fit with a constant background, see Equation (5.3), is applied to the end of the measurement. Here, dead time effects can be neglected. The fit is extrapolated to the complete measurement duration to obtain ideal expectation values $S_n^{ideal}(t)$. Together with the measured *singles* S_n, which are corrected for frame dropping, the correction factors are calculated as

$$sDCF_n^{meas}(t) = \frac{S_n^{ideal}(t)}{S_n(t)}.$$

Afterwards the $sDCF_n^{meas}$ are plotted as a function of the S_n.

The head curves for the vial measurements need some additional attention to combine the 300 s long measurements to a head curve of the complete measurement. The start of a new measurement requires approximately 26 s. This shift is documented within the file names of the raw files as a timestamp with a date from year to second. This results in small gaps in the vial data.

The comparison is done with residual graphs between the $sDCF_n^{meas}(S_n)$ each measurement and the model $sDCF_n^{model}(S_n)$ obtained above in Section 5.5.2. The concept of residual graphs is described in Appendix A. The residuals are calculated as

$$r_n(S_n) = sDCF_n^{meas}(S_n) - sDCF_n^{model}(S_n) = \frac{S_n^{ideal}}{S_n} - \frac{\alpha_n}{1 - \tau_n \cdot S_n}$$

with the model parameters α_n and τ_n. The uncertainties for the residuals are calculated as

$$\sigma_{r,n}^2(S_n) = \left(\frac{\partial}{\partial S_n} r_n(S_n)\right)^2 \cdot (\sigma_n(S_n))^2 .$$

Here, $\sigma_n(S_n)$ are the standard deviations on the count rates S_n for each module n. This approach incorporates the covariance between the $sDCF_n$ and the S_n. To enhance the visualization the number of points per graph is reduced by averaging the values $sDCF_n$ and *single* counts in intervals of 3500 cps *singles*.

5.6.1.3 Results and Discussion

The comparison for module 15 and 22 are presented in Figure 5.14. In general, the cylinder measurements match quite well, with deviations below ±0.2 %. An exception from these deviations are the visible peaks which were excluded from the calculation of the model. The vial data show larger deviations but they are still below ±0.5 %. Here the main exception is the measurement on position 3 with the vial closest to the detector modules 21, 22, 33 and 34. Those modules show deviations of up to 1 %.

For the vial at position 3 several modules show a step similar to module 22 at low count rates. This step can be located in the middle of a 300 s measurement and outside the fit region. Furthermore no frames are dropped at these time points. The step is visible in the *single* head curves. This indicates that the effect is present in the raw data. The actual reason has not been identified but a similar step has not been observed in a later measurement.

The residuals mostly show a linear behavior which indicates a slightly different slope of the $sDCF_n$ for the different experiments. Nevertheless this also indicates a linear dependence on the observed count rates.

For count rates below 0.05×10^6 cps all curves converge to a deviation of about 0.2 %. This is the region used to determine the expectation values and about the value of the factor α. This general scaling of the $sDCF$ is no problem due to the application of the global calibration factor after the images have been reconstructed.

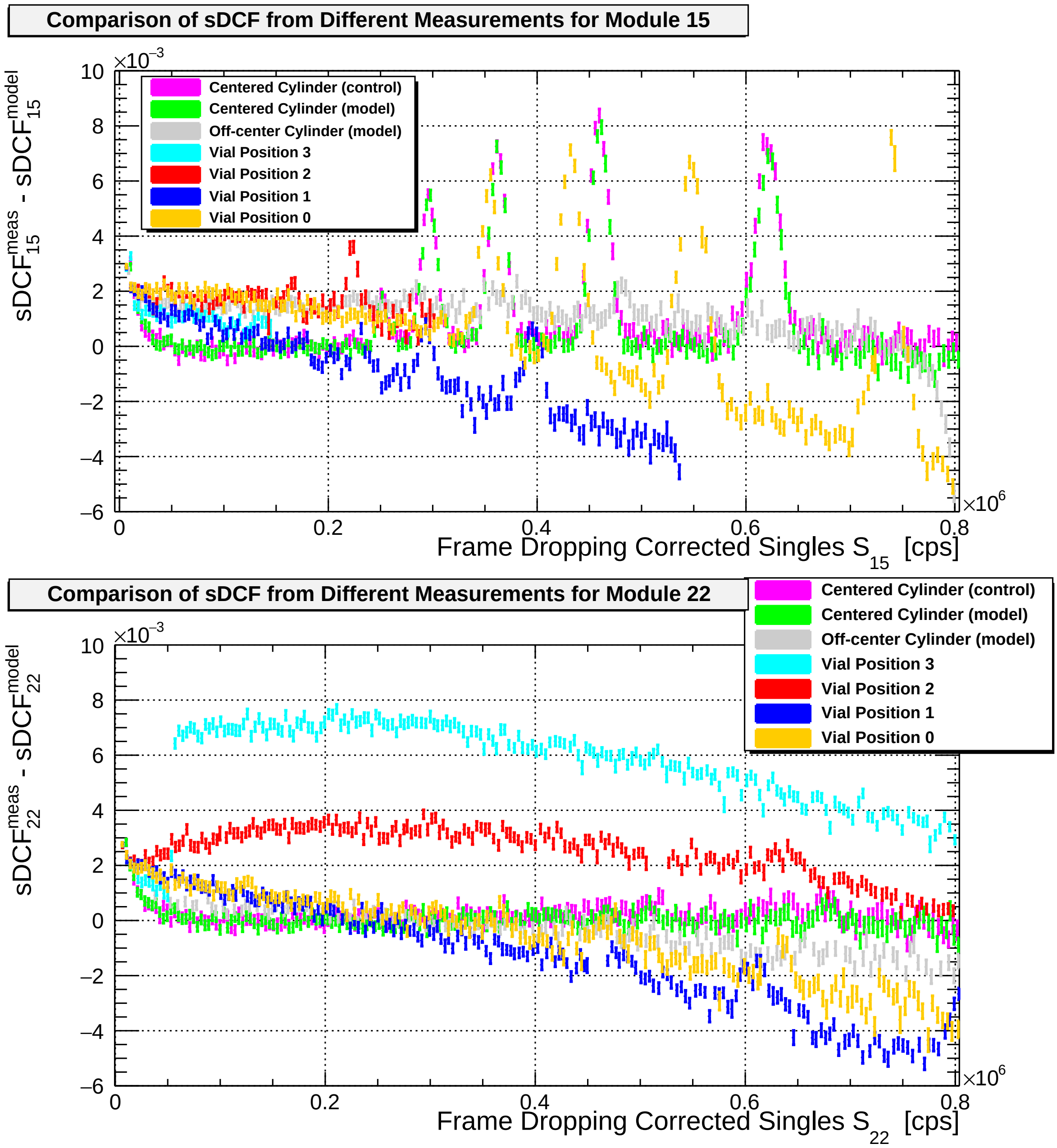

Figure 5.14: $sDCF_n$ from different measurements. The presented $sDCF$ models are obtained from the centered cylinder. The factors calculated from all cylinder measurements match quite well. Differences are visible for the vial data. A stable operation without overlong package was found below 0.75×10^6 cps.

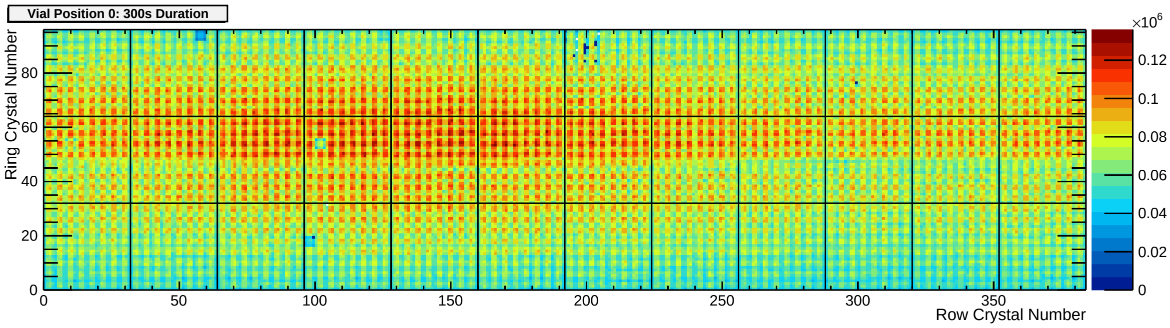

(a) Vial at position 0.

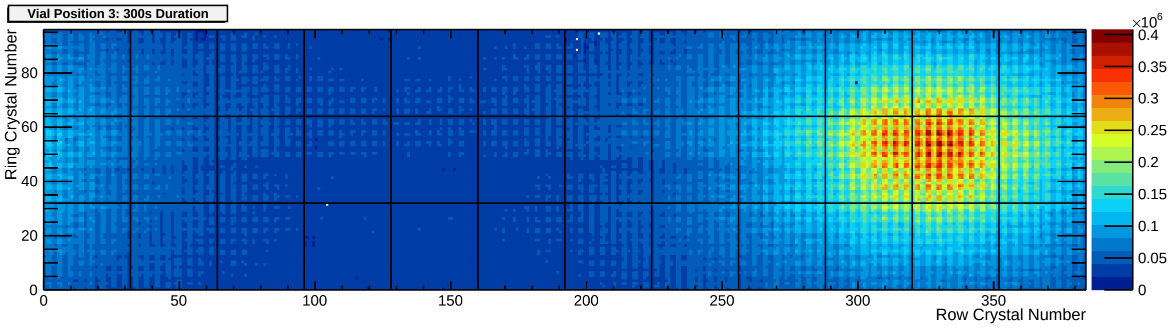

(b) Vial at position 3.

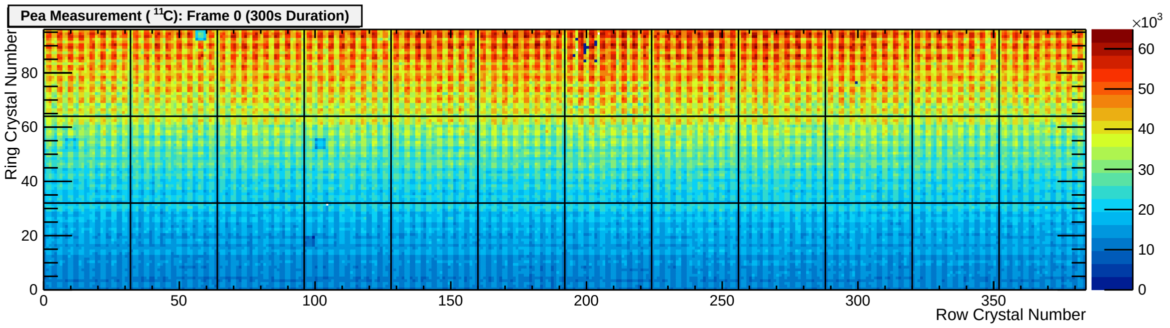

(c) Pea measurement with $[^{11}C]CO_2$ during application. Same data as in Figure 5.1a.

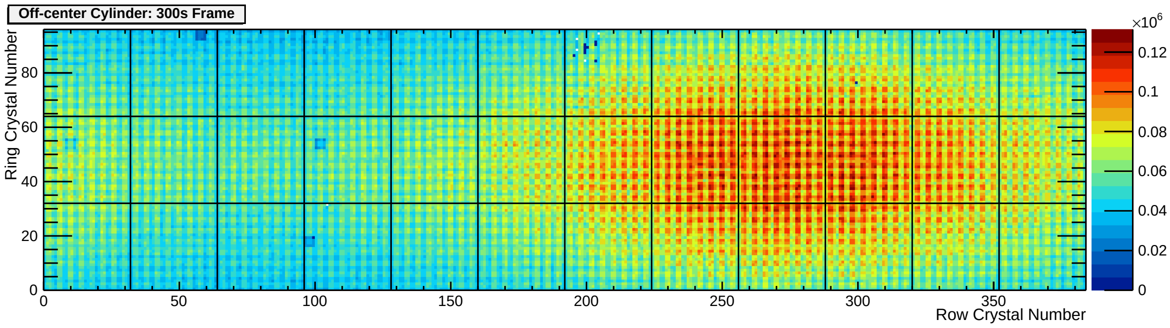

(d) Cylinder placed away from scanner axis.

Figure 5.15: Hit maps of *singles* of the first 300 s measurement without any overlong package. For the two vial positions a clear change of the distribution of count values detected by the crystals of the modules is visible. The cylinder and the vial at Position 3 show a radial dependency on the count rates while the plant measurement has an axial dependency with compatible relative differences.

The presented examples illustrate the differences between the vial data and the cylinder measurements. As mentioned above the firmware was improved between the vial and cylinder measurements. These improvements focused on the handling of measured data in the CCB but did not alter the measurement operation of individual modules. The firmware of the individual detector modules was not changed. It is more likely that the differences result from the setup of the measurement. In Figure 5.15 hit maps of *single* events are presented for the different measurements. The vial close to the modules in Figure 5.15b result in quite different count rates even on a single module. The top left *tile* of module 22 has the crystals with the highest counts in all measurements. On the other *tiles* of module 22 the count values are reduced to 25 % of the maximum value. The same is true for the the neighbouring modules 21, 33 and 34. All these modules show the step in the $sDCF_n$ visible in Figure 5.14. For the vial in the center of the FOV differences on one module are smaller with a decrease to about 50 %. The hit map, Figure 5.15c, of the pea measurement shows quite stable patterns on a module ring. A general decrease is visible towards the bottom of the FOV, where the roots are located. Here, only a small fraction of the ^{11}C has been transported at the start of the measurement. On a single module the count rates are decreased to about 66 % of the maximum value on that module. The off-center cylinder in Figure 5.15d produces a slightly smoother behavior in the hit maps compared to the vial close to the modules due to larger dimension of the cylinder. The decrease on a single module is about 50 %. Therefore, the range of count rates is smaller than for the vial.

The calculations of the *single* count rates is done for one module. Therefore, large count rate variations on a module are not considered. The plant measurement shows that the off-center cylinder is a better model for the differences on one module than the vial close to the detectors. Furthermore, plants are placed in the center of the FOV and not in front of the modules on one side.

As an activity distribution in a plant measurement is a complex superposition from the different root and small organs, the vial data can help to estimate a worst case scenario of the effect on the dead time correction. The maximum observed differences between the $sDCF$ from the vial measurements are up to 0.01 for high count rate values. The $sDCF$ range from 0.99 to 1.08. Thus the product of two $sDCF$ would differ from the real correction factor by less than 2 %. For the current measurements these differences occur mainly for the first few frames as low amounts of activity are used to perform several measurements over the day.

5.6.2 Comparison of Coincidence Dead Time

In the following the $coinDCF$ is analysed for the three different cylinder measurements. The vial measurements are not part of this analysis since the measured raw data of the vial measurements had to be deleted due to disk space limitations. Therefore, the coincidence sorting could not be performed with the latest version of the coincidence sorter.

5.6.2.1 Analysis

For the comparison of the $coinDCF$ the other two cylinder measurements are analyzed as presented in Section 5.4.3. Estimated *trues* $eT_{n,m}$ are calculated from the sorted coincidences. These $eT_{n,m}$ are corrected with the $sDCF$ correction model and the frame dropping correction. Afterwards the $eT^{corr}_{n,m}$ are summed up to obtain eT^{corr}. An exponential fit $eT^{fit}(t)$ (Equation (5.3)) is applied to the region without dead time effect to the resulting head curves of eT^{corr}. Afterwards $coinDCF$ are calculated as

$$coinDCF(t) = eT^{fit}(t)/eT^{corr}(t)$$

and plotted over S_{total}, the number of *single* events measured by all modules.

The comparison of the $coinDCF(S_{total})$ is done as residual graphs (see Appendix A). The residuals are calculated between each of the three measurements and the function obtained in Section 5.5.4. The $coinDCF$ and the S_{total} are averaged in intervals of 7×10^4 cps of the S_{total} before the residuals are calculated. This enhances the visualization by reducing the number of points.

5.6.2.2 Results and Discussion

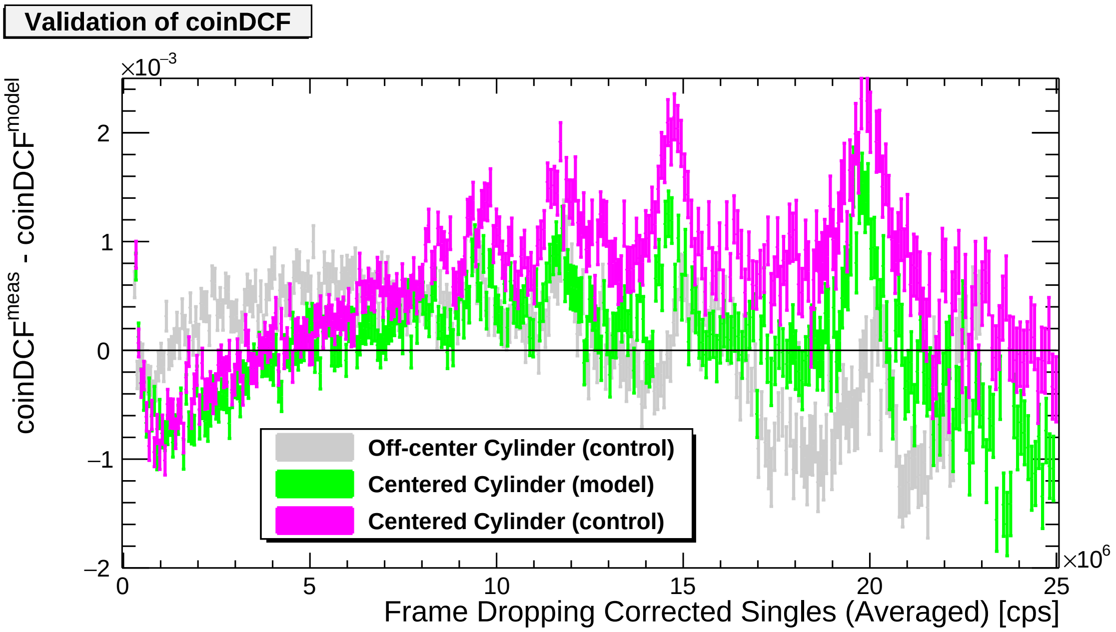

Figure 5.16: Comparison of $coinDCF$ from different measurements. The cylinder measurements show comparable results.

The residuals of the $coinDCF$ from the three measurements are presented in Figure 5.16. The residuals of all three measurements show a parabola shape and indicate the already discussed mismatch of the model. Nevertheless, these deviations are below 0.25 %. The largest deviations result from the peaks on the $coinDCF$, and in general deviations below 0.1 % are observed. The off-center cylinder does not vary too much from the centered cylinder. Therefore the position of the cylinder has no influence.

5.7 Discussion

The investigations in this section present a model to correct for count rate loses during a measurement with *pheno*PET. The USB 3.0 limits the maximum rate of recorded raw data and thus the available statistic. The controlled frame dropping works really well and allows an extension of the dynamic range by a factor of about 3.5 resulting in an maximum measurable activity of about 100 MBq. The dynamic range is limited by the ability of the CCB firmware to handle the data packages provided by the DPC.

All recorded $sDCF$ show a linear behavior and thus no saturation effects due to dead time. A minor global correction factor $coinDCF$ of up to 1.035 is introduced with a maximum deviation of 0.002, which is not expected from the investigation of the coincidence sorter.

The analysis of the dead time between module combinations, called $coinDCF_{n,m}$ indicated a dependency on the position of the phantom. A module combination with a lower count rate showed lower dead time losses compared to the global correction factor $coinDCF$. This might introduce a bias, below 2 %, for low activity regions. This bias depends on the overall count rates due to the activity distribution. A detailed investigation was omitted to work on the other correction for the correction of quantitative images, which were still required at this point.

The dead time on the individual detector modules showed a maximum correction factor of about 1.08, which results in a maximum correction for a LOR close to 1.17. Small volumes with a high activity concentration, close to the modules, introduce a bias of about 0.01 on these modules. This probably results from different behavior of the four *tiles*.

The established correction model could still be improved. For example improvements might result from taking into account the more detailed structures on a module. For example the $sDCF$ can be determined for each DPC or each *die* of the DPCs. A calculation on *die* level would require a further investigation of the clustering algorithm because this combines recorded hits of all *dies* belonging to a *tile* to one *single* event. The clustering algorithm is also a possible reason for the $coinDCF$. The clustering combines all hits within a 5 ns interval to a *single*. The coincidence sorting looks for time differences of 2.5 ns. Thus the clustering can combine two *singles* on one *tile* to one *single*. However, the combination of a hit (e.g. a dark count) with a *single* is more likely. If this hit occurs before the actual *single* it defines the timestamp, which is wrong for the *single*. These effects introduce a further pile-up effect, which is only relevant for coincidences but not for *singles*.

The easiest possibility is to reduce the clustering window to 2.5 ns. An alternative could be a more complex clustering algorithm that uses the positions of the triggered *dies*. Here, ideas might be taken from [132]. This might further improve the separation of two events on a *tile*, which is especially relevant for high count rates. It has to be noted that a change of the calculation of the $sDCF_n$ would influence the obtained $coinDCF$ and $coinDCF_{n,m}$. This might reduce the observed bias. For each investigation all calibrations and all other correction need to be recalculated and investigated for possible changes and dependencies.

One important aspect of the count rate corrections for plant measurements is the gradient along the scanner axis. For the calculation of this model a homogeneous cylinder is measured to determine the correction factors of all modules at the same time. The measurement of the cylinder away from the center of the scanner axis results in a count rate gradient along the rings. The results show that the count rate corrections depends below 0.05 % on the position of the cylinder. It can be expected that the behavior will be similar for a gradient along the scanner axis.

The plant measurements currently performed use the high sensitivity of *pheno*PET to apply only small amounts of $^{11}CO_2$. Thus, the current model and dynamic range are sufficient. In the medium to long term perspective it might be useful to further increase the dynamic range to allow longer measurements with a higher starting activity. Here, several discussions within the *pheno*PET project revealed different possibilities. For example, the data acquisition by the DPC can be reduced. A veto signal allows to block the recording of additional events. Furthermore the firmware of the CCB could be modified to allow the transfer of overlong packages. A last possibility would be to modify the frame dropping correction. At the moment the assumption is that the average number of events is constant. It could be possible to use a truncated mean to estimate the expected number of events per time from the number of recorded packages. The overlong packages should contain the tail with high event numbers of the Poisson distribution. The main advantage of this approach is that no changes to the firmware of *pheno*PET are required.

Chapter 6

Normalization

The image reconstruction for Positron Emission Tomography (PET) implements a model of the imaging system that is used for the calculation of an image of the radioactivity distribution from the measured data. The geometric model of *pheno*PET within PET Reconstruction Software Toolkit (PRESTO) are the crystal positions and dimensions. The Maximum Likelihood Expectation-Maximization (MLEM) algorithm compares the predicted events in a Line-of-Response (LOR) between pairs of crystals with the measured data. This estimation requires a modeling of the measurement process. The normalization calibrates the model of *pheno*PET to the actual measurement. This calibration corrects only static effects, which do not depend on the count rates or the measured object. Examples for effects that contribute to the normalization are different detection efficiencies of crystals or imperfections of the positioning of the crystals compared to the model.

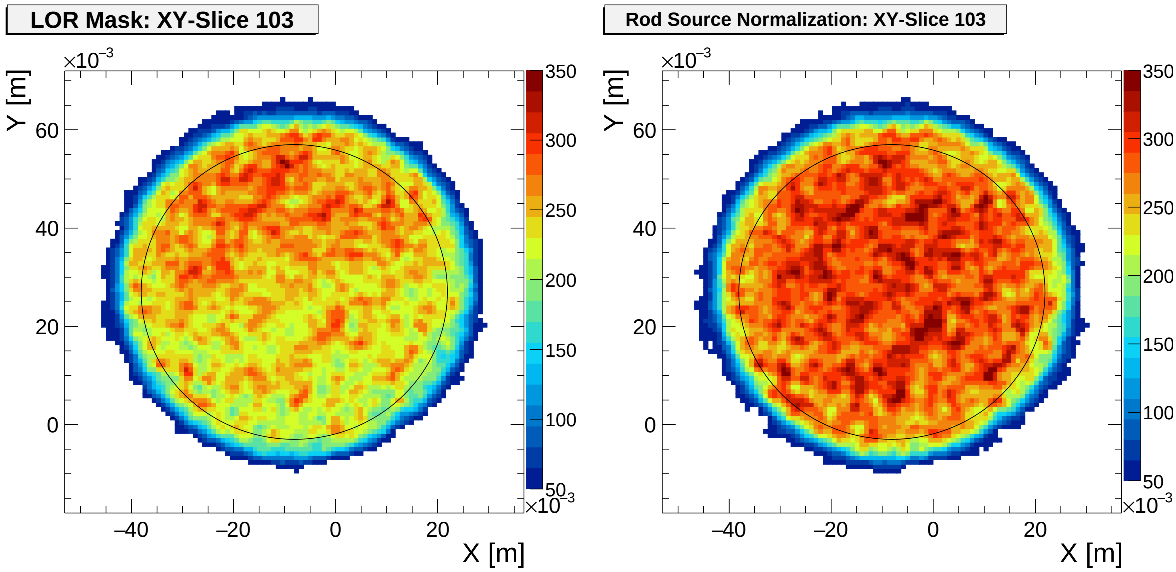

(a) Before normalization.

(b) After normalization.

Figure 6.1: Reduction of radial bias by applying the normalization. The phantom is placed outside the center. The bias is visible for the radial distance to the center of the Field-of-View (FOV).

In Figure 6.1 a slice of a homogeneous cylinder is displayed. The normalization removes a radial bias which results from the different angles of the LORs entering the crystals. This angle leads to different effective crystal length and alters the chance to detect a photon. For *pheno*PET a first model with this geometric component and the crystal efficiencies is implemented and calculated according to [83].

In the following chapter the implementation is presented. As a first step, the model is tested with synthetic data. The second step is the calculation of expectation values in case of a rotating rod source and then the calculation of sensitivities from two measurements. The resulting normalizations indicate a stable operation of *pheno*PET over two years.

6.1 Implemented Normalization Model

The static normalization model implemented for *pheno*PET is based on the work published by Hogg et al. [83]. They propose a component-based normalization with the sensitivity of each crystal ϵ_i, a geometric factor between two crystals g_{ij} and a timing window alignment factor between different modules. The normalization factors are determined with a Likelihood estimation, which is iteratively solved.

The timing factor is not implemented for *pheno*PET. It is assumed to be small because *pheno*PET has a global clock. Furthermore, Matthias Streun implemented a skew correction to minimize temporal misalignment between all *dies*, which is presented in [116] and mentioned in Section 3.2.1.

Hogg et al. describe the average number of measured events $\hat{M}_{ij}$ in each LOR between two crystals i and j as

$$\hat{M}_{ij} = \epsilon_i \epsilon_j \cdot g_{ij} \cdot A_{ij} \cdot \alpha \tag{6.1}$$

with the expected number of events in each LOR A_{ij}. For the fitting Hogg et al. also added a global scaling factor α. Thus, the A_{ij} need to model the relative differences between the LORs. This allows to introduce the side conditions that the average of ϵ_i and g_{ij} are fixed to 1 after each iteration step. The required scaling is absorbed in the global scaling factor α. Afterwards the scaling can be absorbed by the calibration factor, which is presented in Section 7.7

The number of measured events m_{ij} in a measurement is given by a Poisson distribution with mean $\hat{M}_{ij}$. The log likelihood function is then given by

$$\log(L) = \sum_{ij} (m_{ij} \log(\hat{M}_{ij}) - \hat{M}_{ij} - \log(m_{ij}!)) \tag{6.2}$$

Hogg et al. solve this iterative calculation for iteration $n+1$ with the equations

$$\epsilon_i^{(n+1)} = \sum_j m_{ij} \Big/ \sum_j \epsilon_j^{(n)} \cdot g_{ij}^{(n)} \cdot A_{ij} \cdot \alpha^{(n)} \tag{6.3}$$

$$g_{ij}^{(n+1)} = \sum_{kl} m_{kl} \Big/ \sum_{kl} \epsilon_k^{(n)} \epsilon_l^{(n)} A_{kl} \cdot \alpha^{(n)} \text{ with all } kl \text{ belonging to the symmetry set of } g_{ij} \tag{6.4}$$

$$\alpha^{(n+1)} = \sum_{ij} m_{ij} \Big/ \sum_{ij} \epsilon_i^{(n)} \cdot \epsilon_j^{(n)} \cdot g_{ij}^{(n)} \cdot A_{ij} \tag{6.5}$$

The geometric factors use the same symmetries used for the creation of the system matrix with PRESTO, see Section 3.5.1.3. Thus, up to 48 LORs have the same geometric factor g_{ij}.

6.2 Iteration Schema and Starting Values

Hogg et al. obtained the best results for the iteration schema that first calculates the $\epsilon_i^{(n+1)}$ and afterwards the $g_{ij}^{(n+1)}$. During the iteration process already calculated $\epsilon_i^{(n+1)}$ are used instead of the older $\epsilon_i^{(n)}$.

For *pheno*PET the scaling factor α is calculated after each iteration and before the first iteration step. Afterwards the ϵ_i are calculated subsequently. The g_{ij} have no further dependencies, thus their calculation is multi-threaded. Afterwards the new sensitivities are scaled to achieve mean values of 1 for ϵ_i and g_{ij}. Together with the new α the current value of the Likelihood values is calculated according to Equation (6.2). The $\log(m_{ij}!)$ values are constant within a measurement and can be ignored for the maximization. For tests with synthetic data, the Stirling formula is used as approximation. The iteration processed is repeated 41 times because the Likelihood values are slightly higher for odd iteration numbers than for even.

The starting values for the g_{ij} are set to 1. The start values of the crystal efficiencies are extracted from a *prompt* hit map. The counts of each crystal are divided by the number of LORs contributing to this crystal. Afterwards the mean value of all crystals is set to 1 by a division of the average *prompts* per LOR.

6.3 Test with Synthetic Data

In order to verify the algorithm to achieve a component-based normalization, a number of tests are done with synthetic data. Therefore, a measurement with a Poisson distribution is simulated without *random* coincidences. The relative differences between the input normalization factors and the output are compared to each other. The results show that the achievable precision and especially the maximum deviations of single parameters depend on the width of the distributions describing the normalization parameters. Nevertheless, the dominating factor remains the statistics of the acquired measurement.

6.3.1 Method

For the following investigations a ground truth value for each geometric factor g_{ij} and each crystal efficiency ϵ_i is assumed. The ideal expectation value A_{ij} is set to the same value for all LORs. The mean measured value $\hat{M}_{ij}$ are calculated according to Equation (6.1) with $\alpha = 1$. The actual measured values m_{ij} are integer values obtained from a Poisson distribution with mean $\hat{M}_{ij}$.

The crystal efficiencies are obtained from data measured in 2018, which is used in Section 6.4 to calculate a normalization. A *prompt* hit map is filled with the LORs contributing to the FOV with radius 90 mm and a maximum ring difference of 80 crystals. Crystals with values below 6×10^5 events are excluded from the further analysis. The remaining crystals are processed for the calculation of the starting values of the ϵ_i. These values are filled into a histogram, which is used as a probability density function to draw random numbers for each crystal. The geometric efficiencies are random numbers from a Gaussian distribution with a mean value of 1 and varying standard deviations σ_{geo}. All g_{ij}, ϵ_i and m_{ij} are above 0 as a side condition.

Two different cases are studied. The first case addresses the precision for different widths of the distribution of the normalization factors. Therefore, different σ_{geo} =0.05, 0.1, 0.15, 0.2, 0.25 and 0.3 are simulated with $A_{ij} = 45$. The second study models the effect of the overall statistic by changing the A_{ij} =9, 45, 90, 900, 9000 and 90 000 with $\sigma_{geo} = 0.2$. The fixed values are inspired by the actual result of the latest calculated normalization with an average of about 38 *trues* per LOR and a standard deviation of around 0.17 for the g_{ij}. It has to be noted that the g_{ij} do not follow a Gaussian distribution.

The precision for each case is evaluated by the relative difference between the ground truth and the result of the iteration process. The crystal sensitivity relative difference rd_i^{ϵ} and the geometric sensitivity relative difference rd^g_{ij} are given by

$$rd^\epsilon_i = \frac{\epsilon_i^{(n)} - \epsilon_i^{gt}}{\epsilon_i^{gt}} \text{ and } rd^g_{ij} = \frac{g_{ij}^{(n)} - g_{ij}^{gt}}{g_{ij}^{gt}}$$

with the iteration results $\epsilon_i^{(n)}$ and $g_{ij}^{(n)}$ as well as their ground truth values ϵ_i^{gt} and g_{ij}^{gt}. These relative differences are independent of the actual input values. For the evaluation the average crystal sensitivity relative differences $\overline{rd^\epsilon_i}$ and the average geometric sensitivities relative differences $\overline{rd^g_{ij}}$ are calculated from the crystal sensitivity and geometric sensitivity relative differences, respectively.

For the image reconstruction especially the sensitivities of each LOR are important, which are calculated as

$$s_{ij} = \epsilon_i \cdot \epsilon_j \cdot g_{ij}.$$

The deviation of the normalization is addressed with the LOR sensitivity relative difference rd^s_{ij} and the LOR sensitivity absolute relative differences $|rd^s_{ij}|$, which are given by

$$rd^s_{ij} = \frac{s_{ij}^{it} - s_{ij}^{gt}}{s_{ij}^{gt}} \text{ and } |rd^s_{ij}| = \left|\frac{s_{ij}^{it} - s_{ij}^{gt}}{s_{ij}^{gt}}\right|. \tag{6.6}$$

The average values for these two values, $\overline{rd^s_{ij}}$ and $\overline{|rd^s_{ij}|}$, are calculated from the relative differences rd^s_{ij} and $|rd^s_{ij}|$, respectively.

The two values for the sensitivities, $\overline{rd^s_{ij}}$ and $\overline{|rd^s_{ij}|}$, are later used to evaluate the effect of small uncertainties within the calculation of expectation values for measured data on the normalization.

6.3.2 Influence of Geometric Sensitivity Widths

All relative differences for the different σ_{geo} are presented in Figure 6.2 and is discussed in the following. The LOR sensitivity relative differences are well below 10 % for nearly all LORs and σ_{geo}, see Figure 6.2a. Especially for larger σ_{geo} more $rd^s_{ij} < 0$ are visible. The average values in Figure 6.2b shows that for all σ_{geo} an average difference $\overline{rd^s_{ij}}$ close to 0 is observed. The $\overline{rd^s_{ij}}$ do not decrease for larger σ_{geo}. Thus the observed variations can be expected to result from the fit and not from a systematic effect. The $\overline{|rd^s_{ij}|}$ are below 2 % and the visible increase is below 0.1 %. This represents the broader distribution observed for increasing σ_{geo} in Figure 6.2a.

For $\sigma_{geo} > 0.15$ a small fraction of the LORs starts to show $\left|rd^s_{ij}\right| > 10\,\%$. These deviations mainly result from the geometric sensitivities g_{ij}. This is visible in the geometric sensitivity relative differences in Figure 6.2c. In general, these distributions are very similar to those of the rd^s_{ij}. For the $\sigma_{geo} > 0.2$ few rd^g_{ij} with large deviations are visible and for $\sigma_{geo} = 0.3$ some rd^g_{ij} with values up to 200 % occur, but are not displayed. Nevertheless most of the rd^g_{ij} are below 10 %. The distributions of the rd^g_{ij} and rd^s_{ij} do not change significant for $\sigma_{geo} \leq 0.15$.

The crystal sensitivities show maximum relative differences rd^ϵ_i of 0.1 %, shown in Figure 6.2d. This maximum deviation is slightly decreased for smaller σ_{geo}. Therefore, the precision of the ϵ_i is much better than for the g_{ij}.

As expected, rd^g_{ij} and rd^ϵ_i illustrate that the number of contributing LORs is important for the achievable precision of a specific factor. Thus, the introduction of additional symmetries

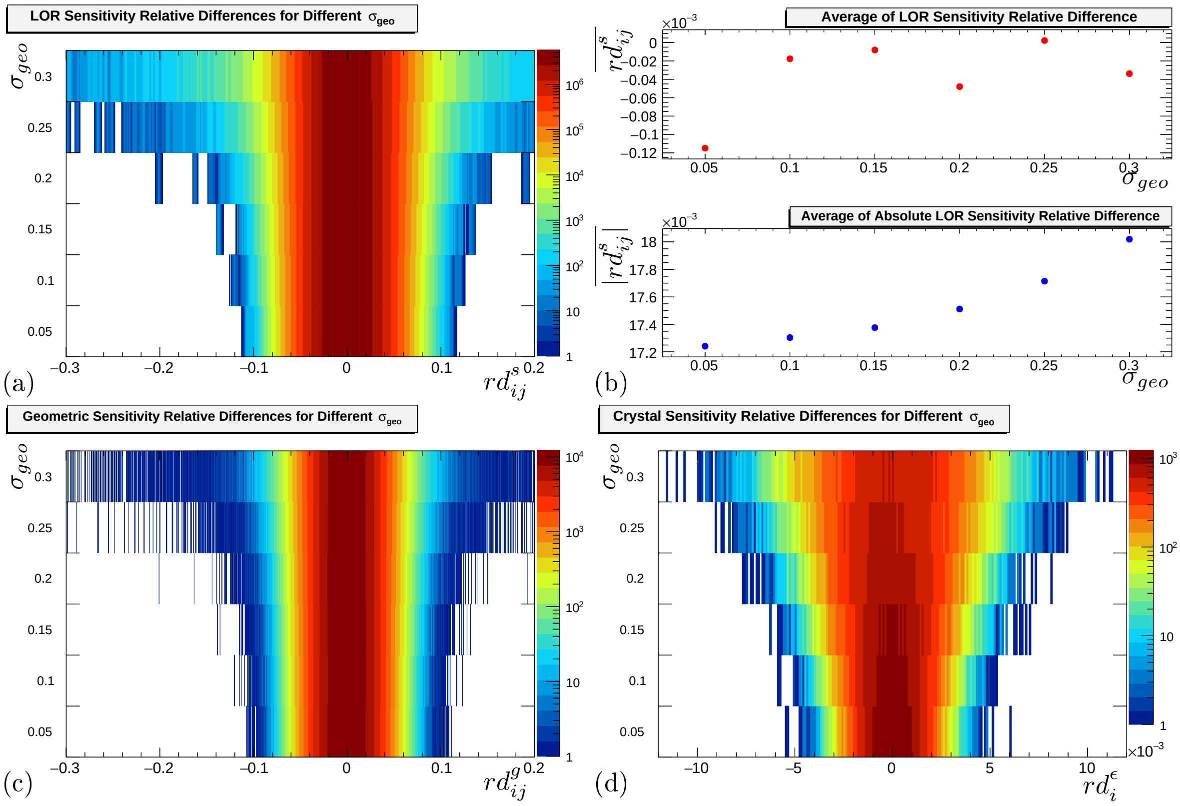

Figure 6.2: Precision of normalization result for different widths of normalization factors. The crystal sensitivities can be determined quite precise compared to the geometric factors. For $\sigma_{geo} > 0.2$ a few g_{ij} start to show large deviations, which are not shown here.

might improve the precision of the g_{ij} and thus of the complete normalization. For a Gaussian distribution of the geometric sensitivities the majority of the ϵ_i, g_{ij} and s_{ij} can be determined with a deviation below 20 % and a $\overline{|rd^s_{ij}|} < 2\,\%$ as depicted in Figure 6.2.

6.3.3 Influence of Overall Statistics

The relative differences depending on the overall statistics are depicted in Figure 6.3. In principle the three relative differences rd^ϵ_i, rd^g_{ij} and rd^s_{ij} behave very similar. For increasing statistics the distribution of the relative differences decrease. The sensitivities s_{ij} show distributions with means close to zero (see Figure 6.3b) and no systematic shift is visible. The maximum deviations are decreased with more events. For an average of 45 events per LOR the maximum rd^s_{ij} are about 20 % compared to the ground truth. The mean of the absolute differences behave as $\overline{|rd^s_{ij}|} \sim 1/\sqrt{A_{ij}}$, which is illustrated by the black line in Figure 6.3b. This is expected for a counting experiment.

As already experienced for the different widths of normalization factors these deviations are dominated by the geometric sensitivities g_{ij}. For the crystal sensitivities ϵ_i the lowest maximum deviations can be obtained for A_{ij} between 90 and 900. Overall the precision of the ϵ_i is below 0.1 % for $A_{ij} \geq 45$, see Figure 6.3d.

The two lowest A_{ij} show for all three parameters that even though the Likelihood approach incorporates the statistical properties of the radioactive decay, the measurement statistics is still relevant to decrease the maximum deviations. Nevertheless, most of the sensitivities s_{ij}

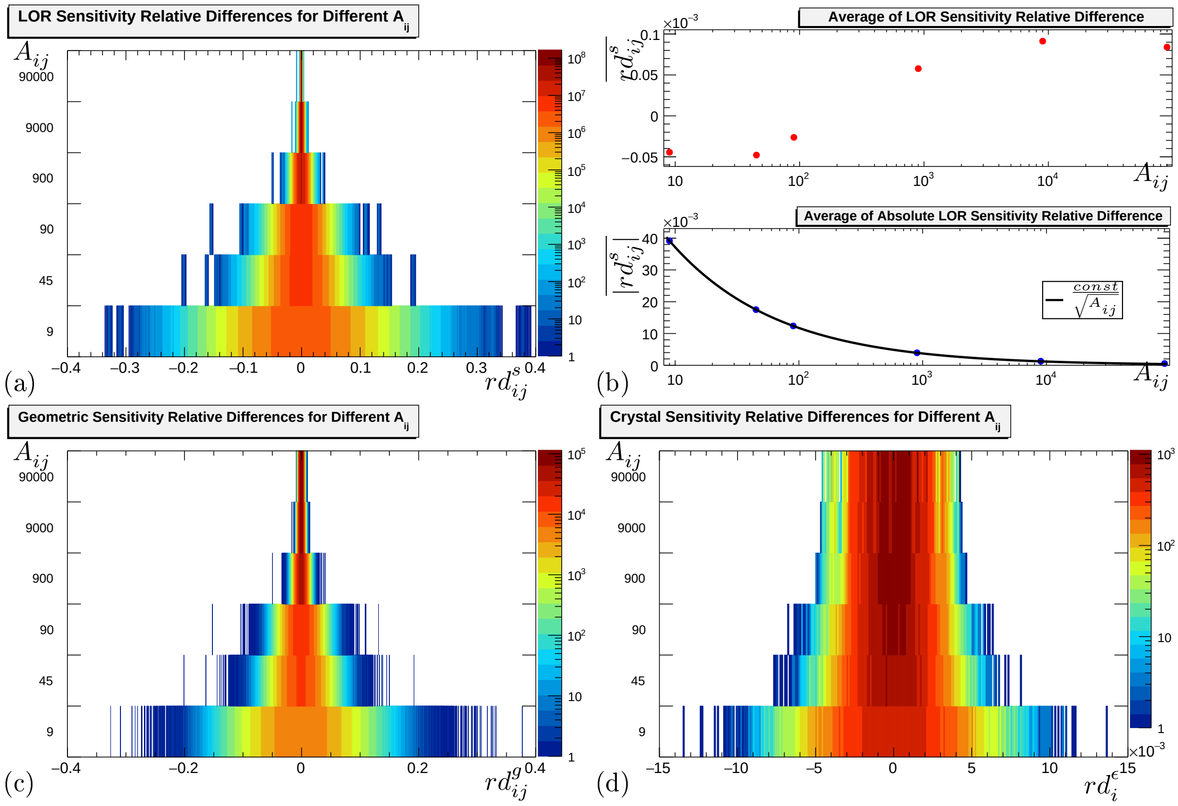

Figure 6.3: Influence of overall statistics on the precision of normalization parameters. For the crystal sensitivities the lowest maximum deviations can be achieved with about $A_{ij} \approx 900$. The geometric sensitivities show larger maximum deviations that dominate the precision of the s_{ij}.

can be determined relatively precise as the tails only have a few 100 entries and the main peak of 10^9 is found. This is well described by the mean of the absolute relative differences.

6.4 Normalization with a Rotating Rod Source

A rotating ^{68}Ge rod source has been used for the normalization of *pheno*PET. For a rod source the fraction of *scattered* coincidences is small and scatter is neglected in the analysis. The rotation of the source outside of the FOV ensures that sensitivities for each LOR are obtained. A major advantage is the possibility to use the normalization data as blank data for attenuation measurements with the same source. This reduces the number of required radioactive sources and equipment to operate *pheno*PET.

For this work two normalization measurements are important. A first normalization was acquired with the preliminary rotation system. It was processed with an older software in 2018. A main challenge there was the calculation of the expectation values because the rotation system was mounted slightly skew compared to the scanner plane and the source was skew in its mount.

Information gained with the first normalization were incorporated in the design and mounting of a new rotation system in 2020. The new system and its mounting is discussed in more details in Section 3.7. A new normalization was calculated after *pheno*PET was moved and mounted on its lifting table. This normalization will be used for future routine operation.

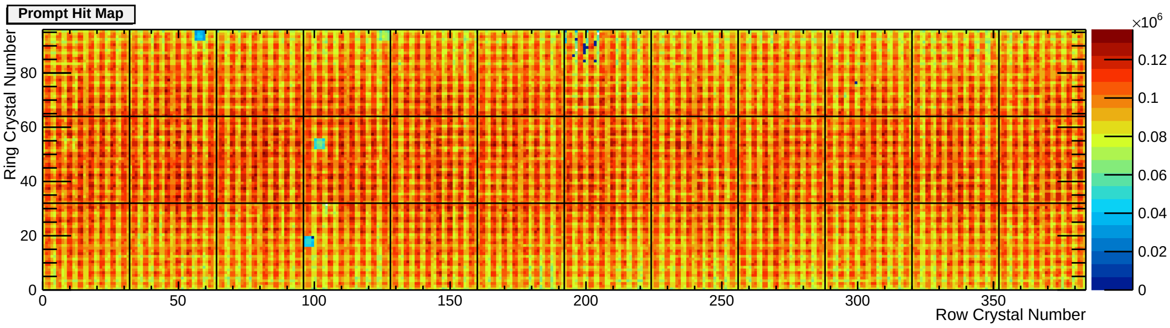

Figure 6.4: Hit map of *prompts* of an 8 h measurement of the rotating rod source. Only LOR contributing to a FOV with a radius of 90 mm are taken into account. A few crystals have no entries and a few 4×4 blocks of crystals attached to a single *die* show significantly less counts. Those are excluded from the fitting.

Both normalizations are compared to justify the presented conclusions and show the stability of the system.

6.4.1 Measurement Setup

For the measurements in 2018 a ^{68}Ge rod was mounted on the rotation system at a radius of about 96 mm from the scanner axis. The source is 300 mm long and had an activity of about 2.4 MBq. The radius and the length of the source ensure that a cylinder shell outside of the FOV is passed. All LORs of the FOV intersect this shell and thus should contain *true* coincidences. The rotation system was operated with a velocity of approximately $2.35\,^{\circ}\,\mathrm{s}^{-1}$. In total, 120 h of data are acquired divided into 15 measurements with a duration of 8 h. This allows the processing of acquired data while the further measurements are running.

The second normalization has been measured with a source of the same type and an activity of 2.88 MBq in 2020. In total 82.5 h of data were acquired with a velocity of $2.4\,^{\circ}\,\mathrm{s}^{-1}$. They were separated into five measurements with a duration of 15 h and one measurement of 7.5 h acquired over one week.

6.4.2 Preparation of Measured Data

The data measured in 2018 were analyzed with the old *phenoSorter* and the *killAll* handling of *multiple* coincidences. The FOV was set to the 11 opposing modules. The sorting of the first measurement gave 63 670 cps *prompts*, 2223 cps *randoms* and 350 cps *multiples*. The number of *randoms* and *multiples* are quite low, thus only a small influence of the coincidence sorter on the resulting normalization is expected. The *prompts* and *randoms* of LORs contributing to the nominal FOV with a diameter of 180 mm are summed up. Here, each measurement is restricted to events between 1 s and 28 749 s due to the slightly different velocity. This ensures that the data originate from full rotations of the source. Variance reduction is applied to the *randoms* within each measurement. Afterwards the *prompt* and *randoms* of all measurements are summed up and *estimated trues* are calculated as the difference between *prompts* and *randoms* in each LOR.

The resulting data for each LOR are used to create a first mask based on a *prompt* hit map given in Figure 6.4. All crystals without any events were masked out. In addition, a few *dies* with their 16 crystals were masked due to the significant reduced count values. The mask contains all LORs to these excluded crystals and excludes those LORs from the calculation of the normalization.

The data analysis for the 2020 data set is the same except for two changes. The sorting is done with the new *phenoGateSorter* and the *takeAllGood* handling of *multiples*. Furthermore, the combination of the six measurements is improved. The radioactive decay between the start of the measurements and during the measurement are corrected. In addition, different measurement durations are corrected. The last measurement is taken as reference. Afterwards, the data of all measurements are averaged. This results in denoised data. This is relevant as these denoised data are also used as blank data for the reconstruction of transmissions measurements. The complete scaling procedure is presented in Section 7.1.4. The masking of crystals has not changed since 2018.

6.4.3 Calculation of Expectation Values

The normalization requires expectation values to calibrate the measured values to the measurement model, which is used for the reconstruction. The activity profile of the rotating rod can be described as a rotating disc in a transaxial plane

$$A(\overrightarrow{r},t) = A_0 \cdot \theta \left(r_s - \left| R \begin{pmatrix} \cos(\omega t) \\ \sin(\omega t) \end{pmatrix} - \overrightarrow{r} \right| \right)$$

with the radius of the radioactive source r_s and its activity A_0, the radius of the rotation R and the angular velocity of ω. $\theta(x)$ is the Heaviside step function. The integration over the a full rotation leads to a cylinder shell. The activity in this shell is not constant but varies with the radius due to the rotation of the source and the cylindrical shape of the rod itself

$$A(r) = \frac{2A_0}{\omega \pi r_s^2} \arccos \left(\frac{R^2 - r_s^2 + r^2}{2rR} \right), \text{ with } R - r_s < r < R + r_s. \tag{6.7}$$

Outside of this range is no activity. The expectation value for each LOR are calculated by the path integral along this LOR. The system matrix, currently used for the reconstruction, is calculated with Volumes-of-Intersection (VOI) but afterwards the matrix elements are scaled to mimic Line-of-Intersection (LOI) values. A calculation of a forward projection with the system matrix is not possible at the moment because the rod source is rotating outside the FOV.

The position of the ^{68}Ge rod relative to the crystals is obtained from a first reconstruction. The mask created from the *prompt* hit map is used as normalization for this reconstruction to exclude LORs without entries. The diameter of the FOV needs to be increased to 200 mm to visualize the rod source. Therefore, the voxel size of the reconstructed image needs to be increased to 1 mm side length in x and y direction, otherwise the system matrix would not fit into the Random-Access Memory (RAM) of the reconstruction computer. The thickness of a slice in z direction is kept at 1 mm. A set of orthogonal slices of the 2018 normalization is presented in Figure 6.5. It is clearly visible that the source is skew. This needs to be incorporated into the forward projection. Furthermore, the rotation axis is not in the center of the FOV.

The skewness of the rod source and the rotation plane is modeled by introducing a dependency on the axial position (z) to the rotation radius $R = R(z)$. The tilt of the activity disc is neglected at this point. The cylinder shell is allowed to have a shift in the x-y-plane, in other words a rotation axis is not the scanner axis. A further improvement of the precision is achieved by limiting the integration interval along the LOR. The intersection points of each LOR with two straight cylinders are calculated. These two cylinders form a cylinder shell completely containing the activity of the rod source and a small additional margin. This results in one or two integration intervals with a reduced length compared to the complete

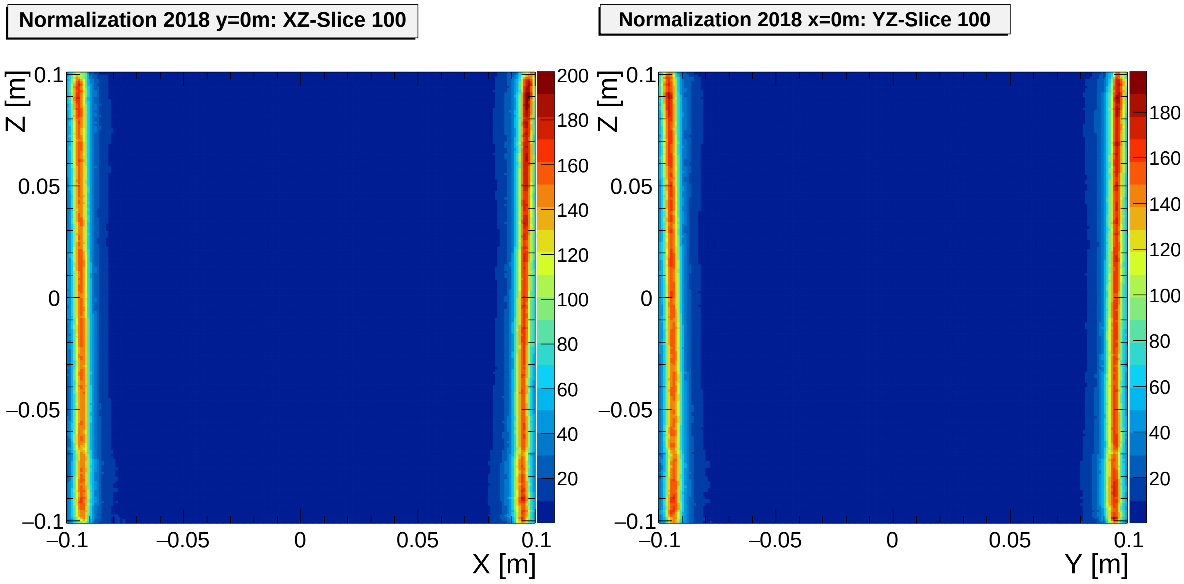

Figure 6.5: Axial slices through the center of the FOV of the rotating rod source measurement in 2018 for normalization. Images are reconstructed only with a *random* correction and some crystals are masked. The skewness of the rod source is visible.

LOR. It has to be noted that the shift and skewness of the source remove all symmetries, thus the expectation values need to be calculated for each LOR.

The numerical integration is performed with the *IntegralFast* function of the ROOT class *TF1* which does a Gauss-Legendre integration [133]. The number of points is set to 250 and the relative precision $\epsilon = 1 \times 10^{-15}$. The integrator of ROOT is set to *AdaptiveSingular* for these calculations.

6.4.4 Localization of the Normalization Phantom

The rod source has an outer diameter of 9.525 mm and a length of 300 mm, thus covers all crystals in axial direction. The radius of the active volume is set to $r_s = 2.5\,\mathrm{mm}$. The radius of the rotation could be measured but the small skewness of the source is more difficult. Furthermore, the position of the rotation axis relative to the crystals is of importance. The required information are obtained from a first reconstruction without a normalization.

Transaxial slices are investigated with the analysis illustrated in Figure 6.6. It has to be noted that the reconstructed images are degraded by the lack of normalization factors. Furthermore, some kind of constant background is visible. Therefore, two profile lines are taken from a slice, one with a constant $x = a$ and one with a constant $y = a$ value. The position of the two crossings with the activity distribution are calculated by searching for the maximum bins. A Gaussian function is fitted to these bins and the two neighboring points in each direction to obtain the peak position.

Afterwards, the center of the rotation axis (r_x, r_y) and the radius R_z can be calculated. For this special case the radius can be calculated for the $x = a$ and $y = a$ values separately which leads to two slightly different values $R_{z,x}$ and $R_{z,y}$. The constant a is taken from the 30 slices around the scanner axis in single slice steps. Thus the fits should not be influenced by the bending of the cylinder shell.

The resulting values in a slice are averaged and the standard deviation is calculated. A linear fit is used to estimate the rotation axis and radius as well as their possible slope. The

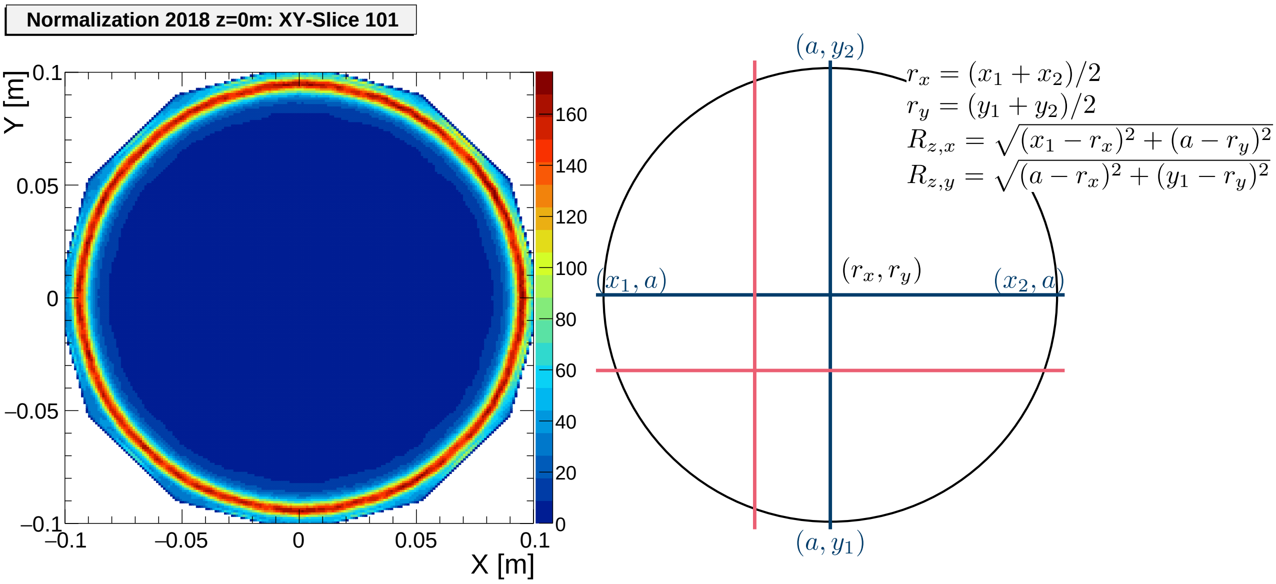

Figure 6.6: Single slice from the 2018 data reconstructed without normalization. On the right side the analysis to obtain the center of the rotation axis and the radius is illustrated.

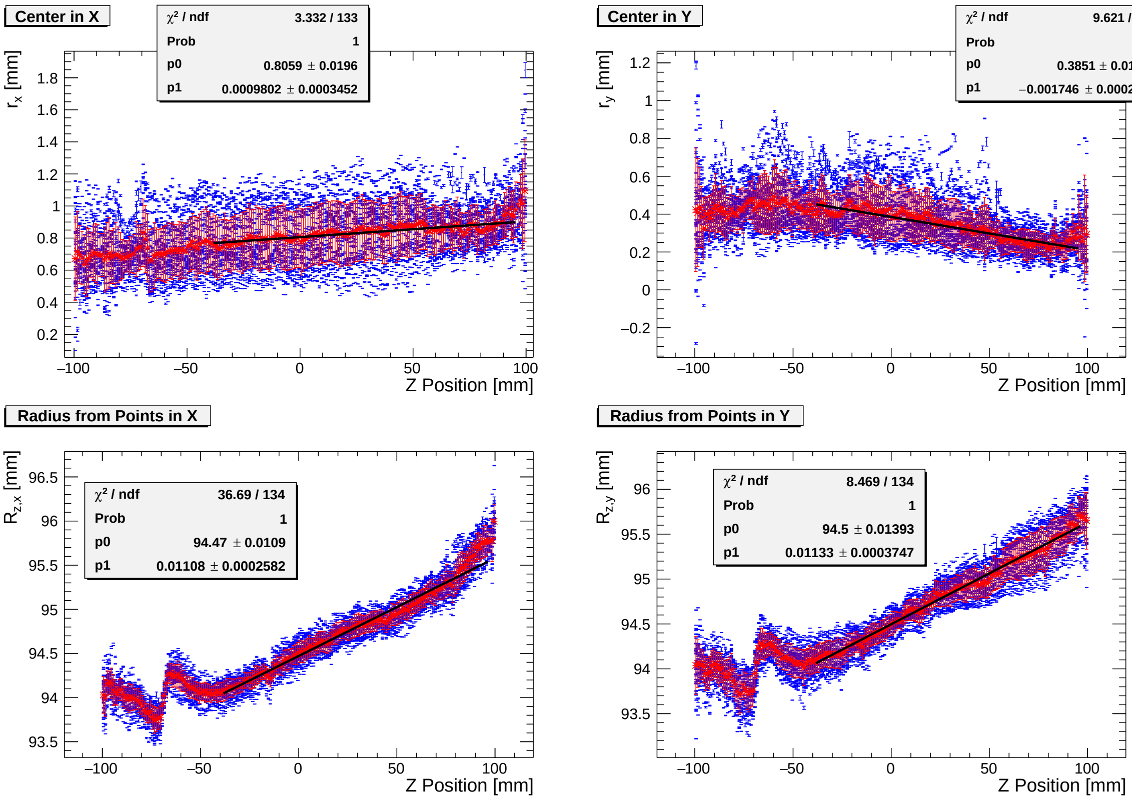

Figure 6.7: Calculated center of rotation and radius from the profile lines with $x = a$ and $y = a$ of each calculation are given in blue for each transaxial slice. The red marks show the mean used for the further estimation. A step is visible in the radii. This results from a step in the reconstructed images that has not been reproduced afterwards.

results are presented in Figure 6.7. The radii show a step, which is visible in the reconstructed image. A few measurements with the source have been analyzed but this step has not been observed again. Thus, this step is taken as an artifact and excluded from the fit. For the remaining points a small slope similar to the reconstructed images is visible. The radius of the source changes by about 2 mm over the complete height of the field of view. The rotation axis shows a small dependency on the axial position, which is well below the voxel size of 1 mm. Thus, this is not taken into account.

The center of the rotation axis is set to $r_x = 0.81\,\text{mm}$ and $r_y = 0.39\,\text{mm}$. The radius of the source is set to

$$R(z) = 0.0112 \cdot \frac{\text{mm}}{\text{mm}} \cdot z + 94.48\,\text{mm}.$$

The same procedure is repeated with the data acquired in 2020. A set of orthogonal slices is presented in Figure 6.8. The cylinder shell is not skew within the resolution of the voxels. The obtained radius is 95.9 mm and the rotation axis is at $r_x = -0.26\,\text{mm}$ and $r_y = -0.17\,\text{mm}$. This is consistent with the shift presented in Section 3.7.2.1.

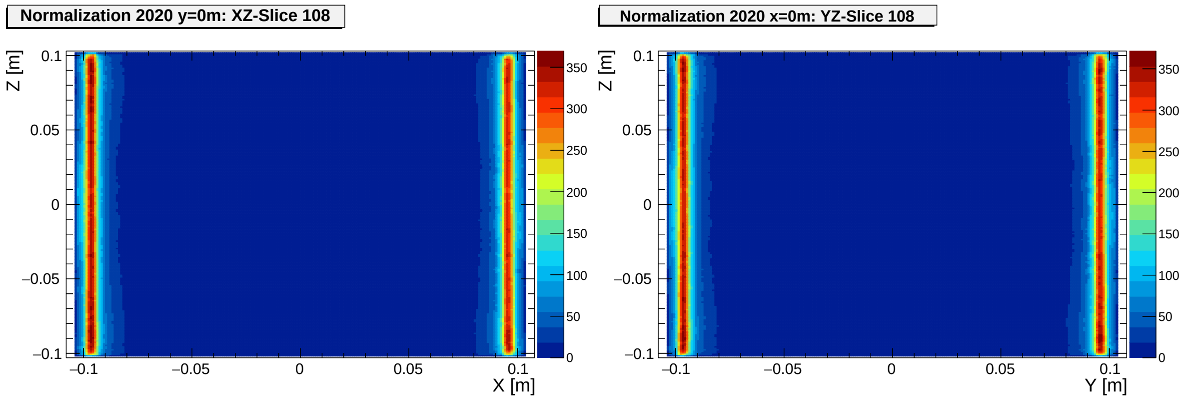

Figure 6.8: Axial slices through the center of the FOV for the rotating rod source measurement in 2020. The images are reconstructed only with a *random* correction and some crystals are masked out. No skewness of the source is visible.

6.4.5 Comparison of Normalization Factors

The normalization factors are computed with the two above presented data and the corresponding expectation values. A correlation of the ϵ_i and the g_{ij} as well as the sensitivity of each LOR s_{ij} from the two data sets are presented in Figure 6.9. The sensitivities show an overall good correlation but two features are visible (Figure 6.9a). For high sensitivities the values are above the black line. This lines represents equality between of the s_{ij}. A second differences arise from a few crystals that show significant different ϵ_i between the two measurements (Figure 6.9c). The crystals are on different modules and at different positions. Thus no systematic effect on the crystal sensitivities can be identified.

The geometric sensitivities show a good correlation in Figure 6.9d. The distributions of the g_{ij} from both years are not symmetric around the forced average values of one and especially range from 0.5 to over 2. Therefore the underlying distribution is not Gaussian. The standard deviation is about 0.18 for both normalizations. Therefore, a comparison with a Gaussian distributed synthetic g_{ij} with $\sigma_{geo} = 0.2$ is most reasonable.

For a comparison with the synthetic data the relative differences between the two normalizations are calculated similar to Equation (6.6) with

$$rd_{ij}^{norm} = (s_{ij}^{2018} - s_{ij}^{2020})/s_{ij}^{2020}$$

In addition the average values are calculated. The results are depicted in Figure 6.9b. The mean deviation $\overline{rd_{ij}^{norm}} \approx 0$, which is similar to the $\overline{rd_{ij}^{s}}$ of the synthetic data (compare Figure 6.3b). The fit to the $\overline{|rd_{ij}^{s}|}$ in Figure 6.3b can be used to estimate $\overline{|rd_{ij}^{s}|} \approx 1.9 \times 10^{-2}$ for 38 *trues* per LOR. For the comparison of two measurements an increase by a factor of $\sqrt{2}$ to about 0.0268 can be expected for Gaussian errors. This is slightly below the observed differences of $\overline{|rd_{ij}^{norm}|} \approx 0.0297$ between the two normalizations. These values illustrate that the distribution of rd_{ij}^{norm} is broader than for the synthetic data.

The peak on the rising flank of rd_{ij}^{s} in Figure 6.9b at about -0.25 results from the few crystals with different values. Excluding the LORs with the five crystals, which show the largest deviations between the two normalizations does not change the $\overline{|rd_{ij}^{norm}|}$. The deviations might be influences by the differences between the real distributions of the g_{ij} compared to the assumed Gaussian for the synthetic data.

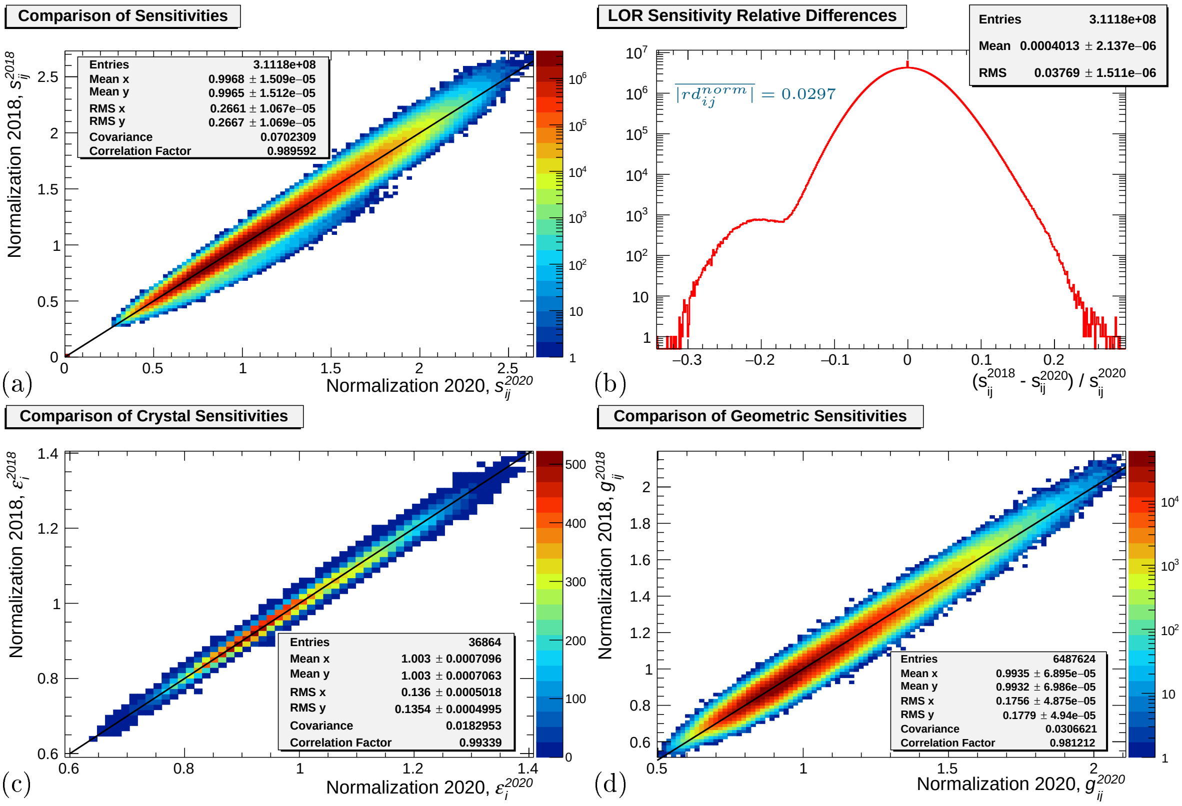

Figure 6.9: Comparison of sensitivities obtained from two different measurements. The overall differences result from a change of the ϵ_i of a few independent crystals. A small difference between the geometric sensitivities is visible but does not change the good over all correlation. These differences might be a result of slightly different scaling.

In Figure 6.10 the crystal sensitivities obtained in 2020 are depicted. A clear dependency on the ring number and the position of the crystal on the module is visible. The dependency on the position on a *tile* results from the crystal matrix with the transparent and reflective layers between the crystals and its coupling to the *pixels* (see Section 3.2.1 and Section 3.4.6.1). The ϵ_i^{2020} show a dependency on the axial position of the ring. This dependency is symmetric to the center of *pheno*PET. In Figure 6.11 an inverse behavior is presented for the g_{ij}^{2020}. Therefore, an insufficient separation of the two components (g_{ij} and ϵ_i) by the iterative fit causes the axial dependencies. This does not harm the overall results for the reconstruction of emission images, but could be tackled with additional symmetries like shift symmetries or additional sensitivities. For example the pattern on each *tile* could be separated as a pattern sensitivities, that only depends on the position of a crystal on a *tile*.

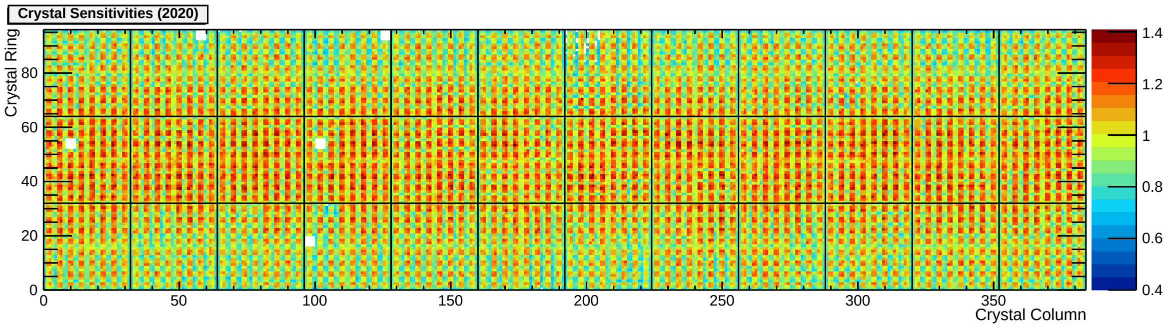

Figure 6.10: Crystal sensitivities (ϵ) obtained from the 2020 measurement. The white crystals were excluded and masked out due to their count rate behavior.

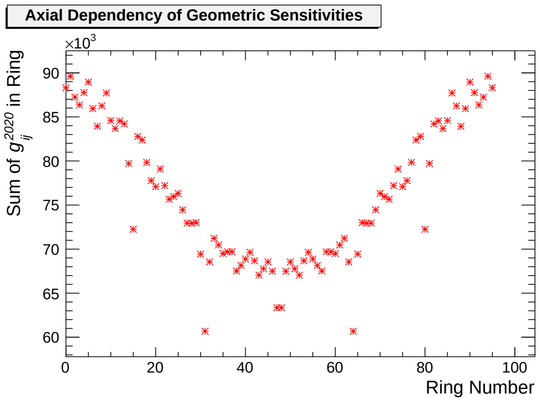

Figure 6.11: The axial dependency is investigated with the sum of all geometric sensitivities between LORs in each ring. The curve is symmetric due to the utilized symmetries.

The overall good correlation ensures that the general findings presented in the following section are not strongly influenced by the different normalizations. Furthermore, the 2018 normalization is not too much degraded due to the skew source. A stability of the normalization over the two years of operation is visible. However, the relative differences between the sensitivities indicate further potential for improvements. The crystals with the deviating sensitivities should be further investigated to confirm one of the two normalization models.

6.4.6 Homogenity of Normalized Data

The effect of the normalization is visualized in Figure 6.12 on a single frame of 5 min of a cylinder phantom filled with ^{18}F diluted in water. An analytic attenuation correction, *random* correction, count rate corrections and decay correction are applied during the reconstruction. The attenuation correction is calculated analytically with Lambert-Beer's Law (compare Section 2.3.3) and the attenuation coefficient of water $\mu_{water} = 0.1\,\mathrm{cm}^{-1}$.The center of the phantom is estimated from the reconstructed emission data without attenuation correction. The dimensions of the phantom are taken from a measurement with a folding rule. The data were reconstructed with the LOR mask and with the normalization obtained from the 2018 rod source measurement.

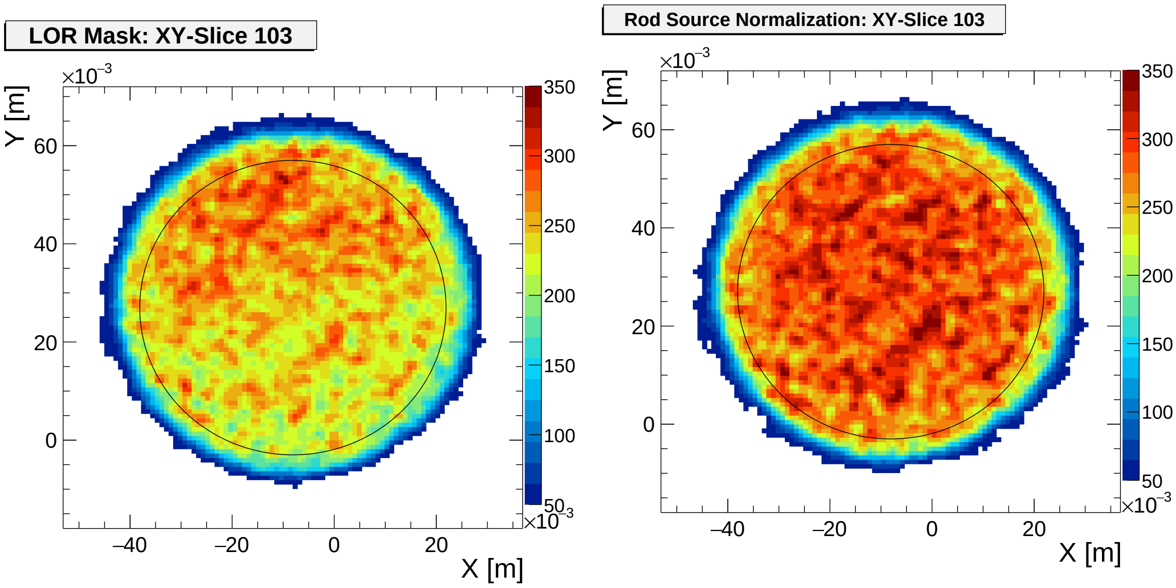

(a) Only mask of LOR to a few crystals.

(b) Normalization obtained from the 2018 rod source data.

Figure 6.12: Reconstruction of an off-center cylinder filled with ^{18}F diluted in water. The frame is 300 s long with a total activity of the cylinder about 3.5 times the ^{68}Ge rod source activity. The reduced bias due to the normalization is best visible for the decreased dependency on the radial distance to the center of the FOV. The black circle indicate a Region of Interest (ROI) used to compare the voxel values.

The reconstruction with the LOR mask (Figure 6.12a) shows slight decrease of the data from the edges of the FOV to the center. This is especially visible in contrast to the data normalized with the rod source data in Figure 6.12b. The bias decreases and is not visible within the fluctuations of the voxel values. The absolute values differ between both reconstructions as the global calibration factor has not been determined. The relative standard deviation decreases due to the normalization from 10.0 % to 8.6 %.

The relative RMS for all 5 min long frames of a centered and the off centered cylinder are presented in Figure 6.13. A clear dependency on the measurement duration and thus on the amount of detected coincidences is visible. The constant relative RMS up to 14×10^3 s results from the frame dropping, which limits the maximum number of measured events. For the centered cylinder the relative RMS is slightly lower due to the normalization. The effect is larger for the off-centered cylinder.

6.4.7 Influences of Expectation Values

The influence of the expectation values on the normalization is investigated by two examples. Therefore, the normalization data acquired in 2020 are analyzed with slightly different expectation values. In the first case, the radius of the source filled with radioactivity, r_s, is increased to 3.5 mm resulting in new sensitivities $s_{ij}(r_s = 3.5\,\text{mm})$. For the second case, the rotation axis is shifted from $x = -0.26$ mm and $y = -0.17$ mm to $x = -0.7$ mm and $y = -0.6$ mm. This increases the shift from about 0.3 mm to 0.9 mm and leads to the sensitivities s_{ij}^{shift}.

The effect of these two small deviations is investigated by calculating the relative differ-

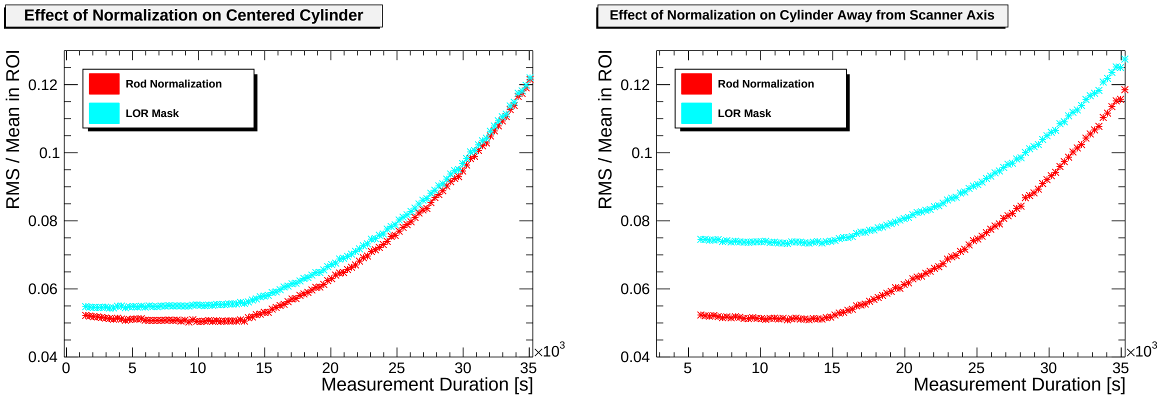

Figure 6.13: Relative Root Mean Square (RMS) of a ROI within a homogenious cylinder filled with ^{18}F diluted in water. The improvement through the normalization is larger for the off-centered cylinder (right). The constant at the start is a result of the frame dropping and the increase results mainly from the lower amount of coincidences in each image frame. An improvement of the relative RMS is visible for both positions. For low count rates the statistical fluctuations dominate the result.

ences for the obtained sensitivities similar to Equation (6.6):

$$rd_{ij}^{r_s} = \frac{s_{ij}(r_s = 3.5\,\mathrm{mm}) - s_{ij}^{2020}}{s_{ij}^{2020}} \text{ and } rd_{ij}^{shift} = \frac{s_{ij}^{shift} - s_{ij}^{2020}}{s_{ij}^{2020}}.$$

In addition, the mean of the absolute LOR sensitivity relative difference $\overline{|rd_{ij}^{r_s}|}$ and $\overline{|rd_{ij}^{shift}|}$ are calculated.

The $rd_{ij}^{r_s}$ in Figure 6.14a show only small deviations. A small number of LORs show larger deviations of up to -0.008. Most of the LORs seem not to be effected by the increased radius of the radioactive volume. The mean of the absolute relative differences is $\overline{|rd_{ij}^{r_s}|} = 0.8 \times 10^{-3}$. This is well below the mean of the absolute differences obtained from synthetic data of 1.9×10^{-2} (estimated from Figure 6.3b for 38 *trues* per LOR). Thus, a different radius of the source seems not to influence the normalization.

For the shifted source the rd_{ij}^{shift} in Figure 6.14b reveal that nearly all LORs show deviations. Here, the shifted activity distribution alters all expectation values except for LORs parallel to the direction of the shift. The mean of the absolute relative differences is $\overline{|rd_{ij}^{shift}|} = 0.6 \times 10^{-2}$. This is in the range of the expected precision for these acquired data. Thus, the position of the rotation axis is quite important for the normalization.

6.4.8 Discussion of Expectation Values

The calculation of the expectation values uses assumptions. The above investigations show that the position of the rotation axis is an important aspect. A smaller effect is observed for the size of the radioactive volume within the source.

The rod source is quite thin but still consists of metal and the material containing the ^{68}Ge. Therefore, small effects due to attenuation or scatter might occur. The attenuation caused by different positions within the activity disc should average out for all LORs in a ring combination due to the rotation. More important differences could result from the different path length of the LORs due to ring differences.

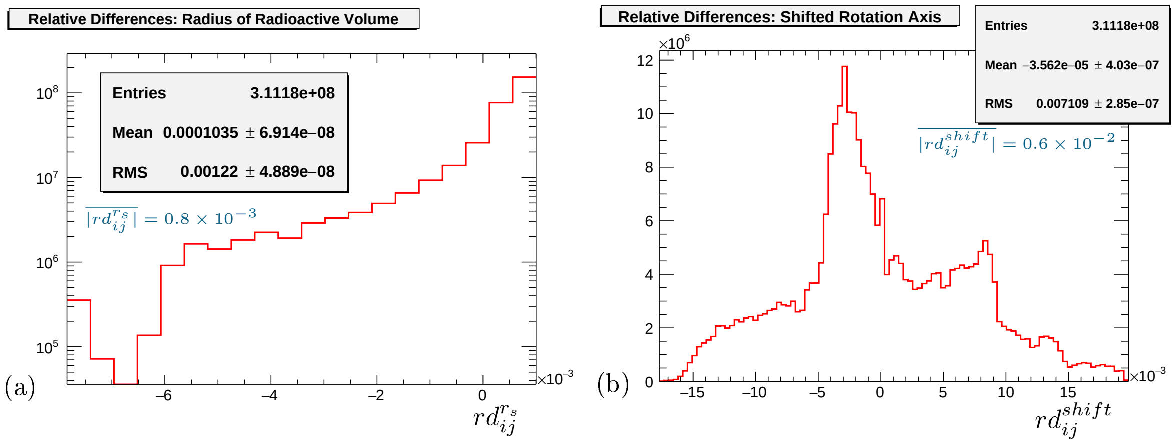

Figure 6.14: Influence of small variations on the obtained normalization presented as relative differences of the sensitivities. (a) Changes due to an increased radius of the radioactive source r_s and (b) for a small shift of the rotation axis.

The ^{68}Ge decays into ^{68}Ga which has a β^+ decay with a mean kinetic energy of about 836 keV [49]. Thus, an effect of the positron range is possible. An alternative to Equation (6.7) might be the simulation of the source with Geant 4. This requires detailed information on the source geometry and materials. It has to be noted that a full Monte Carlo simulation of the measurement as A_{ij} introduces additional challenges. Most importantly the simulation models geometric effects and thus the g_{ij} cannot be determined. The small deviations observed for the larger radius of the ^{68}Ge rod indicate a small effect of these aspects. Therefore, these tests have a low priority.

6.5 Discussion

A component based normalization with a rotating rod source has been computed. The normalization has not changed significantly over two year of operation and the performance of a few crystals has even improved.

The reconstructed slices of an off-centered cylinder show a visible bias without normalization that is removed by the normalization. The homogeneity of the reconstructed values is investigated with the relative RMS. For a centered cylinder the decrease of the relative RMS is much smaller than for the off-center cylinder. Here, additional effects like *scattered* coincidences need to be taken into account. Furthermore, the homogeneity depends on the number of events in each image frame.

The calculation of expectation values is done with a numerical integration. It has been shown that the actual radius of the source is less important than the correct positioning of the rotation axis. Furthermore, the rotation radius should be known quite precise. The calculation of the expectation values works but different approaches can be investigated, for example switching from LOI to VOI integrals might have an effect. This switching is expected to have only a small effect due to the scaling to LOI of the system matrix.

The investigation of the fit algorithm with synthetic data reveals that the width of the geometric sensitivities influences the recovery of all sensitivities. This effect can be compensated by an overall increased number of measured events. The acquisition of more statistics would require months of measurements. This is easier done with a new ^{68}Ge rod, which might have an activity 10 to 20 times higher than the current source. The disadvantage is the increased occurrence of dead time effects. The new normalization should again be based on the same data acquired as blank scan for the transmission reconstruction.

Further improvement of the normalization might result from the introduction of additional parameters. For example a crystal matrix factor could contain the pattern on each *tile* resulting from the transparent and reflective coupling of the crystals. Additionally, a factor to incorporate the misalignment of each *tile* might be possible. This misalignment can either result from a shifted position of the complete module or a shift between the crystal matrix and the Digital Photon Counter (DPC). The separation of these misalignments would allow the addition of further symmetries. For example shift symmetries between module rings could be included. In addition the inclusion of shift symmetries between crystal rings could be investigated.

Hogg et al. [83] used a homogeneous ^{68}Ge cylinder to calculate the crystal sensitivities. A homogeneous cylinder has also been studied during this thesis. The main issue was the occurrence of *scattered* coincidences, that spoil the normalization. *Scattered* coincidences can also result from decays outside of the FOV. Thus, the estimation is really complicated, especially because the used source is not as high as the FOV. This can be compensated by measuring the source at two positions, but this approach results in a more complex setup for the estimation of *scattered* coincidences. Close to the end of this project PRESTO was extended with a scatter simulation that can be used to estimate the number of *scattered* coincidences. The calculation of the normalization from a homogeneous cylinder could be used to further validate the normalization.

Correction of Photon Interaction with Plants and Their Soil

The two photons created by the annihilation of a positron need to travel through the plant and the medium, soil or water surrounding the roots. The dominant interaction process here is Compton scattering which leads to attenuation in the original Lines-of-Response (LOR). Additionally, the photons contribute as *scattered* events to another LOR.

For *pheno*PET the attenuation map is reconstructed from two measurements with a rotating rod source, one with the object and one without the object. To get a 3D attenuation map, an iterative algorithm is applied. The effect of *scattered* coincidences is estimated with a Monte Carlo simulation, which is part of PET Reconstruction Software Toolkit (PRESTO). Both algorithms are presented in detail. The reconstruction and the effect on the quantification of the activity concentrations are demonstrated with measurements of homogeneous cylinder phantoms. These show bias free results for pot sizes already established in PlanTIS. For larger pots additional optimization is required to reduce a remaining axial bias of up to 20 % in emission images.

The attenuation of a pot depends on the soil type and the water content of the soil. In hydroponics the water level has an impact of attenuation. In long term plant experiments, both the soil moisture and the water surface level can change due to plant water uptake.

7.1 Measurement of Attenuation Coefficients

The attenuation correction for *pheno*PET is obtained from a transmission reconstruction. This uses measurements with a rotating ^{68}Ge rod source. In this section the iterative algorithm for the transmission reconstruction and the calculation of the attenuation correction are presented. Afterwards the measurement and analysis of the blank measurement, done without an object, and the transmission measurement for each object are presented. The reconstruction requires a correction of the decay of the ^{68}Ge. Afterwards, the repositioning of the rod source and the influence of ^{176}Lu on the transmission and blank data are studied.

7.1.1 Transmissions Reconstruction Algorithm

The algorithm for the reconstruction of transmission data is based on the work by Rothfuss et al. [134]. They investigated the use of lutetium-yttrium oxyorthosilicate (LYSO) as transmission source and identify decays of the ^{176}Lu with Time of Flight (TOF) between detector crystals. A first calculation of the attenuation map is performed with Maximum Likelihood for Transmission Reconstruction (MLTR), which was motivated by [93, 135]. Afterwards Rothfuss et al. investigated a further combined reconstruction of transmission and emission data. A version of this MLTR is integrated into PRESTO.

In the following the MLTR implementation in PRESTO is presented in combination with the adaptations for *pheno*PET. Van Slambrouck et al. [136, 137] proposed to combine the scatter estimates with the common additive correction for *random* coincidences. Therefore, the data measured in LOR i are modeled as

$$\hat{p}_i(\mu) = a_i B_i + VRR_i + SE_i \tag{7.1}$$

$$a_i = \exp\left(-\sum_j c_{ij}\mu_j\right) \tag{7.2}$$

with

$\hat{p}_i$	mean expected *prompts*
a_i	attenuation in LOR
B_i	blank measurement
VRR_i	Variance Reduced Randoms of transmission scan
SE_i	scatter estimate
c_{ij}	matrix element of LOR i and voxel j
μ_j	attenuation of voxel j in cm^{-1}

This equation system is solved with the maximum likelihood estimation

$$L(\mu) = \sum_j \left(p_i \ln(\hat{p}_i(\mu)) - \hat{p}_i\right),$$

with a Poisson distribution of the measured value p_i. Rothfuss et al. use a Gaussian Prior in the reconstruction to smooth the values of neighboring crystals. This prior is not implemented in PRESTO. A scaled gradient ascent algorithm leads to the iterative update n of the attenuation coefficient $\mu_j^{(n)}$:

$$\mu_j^{(0)} = 0 \tag{7.3}$$

$$\mu_j^{(n+1)} = \mu_j^{(n)} + \alpha_{relax} \frac{\sum_i c_{ij} B_i a_i^{(n)} \left(1 - p_i / \left(B_i a_i^{(n)} + VRR_i + SE_i\right)\right)}{\sum_i c_{ij} \left(B_i a_i^{(n)}\right)^2 / \left(B_i a_i^{(n)} + VRR_i + SE_i\right)} \tag{7.4}$$

$$\text{with } a_i^{(n)} = \exp\left(-\sum_j c_{ij} \mu_j^{(n)}\right). \tag{7.5}$$

The relaxation parameter α_{relax} controls the convergence of the iterative procedure. Rothfuss et al. used a value of 1.5 over the transaxial diameter of the reconstructed image. For *pheno*PET a value of $\alpha_{relax} = 0.1$ is used. In Appendix B a number of different parameters is investigated. In general, all $\alpha_{relax} < 0.2$ seem possible together with a suitable number of iterations. The scatter estimates are simulated with the Monte Carlo simulation presented in Section 7.2 and the scaling to the measurement is presented in Section 7.2.2. In PRESTO the sums within the update formula only take into account LORs with $B_i a_i^{(n)} + VRR_i + SE_i > 0$. This is used for the exclusion of LORs, which were already excluded from the calculation of the normalization (see Section 6.4.2). Furthermore, a lower threshold of 1×10^{-30} is applied to the $\mu_i^{(n)}$ after the calculation of iteration n.

The attenuation coefficients depend on the energy of the photon. Thus, data acquired from LYSO need to be scaled. For *pheno*PET a ^{68}Ge rod source is used with 511 keV photons. Thus no scaling due to the photon energy is required.

The determination of scatter estimates requires information on the attenuation map. Therefore, a first reconstruction is done without scatter estimates. This first reconstruction is scaled with an object depending factor, to achieve a better estimate of the attenuation map. Afterwards, a scatter simulation is done and used for a second reconstruction. This procedure is presented in more details in Section 7.3 and validated for measurements in Section 7.5.

The energy window used for the coincidence sorting accepts *scattered* coincidences. Therefore, reconstructed attenuation maps have systematic lower attenuation coefficients. The object depending scaling factor accounts for these differences to reduce the required number of scatter iterations. The scaling factor is obtained from the reconstruction of a known object like a plant pot filled with water. The fraction of *scattered* coincidences depends on the size of the object, therefore the scaling factor is object dependent. More details on the effect of Compton scattering and the reconstruction are presented in Section 7.3.

The attenuation correction is calculated with Equation (7.5) and the $\mu^{(n)}$ after the last iteration step. These $a_i^{(n)}$ are saved for access during the reconstruction.

7.1.2 Blank Measurement for Reconstruction

The blank data have already been discussed in Section 6.4 during the calculation of the normalization. The blank data originate from five measurements with a duration of 15 h and one measurement with a duration of 7.5 h during one week. The ^{68}Ge rod is orbiting with an angular velocity of $2.4\,^\circ\,\mathrm{s}^{-1}$.

The data are analyzed with the default parameters for clustering and coincidence sorting. The coincidence sorting accepts a maximum time difference between two *singles* of 2.5 ns and *singles* need to be in the energy window of 348 keV to 652 keV[1].

The data of the six measurements are combined to a single measurement. Therefore, the first five measurements are scaled to the same start point and duration as the last measurement with the procedure presented in Section 7.1.4. The last measurement has a duration of 15 h.

7.1.3 Acquisition of Transmission Measurements

The acquisition of a transmission measurement is done with the object in place. The angular velocity of the ^{68}Ge rod source is kept at $2.4\,^\circ\,\mathrm{s}^{-1}$. Therefore, the measurement duration needs to be a multiple of 2.5 min for a full cycle. The further processing is done with the same parameters used for the blank measurement.

The investigations in this chapter reveal that a 15 h and 0.5 h long measurements provide similar results. The 15 h measurements provide better information on the edges of the pot. Here, more iteration steps are possible for the MLTR leaving a similar noise within the attenuation map compared to a 0.5 h measurement.

7.1.4 Correction of Transmission Source Decay

The measurement of blank data should contain a large number of events to provide an expectation value for each LOR. Here, a number of separate measurements are combined to acquire new measurements and analyze previous measurements at the same time. Furthermore, the measurement of an object are shorter and acquired at a later time point. Therefore, the blank data are corrected for the decay of the source and the different measurement duration.

The number of decay $N(t, \Delta t)$ in a time window from t to $t + \Delta t$ is given by

$$N(t, \Delta t) = \int_t^{t+\Delta t} \dot{N}(t')dt' = \int_t^{t+\Delta t} \dot{N}_0 \cdot \exp(-\lambda t')dt'$$

with $\dot{N}_0$ the number of decay per time at an arbitrary time point defined as $t = 0$. The integration gives

$$N(t, \Delta t) = \dot{N}_0 \lambda^{-1} \cdot \exp(-\lambda t) \cdot [1 - \exp(-\lambda \Delta t)]$$

The scaling factor $\alpha_{1,2}$ between two measurements with start time points t_1 and t_2 and durations Δt_1 and Δt_2 is therefore given by

$$\alpha_{1,2} = \frac{N(t_2, \Delta t_2)}{N(t_1, \Delta t_1)} = \exp(\lambda[t_1 - t_2]) \cdot \frac{1 - \exp(-\lambda \Delta t_2)}{1 - \exp(-\lambda \Delta t_1)}. \tag{7.6}$$

---

[1] Energy calibration of *pheno*PET does not account for the saturation of SiPM cells, see Section 3.4.4.1.

The factor $\alpha_{1,2}$ scales the number of expected events in the two measurements to the same number. The exponential function accounts for the radioactive decay between the two measurements. The fraction accounts for different measurement durations and the decay duration of the measurement. For short measurements with $\lambda\Delta t_1 \ll 1$ and $\lambda\Delta t_2 \ll 1$ this fraction can be approximated as t_2/t_1.

7.1.5 Influence of Radiation from Detector Crystals on Blank Data

The detector crystals contain ^{176}Lu, which results in a constant background radiation. The decay schema of ^{176}Lu is presented in Table 2.1 in Section 2.4. The electron originating from the decay and the subsequent photons are measured by *pheno*PET. The different photons and the electrons can be combined to energy depositions within the energy window [50]. Therefore, those events can be sorted as coincidences [138]. This results in a event rate of about $\dot{N}_{Lu} \approx (2276 \pm 3)\,\mathrm{cps}$ *estimated trues* in all LORs, obtained from a 300 s long measurement without any other activity inside the Field-of-View (FOV). Estimated *trues* are the differences between *prompt* and delayed coincidences. During a blank measurements with the ^{68}Ge rod about $(41\,840 \pm 1)\,\mathrm{cps}$ *estimated trues* were detected. This results in a fraction of about 5.4 % events from the ^{176}Lu. The measurement model for the scaling of the activity of the rod source $N_{Ge}(t, \Delta t)$ is extended to

$$N_{meas}(t, \Delta t) = N_{Ge}(t, \Delta t) + \dot{N}_{Lu} \cdot \Delta t \tag{7.7}$$

with the duration of the measurement Δt. While this equation is valid for each LOR the number of events from a ^{176}Lu decay is too low for a direct measurement. For the current FOV and acceptance of LORs it would require about 38 h to achieve an average of 1 event/LOR. The blank data have an average about 39 event/LOR. A similar number of events from the ^{176}Lu would require 1.5 month of measurement.

A rough estimation of the effect can be done by comparing the total count rates of a blank scan and the ^{176}Lu decays. The count rates in the scaling of the blank measurement in Equation (7.6) can be substituted with Equation (7.7). This leads to the corrected scaling formula

$$\begin{aligned} N_{Ge,2} &= \alpha_{1,2} \cdot N_{Ge,1} \\ N_{meas,2} - \dot{N}_{Lu} \cdot \Delta t_2 &= \alpha_{1,2} \cdot \left[N_{meas,1} - \dot{N}_{Lu} \cdot \Delta t_1 \right] \\ N_{meas,2} &= \alpha_{1,2} \cdot N_{meas,1} + \dot{N}_{Lu} \cdot [\Delta t_2 - \alpha_{1,2} \cdot \Delta t_1] \end{aligned} \tag{7.8}$$

The relative difference to the original scaling is then given by

$$\theta_{rel} = \frac{\dot{N}_{Lu} \cdot [\Delta t_2 - \alpha_{1,2} \cdot \Delta t_1]}{\alpha_{1,2} \cdot N_{meas,1}.} \tag{7.9}$$

For the current blank data with $N_{meas,1} = 41\,840\,\mathrm{cps}$ and $\Delta t_2 = \Delta t_1 = 15\,\mathrm{h}$ a difference of $\theta_{rel} = (5.440 \pm 0.008)\,\%$ would be reached after one half life of ^{68}Ge, about 270 d.

A corrected scaling with a high statistics measurement of the ^{176}Lu event rates could lead to an improvement, especially for old blank scans. The deviations of 5 % after 270 d are small and could be corrected by the calibration of the attenuation map after the reconstruction. This calibration could be determined with a short transmission measurement. Furthermore, a stronger ^{68}Ge rod would decrease this effect. The current approach is the acquisition of new blank data to keep the systematic error due to the scaling of the $\dot{N}_{Lu}$ neglectable.

7.1.6 Reproducibility of Rod Source Positioning

The mount of the ^{68}Ge rod source is depicted in Figure 3.13b. The source is fixed by the screw, that needs to be set tight for every measurement. Due to different strength during the tightening of the screw the source might be tilted.

7.1.6.1 Method

The blank measurement was acquired without a remounting of the source but potential transmission measurements might be tilted relative to the blank measurement. Thus, two additional blank measurements of 15 h were done to investigate the reproducibility of the source positioning. Before each measurement the source is removed and mounted again.

A possible effect due to a tilted source should be most prominent in the top crystal ring. The number of *estimated trues* for each LOR eT_i is calculated as the difference between the *prompts* (p) and Variance Reduced Randoms (VRR). To test the skewness of the source, the average counts of all LORs are plotted along the radial distance. The counts within a bin are calculated as:

$$N_{bin} = \frac{1}{m}\sum_{i=0}^{m} eT_i = \frac{1}{m}\sum_{i=0}^{m}(p_m - VRR_m)$$

$$\sigma_{bin} = \frac{1}{m}\sqrt{\sum_{i=0}^{m} eT_i}$$

with m the number of LORs in this bin. The N_{bin} are plotted over the radial distance with a bin width of 1 mm.

The decay of the source between the measurements is corrected. The two newly acquired measurements are compared to the blank scan and a single measurement of the complete blank scan.

7.1.6.2 Results

Three parts of the curve are presented in Figure 7.1. The two plots zoomed on the radius of the source show differences between the two test measurements and the single blank measurement. The maximum values are shifted by one bin. The source position therefore varies about ±1 mm in the top ring.

The average count numbers in the center are about three events per LOR in 15 h for all four measurements. The resulting high statistical fluctuations are larger than a possible systematic difference due to the position of the source. For a plant study the transmission measurements should be shorter and thus a possible effect even smaller.

7.2 PRESTO Scatter Simulation

Close to the end of this project Jürgen Scheins added a Monte Carlo simulation to PRESTO. The simulation is intended for the scatter correction in routine operation but is not yet fast enough. A number of investigations are presented in the following sections. These examples give first insights on the achievable image quality for the future routine operation. Scheins et al. published a validation of the simulation with GEANT 4 [139]. This validation applies an improved simulation. Especially, improvements on the computational speed have been implemented but are not yet installed for *pheno*PET. Here, first results are presented to

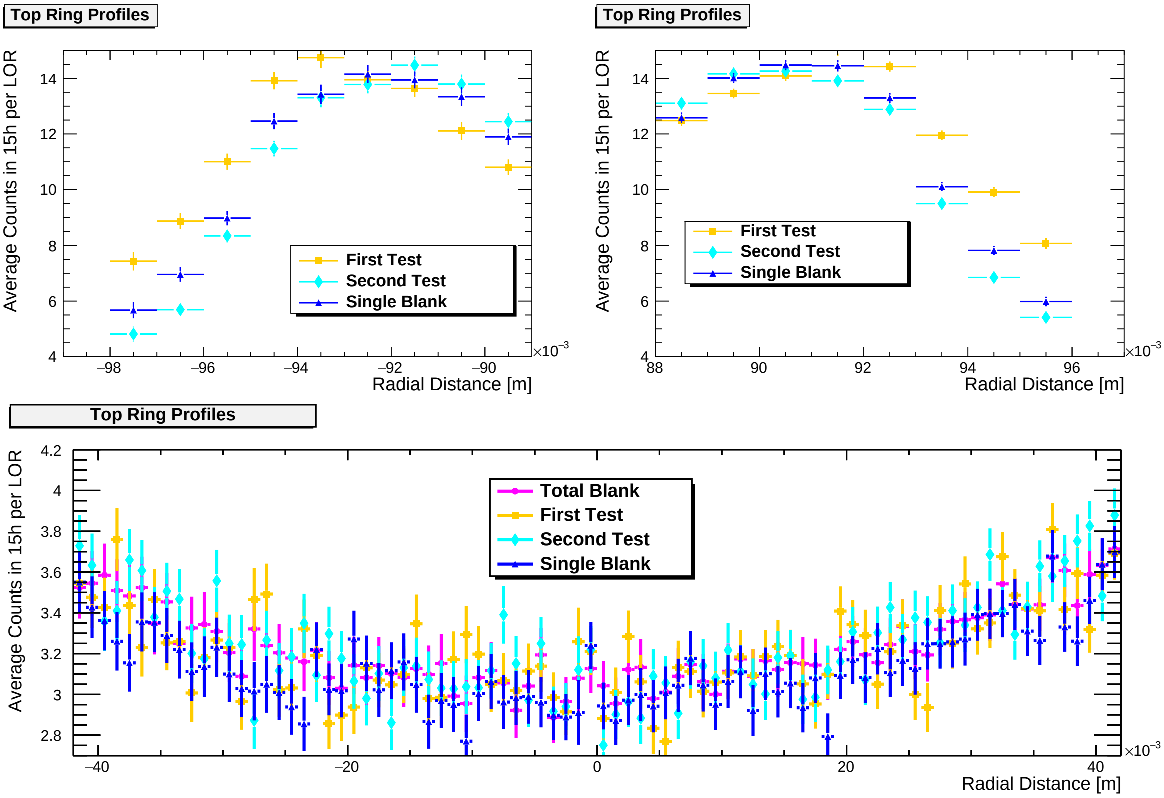

Figure 7.1: Average *estimated trues* in bin of radial distance. The three different plots are zoomed to the interesting regions. The single blank and the two test measurements cover the full range. The data of the total blank are only calculated for the actual FOV with a radius of 90 mm.

demonstrate the workflow and possible performance. Optimizations of individual processing steps or from PRESTO can readily be integrated.

7.2.1 Simulation Procedure and Setup for *pheno*PET

The Monte Carlo simulation implemented in PRESTO (see documentation [140]) is designed to track photons and simulate their interaction with the imaged object and the detector. The interaction of the photons with the detector uses the cross sections of cerium-doped lutetium oxyorthosilicate (LSO).The crystal positions are simplified with an equidistant crystal pitch. The objects within the FOV are provided as a voxelized attenuation map.For the object the cross section of water is assumed, which is justified for mainly organic objects like plastic, soil and plants. All implemented cross sections are extracted from GEANT 4 with the Penelope model.

The simulation is performed in rounds. Each round starts with the generation of a number of photons. For the presented studies 3×10^7 primary events are created per round. A primary event contains a decay position and a direction. All photon pairs with the photons A and B are tracked through the voxels of the attenuation map. Photons below an energy threshold (210 keV for *pheno*PET) are discarded. A multiplexing option for the tracking is implemented, which means that the tracking of both photons (A & B) of a primary is simulated additional times. This gives different final states (A_t & B_t) for the two photons of a primary.

The next step is the detector simulation. Therefore, each photon is tracked through the crystals and the interaction is simulated. The resulting energy deposition is smeared with a Gaussian distribution with a Full Width at Half Maximum (FWHM) of 17 % at 511 keV. Events with energy values below a lower threshold are discarded. A lower energy threshold of 310 keV is used in the PRESTO simulation for the energy window of 348 keV to 652 keV[2] applied in measurement. In pure simulation studies a threshold of 348 keV is applied. This detector simulation can also be multiplexed, i.e. simulated additional times similar the tracking. This results in more final states for each tracked photon and thus for each primary photon (A_{td} & B_{td}).

In the last step the detector interactions of a primary event are combined to coincidences. Therefore, all hits of the first photon A_{td} and all hits of the second photon B_{td} are combined. For example a multiplexing of the tracking of two and a multiplexing of the detector interactions by two increases the number of potential coincidences by a factor of 16. On the down side the multiplexing can introduce a dependence between individual coincidences. Therefore, in this example the improvement on the precision is below 16.

The results of the simulation are the number of unscattered events for each LOR and the number of scattered events for each LOR. These numbers are saved for further analysis.

For *pheno*PET all attenuation maps handed over to the simulation are extended by the aluminum shielding of the plant port. The voxels within a cylinder shell with radii from 105 mm to 107 mm are set to $\mu = 0.22\,\mathrm{cm}^{-1}$ for aluminum [43]. An investigation for the correction of transmission measurements revealed a radial bias of the attenuation coefficients from $0.104\,\mathrm{cm}^{-1}$ down to $0.085\,\mathrm{cm}^{-1}$ without this shielding added to the simulation. This bias is about 20 %. The scatter fraction, which is the ratio of scattered and scattered plus unscattered coincidences, increases in the scatter simulation from 19.5 % to 26.7 % with the shielding.

7.2.2 Scatter Estimates for Image Reconstruction

For the scatter correction, the simulated events need to be scaled to match the number of measured events. The Ordinary Poisson Maximum Likelihood Expectation-Maximization (OP-MLEM) takes the scatter component as an additive correction to the *estimated true* coincidences, analog to *random* coincidences. Therefore, the simulated values need to be calibrated to the measured data with the sensitivities. Those sensitivities are not modeled in the simulation. The scatter estimate of LOR SE_{ij} is obtained by

$$SE_{ij} = \frac{\sum_{ab}(p_{ab}^{meas} - VRR_{ab}^{meas})}{\sum_{ab}(\epsilon_a^{sim}\epsilon_b^{sim} \cdot g_{ab}^{sim} \cdot t_{ab}^{sim} + \epsilon_a^{sim}\epsilon_b^{sim} sca_{ab}^{sim})} \cdot \epsilon_i^{sim}\epsilon_j^{sim} \cdot sca_{ij}^{sim}$$

with the number of simulated scattered events sca_{ij}^{sim} and unscatted events t_{ij}^{sim} as well as the measured *prompts* p_{ab}^{meas} and variance reduced randoms VRR_{ab}^{meas}. In this case ϵ_i^{sim} and ϵ_j^{sim} are the sensitivities of the two crystals, i and j, defining the LOR and g_{ij}^{sim} its geometric sensitivity. All global scaling factors used during the calculation of the normalization cancels due to the occurrence of $\epsilon_i^{sim}\epsilon_j^{sim}$ in the numerator and denominator.

The sums for the scaling are calculated over a and b in a ring combination, which contains all LORs between two crystal rings. For plant measurements inhomogeneous activity distributions are expected and thus the scaling at the top and the bottom of the FOV can be different. Furthermore, the shot of the plant outside the FOV accumulates a large amount of tracer and might influence the scaling. This can produce scattered events, which are not taken into account by the simulation.

---

[2] Energy calibration of *pheno*PET does not account for the saturation of SiPM cells, see Section 3.4.4.1.

7.2.3 Sensitivities for Scaling of Scattered Coincidences

The scaling for the scatter estimates SE_{ij} requires sensitivities. These sensitivities, ϵ_i^{sim} and g_{ij}^{sim}, calibrate the model of the simulation to an actual measurement. The component base normalization model presented in Chapter 6 is used. The blank data are again used as measured data. For the expectation values (A_{ij}) a simulation with a cylinder shell as radioactive source is performed. This shell has a radius of 95.9 mm, which was obtained for the blank data (see Section 6.4.4). In total 1000 rounds are simulated with again 3×10^7 events per round. The further preparation and processing of the data is the same as in Chapter 6 but the number of iterations is reduced to 40.

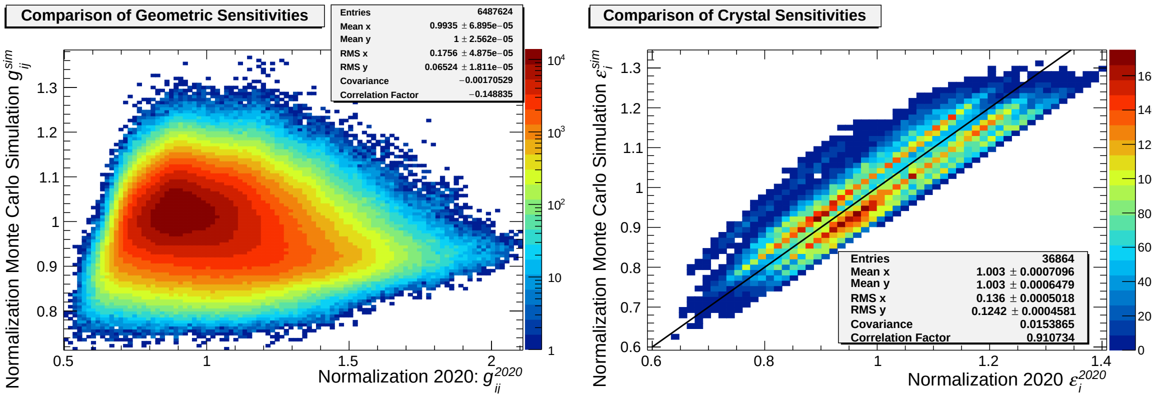

Figure 7.2: Comparison of sensitivities for normalization of an emission measurement and normalization of a simulation with PRESTO. There is no correlation between geometric sensitivities. The crystal sensitivities show quite good correlation. The black line illustrates the equality of both values.

In Figure 7.2 the obtained ϵ_i^{sim} and g_{ij}^{sim} are compared to the normalization for the reconstruction of emission images ϵ_i^{2020} and g_{ij}^{2020}. The geometric sensitivities differ largely between the two cases. The correlation coefficient of about −0.14 indicates no correlation between the two cases. This indicates that the geometric sensitivities correct different effects for the Monte Carlo simulation (g_{ij}^{sim}) and for a forward projection with line integrals (g_{ij}^{2020}). A first difference is that the Monte Carlo simulation already models geometric effects, which are not considered calculation of line integrals in the forward projections. One aspect is the effective length of a crystal depending on the direction of a photon. A second difference is the approximation of crystal positions as a regular grid by the Monte Carlo simulation.

The crystal sensitivities in Figure 7.2 match quite well and show a correlation coefficient above 0.9. For the ϵ_i^{sim}, the iterative fit does not result in the axial dependency observed for the ϵ_i^{2020} (Figure 6.10). This results in the splitting parallel to $\epsilon_i^{sim}=\epsilon_i^{2020}$.

The comparison underlines the importance of a dedicated sensitivities (ϵ_i and g_{ij}) for simulated data. These sensitivities will be applied for all calculation of SE_{ij}, that will be applied during the image reconstruction.

7.3 Influence and Correction of Compton Scattering on Transmission Reconstruction

The transmission measurements with *pheno*PET are done with a rotating rod source without a suppression of *scattered* coincidences. Therefore scattered photons, losing only a small part of their energy, are afterwards accepted in the energy window from 348 keV to 652 keV[3]. Thus events are transfered from one LOR to another. This decreases the attenuation coefficient of this LOR. Bailey et al. [34] describe this as broad beam case compared to the narrow beam case used to determine the theoretical attenuation coefficients. The scatter simulation is used to demonstrate the effect on a transmission reconstruction and the possible correction.

7.3.1 Simulation Setup and Data Analysis

The simulation of PRESTO is used for the investigation of the transmission reconstruction. The object is a cylinder of water with an attenuation coefficient of $\mu_{water} = 0.095\,93\,\mathrm{cm}^{-1}$. It has a radius of 40 mm and a height of 163 mm and its center is located at (8.1 mm, 27 mm, −18 mm). The cylinder is transformed in a voxelized image of 216 mm × 216 mm × 203 mm and a voxel size of 0.9 mm × 0.9 mm × 1 mm. The aluminum shielding of the plant port was not implemented for this investigation. The rotating rod source is simulated as a cylinder shell with a radius of 97 mm and a height of 208 mm.

The transmission measurement is repeated 20 rounds and the blank simulation 2000 rounds. Each round simulates 3×10^7 photon pairs. For this investigation the lower energy threshold for *singles* was set to 350 keV. The simulations are done with both multiplexing options set to two. The images are reconstructed with $\alpha_{relax} = 0.1$ and 10 iterations. The first reconstruction uses only the unscattered events as transmissions data and an additional image with 30 iterations is computed. For the next reconstruction the scattered events are added to the transmission data.

For the investigation of a possible scatter correction the obtained attenuation map with scatter is studied further. The mean attenuation coefficient within the cylinder phantom is scaled to the input value μ_{water}. Afterwards all voxels with negative attenuation coefficients are set to zero. This scaled image is used as input for a second set of simulations. Here, the required number of events is studied to correct the scatter background. Therefore, simulations are executed with 40, 400 and 1000 rounds. The results of these simulations are used to calculate scatter estimates for transmission reconstructions. The scaling in Section 7.2.2 is applied with $\epsilon_i^{sim} = g_{ij}^{sim} = 1$ as all values were simulated with the same setup.

The attenuation maps are analyzed with different Regions of Interest. An axial dependency is investigated with a ROI with a height of 155 mm and a radius of $r_{ROI} = 36.4\,\mathrm{mm}$, which is divided into six parts of the same height. The radial dependency is investigated by calculating the average attenuation coefficient within cylinder ROIs with different radii r_{ROI} and a height of 155 mm. This results in expected average values of

$$\overline{\mu^{ex}} = \begin{cases} \mu_{water}, & \text{for } r_{ROI} < r_{cyl} \\ \mu_{water} \cdot r_{cyl}^2 / r_{ROI}^2, & \text{otherwise} \end{cases}$$

with the radius of the phantom r_{cyl}.

7.3.2 Results

The mean attenuation coefficients of the different ROIs are presented in Figure 7.3. The values of the axial ROI (Figure 7.3a) show a good match between the reconstruction without *scattered* coincidences and the expected attenuation $\overline{\mu^{ex}}$. For the reconstruction with 10 iterations the mean is about $0.094\,\mathrm{cm}^{-1}$, which is only 2 % below the expected value. In Figure 7.3b it becomes clear that an increasing bias is visible for large ROIs, which approach

---

[3] Energy calibration of *pheno*PET does not account for the saturation of SiPM cells, see Section 3.4.4.1.

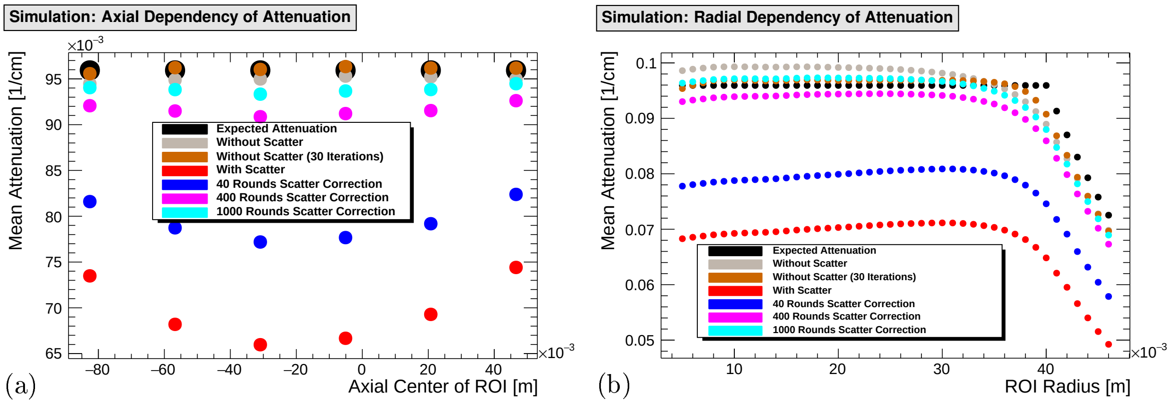

Figure 7.3: Mean of ROIs from reconstruction of simulated data. Unless mentioned otherwise, the images are reconstructed with 10 iterations.

the edges of the phantom. The reconstruction with 30 iterations without scatter further reduces this difference especially at the edges of the phantom.

The addition of *scattered* coincidences leads to an overall reduction of attenuation coefficients by about 30 % and introduces an axial bias as depicted in Figure 7.3a. The values of the ROIs ranges from about $0.066\,\mathrm{cm}^{-1}$ to $0.074\,\mathrm{cm}^{-1}$, which is a width of about 12 % compared to the average value. A reduction of the bias is achieved by adding more rounds of scatter correction. For 400 rounds the overall differences is about 4 % and for 1000 round this further decrease to about 2 %. The bias in the center of the cylinder is decreased with higher statistics of the scatter simulation.

In Figure 7.3b, the results of the ROI with different radii show a further radial dependency especially at the edge of the cylinder phantom in the range of $r_{ROI} = 35\,\mathrm{mm}$ to 40 mm. The reconstruction without scatter demonstrates that the bias can be further reduced with an increased number of iterations. This increases the noise specially for short measurement like 0.5 h. The reconstruction with *scattered* coincidences and without a correction shows a decrease below 3 % of the mean towards the center of the cylinder. The increased rounds of scatter simulation reduce the bias and increase the overall curves towards the expected values. For 1000 rounds the mean matches the expectation results without scatter and 30 iterations in the central part of the cylinder (5 mm to 30 mm).

A further reconstruction was done with the *scattered* coincidences of the transmission simulation as scatter correction. This reconstruction gives the same values as the reconstruction without *scattered* coincidences. For the transmission reconstruction *scattered* coincidences in LORs, that pass through the object, are important. Most of the primary photons pairs do not pass through the object. Furthermore, photons can be scattered into LORs outside of the object. Therefore, it is most likely that the high number of primary events in the scatter simulation are required to assign *scattered* coincidences to the LORs that pass through the object. This matches the statement in [71], that a scatter correction requires expectation values and no noisy estimates.

7.3.3 Discussion

The presented results show that the Compton scattering within the object results in a systematic reduction of the attenuation coefficient. The simulations proves that a reconstruction without *scattered* events results in the expected attenuation map. Nevertheless the simulation also indicates that a minor radial bias remains even for only unscattered events.

The reduction of the attenuation coefficients has an axial dependency. In the center of the object scattered photons can contribute from above and below resulting in a larger reduction. LORs closer to the edge opening of *pheno*PET have a higher chance to leave the detector and count as attenuated.

The presented estimation of *scattered* events for the transmission reconstruction showed a significant improvement for the run with 400 repetitions, which took about 6 h on 30 threads. Even better results can be obtained for a simulation of 1000 repetitions, which requires 16.3 h on 30 threads. Those durations are quite long for a single measurement. The easiest improvement is to increase the number of threads to 46 on *phenoreco*. Further improvements are discussed in Section 7.8.

The bias close to the borders of the cylinder remains and is most likely caused by the low amount of material that could attenuate photons. In actual measurements this region will mainly contain the walls of the pot or the phantom. The bias can therefore be assumed to have only a small influence on the activity distribution.

7.4 Measurement Setups for Investigation of Image Quality

The simulation study proved that a correction of the scatter component in transmission measurements is required. Furthermore, the procedure with the Monte Carlo scatter simulation has been implemented. The quantitative reconstruction of emission images also requires a correction of *scattered* coincidences. In addition, a calibration of the activity concentrations into Becquerel per volume is required for a comparison of different measurements and detectors. The required investigation can be done even though the simulation take too long for a routine operation.

The measurements are done with two cylinder phantoms with different dimensions. Both phantoms were filled with ^{18}F diluted in water in cooperation with Lutz Tellmann at the Institute of Neuroscience and Medicine: Medical Imaging Physics (INM-4). The activity concentration was determined in two ways. First, the fillable volume of each phantom is obtained by weighing it empty and filled with water. This volume is combined with a measurement of the activity filled into the phantom, which is measured with a Curiemeter. Second, a number of small samples (≈ 1 ml) are taken from the filled phantom after mixing the activity. Those are measured with a well counter. The sample volume is determined by weighing. Afterwards the phantoms were transported to *pheno*PET for emission measurements.

The small cylinder phantom has a diameter of 80 mm, a height of 163 mm and a fillable volume of about 510 mL. The phantom is placed on a socket made of Polyvinyl chloride (PVC) in a way that its top is close to the end of the FOV. A hole in the top of the socket fits quite precise to the phantoms bottom. The socket is fixed by the three pins on the source mount (see Figure 3.13b). Thus, a fixation in the transaxial plane is achieved. The emission measurement was acquired for $24\,\mathrm{h} = 86\,400\,\mathrm{s}$ with an activity of about 90 MBq at the start of the measurement.

The large cylinder phantom has an outer diameter of 150 mm and a height of 225 mm. The fillable volume is designed with a diameter of 140 mm and a height of 200 mm, resulting in a volume of 3079 ml. The measurement gives a consistent volume of 3073 mL. The bottom contains three holes for the pins of the positioning system. The emission measurement was acquired for 30 min. At the start the activity within the phantom was about 76 MBq.

For both phantoms a 15 h long transmission measurement is acquired after the activity is negligible compared to the transmission source. The phantoms needed to be removed for the mounting of the ^{68}Ge rod source due a lack of space. Afterwards the phantom was again placed on the positioning system.

7.5 Transmission Reconstruction of Measurements with Scatter Correction

The next step of the analysis focuses on the investigation of the transmission reconstruction for measured data together with the correction of *scattered* coincidences. The possible precision of the scatter correction is evaluated with different simulations with different attenuation maps as input. Those inputs include a synthetic attenuation map and different attenuation maps obtained from the measured data. A bias is found to remain within all corrected attenuation maps. For the small phantom a bias of 5.5 % compared to the expected value is observed. The large cylinder shows a similar radial bias but also an axial bias of up to 7.7 %.

7.5.1 Image Reconstruction and Estimation of Scatter Correction

The transmission measurements of the two cylinders described in Section 7.4 are analyzed in this section. For both measurements in total five attenuation maps are created and analyzed. All images are reconstructed with $\alpha_{relax} = 0.1$ and 30 iterations.

The scatter simulations are done with 1000 rounds with 3×10^7 events in each round. The source is a cylinder shell with a height of 206 mm to cover the complete FOV and a radius of 95.9 mm, which was obtained for the blank and normalization data (see Section 6.4.4).

Scenario 1: Ideal attenuation map is defined from the known geometry and materials. The attenuation coefficients are obtained from the XCOM database [43]. The large cylinder is modeled as a cylinder of water. This cylinder has a diameter of 150 mm and a height of 206 mm.

The small cylinder phantom is modeled as a cylinder of water. In addition the PVC socket is modeled as a cylinder with a diameter of 50 mm and a height of 55 mm. The attenuation coefficient is increased to $0.1257\,\mathrm{cm}^{-1}$, except for a hole with a diameter of 4 mm in the center of the socket. This hole was used to determine the position of the socket and phantom in a reconstructed image.

Scenario 2: 15 h & ideal scatter correction combines the measured data with scatter estimates from the idealized attenuation maps from scenario 1. Therefore, the ideal attenuation map is used as input for the scatter simulation with PRESTO.

Scenario 3: 15 h & scatter correction obtains an estimation of the scatter from the measurement. Therefore, a first reconstruction is done without scatter estimates. This raw reconstruction is scaled to achieve a mean attenuation of water within a ROI. These ROIs have a diameter of 120 mm for the large cylinder and 60 mm for the small cylinder. The height are 175 mm and 113 mm, respectively.

The scaled attenuation map is used as input for the scatter simulation. The scatter estimates are combined with the measured data for a second reconstruction. It has to be noted that the scaling factors depend on the size of the phantom. Therefore, a new scaling factor needs to be obtained for each pot size.

Scenario 4: 15 h, only scaled is the scaled attenuation map from scenario 3. Here no further corrections are applied.

Scenario 5: 0.5 h & scatter correction is the same procedure as in scenario 2 except for two adaptions. The measured data only contain events from 30 min. Furthermore, the number of iterations for the image reconstruction is reduced to seven. This decreases the noise due to the lower statistics.

7.5.2 Evaluation of Attenuation Maps

The analysis is done with different ROIs, similar to the analysis of the simulated transmission measurement (see Section 7.3.1). Along the scanner axis 10 ROIs are defined with equal height and a radius of 60 mm for the large cylinder and 30 mm for the small one. In addition, a number of ROIs with different radii are analyzed. Here, for the large cylinder a height of 175 mm is used and for the small one a height of 113 mm. For each ROI the average attenuation coefficient is calculated and plotted over the position of the ROI.

7.5.3 Results

The average attenuation for the different ROIs of the small cylinder are presented in Figure 7.4. The ROIs with different radii, Figure 7.4a show a decreasing average for the scaled attenuation map. The 15 h measurement with any of the scatter correction does not show this bias, except for a small decrease in the center. The 0.5 h long measurement has values similar to the ideal correction for $r_{ROI} < 30$ mm. For larger radii a decrease is visible resulting from the reduced number of iterations. For radii above 38 mm all scenarios decrease before the border of the cylinder has been reached. This behavior is already known from the simulation study in Section 7.3.

The axial slices in Figure 7.4b show a similar behavior. The scaled attenuation map has a bias towards the top of the FOV within the water. This bias is resolved by the scatter correction. The ideal scatter correction is about 5.5 % below the expected value within the ROI used for the scaling. For the scatter corrections obtained from the measured attenuation maps these differences slightly increase to 6.9 % and 6.5 % for the 15 h and 0.5 h measurements, respectively. This good agreement between the two corrections obtained from measured attenuation maps results from the chosen radius of 30 mm as visible in the radial ROIs in Figure 7.4a.

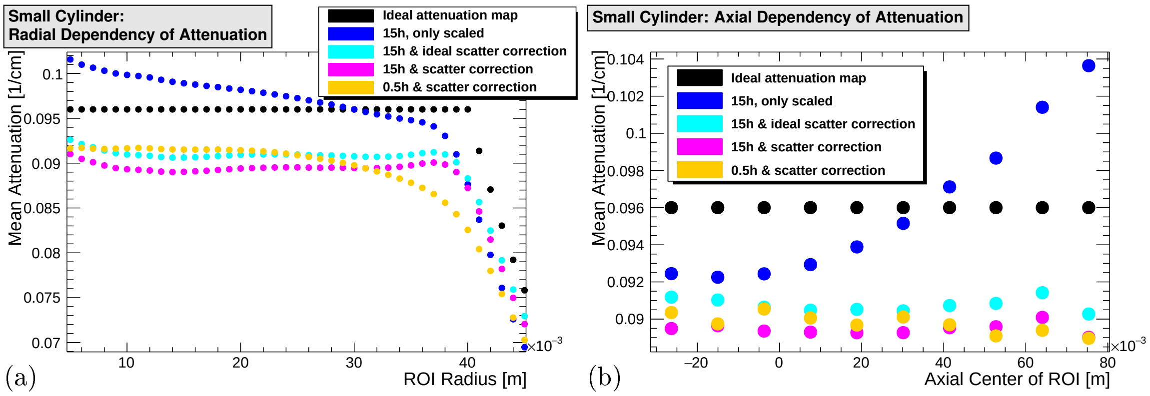

Figure 7.4: Radial and axial profiles of a measured small cylinder phantom filled with water. The scatter estimation contains the same statistics but is obtained from different attenuation maps. A bias along the scanner axis is visible. This most probably results from *scattered* coincidences from outside the FOV.

The result for the large cylinder are presented in Figure 7.5. The reconstructed radial profiles, Figure 7.5a, behave quite similar but all have a small bias compared to the expected value represented by the ideal attenuation map. The best match is visible for the 15 h long measurement and the ideal attenuation map as input for the scatter correction for the 15 h measurement. Here, small differences are visible for large radii. The observed bias for $r_{ROI} = 70\,\text{mm}$ is 4.4 %. The general shape of the measurement with scatter estimates from the measurement are similar. Their differences increase to about 4.7 % and 5.0 % for the 0.5 h and the 15 h, respectively. The scaled attenuation map shows a good match for the ROI used for the scaling. Nevertheless for different radii a bias of up to 2.5 % is observed. All profiles have the already know bias at the edges of the phantom.

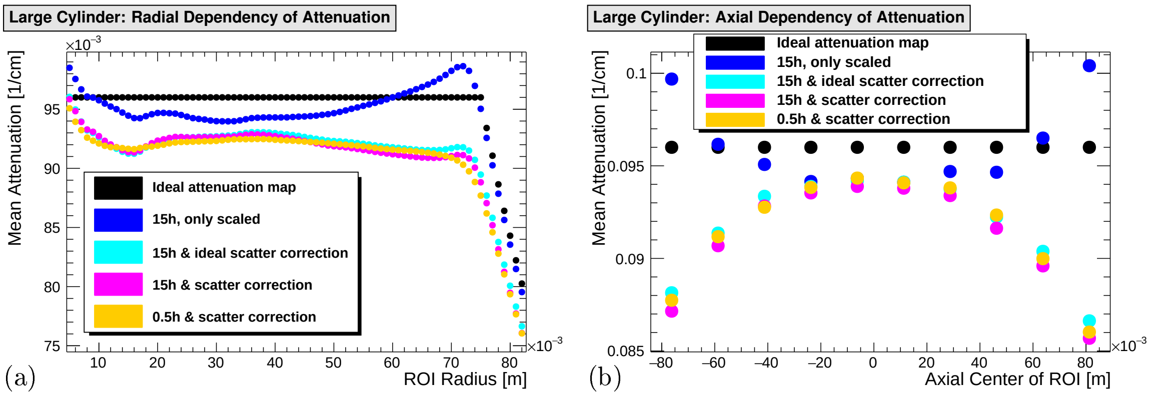

(a) (b)

Figure 7.5: Radial and axial profiles of a measured large cylinder phantom filled with water. The scatter estimates contains the same statistics but are obtained from different attenuation maps. A bias along the scanner axis is visible. This most probably results from *scattered* coincidences from outside the FOV.

The axial profiles, Figure 7.5b, show a relative good match in the center of the FOV but a bias towards the ends of the FOV. In the center a bias of about 2.1 % is visible to the edges this increases to up to 11 %. The scaled attenuation map shows the decrease in the center already observed in the simulation study. The maximum bias is about 7.4 % compared to the center of the FOV.

7.5.4 Discussion

The reconstruction of a transmission measurement with a single scatter iteration step gives good results. The scatter estimates obtained from a scaled attenuation map without scatter correction give results of a similar quality as from the ideal attenuation map.

In this study the scaling factors were directly obtained from the measurement. Those factors should be applicable for objects of a similar size. For plant measurements this factor can be obtained for each pot size once and applied to further measurements.

The radial profiles show only a difference of about 5 % to the absolute value. In addition, only a minor radial dependency remains. The reconstruction of the edges is more challenging. It depends on the number of iterations and is limited by the resolution of *pheno*PET.

The axial bias for the small cylinder is removed by the scatter correction. For the large cylinder this is not yet achieved with a bias of up to 11 %. This bias might result from the ^{68}Ge rod and the phantom being partly outside of the FOV. Here, coincidences can be scattered into the FOV. A correction could be achieved by moving the table to different positions and combining the information from two or more scans. In a plant study the pot will be within the FOV. The shoot of this plant and the cuvette will partly be outside of the FOV. Therefore, a bias from the shoot and the glass of the cuvette can be expected. This region contains a large amount of air. Therefore, a smaller amount of *scattered* coincidences and thus a smaller bias can be expected than for a solid cylinder of water.

The mainly flat radial curves and the flat axial curve of the small cylinder indicate that the profile of the *scattered* coincidences are obtained quite well. In contrast to the study with simulated data the reconstructions of the attenuation maps with any kind of scatter correction do not reach the expected value for water. This indicates further differences and effects that should be taken into account to improve the results.

One possibility addresses the setup of *pheno*PET and especially the additional material between the plant port and the detectors. This mainly consists of extruded polystyrene (XPS) which has a density of about $0.033\,\mathrm{g/cm^3}$ and a thickness of about 15 mm. This results in a scattering of about 1 % of the coincidences with the attenuation coefficient from the XCOM database [43]. For the aluminum shielding this fraction is about 8 %. These values assume a LOR perpendicular to the cylinder shell. Furthermore, the resulting mispositioning due to the XPS is smaller due to the shorter distance between the interaction and the detector crystals. Another possible improvement might be a more accurate modelling of the activity distribution created by the rotating rod source. At the moment the cross section of aluminum is simulated by scaling the cross section of water. This might cause a bias.

The reconstruction of the small cylinder reveals a quite large bias for the short measurement at the edges of the cylinder. For the large cylinder this bias is not observed. The shorter measurements are reconstructed with a lower number of iterations. This might be insufficient for a convergence of the small cylinder but keeps the fluctuation low. A further difference is the number of events per LOR due to the different radial distances. For the large cylinder more events are expected at the edge of the cylinder. Therefore, more events can be attenuated than for the small cylinder. This higher statistics should improve the convergence.

The number of expected events can be increased with a smaller radius of the rotating source. This would require a separate blank measurement as reference. Here, dedicated blank data for the most common pots should be established. The current blank data cover the full FOV and is thus applicable for arbitrary objects.

A stronger transmission source can be used to increase the quality of the attenuation maps or to reduce the duration of transmission measurements. As drawback this might cause dead time effects. This could be corrected with the dead time model obtained for emission reconstruction. Another possibility is to increase the number of sources. This distributes the activity to several sectors and should reduce the dead time effects on a single module. For example, the Siemens HR+ uses three sources.

Further improvements could result from an optimization of *pheno*PET. The aluminum shielding could be replaced with a plastic shielding. For polyethylene this would decrease the attenuation coefficient by a factor of two. The energy window could be narrowed to suppress *scattered* coincidences. Rothfuss et al. [134] used the TOF for an additional discrimination. This could be possible with *pheno*PET but requires an adaptation of the trigger and validation schema to improve the timing resolution towards 0.3 ns [114, 141]. Huesman et al. [92] describe the possibility to reduce the effect of *scattered* events by taking into account the position of the ^{68}Ge rod. All these changes can reduce the amount of *scattered* coincidences and therefore reduce the required corrections.

7.6 Analysis of Emission Data

The reconstruction of an attenuation map provides the required input for the scatter correction during a reconstruction of emission data. The iterative scatter correction (Section 2.7.3.5) is the last step required for a quantitative reconstruction. In the following section two questions are answered with the cylinder measurements presented in Section 7.4. The first question is the required number of simulated photon pairs for a scatter correction. Therefore, the ideal attenuation maps are used and reconstructed with different numbers of scatter iterations and different numbers of rounds. It is shown that for both phantoms two scatter iterations are sufficient. The number of rounds per scatter iteration depends on the phantom size until the mean converges.

The second question is the influence of the attenuation maps on the emission images. Here, the attenuation map scenarios introduced in Section 7.5.1 are used as input for the correction of attenuation and scatter. It is shown that for the different approaches similar results are obtained including a similar remaining bias. The largest bias remains with the scaled attenuation map, which are not corrected for scatter.

7.6.1 Convergence of Iterative Scatter Correction

The convergence of the iterative scatter correction depends on two parameters: The number of primary photon pairs used within the simulation and the number of scatter iterations. These two factors are investigated in this section.

7.6.1.1 Method

The investigation of the iterative calculation is done with a 30 min frame from the two emission scans presented in Section 7.4. For the small cylinder the start of the frame is at 27.5 min after the start of the measurement. The frame of the large cylinder is not shifted in time. For the following investigations, the ideal attenuation maps with fixed attenuation coefficients are used, see Scenario 1 in Section 7.5.1.

Effect of Different Numbers of Scatter iterations The first investigation focuses on the number of required scatter iterations. Therefore, the small cylinder phantom is investigated. The Monte Carlo simulation for each scatter iteration is done with 400 rounds. The reconstruction of the emission images is done with 15 iterations and applies all corrections: the normalization acquired in 2020, the dead time correction, an attenuation correction computed from the ideal attenuation maps and a decay correction for ^{18}F.

The reconstructed emission images are analyzed with the ROI analysis already applied to the transmission data, see Section 7.3.1. The dimensions of the ROIs are kept the same as for the investigation of the scatter correction and for the reconstruction of measured attenuation maps in Section 7.5.2.

Effect of Statistics per Scatter Simulation The effect of the statistics used in the Monte Carlo simulation is investigated with the large and the small cylinder phantom. Therefore, reconstructions of both phantoms are reconstructed with two scatter iterations. Theses reconstructions are performed with different numbers of rounds for the two required scatter simulation.

The first step of the analysis illustrates the homogeneity depending on the number of rounds. Therefore, the ROIs with different radii and the cylinder slices along the scanner axis are analyzed.

The convergence depending on the number of rounds r_{sca} is illustrated by comparing the mean values of the ROIs, $\overline{\lambda_{ROI}}$. A cylinder ROI with a radius of 60 mm and a height of 175 mm is analyzed for the large cylinder. For the small cylinder a radius of 30 mm and a height of 113 mm is analyzed. Afterwards, the convergence c_{sca} is calculated as

$$c_{sca}(r_{sca}) = \frac{\overline{\lambda_{ROI}}(r_{sca}^{max})}{\overline{\lambda_{ROI}}(r_{sca})}.$$

The reference value is the reconstruction with the largest number of rounds, r_{sca}^{max}. This number differs for the large and small cylinder.

7.6.1.2 Results

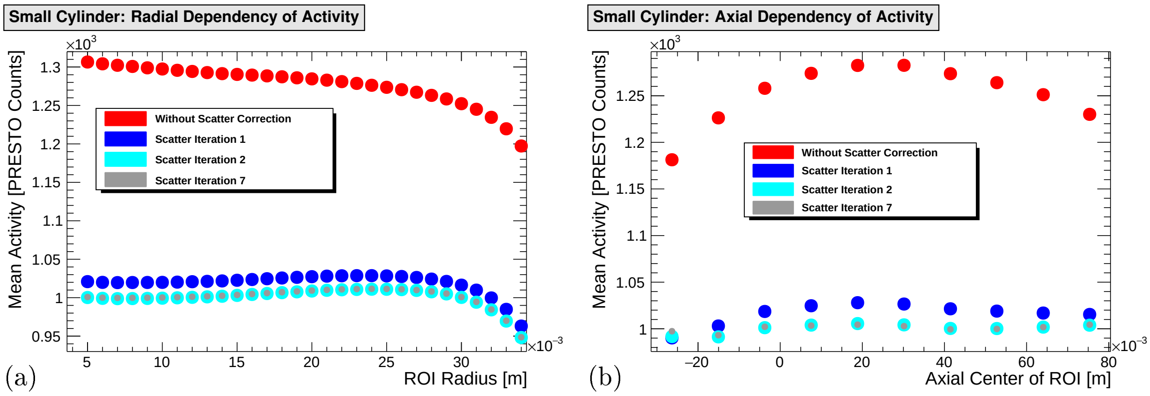

(a) (b)

Figure 7.6: Radial and axial profiles of a measured small cylinder phantom filled with ^{18}F diluted in water. Each scatter estimation contains the same statistics. A strong reduction of the bias and a reduction of the mean activity in the ROI is visible for the first scatter iteration. After the second scatter iteration only small changes occur, as visible by scatter iteration 7. The intermediate iteration steps are not displayed.

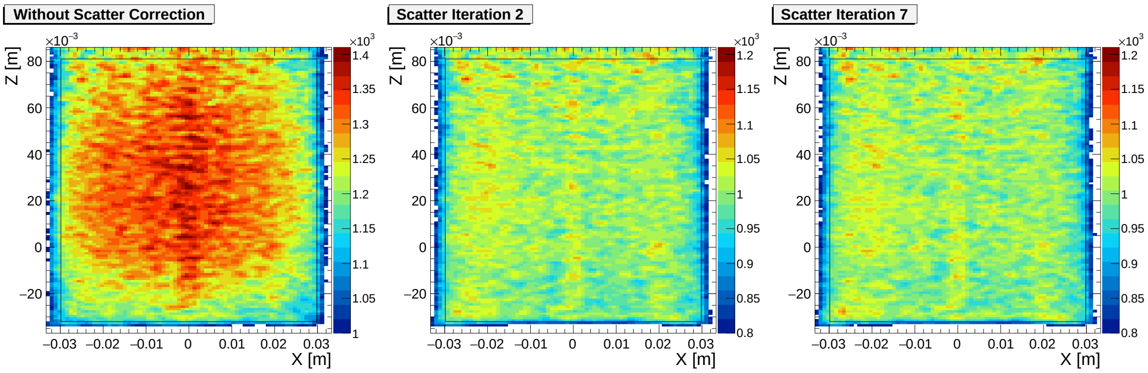

Figure 7.7: Slices through the center of the FOV for different scatter iterations. The clear improvement after two scatter iterations is visible. For seven iterations no further improvements are visible compared to two iterations for this homogeneous filled cylinder.

Effect of Different Numbers of scatter iterations Radial and axial profiles of the small cylinder for different scatter iterations are presented in Figure 7.6. In both cases the largest improvement is visible for the first scatter iteration. The radial profiles, Figure 7.6a, show a small decrease of the absolute values with the second iteration. The shape of the curves do not change significantly. Further scatter iterations do not change the results. For the axial bias, Figure 7.6b, the second scatter iteration further flattens the curve. The additional scatter iterations up to the seventh show minor changes, which are well below 1 %.

The effect of the scatter correction on a slice is displayed in Figure 7.7. Without any scatter correction an axial and a radial bias are visible. Those are removed after two scatter corrections, as observed in Figure 7.6. After two scatter iterations the majority of the voxels deviates about ±5 % from the mean of 10^3 PRESTO Counts. In all three slices the behavior for positive and negative X values is similar. Therefore, the ROIs presented in Figure 7.6a present a estimate of the overall behavior. Two scatter iterations lead to a convergence of the distribution and are therefore used for the further investigations.

Effect of Statistics per Scatter Simulation The axial and radial profiles for the emission reconstruction of the large cylinder phantom are displayed in Figure 7.8. In both profiles a strong decrease of the absolute values is observed by increasing the r_{sca} from 100 to 1000. In the radial profiles, Figure 7.8a, only a radial bias, well below 2 %, is visible for a radius smaller than 60 mm. For a radius between 65 mm and 70 mm a decrease is visible. This has already been observed in the transmission reconstructions as an effect of the number of iterations.

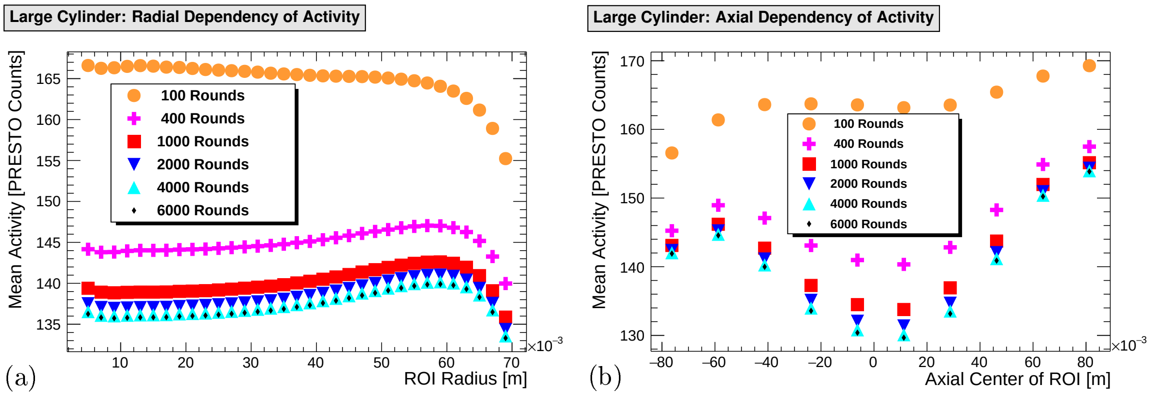

Figure 7.8: Radial and axial profiles of a measured large cylinder phantom filled with ^{18}F diluted in water. A strong reduction of the bias is visible for reconstructions, when increasing the statistics towards 1000 rounds per simulation. The already known convergence of the mean activity in the ROI is visible.

The axial profiles, Figure 7.8b, show a different behavior. The decrease of the absolute values is observed similar to the radial profiles but a bias remains. For 6000 rounds the difference between maximum and minimum is close to 20 % of the minimum mean value for a ROI. The minimum is close to the axial center of the FOV. But the shape of the curve is not symmetric, a maximum is observed at $z \approx -60$ mm and the absolute maximum is observed for $z \geq 80$ mm. The emission reconstruction of the small cylinder presented above and the transmission reconstructions presented in Section 7.5 do not show a similar behavior. This axial bias should be investigated further before large plots are used for quantitative measurements of plants with *pheno*PET.

Beside the observed bias the distribution did converge. In Figure 7.9 the convergence of the mean is illustrated. For the small cylinder already 400 rounds are sufficient to reduce the deviation below 1 % compared to 2000 rounds. For the large cylinder the convergence is much slower with a deviation of 1 % for 1000 rounds compared to 6000 rounds. Therefore, the required statistics for convergence depends on the size of the object or the size of the activity distribution or both. A further investigation should focus on the identification of the minimum required statistics per scatter simulation depending on the measured plant.

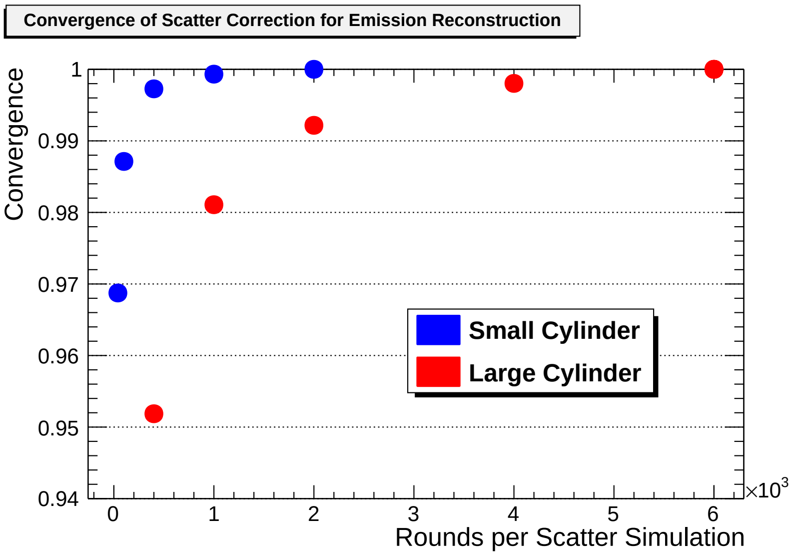

Figure 7.9: Convergence of scatter correction with ideal attenuation map. The convergence is much slower for the larger cylinder phantom. The number of rounds are simulated for each of the two scatter iterations.

7.6.2 Effect of Attenuation Maps on Scatter Correction

The creation of an analytic attenuation map is challenging for a plant in a pot. Therefore, the four data driven attenuation maps, defined in Section 7.5, are studied further. The emission image shows a remaining axial bias for the large cylinder phantom but a nearly bias free reconstruction of the small cylinder, if *scattered* coincidences are corrected for transmission and emission data.

7.6.2.1 Image Reconstructions and Analysis

The emission reconstructions are done with the five different attenuation map scenarios introduced in Section 7.5.1. For both cylinder phantoms a reconstruction is done with each of the five attenuation maps used for the correction of attenuation and scatter. The scatter correction is done with two iterations and 400 rounds for the small cylinder and 4000 rounds for the large cylinder. Those values showed similar results, as presented in Figure 7.9, and reduce the required computational effort.

The analysis is done in the same way as the investigation with the two ideal attenuation maps in Section 7.6.1. The ROIs with increasing radius are used to investigate a radial bias and the different cylinder slice ROIs are used to investigate an axial bias.

7.6.2.2 Results

The radial and axial profiles for the emission reconstruction of the large cylinder phantom are presented in Figure 7.10. The radial profiles (Figure 7.10a) show similar shapes with slightly different absolute values for all attenuation maps. All curves show a differences of about 4 PRESTO Counts between the maximum at a radius of 60 mm and the minimum at about 10 mm. This bias is around 3 % compared to the minimum of each curve. An exception is the scaled attenuation map, with an increased difference of about 4.5 %.

The axial profiles are given in Figure 7.10b. The bias observed for the reconstructions with the ideal attenuation map is reduced for the three reconstruction with a measured attenuation map, 15 h & ideal scatter correction, 15 h & scatter correction and 0.5 h & scatter correction. Here, especially the large values at the top of the FOV are reduced. The shape of these emission profiles is more symmetric around the minimum at $z = 0\,\text{mm}$. The two maxima at

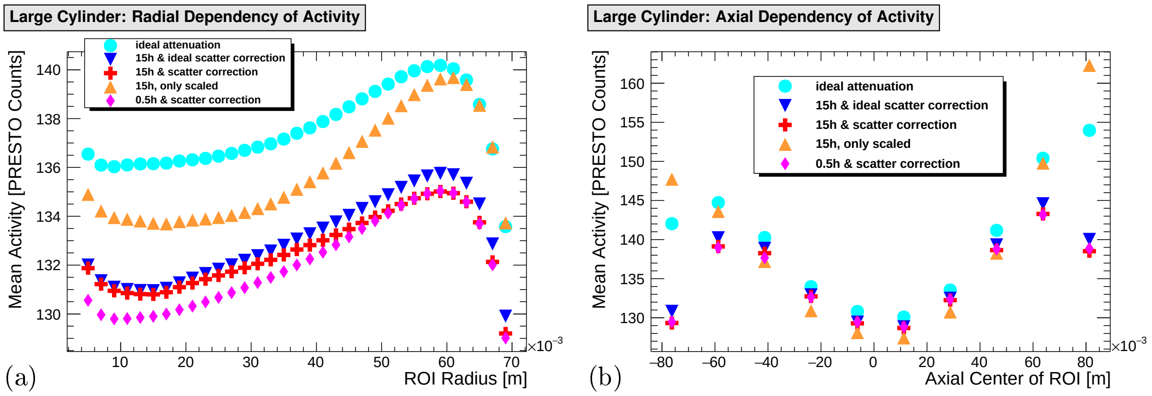

Figure 7.10: Radial and axial bias of emission reconstruction with different attenuation maps. The ROIs illustrate the bias for reconstructions of the large cylinder phantom. For all emission reconstructions two iterations of scatter correction are applied. The radial bias is similar for all attenuation maps. The axial bias is reduced for measured attenuation maps, where a scatter correction was included in the transmission reconstruction.

$z = -60$ mm and $z = 60$ mm have slightly different absolute values. This gives a bias of about 12 %, compared to the 20 % for the ideal attenuation map. For the emission images with the scaled attenuation map the axial bias is increased close to 27.5 % with a maximal mean of 162 PRESTO Counts at $z = 80$ mm and a minimum of 127 PRESTO Counts at $z = 0$ mm.

For the large cylinder the bias, which refers to the difference of the maximum and the minimum of a curve, observed for the ideal attenuation map is reduced with measured transmission data. This might indicate an issue in the definition of the ideal attenuation map. A significant reduction of the axial bias can be achieved by applying a scatter correction during the transmission reconstruction.

The emission reconstructions of the small cylinder phantom show a similar behavior. The emission images with the ideal attenuation map showed only a small axial bias, as presented above in Figure 7.6. The reconstructions with measured attenuation show similar behavior. Only for the scaled attenuation map an axial bias is observed. This is a linear increase of 10 % along the height of the phantom.

7.6.3 Discussion

The transmission and emission reconstruction with scatter correction already show promising results. The correction of scatter and attenuation removes the bias for the small cylinder phantom. This has a size similar to pots measured with PlanTIS. Those pots are therefore prominent in the current experimental designs. The larger cylinder phantom has a remaining axial bias that is not fully understood. Here, the measurement of activity and scattering matter outside of the axial FOV might be a challenge. The best starting point is to improve the transmission reconstruction and reduce the remaining axial bias in the transmission images. The strange part is, that the bias in the emission image and the attenuation maps have a different behavior.

The limiting factor for plant measurements remains the duration of the scatter simulation. Possible improvements have already been discussed previously in Section 7.5.4 for the detailed investigation of transmission reconstruction with scatter correction. For the emission reconstruction an optimization of the required statistics within the simulation for different activity distributions could lead to a reduction of the simulation time. One possibility might be a correlation between the convergence of the scatter correction and the activity distribution as well as the number of LORs with events.This would allow an automated adaptation of the number of primary events in each simulation to obtain robust results. An alternative could be a correlation between the different time points of a measurement and the required statistics for the scatter simulation. This could introduce dependencies, for example on the plant, the plants age, the pot size and the soil type.

7.7 Calculation of Calibration Factors

The previous section established different attenuation and scatter corrections. Those reduce the observed bias for the homogeneous cylinder phantoms. The calculation of absolute calibration factors towards MBq ml^{-1} allows a comparison of the two measurements. Calibration factors compare the reconstructed activity distribution with reference measurements. These factors allow an easy comparison of different measurements. In the following section calibration factors of all attenuation map scenarios of Section 7.5.1 are compared.

It is shown, that the maximum deviation between all calibration factors is below 8 %. For the emission images with the attenuation maps of the 15 h & scatter correction and 0.5 h & scatter correction scenarios the mean calibration factors differ below 1.5 %.

7.7.1 Method

The calibration factor compares the mean voxel intensity of a ROI, $\overline{\lambda_{ROI}}$, with the true activity concentration obtained from a reference measurement. This mean is divided by the frame duration t_{frame} to obtain a measured activity concentration AC_{meas}. The calibration factor CF is given by

$$CF = \frac{AC_{ref}}{AC_{meas}} = \frac{AC_{ref} \cdot t_{frame}}{\overline{\lambda_{ROI}}}$$

with the reference activity concentration AC_{ref}, see Section 7.4. This results in the calibration factor CF^{curie} with the activity concentration obtained from the Curiemeter AC_{ref}^{curie} and CF^{well} with the activity concentration obtained from the well counter AC_{ref}^{well}. The ratio of $\overline{\lambda_{ROI}}$ over t_{frame} is given in PRESTO Counts s^{-1}, which is abbreviated as pcps.

The activity calibration factors are calculated for the images reconstructed using the different attenuation maps defined in Section 7.5.1. The scatter correction is done with the parameters defined in the previous section. This means two scatter iterations and 400 rounds per simulation for the small cylinder and 4000 rounds for the large cylinder. The cylinder ROIs defined in Section 7.6.2 are used. For the large cylinder a radius of 60 mm and a height of 175 mm are applied and for the small cylinder a radius of 30 mm and a height of 113 mm.

7.7.2 Results

The calibration factors are presented in Figure 7.11. Here, the differences between the reference values are visible. The values obtained from the well counter differ by 2.5 % and 4.5 % from the Curiemeter for the large and small cylinder, respectively. In the INM-4 variations of up to 5 % between the reference measurements are acceptable as observed by their weekly calibration measurements. Furthermore, smaller differences between the different attenuation maps are visible. For the ideal attenuation map the results from the Curiemeter match quite good but for the two measured Scenarios (15 h & scatter correction and 0.5 h & scatter correction) the results from the well counter match better.

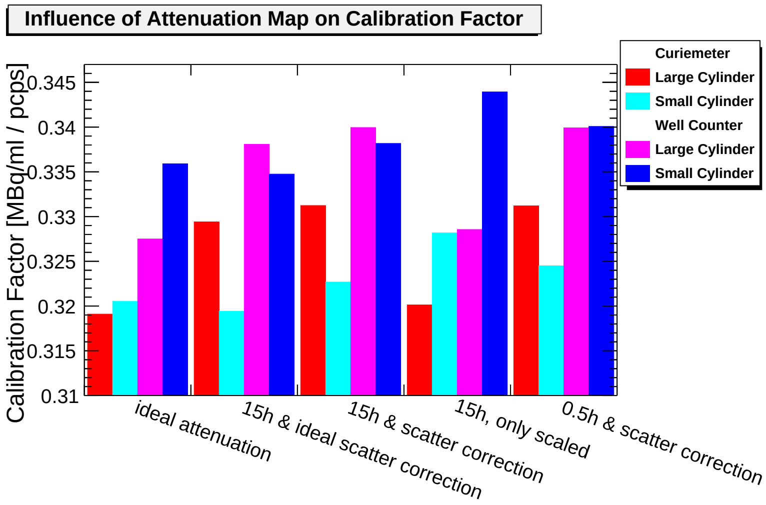

Figure 7.11: Calibration factors calculated from both cylinder phantoms for both reference measurement each. All calibration factors are in the same range and a maximum deviation of 7 % is visible for the attenuation maps without scatter correction. This is dominated by the difference of 4.5 % between the two reference measurements for the small cylinder.

For the actual application the Scenarios 15 h & scatter correction and 0.5 h & scatter correction are interesting. The mean activities for the large cylinder differs by 0.01 % for the 15 h and the 0.5 h duration. For the small cylinder a difference of about 0.6 % is observed between the 15 h and the 0.5 h duration. Therefore, it is reasonable to assume that the duration of the attenuation map has no effect on the calibration factor.

The reconstruction with the scaled 15 h transmission data also results in similar calibration factors, even though a quite large axial bias has been observed.

7.7.3 Discussion

The presented calibration factors show a maximum deviation of 7 % between the different scenarios and reference values. This is only slightly larger than the maximum difference of 4.7 % between the reference measurements with the Curiemeter and the well counter. The 0.5 h and 15 h measurement with fully data based attenuation corrections are the best examples for an actual measurement. The average and standard deviation of the four calibration factors gives $\overline{CF}_{15\,\mathrm{h}} = (0.3330 \pm 0.0068)\,\mathrm{MBq\,ml^{-1}/pcps}$ for the 15 h long measurement and $\overline{CF}_{0.5\,\mathrm{h}} = (0.3340 \pm 0.0066)\,\mathrm{MBq\,ml^{-1}/pcps}$ for the 0.5 h long measurement. Those values differ by about 0.3 %. Therefore, each of them is a good approach for the comparison of measurements.

7.8 Simulation Duration and Effect of Multiplexing

The previous investigations focused on the convergence of the reconstruction. For a routine operation the required computation time is important. The main duration is required for the scatter simulations. The investigation of the large cylinder in Section 7.6.1 revealed, that the main bias is removed with 400 rounds but the convergence required 4000 rounds. The remaining absolute difference can be incorporated into the calibration factor. For the small cylinder phantom similar observations are presented below. The main bias is removed with 40 rounds but a full convergence is reached with 400 rounds. Pots with a similar size are the current experimental focus. Therefore, the following investigations focus on the small cylinder phantom. Besides the simulation duration the effect of the two multiplexing options is investigated.

7.8.1 Method

The measurement of the small cylinder already used in Section 7.6.1 with the ideal attenuation map (see Section 7.5.1) are used. The image reconstructions are done with two scatter iterations and four different setups of the simulation. The first simulation keeps the multiplexing of the photon tracking and the detector multiplexing at their default values of two. The second simulation disables the detector multiplexing and the third setup disables both multiplexing options. The fourth setup uses the default multiplexing options with larger voxels of the attenuation map. These larger voxels are obtained by rebinning the attenuation map after the aluminum shielding of the plant port has been added. For all simulations 46 threads are used.

For the estimation of the required timing for each case a reconstruction with 40 simulation rounds per iteration and a second with 400 rounds is done. The duration of each simulation and each reconstruction is measured. Additional information, like the duration of different steps of the simulations, are provided by the output of different functions.

The required time of the reconstruction with and without scaling of scatter is obtained by averaging the durations. The time per round is calculated with a linear slope between the 40 and 400 rounds.

The last step is the comparison of the bias. Therefore, the analysis of the different ROIs used in Section 7.6.1 is compared for a few results.

7.8.2 Results

The reconstruction of a single frame of presorted projection data together with the loading of the system matrix and all corrections takes about 10 min. Here, each iteration during the OP-MLEM takes about 25 s which results in the majority of 6.25 min for 15 iterations on 46 threads. The scaling of scatter estimates requires about 2 min on a single thread for a frame. These times do not depend on the simulation for the scatter correction.

A simulation with the default multiplexing options requires 48.13 s per round. The output of the simulation shows, that the tracking of photons required 18.5 s and the detector simulation 22.15 s in an exemplary round. For the simulations without the multiplexing of the detector simulation, a round takes 45.3 s with 20.2 s for detector simulation in an example round. In the simulation without multiplexing a single round requires 31.3 s. Here, the tracking requires 15.4 s and the detector simulation 10 s. These times show that the tracking does not scale linear with the number of multiplexing. For the detector simulation, the multiplexing only slightly increases the duration of the simulation. The detector simulation is a factor of two faster, if the multiplexing during the tracking is deactivated. Here, a linear dependency is indicated. These two observations indicate, that the main operation is the identification of the appropriate detector crystals. The simulation of the interaction with the crystal seems to be much faster for *pheno*PET. The last simulation setup rebinned arrays of $2 \times 2 \times 2$ voxels to one voxel. This reduces the simulation of a single round to 42.8 s. An example round required for the tracking 13.64 s, which is about 25 % faster than without rebinning.

For the selection of a simulation setup the resulting images are important. Therefore, the ROI profiles for a selected reconstructions with different configurations are presented in Figure 7.12. The profiles for 40 rounds with multiplexing give results similar to 400 rounds without multiplexing. For 40 rounds without multiplexing a larger axial bias is visible. The results for the 40 rounds without multiplexing of the detector simulation have larger absolute values and a slightly increased axial bias. The increased voxel size does not change the results compared to the smaller voxel.

The reconstruction with 40 rounds and multiplexing are mainly bias free but the absolute

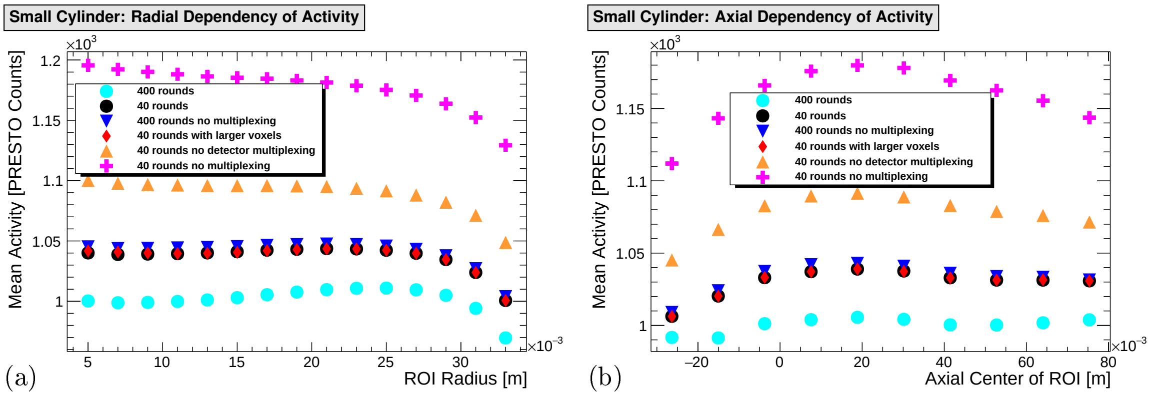

Figure 7.12: Radial and axial profiles of a measured small cylinder phantom filled with ^{18}F diluted in water with an synthetic attenuation map. The improvement through the multiplexed tracking is visible, especially when compared to the 40 without multiplexing. The detector multiplexing shows only a minor improvement of the convergence compared to the tracking multiplexing. The rebinning to larger voxels does not alter the results.

values are about 3 % larger than for 400 rounds. This difference can be taken into account by the calibration factor, which depends on the size of the object. In the case of the small cylinder this results in a calibration factor of $CF^{40}_{62\,\mathrm{mm}} = 0.323\,\mathrm{MBq\,ml^{-1}/pcps}$ instead of $\overline{CF}_{15\,\mathrm{h}} = 0.333\,\mathrm{MBq\,ml^{-1}/pcps}$ presented in the previous section.

7.8.3 Outlook

The above discussion reveals some potential for optimization. The scaling of scatter estimates required the loading of three additional projection spaces with the results of each LOR, each having a size of about 10 GB. These additional 30 GB are too much during an execution of the reconstruction, because the Random-Access Memory (RAM) is already occupied with the system matrix, other corrections and the already required projection spaces. Here, further optimizations of the work flow need to be done.

The duration of simulation rounds reveals, that the identification of detector crystals is quite time consuming. The current attenuation maps have a dimension of 216 mm in the transaxial plane. This covers the majority of the distance between two opposite modules of 255 mm. Here, a different approach for the crystal identification might be of advantage. Small improvements of the tracking can be achieved by reducing the number of bins. The presented example still requires about 25 min per simulation. Further adjustment could be achieved by increasing the number for the tracking and detector simulation multiplexing.

In the current setup, three plants per day are measured for 2 h each. The default frame length of 5 min allows 20 min for the reconstruction of each frame. Here, the two scatter iterations are too long. A major improvement is the usage of the *petstore* computer for reconstructions. This provides only up 32 threads but offers the required RAM. This becomes important as soon as daily measurements are performed. Also a software upgrade might prove useful. In their validation paper [139], Scheins et al. apply an advanced implementation of the simulation that is a factor of two faster due to further optimizations. Another idea is to perform the scatter simulation for each second frame. The scatter estimates for the skipped frames would than be estimates by averaging the two neighboring frames. These ideas could provide a speedup of up by a factor of 4 to 8. Furthermore, the number of scatter iterations could be to reduce from two to one. The investigations in Section 7.6.1 showed, that this removes the majority of the bias for the small cylinder phantom.

The required simulation rounds and scatter iterations should be validated for plant measurements. Their activity distribution has fewer voxels.

Further improvements might be achieved by an optimization of the Monte Carlo simulation. Methods implemented by Holdsworth et al. [103, 104] might be applicable. For example, they restricted the possible emission directions of photons. The comparison of the implemented method to other procedures should be done in terms of computational effort and image quality. For example a single scatter simulation (SSS) like Werling et al. [98] or an implementation including double scattered events like presented by Watson et al. [100] seem reasonable. Ma et al. report improvements of a GATE simulation running on a Graphics Processing Unit (GPU) over a SSS for 1.2×10^{10} primaries [101]. They investigated the contrast of hot spheres to a homogeneous cylinder phantom. This cylinder has dimensions similar to the large cylinder phantom investigated in Section 7.6.1. The number of 1.2×10^{10} primaries is reached with 400 simulation rounds without any multiplexing. The above investigations show a similar results for 40 rounds with multiplexing instead of 400 rounds for the small cylinder phantom. Furthermore, the convergence behavior (Section 7.6.1) indicate that for the small cylinder a lower number of primaries would be sufficient. Therefore, a SSS can be expected to produce a lower image quality than the current Monte Carlo simulations. Ma et al. report a duration of about 45 s for 3×10^7 events on one of their GPU cores. This is a bit slower as for the 46 thread, which require 31.3 s. PRESTO simulation with multiplexing are significant faster due to the reduced number of rounds. In contrast Watson et al. report only a few seconds per simulation [100] with their SSS extended for double scattered events.

7.9 Attenuation Coefficients of Different Soil Types and Hydroponics

The attenuation of a medium depends on the density and the chemical composition of the material. Thus different attenuation is expected for water and soil. Lee et al. estimated the attenuation by comparing the height of the 511 keV photon peak for water, wet and dry soil compared to air [142]. The highest attenuation was found for water and the lowest for dry soil. Thus, the water content changes the attenuation of the medium.

At the moment our plant measurements are mainly done in hydroponics. For hydroponics a root support structure made out of plastics is in the water and might have an influence on the attenuation. Prior Positron Emission Tomography (PET) experiments were also done with Speyer 2.1 soil [143] and in the future Graberde[4] might be used. Graberde is a black peat soil and for example used in drought experiments [144]. It has a much lower density then Speyer soil and thus a lower attenuation is expected. The transmission reconstruction is used to compare the attenuation coefficients of hydroponics with wet and dry soil of both types.

7.9.1 Experimental Setup

The different growth media are measured in a pot used for plant measurements with PlanTIS. The pot is presented in Figure 7.13 and is designed for experiments with hydroponics. Therefore, a septum is included in the bottom for the oxygenation of the medium. All measurements are done with this bottom of red plastic, which is analyzed as reference. The hydroponics pot is filled with water and the support structure is added. The further preparation of each soil sample is different.

---

[4] Plantaflor Humus Verkaufs-GmbH: Oldenburger Straße 4, D-49377 Vechta

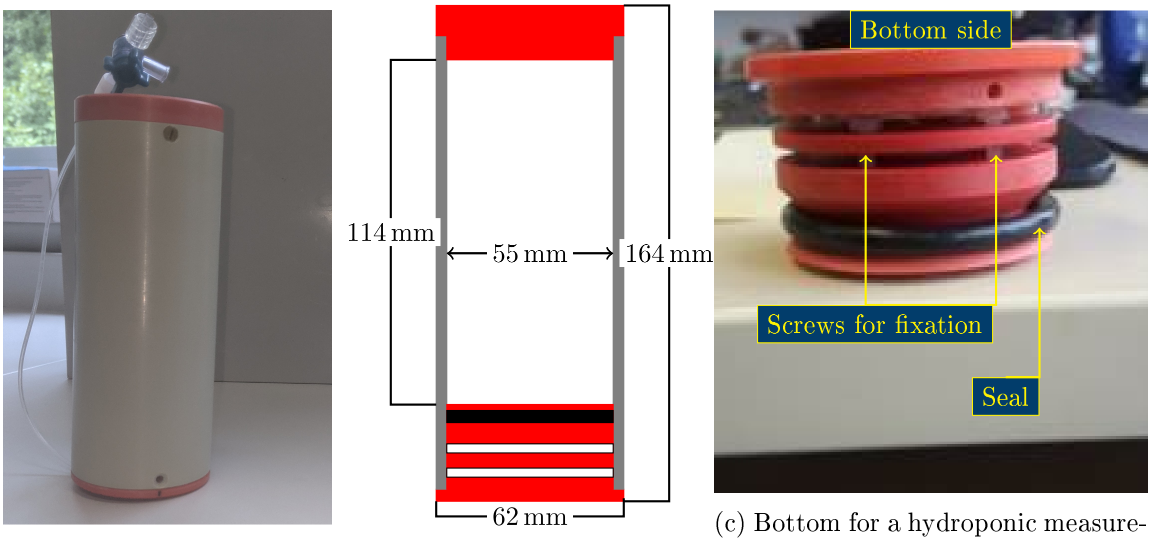

(a) Image of 62 mm pot.

(b) Sketch of a pot.

(c) Bottom for a hydroponic measurement.

Figure 7.13: Pot used for investigation of different growth media. Pots are designed for measurements with hydroponics.

The first measurement was done with Speyer soil. Here, dry and wet soil were measured in the same pot and separated by foil. The dry soil is taken from old experiments and dried down in a green house. The wet soil contains additional 11 % of water relative to the resulting mass. The wet soil is placed at the bottom of the pot and the dry above.

For the Graberde one pot is filled with dry soil and one with wet soil. Both pots are sealed with foil. The dry soil is taken from old experiments. Previous experiments measured a humidity of about 40 % of the mass [145]. This is increased to about 70 % by mixing the same mass of dry soil and water.

The pots are positioned inside *pheno*PET. Each transmission measurement is acquired for 15 h. The reconstruction is done with $\alpha_{relax} = 0.1$ and 30 iterations. The scatter correction uses one scatter iteration with a scatter simulation of 1000 rounds. Each round contains 3×10^7 primaries and both multiplexing options are set to two. The attenuation maps without scatter correction are scaled by 1.41 for the scatter simulations. This scaling factor is obtained from a reconstruction of a pot filled with water.

For the comparison the mean attenuation in a ROI is determined for each medium. Furthermore, the density of each sample is estimated. In addition the mean attenuation of a torus that contains the red plastic of the bottom part is analyzed. These values are compared for the different measurements. The expected attenuation coefficients for water, the red plastic and the support structure for hydroponics are obtained from the XCOM database [43] with the chemical properties and density found in their data sheets. For the red plastic the mean of all measurements is compared to the expectation.

7.9.2 Results

In Table 7.1 the properties of the red plastic and water are presented. The ratios between the expected attenuation coefficient and the mean attenuation coefficient from a reconstruction without scatter correction of both materials are 1.4 and 1.41 and differ below 1 %. This is within the relative standard deviation for the red plastic of about 1.4 % and consistent with the scaling factor applied before the scatter simulation.

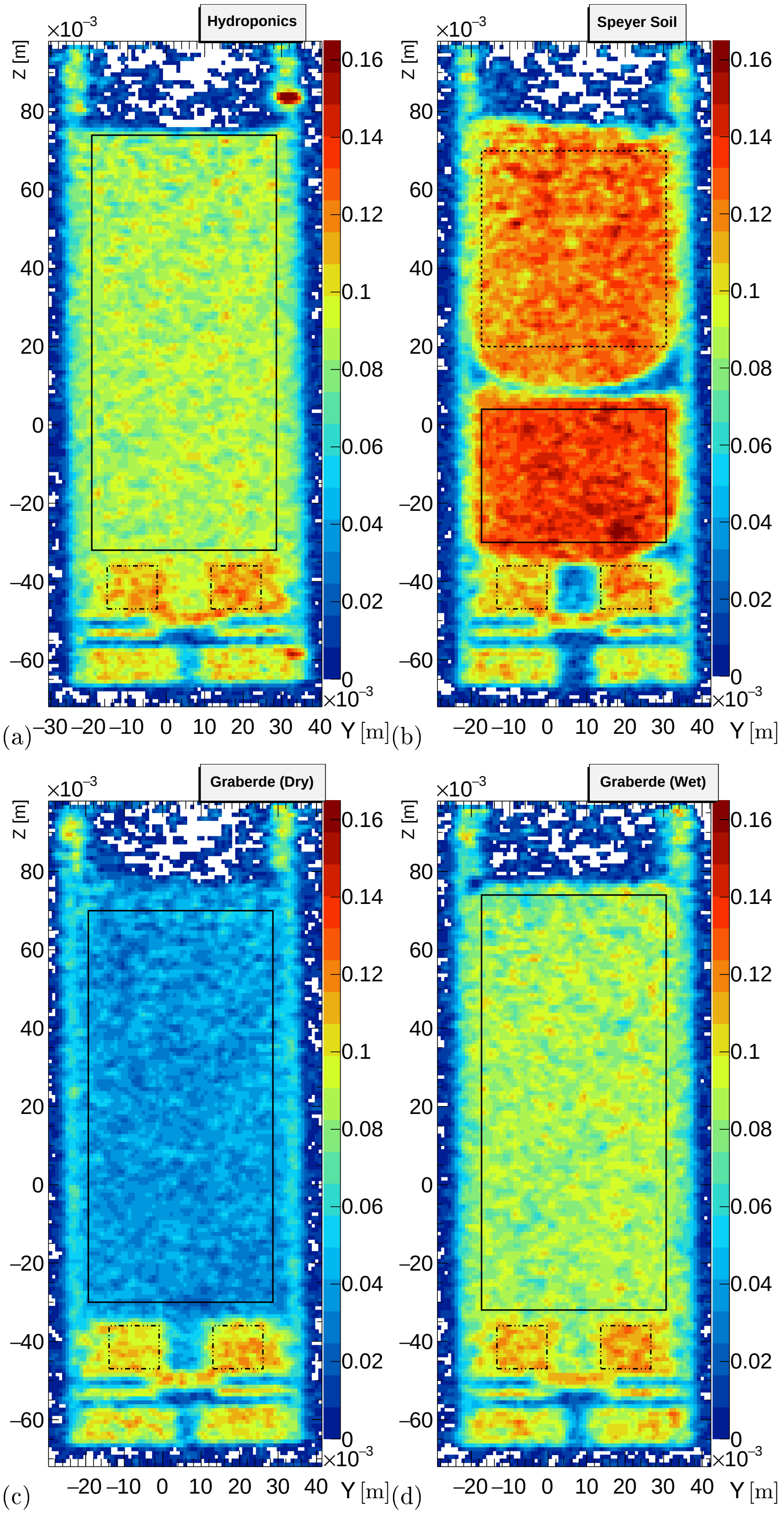

Figure 7.14: Axial slices through the center of the ROI in x direction. The color scale gives the reconstructed attenuation in cm^{-1}. The black lines indicate the ROIs used for the analysis.

Table 7.1: The mass attenuation coefficient μ_{mass} of the major materials taken from the XCOM Database. The measured values are obtained from the ROIs of the small pots. The result of the red plastic is the mean and standard deviation of all five measurements.

Material	Water (H_2O)	red plastic (H_3C_2Cl)	PMMA ($C_5H_8O_2$)
Density ρ [g/cm^3]	0.9982	1.4	1.19
μ_{mass} [cm^2/g]	9.687×10^{-2}	8.981×10^{-2}	9.410×10^{-2}
$\mu = \mu_{mass} \cdot \rho$ [cm^{-1}]	0.0967	0.1257	0.112
Mean from ROI without scatter correction $\overline{\mu_{ROI}^{noSca}}$ [a.u.]	0.069	0.0889 ± 0.0013	–
Ratio $\mu / \overline{\mu_{ROI}^{noSca}}$ [cm^{-1}/a.u.]	1.40	1.41	–
Mean from ROI with scatter correction $\overline{\mu_{ROI}^{meas}}$ [cm^{-1}]	0.088	0.108 ± 0.003	–
Ratio $\overline{\mu_{ROI}^{meas}} / \mu$ [cm^{-1}/cm^{-1}]	0.91	0.86	–

One axial slice in the y-z planes for the different growth media are presented in Figure 7.14. Their different attenuation coefficients are visible, especially when compared to the red plastic in the bottom. Within the red plastic, small cavities of air can be identified. The resolution is not good enough to identify fine structures like the plastic screws connecting the different parts of the bottom. The ROI containing each medium look homogeneous. A decrease of the attenuation is visible towards the borders of the pots.

The attenuation coefficients for the red plastic in Figure 7.15a show similar results for hydroponics, Speyer and wet Graberde. The result for dry Graberde differs by about 5 % from these values. The mean attenuation of the red plastic is 14 % below the expected value as given in Table 7.1.

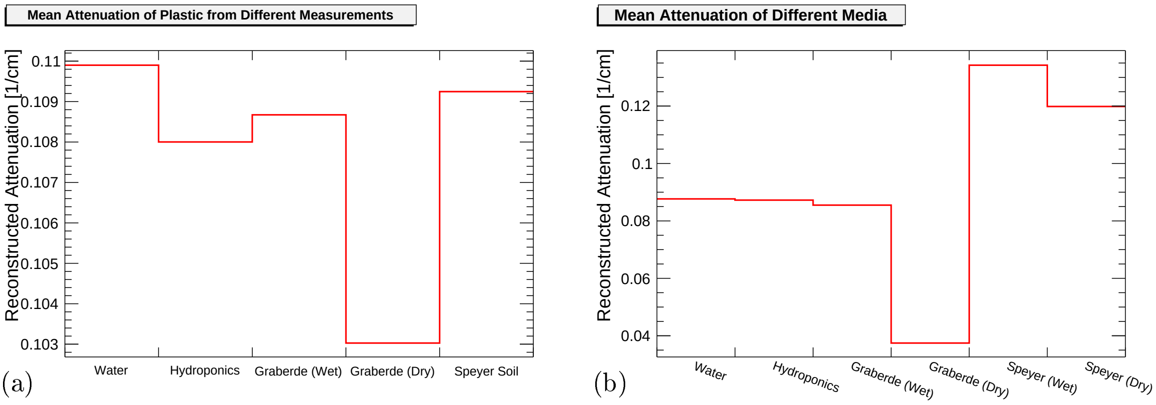

Figure 7.15: Average attenuation coefficients in ROI of the different growth media and the red plastic in the bottom of the pot for each measurement.

The mean values for all growth media ROIs are depicted in Figure 7.15b. The attenuation of pure water and hydroponics show only neglectable differences. Here, a difference of about 9 % to the expected attenuation is visible (Table 7.1). The supporting structure for hydroponics consists of PMMA, which has a slightly higher attenuation than water, see Table 7.1. The resolution is not good enough to identify the supporting structure in the slices as depicted in Figure 7.14a.

The water content is the main source of attenuation for Graberde. The wet soil has an attenuation coefficient 2.28 times larger than the dry soil. The density of the dry Graberde is about 0.436 g/cm^3 and for the wet Graberde about 1.009 g/cm^3. This gives a ratio of 2.31, which differs below 1.3 % from the ratio of the attenuation coefficients.

For Speyer soil the additional water slightly increases the attenuation by about 11 %. The density for wet soil is estimated to 1.59 g/cm^3 and 1.46 g/cm^3 for the dry soil. The estimation of the density is spoiled due to the foil separating the two samples of different humidities. The foil is not flat as visible in the slice and includes some air, see Figure 7.14b. The assumed cylinder volume is therefore a bit larger than the volume of the soil resulting in an underestimated density. These densities differ by about 8 %, which is close to the increase of the attenuation coefficient.

7.9.3 Discussion

The presented results confirm a dependency of the attenuation coefficient on the water content of the soil. In addition the composition and density of the soil have a strong impact on the attenuation. A transmission measurement should be performed once before an emission measurement. A further investigation of the dynamics of the water content over a day is done in the following section.

The attenuation coefficients of the red plastic and water show that the scaling of the attenuation map results in the correct mean attenuation. Therefore, the scaling of the attenuation maps for the scatter correction of the transmission reconstruction will provide robust results. Especially it is sufficient to obtain a scaling factor from water for plant measurements. The observations of the cylinder phantoms in Section 7.5 revealed that this scaling depends on the size of the object.

The attenuation of water is about 9 % below the expected value. For the red plastic an larger deviation of 14 % is observed, see Table 7.1. In Section 7.5 deviations to the expected value of 6.9 % and 4.4 % are observed for the cylinder phantoms with a radius of 40 mm and 75 mm, respectively. Therefore, the remaining bias seems to be larger for smaller objects. Here, possible improvements should be investigated.

7.10 Dependency of Attenuation on Water Uptake During a Measurement

At the moment typical plant measurements run for two hours. Furthermore, a plant can be labeled with tracer multiple times over the day without watering. The previous investigation showed that the attenuation depends on the water content of the soil. Here, we study how strong the water uptake by a plant during a measurement influences the attenuation.

7.10.1 Method

The measurements are done with pea plants grown in hydroponics and in Speyer soil in a climate chamber. The Speyer soil was selected because it has already been used for PET measurements. Watering was done by weighing the pot and adding water until a defined weight is reached. The plants were measured three weeks after sowing.

The plants were transported and placed inside *pheno*PET at the evening after watering. The transmission scans were started in the morning and run for 7.5 h. After the measurements the plants were weighted. During the measurement two half circles made of plastic are placed as a cap on the top of the medium. This reduces a possible evaporation from the soil. The climate chamber was not yet operational but the ventilation has a high air exchange that resulted in stable conditions. During the measurement light was provided by new Light-emitting diode (LED) panels mounted above *pheno*PET. The daily cycle was similar to the climate chambers but with a higher light intensity.

For the analysis, the transmissions scans are split into 30 min long frames and reconstructed with 7 iterations. The scatter correction was not yet operational for these reconstructions. The image is divided in cylindrical ROIs with a height of 5 mm. The radius and height differ for both measurements because both pots were a bit skew and the pot filled with soil did not contain the bottom part. The ROI for hydroponics has a radius of 25 mm and a total height of 130 mm and the ROI for Speyer soil a radius of 24 mm and a total height of 140 mm. For each ROI the mean attenuation coefficient and its Root Mean Square (RMS) is calculated and plotted over the frame number. A linear function is fitted to each graph and the ratio between the values of the fit function for the first and last frame are calculated. This ratio is plotted over the measurement duration in units of the frames. The same procedure is done with the mean of a ROI covering the complete height. The water consumption over the day can be estimated from the watering before and after the measurement day.

7.10.2 Results

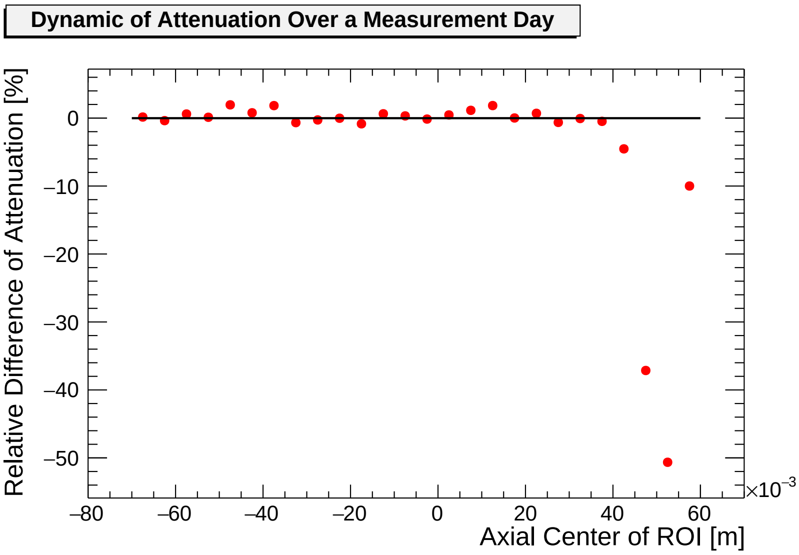

Figure 7.16: Change of attenuation for a pea plant grown in hydroponics over a measurement day as function of the axial position. The black lines marks the average change of all ROIs. The highest ROI (55 mm to 60 mm) contains parts of the plastic support structure and thus only a small change is visible.

The dynamic of the attenuation for the pea in hydroponics are plotted in Figure 7.16 as function of the axial position. The four highest ROIs show large reductions of the attenuation. The lower ROIs do not show a change of the attenuation. The ROI from 50 mm to 55 mm shows the largest relative decrease of 50 % with an absolute value of 12×10^{-3} a.u. for the first frame. The next lower ROI has a lower relative difference of 40 % but a higher maximum value of 50 a.u.. The attenuation of water was measured in Section 7.9 to be higher at about 69 a.u.. The absolute differences in the presented and the expected value result from air already part of the upper ROI as illustrated by Figure 7.17a. The last frame in Figure 7.17b illustrates the reduction of the water height. A comparison of the voxels between the two time points indicate a decrease between 2 mm and 4 mm. This estimation is challenging as the voxels indicate a bulge of the water surface with a peak in the center of the pot and a decrease towards the borders.

The weight difference is about 19 g in 24 h. This equals a lowering of the water surface of about 8 mm. The real difference should be slightly higher due to the plant and support structure. The transpiration is a consequence of photo synthesis, which requires light [26]. Van

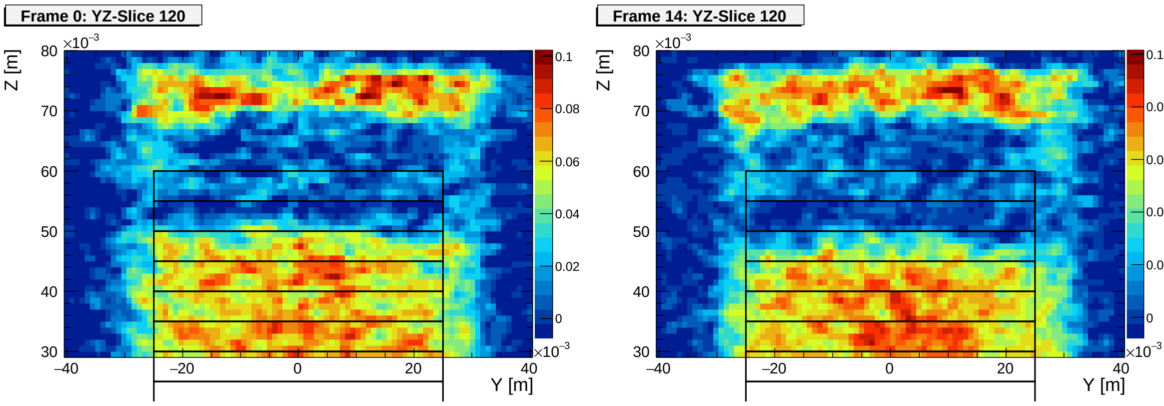

(a) Start of this measurement.

(b) 7 h after start of this measurement.

Figure 7.17: Axial slices zoomed to the top of the pot from the first and last frame of the measurement. A decrease of the water is visible as well as the cap on to of the pot. The plant cannot be seen.

Dusschoten et al. [146] measured the water uptake of maize plants and reported that the main uptake happens during day time. Therefore, the light of the LEDs leads to a decrease of about 4.2 mm during the measurement. This assumes a constant transpiration and ignores the effect of evaporation during the night. This value is similar to the above observed differences. It has to be noted that an exact comparison is difficult due to the voxel size and the uncertainties. Furthermore, previous reconstructions have shown that the estimation of borders is difficult for 0.5 h long frame. Finally, the plant is located in the middle of the pot and thus will influence the attenuation as well as the shape of the water surface.

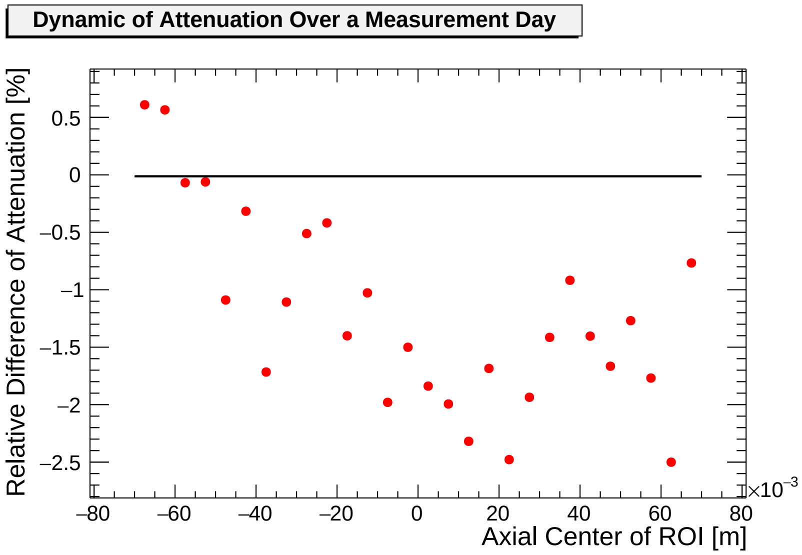

Figure 7.18: Relative change of attenuation for a pea plant grown in Speyer soil over a measurement day. Each dot represents a 5 mm height ROI. The black lines marks average change for all ROIs.

The relative differences for the Speyer soil are given in Figure 7.18. These differences indicate a reduction of the attenuation in the majority of small ROIs. For the lowest ROIs a small increase is observed. This could be a result of water moving vertically through the soil down to the bottom. Van Dusschoten et al. [146] measured a vertical water movement for their maize plants. The weight difference of 24.6 g is a bit larger than for hydroponics but the relative changes of the attenuation are smaller. This is a result of the high attenuation coefficient of dry Speyer soil.

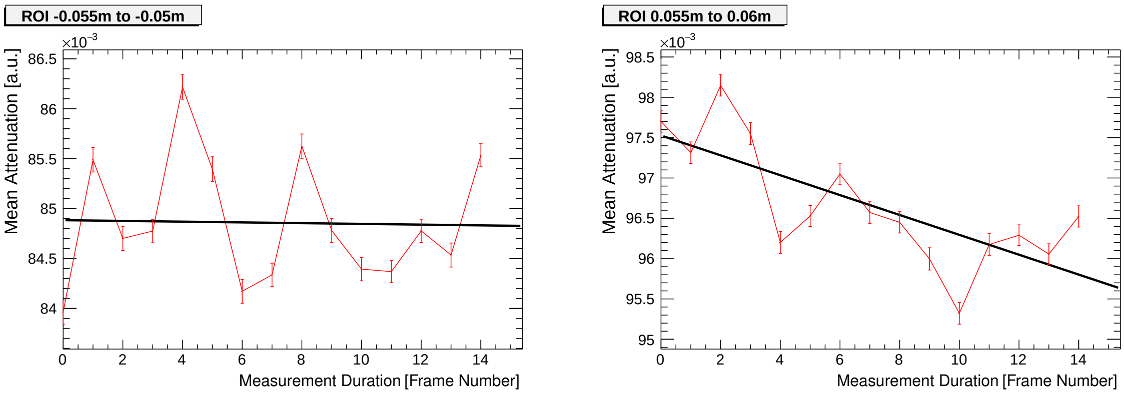

Figure 7.19: Examples for two ROIs presented in Figure 7.18. The values of the fits for the first and the last frame are used to determine the relative difference over the day. Each frame has a duration of 30 min.

The decrease of the attenuation in the upper part ($z > 0\,\mathrm{m}$) covers a range between $-0.5\,\%$ and $-2.5\,\%$. In the underlying fits similar deviations of the data points from their fits are observed, as depicted by the two examples in Figure 7.19. Therefore, a discussion on systematic effects, like information on different water uptake in the small ROIs, should be omitted without further measurements.

7.10.3 Discussion

For Speyer soil and hydroponics a decrease of the attenuation can be observed during a measurement day. In hydroponics the water height decrease and thus mainly the attenuation for the upper region is influenced. Thus, an analysis of the lower part of the pot should not be influenced. The experiments with PlanTIS are also done in hydroponics. These experiments are done with the gas exchange system and an oxigenation of the water. The measurements of the gas exchange system contain the transpiration rate, i.e. the amount of water added to the air by passing through the cuvette. For eight similar plants, this system measured an average water uptake of 51 g with a standard deviation of 16 g (six days measurement per plant, 14 h of light). Therefore, the lowering of the water surface in hydroponics can be expected to be larger than observed above.

The relative difference of the attenuation during a measurement day for Speyer soil are quite small with a maximum of $-2.5\,\%$. For the scatter corrected attenuation maps a remaining bias around $-5\,\%$ on the absolute scale is found for a slightly larger phantom, see Section 7.5. The question remains open, how the dynamics of the attenuation propagates towards an emission measurement. Here, the limiting factor were the moving of *pheno*PET into the new laboratory.

The results indicate that for a lighter soil like Graberde the effect of water on the attenuation during a measurement will be larger. Therefore, test measurements with each soil and plant combination are reasonable to investigate the attenuation over a day.

A few ideas might help to improve the attenuation correction over a measurement day. It is possible to measure the humidity of the soil and automatically water the plants. One possibility for this measurement is to use the humidity measured by the gas exchange system.

Further possibilities might result from models of the water content over the day like presented by van Dusschoten et al. [146]. Here, the correlation with the attenuation coefficient could be investigated. Typically, plants are placed in *pheno*PET the evening before the measurement. Thus, over night a long term transmission measurement could be acquired as a starting point for a model of the attenuation over the day.

7.11 Conclusion and Outlook

The presented investigations show that the transmission reconstruction is in general suited for the determination of an attenuation correction. A measurement duration of 30 min and a reconstruction with 7 iterations and $\alpha_{relax} = 0.1$ gives good results for a measurement duration suitable for routine operation. Better results are obtained for 15 h long measurements and 30 iterations. Both measurements require a scatter correction, which requires a quite long simulation duration. This estimation uses a scaled attenuation map as input. These scaling factors depend on the size of the phantom. For the investigated soil, plastic and water no strong dependency on the material was observed.

The attenuation map of a current used pot ($r = 31$ mm) filled with water shows a bias of about 9 % on the absolute attenuation coefficient. A cylinder phantom ($r = 40$ mm) leads to a smaller bias of about 6.5 %. For a cylinder phantom covering the full FOV a bias of 5 % and an additional axial dependency with deviations between 2 % and 11 % to the expected value are observed.

The plant port shielding introduces a quite large amount of scatter, that needs to be considered during the simulations. An substitution by another material or a reduced thickness will lead to an improvement. Further improvement of the setup could be done with a new mount for the ^{68}Ge rod source. Furthermore, the source should be mountable with an object in the FOV. Two possibilities are a spring or a cone shaped adaptor.

Alternative approaches for the reconstruction could also be promising. Rothfuss et al. [134] continue their investigation and perform a simultaneous reconstruction of emission and transmission, which requires TOF. Here, the usage of the ^{176}Lu decay would also be interesting. This requires a change of the trigger mode of *pheno*PET to achieve the temporal resolution of about 0.298 ns presented in [116]. Thus, further extensive work would be required.

The investigation of the growth media showed different results for the two soils, Speyer and Graberde, and different dependencies on the water content. Therefore, the attenuation correction should be studied carefully for each system of a plant in a specific age and a growth medium. This is especially important if the treatment, for example drought, changes the attenuation.

The already available attenuation maps lead to a large improvement of the reconstruction of emission images. The scatter correction gives stable results after two iterations. The required statistics per scatter iteration for a convergence of the mean depend on the object size. For cylinder with a radius of 40 mm, which is a bit larger than current used pots ($r = 31$ mm), a bias is well below 2 %. For a large cylinder phantom, covering the FOV, the radial bias is below 3 % but an axial bias of up to 12 % is observed.

The calibration factor obtained for different approaches to the transmission reconstruction have a maximum deviation of 8 %. The mean calibration factor of a 0.5 h and a 15 h transmission scan differ by about 0.3 %. To pick one factor, the value from the 15 h long transmission scan of 0.333 MBq ml^{-1}/pcps is recommended for the comparison of further studies. The calibration factors seem not to be effected by the remaining bias in the emission images of the large cylinder.

The measurement of pots with a size similar to ones already used within PlanTIS is expected to be mainly bias free (< 2 %). A possible effect of the shoot and the cuvette, which can *scattered* coincidences into the FOV, should nevertheless be investigated. For larger pots additional work might be required to reduce the current bias of up to 12 %.

The main challenges for the scatter simulation are the quite long simulation durations. The investigations show that the bias does not change much even though the mean activity concentration has not yet fully converged. Therefore, an object depending calibration factor provides a large potential for a significant speed up. For the small pots the bias is mainly removed after 40 rounds, which requires about 33 min per simulation. Here, only an axial bias below 2.5 % remains. A difference of the mean activity concentration of about 3 % is observed relative to the converged mean after 400 rounds. These 400 rounds also removed the axial bias. This convergence behavior should be validated for measurements of plants.

Chapter 8

Validation of Performance and Operation Stability

In the previous chapters the required corrections for quantitative images have been presented. Here, the achieved performance of *pheno*PET is demonstrated. The first aspect is the stability of the temperatures on the Digital Photon Counter (DPC) and the influence on the sensitivity. The second aspect is the stability of the dynamic corrections during a measurement. Finally, the spatial resolution is determined.

8.1 Temperature Stability

The operation of Silicon photomultipliers (SiPM) requires a constant temperature due to the dependency of the dark count rate and detection efficiency on the temperature of the detector. In the following section the improvements due to the warm up mode and the temperature behavior during dynamic measurements are investigated.

The analysis focuses on the temperatures measured by the sensors on each DPC. These values can be read out with the control software *DPCShell*. During a measurement, the temperature can be extracted from the data packages (see Section 3.2.1). The temperature values are averaged in 1 s intervals.

8.1.1 Temperature Behavior for Constant Activity Distributions

The effect of the warm up mode is investigated with two measurements of a ^{68}Ge rod source with 1.62 MBq. The rod is placed in front of sector 8, which contains the modules 8, 20 and 32. The first measurement was started with active warm up mode right after the source was placed inside the Field-of-View (FOV). The second measurement was started without the warm up mode and initially cold modules. Right before the start of each measurement the temperature sensors are read out over the *DPCShell*.

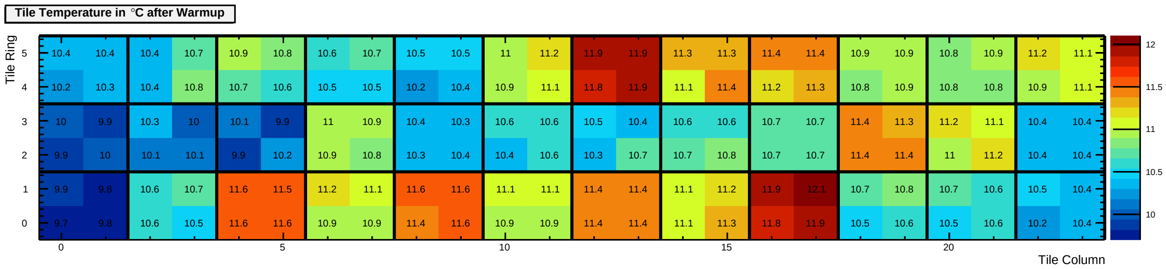

Figure 8.1: Temperature of *tiles* with active warm up mode. The data were read out over the firmware before the measurement was started. Black lines illustrate the detector modules.

In Figure 8.1 the temperatures of all *tiles* are depicted for the running warm up mode. The position dependency could result from the setup of the cooling system. Further differences might result from different thermal coupling between a *tile* and the cooling system. It has to be noted that the *tile* temperatures differ from the temperature setting of the cooler because the cooler is regulated to the temperature of its reservoir (3.5 °C) and not to the sensors on the DPCs.

The *single* and coincidence count rates of one module and the temperatures of three *tiles* are presented in Figure 8.2. The measurement without warm up shows a loss of detected coincidences due to a temperature increase of up to 3 °C over 25 min=1500 s as depicted in

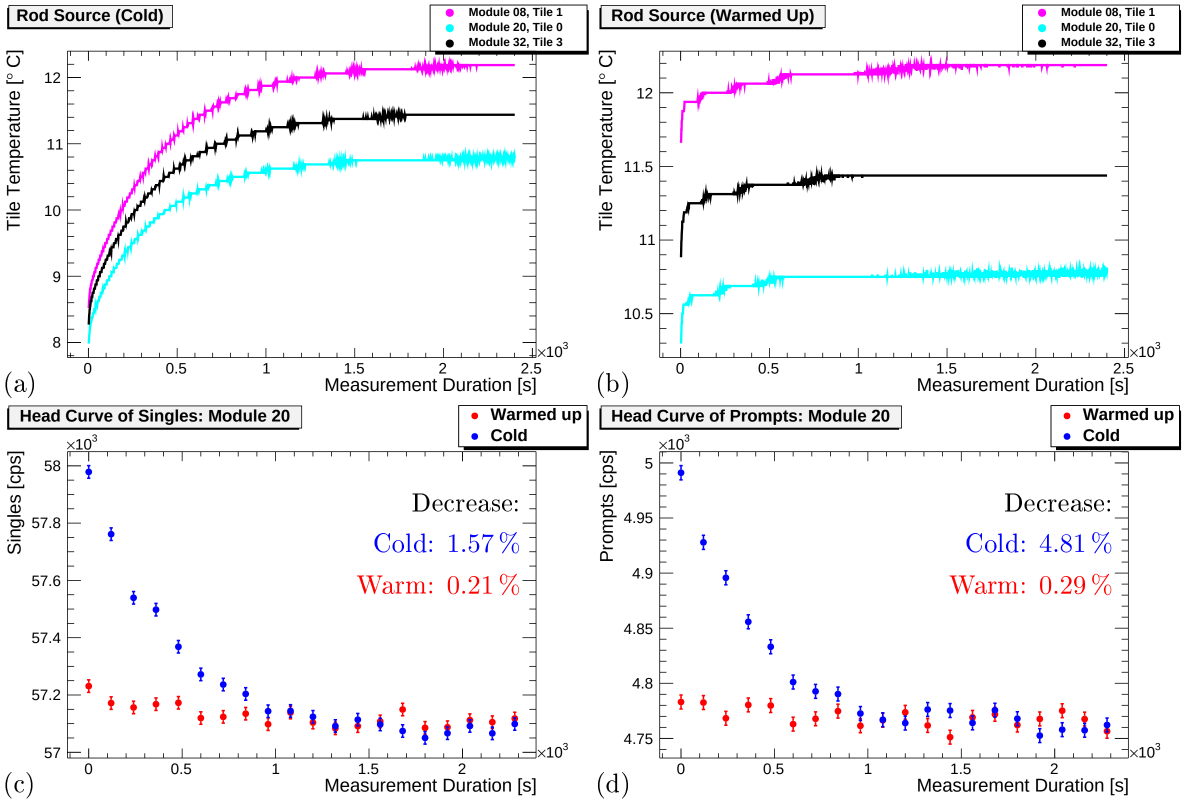

(a) (b) (c) (d)

Figure 8.2: Temperature behavior after the start of a measurement and resulting count rates. The reduced temperature increase due to the warm up is visible. The temperature curves of different tiles have a similar shape but different absolute values. The *prompt* coincidences and *singles* of module 20 are displayed to show the effect on the count rates. Both count rates are averaged values over 120 s. The loss of *singles* and *prompts* is reduced due to the lower temperature increase and hardly visible within the plots.

Figure 8.2a. For example, the temperature of *tile* 0 on module 20 raises from 7.98 °C to 10.78 °C. In Figure 8.2b the temperature with activated warm up mode shows an increase from 10.3 °C to 10.78 °C for the same *tile*. This warm up shows a steep increase right after the start of the measurement. After about 600 s a stable temperature is reached about 0.5 °C above the initial temperature. This increase is smaller and a stable temperature is reached faster than without warm up mode. The temperature curves of all *tiles* are similar during a measurement as visible in Figure 8.2a and Figure 8.2b. Therefore, we focus on a single example in the following discussion.

The *singles* measured by module 20 are shown in Figure 8.2c. Here, the warm up mode reduces the variation from about 1.57 % to 0.21 %. For coincidences larger variations are observed in Figure 8.2d, 4.81 % without warm up and 0.29 % with warm up. Therefore, the warm up mode reduces the change of the sensitivities.

Before the measurement, *tile* 0 of module 20 shows a temperature of about 10.7 °C in the warmed up state (compare Figure 8.1). The warm up mode is a measurement without saving data to disc, see Section 3.2.2. Right after the start of the data acquisition, the temperature has dropped to 10.3 °C (Figure 8.2b). The start of the data acquisition requires a restart of the system, which includes a shut down and setting of the bias voltage. During the 26 s of this restart, the cooling system cools down the detector *tiles*. This is visible in the small decrease and following steep rise of the temperature after the start of the data acquisition.

8.1.2 Temperature Behavior During a Dynamic Measurements

Here, the count rates and temperatures are investigated during a dynamic measurement. The behavior of all *tiles* is similar, and therefore only one *tile* on module 20 is investigated. The presented *singles* count rates are the sum over all four *tiles* of the module.

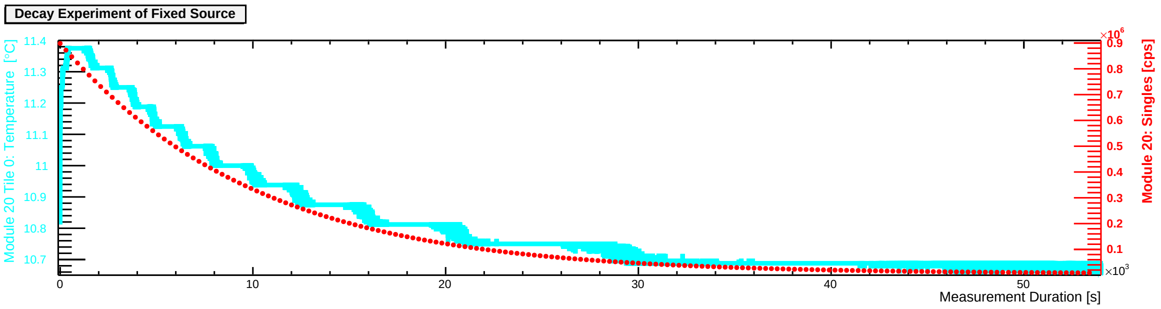

Figure 8.3: The temperature of a single *tile* and *single* count rates of the complete module. The phantom is a ^{18}F filled cylinder and placed close to the center of the FOV. The phantom was in the FOV before the measurement was started and thus the modules were warmed up further. *pheno*PET was still located in the old laboratory and thus the environmental temperature might have an small influence on the absolute values.

The temperature and count rate behavior of a decay experiment is depicted in Figure 8.3. The phantom was already placed within the FOV while the source decayed close to the dynamic range of *pheno*PET. After the start of the data acquisition a steep increase of the temperature is visible. This is followed by a slow increase until the temperature reaches the temporary equilibrium at about 11.4 °C, which is 0.6 °C above the warmed up system in Figure 8.2b. Afterwards the temperature decreases in proportion to the measured *singles*. This correlation between count rates and temperatures results from the processing operations required for each ingoing photon. Each operation releases a small amount of heat. At the end of the measurement the temperature reaches the temperature of the warmed up system of 10.7 °C.

8.1.3 Consequences for Routine Operation

The temperatures during a data acquisition show a clear dependency on the event rates and thus decrease the sensitivity for increasing rates. This loss of sensitivity should be compensated by the count rate corrections which are based on the count rates of the individual detector modules. Nevertheless, this is only true if a stable operation temperature for the given count rates has been reached. Here, the warm up mode is a valuable method to reduce the systematic variations.

Furthermore, a small increase of the temperature during the first 10 min of a measurement is observed. To minimize the effect on the measurement of plants, the data acquisition should be started before the time interval of interest. The current measurement protocols, start the data acquisition during the labeling of the plant. The tubes of the gas exchange system pass through the FOV and therefore the activity passes through the FOV. This should be sufficient for a warm up of the system. For future experiments this should be incorporated into the experimental protocol.

Additional challenges might result during the operation of the climate chamber, which can be operated at temperatures between 10 °C and 30 °C. A temperature dependency should be especially relevant for dynamic temperature changes over the day.

8.2 Performance in a Dynamic Measurement

In the following section the stability of a reconstruction over time is investigated using a homogeneous cylinder phantom. A frame length of 5 min, which is applied in plant measurements, is used. In addition noise-equivalent count rates (NECRs) are calculated to investigate the noise within the reconstructed images. The stability is shown to be within 2 %. The lowest level of noise is obtained for an activity of about 25 MBq, when the frame dropping is not active.

8.2.1 Measurement Setup, Data Processing and Image Reconstruction

The measurement of the small cylinder phantom already used for the evaluation of the scatter and attenuation corrections is used. The measurement setup and details of the measurement are presented in Section 7.4. The cylinder phantom has a volume of about 510 ml with a radius of 40 mm and a height of 163 mm. Reference measurements provide an activity concentration of $AC_{ref}^{curie} = 0.178\,\mathrm{MBq\,ml^{-1}}$ with the Curie meter and $AC_{ref}^{well} = 0.187\,\mathrm{MBq\,ml^{-1}}$ with a well counter. The Curie meter indicates a total activity of about 90 MBq at the start of the measurement. In contrast to the previous analysis not a single image frame of 30 min but the full duration of 24 h is analyzed.

8.2.1.1 Image Reconstruction

The emission reconstruction was applied on 5 min frames. The number of frames is reduced by shifting the start of each frame by 20 min. The Ordinary Poisson Maximum Likelihood Expectation-Maximization (OP-MLEM) is applied with 15 iterations. The normalization and count rate corrections are the same as presented in the previous chapters. In addition the decay of the ^{18}F is corrected. The attenuation data are obtained from a 15 h long transmission measurement and reconstructed with one scatter iteration, see Scenario 3 in Section 7.5.1. The scatter simulation contains 1000 rounds with 3×10^7 primaries with detector multiplexing and tracking multiplexing set to two. The Maximum Likelihood for Transmission Reconstruction (MLTR) is performed with 30 iterations.

The scatter correction for the emission data is done with two scatter iterations for each frame. For each scatter iteration 40 rounds are simulated with 3×10^7 primaries per round. The multiplexing options, tracking and detector simulation, are set to two. In the emission image an upper threshold is applied for the activity concentration AC before a scatter simulation to speed up the simulations to a reasonable duration. This threshold is the 99.9 % quantile from a histogram with 10^6 bins. Therefore, the actual number of voxels may slightly differ for each frame. The quantile of 99.9 % was chosen by comparing histograms of a few emission reconstructions. Separate reconstructions without this quantile cut off before the simulations are done for four frames. All reconstructed frames are calibrated with $CF_{62\,\mathrm{mm}}^{40} = 0.323\,\mathrm{MBq\,ml^{-1}/pcps}$, which is quoted in Section 7.8.

8.2.2 Stability over Dynamic Range

The first analysis focuses on the stability of the reconstructed images over time. In addition it is shown that the applied cut off based on the quantile does not influence the presented results.

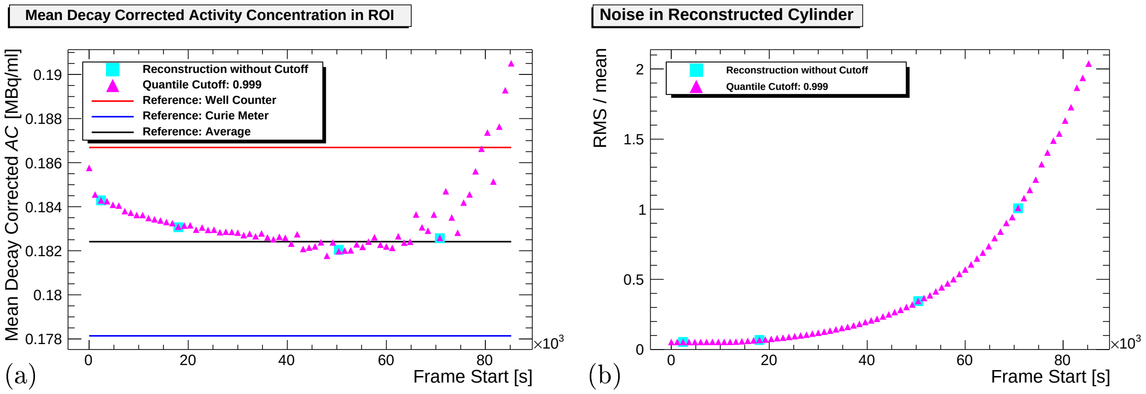

Figure 8.4: Stability of quantification and noise during a decay experiment covering the whole dynamic range. A good agreement is visible between the activity concentrations (AC) reconstructed with and without cutoff.

8.2.2.1 Image Analysis

In each reconstructed frame the activity in a Region of Interest (ROI) with a radius of 30 mm and a height of 113 mm is investigated. The mean intensity within this ROI is calculated to observe the stability of the reconstruction over time. In addition, the Root Mean Square (RMS) is calculated and divided by the mean. The relative RMS is used to investigate the level of noise.

8.2.2.2 Results

The stability over the whole dynamic range and the relative RMS in the reconstructed frames is depicted in Figure 8.4. The mean in Figure 8.4a show a small systematic decrease of about 2 % in the first 40×10^3 s. For a time after 60×10^3 s the mean increases drastically. This is over $9\,t_{1/2}$ after the start of the measurements. Here, only 0.1 % of the activity remains, which is about 0.18 MBq. The activity of the ^{176}Lu in the lutetium-yttrium oxyorthosilicate (LYSO) is estimated to be about 0.356 MBq, see Section 3.6. These decays of the ^{176}Lu introduces a constant background into the FOV. Most likely this background is scaled up by the decay correction and leads to the observed increase of the mean.

The analysis above in Section 8.1 shows a small change of the sensitivity within the first 10 min of a measurement due to a warm up of the DPC after the start of a measurement. Therefore, an exclusion of the first frame reduces the systematic decrease to about 1.1 % with a range of 0.002 MBq ml^{-1} compared to a minimum at 0.182 MBq ml^{-1}.

In Figure 8.4b the relative RMS illustrates the noise in the cylinder phantom. During the first 20×10^3 s the noise is constant below 10 %. For time points after 60×10^3 s, where the ^{176}Lu becomes relevant, the relative RMS increases above one. Therefore, the activity concentration in the homogeneous cylinder phantom is to low for an adequate reconstruction.

In Figure 8.4 a good agreement is visible between the reconstruction with the cutoff and reconstruction without the cutoff. The cutoff for the scatter simulations is necessary because otherwise the simulations were too slow. For example, a frame after 5 h=2.7 $t_{1/2}$ required about 112 s per round compared to about 67 s for a frame only 40 min=0.4 $t_{1/2}$ after the start of the measurement. In representative rounds the duration for the creation of photon pairs increased from 7.5 s to about 29 s for the frame at 0.4 $t_{1/2}$ and at 2.7 $t_{1/2}$, respectively. The tracking of the photons increased from 35.74 s to about 60 s for the same rounds. The last frame reconstructed without the cutoff starts about 19 h=10.8 $t_{1/2}$ and required 45 min per round. This is longer than a full simulation for the earlier frames.

8.2.2.3 Discussion

Overall the reconstructed mean activity concentration shows a good accuracy of the dynamic corrections leading to deviations between 1 % and 2 %. Similar results have been discussed for the comparison of the count rate corrections in Section 5.7. A typical plant measurements covers $6\,t_{1/2}$. The overall activity within the pot is typically lower than in this decay experiment and not distributed over the complete volume. Therefore, the relevant parameter is the activity concentration in the plant instead of the total activity. Therefore, it might be required to introduce a correction for ^{176}Lu into the reconstruction. An alternative approach is to omit the decay correction during the image reconstruction and consider the decay as well as the constant ^{176}Lu background in the data analysis.

The main challenge is the increase of the simulation duration for later frames. The main increase is observed within the source simulation, which might result from an internal evaluation of the activity distribution before it is passed to the tracking. The increased duration of the tracking of the photons is not yet understood.

Especially, the last frame without the cutoff is typically not included in a measurement. Here, the main difference between the four frames without the cutoff is an increasing RMS. This raises the question, if there is a dependency on the noise in the image. At this point it remains unclear, if the structure of a root system influence the simulation duration compared to the investigated homogeneous cylinder. The quantile of 99.9 % was chosen without a detailed investigation of all images or the effect on the image quality. This should especially be done for plant measurements. In a root system the hottest voxels might belong to an organ, which accumulates tracer. The application of a global cut off could therefore alter the biological interpretation. Therefore, alternative approaches should be investigated. For example, a Gaussian filter could be applied to average neighboring voxels. A more detailed investigation for measurements of plants will be done as soon as the climate chamber and the gas exchange system are operational in the new laboratory.

8.2.3 Signal-To-Noise with Noise-Equivalent Count Rates

Noise-equivalent count rates (NECRs) are defined as a quantity which is proportional to the signal-to-noise ratio [147]. Cherry et al. point out that this proportionality has been demonstrated for homogeneous cylinder phantoms [33]. Furthermore, NECR of specific phantoms are used for the performance characterisation evaluation of Positron Emission Tomography (PET) scanners [65, 148]. For *pheno*PET the NECR are calculated for the reconstruction of the small cylinder phantom analyzed in the previous section.

8.2.3.1 Method

The NECR are calculated according to

$$NECR = \frac{(T_{coin})^2}{T_{coin} + SE + VRR} \tag{8.1}$$

$$= \frac{(p - SE - VRR)^2}{p} \tag{8.2}$$

with the *true* coincidences T_{coin}, *prompt* coincidences p, the scatter estimates SE and the Variance Reduced Randoms VRR. These numbers are the sum over all Lines-of-Response

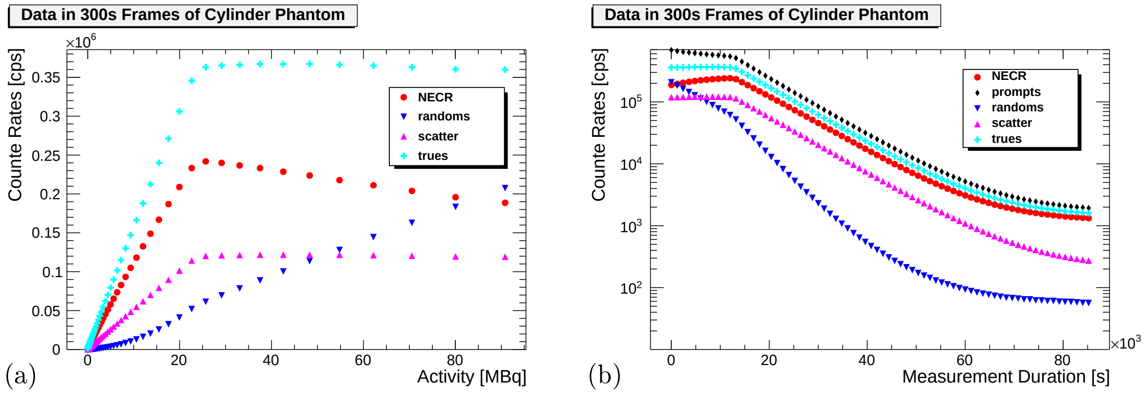

Figure 8.5: NECR for 300 s long frames of a homogeneous phantom with ^{18}F. Both curves show that the lowest noise is achieved, when the frame dropping stops. At this time the fraction of *true* coincidences within the *prompts* has its maximum.

(LOR) contributing to the FOV. The details of the measurement setup and image reconstruction to obtain scatter estimates are presented in Section 8.2.2. The scatter estimates are taken from the second iteration with the cutoff. The individual count rates are calculated for each reconstructed frame and plotted over the total activity provided by the Curie meter. In addition, the count rates are plotted over the measurement duration.

8.2.3.2 Results

The different count rates in the frames are presented in Figure 8.5. The dependency on the total activity in Figure 8.5a shows a peak NECR at about 25 MBq with about 240 kcps. For higher activities a small decrease is visible. At the same activity the *true* coincidences reach a maximum and stay at this value. The *random* coincidences raise over the complete measurement.

The explanation for these count rate behavior is the start of the frame dropping for activities above 25 MBq. This limits the maximum number of *true* coincidences because the number of hits recorded on the modules is kept constant. On the other hand the number of raw data frames is reduced to keep the data rate at a constant value. Therefore, the time difference between *singles* is decreased, which results in more *random* coincidences. This is better visible in Figure 8.5b. At about 15×10^3 s the *trues* reach a maximum value. The *prompt* and *random* coincidences continue to decrease during the measurement.

8.2.3.3 Discussion

The NECR show the best signal-to-noise ratio at an activity of about 25 MBq or 15×10^3 s after the start of the measurement. This is in agreement with the observation for the noise in Section 8.2.2. There, an increase is visible after 20×10^3 s. The count rates give a more precise time due to the scale of the graphs. The count rates in Figure 8.5b show that after 60×10^3 s the exponential decay is no longer prominent. Here, the constant count rate from the ^{176}Lu remains.

Cherry et al. point out that the NECR values depend on the actual phantom and the measurement parameters [33]. Furthermore, the results depend on the calculation of the NECR. For example, the calculation by Cherry et al. slightly differs from the one suggested by the NEMA standards [65, 148]. The NEMA standards use NECR to compare the performance of different scanners. These measurements use scatter phantoms, solid cylinders with specific dimensions and a hole for a rod source filled with ^{18}F. Therefore, a comparison of different results has to be done carefully.

For the PlanTIS system the peak NECR were observed at 32 MBq for a mice size phantom and 24 MBq for a rat size phantom [149]. For *pheno*PET the peak NECR is observed at 25 MBq due to the frame dropping. Therefore, the peak NECR will be observed around 25 MBq. The peak NECR for *pheno*PET are about 240 kcps. For PlanTIS the peak count rates 20 kcps and 7 kcps are reported for the mice and the rat size phantom, respectively [149]. The cylinder phantom has a larger scatter fraction due to its diameter of 80 mm compared to the 50 mm of the rat sized scatter phantom. Therefore, higher peak NECR can be expected for the two scatter phantoms.

Hallen et al. report a peak NECR of 407 kcps at 46 MBq for the rat size scatter phantom [150]. Their PET uses the same DPC technology to measure a smaller FOV with a height of 96.6 mm and a distance between the detector modules of 209.6 mm. The results of Hallen et al. support the expectation of a higher peak NECR for *pheno*PET. A higher maximum activity for *pheno*PET will require an adaptation of the data transfer.

8.3 Spatial Resolution

The spatial resolution of *pheno*PET was measured previously by Streun et al. with a hot rod phantom to be 1.6 mm [114]. The aim of redoing this measurement is to confirm this resolution with the improvements and newly introduced corrections. These changes also include a new version of the reconstruction software which also changed the calculation of the system matrix. The previous version of PET Reconstruction Software Toolkit (PRESTO) used a generic detector layer to rebin the results of LORs between individual crystals (see [121]). The current version of PRESTO omits this generic detector layer [122].

8.3.1 Phantom Preparation and Measurement

The measurement uses the same phantom as Streun et al. [114]. The hot rod phantom has a diameter of 74 mm and a rod length of 64 mm and is depicted in Figure 8.6. The fillable rods with specific diameter are separated by their diameter. Streun et al. filled the phantom with about 20 MBq of ^{18}F and measured for 60 min. These image were reconstructed with 52 iterations and corrected for Variance Reduced Randoms (VRR).

The ^{18}F is provided in a vial diluted in about 0.5 ml water. The sample is filled into a volumetric flask and mixed with about 40 ml of water by a magnetic stir. A sample is taken out to determine the activity concentration with a Curie meter. The activity is filled into a syringe (60 ml). It is slowly injected into the phantom with a thin and long needle (∅0.9 mm), 70 mm) starting from the bottom. Here, all rods are connected and thus the amount of air bubbles within the rods is minimized.

The phantom is placed on the same Polyvinyl chloride (PVC) mount as the cylinder phantom with the height adopted to the center of the FOV. The fixation to the PVC is achieved with a hole in the socket and adhesive tape. At the start of the measurement the activity is estimated to about 37.7 MBq.

The attenuation map is acquired a few days after the emission scan for 15 h. This measurement is reconstructed with one scatter iteration containing 1000 simulation rounds with both multiplexing options set to two. The small cylinder phantom is used to calculate a scaling factor for the attenuation map of 1.59. This factor is applied to the attenuation map before the scatter simulation. The phantom needs to be removed from the FOV to mount the ^{68}Ge

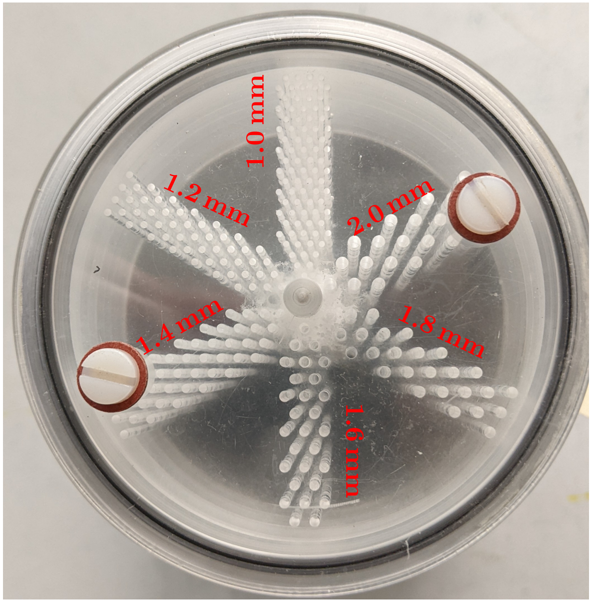

Figure 8.6: Hot rod phantom. The diameters of the different rods are given. Two neighboring rods in each array are separated by their diameter.

rod source. This should only cause a negligible effect due to the fixation of the phantom and the positioning system.

The emission reconstruction is done with a frame of 60 min with 52 iterations. The voxel sizes and the FOV are changed for this measurement. The voxel size in the axial plane is reduced to 0.4 mm from the default value of 0.9 mm. Therefore, the radius of the FOV is halved to 45 mm. This keeps the size of the system matrix manageable for the available Random-Access Memory (RAM). The scatter correction is done with two iterations, each with 400 rounds of simulation. A calibration to $\mathrm{MBq\,ml^{-1}}$ is not applied.

8.3.2 Results

The reconstructed image is defined by 1.82×10^9 *prompts* and 1.19×10^8 *random* coincidences. The second scatter iteration contains 32.7 % of scattered coincidences, including the normalization for the simulation. This results in about 1.14×10^9 *true* coincidences.

In Figure 8.7 a single slice of the hot rod phantom is presented. After 15 iterations, see Figure 8.7a, a clear separation of the 1.8 mm rods is possible. The 1.6 mm rods are much more smeared out and thus harder to distinguished. In Figure 8.7b the 1.6 mm rods can be clearly distinguished after 52 iterations.

8.3.3 Discussion

The spatial resolution of 1.6 mm reported by Streun et al. in [114] is confirmed. This requires 52 iterations for both measurements. At the moment reconstructions are done with 15 iterations. This case shows a lower spatial resolution with a good separation at 1.8 mm.

The first generation system PlanTIS has a spatial resolution between 1.2 mm and 1.4 mm with Derenzo phantom filled with ^{18}F [151]. A measurement with another phantom and ^{11}C results in a resolution of 2.4 mm [19]. They explain the difficult separation of 1.6 mm rods by the larger energy of the ^{11}C decay, which leads to an increased positron range.

In [33, 152] different contributions to the spatial resolution are discussed. The dominant effect is the resolution of the detector crystals which are a bit broader for PlanTIS with 2 mm side width. On the other hand PlanTIS has the advantage of a dual layer system with depth of interaction information and a one-to-one coupling between crystals and Photo Multiplier

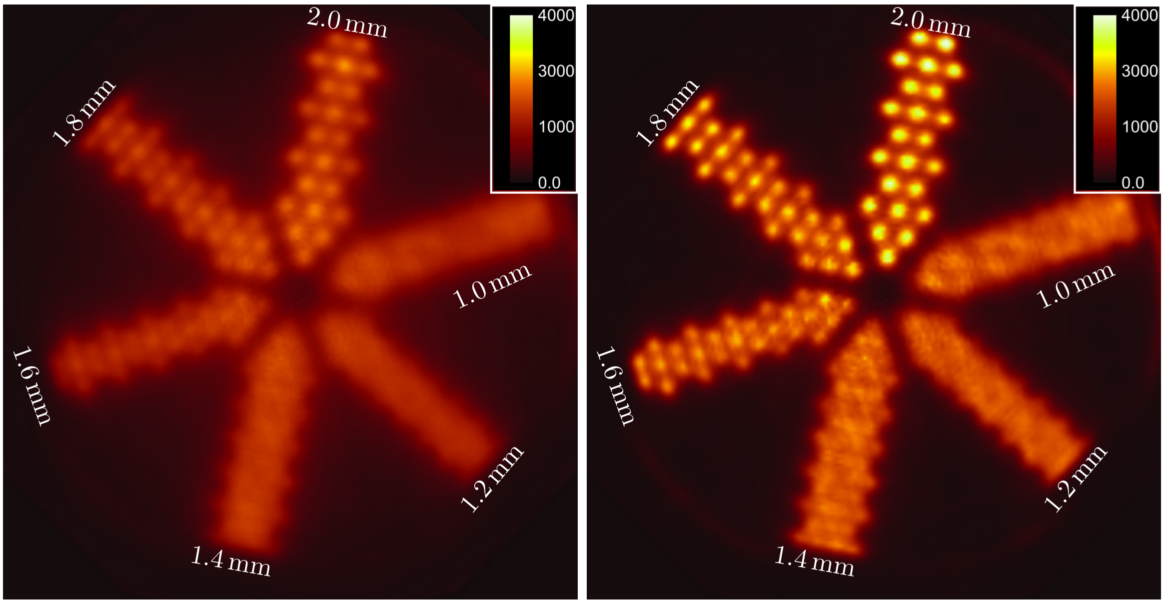

(a) 15 iterations. (b) 52 iterations.

Figure 8.7: Spatial Resolution after different iteration steps illustrated by the same slice of 60 min. All corrections except the calibration are taken into account. The rod diameters are given.

Tube (PMT) channels. For *pheno*PET the light is spread on up to four SiPM. Here, different crystal efficiencies are observed, see Chapter 6. Sensitivities of 0.5 and 1.5 on neighbouring crystals might hint towards issues with the crystal identification, which might further limit the spatial resolution. The acollinarity of the annihilation is the second physical limit, which depends on the diameter of the system. Here, the radial FOV of *pheno*PET is about twice the one of PlanTIS with 101 mm [19]. Thus the spatial resolution of *pheno*PET is degraded.

In [152] two further aspects are mentioned, that might have an influence on the spatial resolution. The first aspect is the sampling error, which results from different numbers of LORs passing through each voxel. The second aspect is the depth of interaction, which alters the effective dimension of detectors with radial position of a LOR. Both effects introduce a radial dependency on the spatial resolution and are not yet investigated in more detail for *pheno*PET.

For *pheno*PET the improved system and the additional corrections are not altering the spatial resolution in comparison to Streun et al.. Here, the optimizations of *pheno*PET discussed in Section 7.5.4 might lead to further improvements.

8.4 Summary

The presented investigations prove an improved stability of the detector temperature by the newly introduced warm up mode. Only a measurement with a very high activity shows a visible decrease on the count rates within the first 10 min. This can be reduced in the measurement of a plant by starting the measurement during the labeling with [^{11}C]CO$_2$. The robustness of the dynamic corrections is well below 2 % for a homogeneous cylinder phantom covering the full dynamic range. The robustness reaches 1.1 %, if the first frame is excluded, which is degraded by the increasing temperature. The spatial resolution of *pheno*PET is about 1.8 mm for a typical reconstruction with 15 iterations. A better resolution of 1.6 mm is possible, if the number of iterations is increased to 52. Here, the main challenge is the required computational effort for the reconstruction.

The main challenge is the dynamic scatter correction. The investigations show a dependency on the noise in the image. Therefore, a reconstruction protocol needs to be developed for plant measurements. This will contain some kind of filtering before a scatter simulation is performed. Here, plant measurements are lacking for the optimization of the different parameters.

Chapter 9

Conclusion and Outlook

In this thesis all corrections required for quantitative image reconstruction with *pheno*PET have been implemented and the possible performance has been investigated. In addition, several improvements of the performance have been achieved. These corrections and improvements have been validated with simulations and measurements of phantoms. An optimization for plant measurements requires a fully working and understood climate chamber. This will be achieved in the near future.

The extensive use of *pheno*PET revealed a few technical problems. Those were solved in cooperation with the development team at the Central Institute of Engineering, Electronics and Analytics (ZEA), Electronic Systems (ZEA-2). This increased the dynamic range as well as the stability and the overall performance of *pheno*PET.

Emission and transmission measurements are done with the same settings. Single photon events are obtained from a clustering window on each tile with a clustering window of 5 ns. The coincidence sorting is restricted to *singles* in the energy window from 348 keV to 652 keV. Here, it has to be noted that energy calibration of *pheno*PET does not consider the saturation of the Silicon photomultipliers (SiPM), which results in an actual lower energy cut of about 310 keV. The consideration of this saturation by the calibration would simplify the interpretation of raw data and simplify comparisons with other measurements. The coincidence sorting has been changed to a multi-window sorter with a coincidence window of 2.5 ns. The warm up of the detectors leads to a small decrease of the sensitivity in the first 10 min. Therefore, especially measurements with high activities should be started before the time of interest. For plant measurements this can be realized during the application of the tracer.

The emission measurement is limited by the available memory on the detector modules and the data transfer from *pheno*PET to disc over USB 3.0. Here, the frame dropping as part of the count rate corrections allows for a maximum activity of about 100 MBq in a centered cylinder phantom. The best noise-equivalent count rate (NECR) is achieved for an activity of about 25 MBq, when the frame dropping is not necessary and all data are saved. The maximum frame dropping discards up to 75 % of the data packages. For the maximum activity each detector module shows a dead time below 10 %. The dead time is still in the linear region and does not show any saturation effects. A global correction factor accounts for a minor deviation of about 3 %. This might result from pile-up caused by a difference between coincidence and clustering window. A reduction of the clustering window to the length of the coincidence window should reduce this effect. At the same time, a further reduction of the coincidence window size should be investigated, for example 2 ns. A further possibility is the improvement of the clustering algorithm for high count rates by including the spatial information of hits on a *tile* as further criteria.

The component-based normalization with a rotating rod source removes the main radial bias in the Field-of-View (FOV). The comparison of two normalizations showed a good stability over one and a half year. The normalization leaves an axial bias in the images. This bias is reduced well below 2.5 % by the correction of scattered coincidences for a small cylinder phantom. This cylinder has a similar size as pots used in current plant studies with the older PlanTIS system. For a cylinder phantom covering the majority of the FOV an axial bias of 12 % remains. This bias should be further investigated.

The scatter correction is done in two iteration steps. The required simulation depends on the size of the phantom. For the small cylinder phantom images can be reconstructed with a duration of about 30 min per scatter iteration. Each scatter simulation contains 12×10^8 primary photon pairs with a multiplexed tracking and a multiplexed detector simulation. This should also be sufficient for pots in a similar size. For the large cylinder a simulation duration of several hours is required to achieve a similar convergence. The scaling of scatter estimates towards the measured data requires a separate normalization. A reduction of *scattered* coincidences can be achieved by replacing the aluminum shielding in the plant port with a less dense material. Here, a similar protection to the extruded polystyrene (XPS) structure beneath the shielding is important.

The attenuation map for the scatter correction and attenuation correction is obtained from a transmission measurement with a rotating rod source. Here, a 30 min measurement with an activity of 2.8 MBq is sufficient. The reconstruction requires a scatter correction with one scatter iteration. The required simulation takes several hours. For the scatter simulation, the attenuation map is scaled by an object depending factor. This scaling factor is obtained from the measurement of a water filled phantom with the same dimensions. The blank data are the same as for the normalization.

After the full pipeline and laboratory are operational the next measurements should be used to optimize the measurement and reconstruction protocols for plant measurements. Here, an important aspect is the required statistics and therefore simulation duration for each scatter simulation. A further challenge is the observed longer simulation duration for higher noise in a homogeneous cylinder. The first step is to investigate a suitable filtering or threshold approach to limit the simulation durations without introducing a bias. Furthermore, a detailed investigation on the measurable activity concentration for a dynamic study should be done. This could also be used to study a possible dependency of the required simulation statistics on the convergence of the reconstructed activity distribution. The current simulation durations are too long for a routine operation with three measurements a day. The three reconstructions without any scatter simulation require about half a day. Here, further concepts and improvements for the scatter correction will be developed and implemented in the near future. This includes more computational power.

The overall calibration factors for the emission images differ below 5 % between two measurements with measured attenuation maps, that are corrected for scatter. The reference measurements for the calibration showed a maximum deviation of 4.7 %. In a 24 h decay experiment with ^{18}F differences below 1.1 % have been observed in the reconstructed images.

The spatial resolution has been validated with a hot rod phantom. In a typical plant measurement a spatial resolution of 1.8 mm is achieved. Further iteration steps in the reconstruction allow a good separation of 1.6 mm rods.

In conclusion *pheno*PET is able to measure plants in pots already established for PlanTIS with a higher sensitivity. In contrast to PlanTIS attenuation maps can be acquired and applied during the reconstruction instead of a analytic cylinder of water. A further improvement is the possibility to correct for *scattered* coincidences. At the moment the functionality and reliability of the climate chamber and the gas exchange system for the application of [^{11}C]CO$_2$ are validated. The next steps will focus on establishment of routine protocols for measurements including the number of attenuation measurements and the statistics for each scatter iteration. Furthermore, the interaction between *pheno*PET and the climate chamber can be addressed as soon as the climate chamber is fully operational. These new measurements will provide valuable insight on the operation stability and usability. The major goal are more plant measurements. Those should include the establishment of new plant and soil systems as well as further treatments. In the long term perspective, this will allow more complex studies, which will lead to further insights in plant science.

Bibliography

[1] Fabio Fiorani and Ulrich Schurr. “Future Scenarios for Plant Phenotyping”. In: *Annual Review of Plant Biology* 64.1 (2013). PMID: 23451789, pp. 267–291. eprint: `https://doi.org/10.1146/annurev-arplant-050312-120137`.

[2] J. MOORBY, M. EBERT, and N. T. S. EVANS. “The Translocation of 11C-labelled Photosynthate in the Soybean”. In: *Journal of Experimental Botany* 14.2 (May 1963), pp. 210–220. ISSN: 0022-0957. eprint: `https://academic.oup.com/jxb/article-pdf/14/2/210/1385558/14-2-210.pdf`.

[3] Tamikazu Kume, Shinpei Matsuhashi, and Masamitsu Shimazu. “Uptake and transport of positron-emitting tracer in plants”. In: *Applied Radiation and Isotopes* 48.8 (Mar. 1997).

[4] Siegfried Jahnke et al. “Combined MRI-PET dissects dynamic changes in plant structures and functions”. In: *The Plant Journal* 59.4 (Aug. 2009), pp. 634–644.

[5] Abhijit A. Karve et al. “In vivo quantitative imaging of photoassimilate transport dynamics and allocation in large plants using a commercial positron emission tomography (PET) scanner”. eng. In: *BMC plant biology* 15 (Nov. 2015). 26552889[pmid], pp. 273–273. ISSN: 1471-2229.

[6] Michiel Hubeau and Kathy Steppe. “Plant-PET Scans: In Vivo Mapping of Xylem and Phloem Functioning”. In: *Trends in Plant Science* 20.10 (Oct. 2015), pp. 676–685. ISSN: 1360-1385.

[7] T. M. Nakanishi et al. “Water movement in a plant sample by neutron beam analysis as well as positron emission tracer imaging system”. In: *Journal of Radioanalytical and Nuclear Chemistry* 255.1 (Jan. 2003), pp. 149–153. ISSN: 1588-2780.

[8] Etsuko Hattori et al. “Incorporation and translocation of 2-deoxy-2-[(18)F]fluoro-D-glucose in Sorghum bicolor (L.) Moench monitored using a planar positron imaging system”. In: *Planta* 227.5 (Apr. 2008), pp. 1181–1186. ISSN: 0032-0935.

[9] Shoichiro Kiyomiya et al. “Real Time Visualization of 13N-Translocation in Rice under Different Environmental Conditions Using Positron Emitting Tracer Imaging System”. In: *Plant Physiology* 125.4 (2001), pp. 1743–1753. ISSN: 0032-0889. eprint: `http://www.plantphysiol.org/content/125/4/1743.full.pdf`.

[10] Horst Marschner. *Mineral nutrition of higher plants*. London San Diego: Academic Press, 1995. ISBN: 9780124735422.

[11] Takashi Tsukamoto et al. “52Fe Translocation in Barley as Monitored by a Positron-Emitting Tracer Imaging System (PETIS): Evidence for the Direct Translocation of Fe from Roots to Young Leaves via Phloem”. In: *Plant and Cell Physiology* 50.1 (Dec. 2008), pp. 48–57. ISSN: 0032-0781. eprint: `https://academic.oup.com/pcp/article-pdf/50/1/48/17111657/pcn192.pdf`.

[12] Gihan P. Ruwanpathirana et al. “Continuous monitoring of plant sodium transport dynamics using clinical PET”. In: *Plant Methods* 17.1 (Jan. 2021), p. 8. ISSN: 1746-4811.

[13] David L. Alexoff et al. “PET imaging of thin objects: measuring the effects of positron range and partial-volume averaging in the leaf of Nicotiana tabacum”. In: *Nuclear Medicine and Biology* 38.2 (2011), pp. 191–200. ISSN: 0969-8051.

[14] Denisa Partelová et al. “Imaging and analysis of thin structures using positron emission tomography: Thin phantoms and in vivo tobacco leaves study”. In: *Applied Radiation and Isotopes* 115 (2016), pp. 87–96. ISSN: 0969-8043.

[15] Alexander K. Converse et al. “Mathematical modeling of positron emission tomography (PET) data to assess radiofluoride transport in living plants following petiolar administration”. In: *Plant Methods* 11.1 (Mar. 2015), p. 18. ISSN: 1746-4811.

[16] Qiang Wang et al. “A dedicated high resolution PET imager for plant sciences”. In: *Physics in Medicine and Biology* 59 (Jan. 2014).

[17] Yu-Fen Chang et al. “Applying a Modular PET System to Investigate Bioremediation of Subsurface Contamination: A Proof-of-Principle Study”. In: *Journal of Physics: Conference Series* 1120 (Nov. 2018), p. 012077.

[18] Keisuke Kurita et al. “Fruit PET: 3-D imaging of carbon distribution in fruit using OpenPET”. In: *Nuclear Instruments and Methods in Physics Research Section A: Accelerators, Spectrometers, Detectors and Associated Equipment* (2019). ISSN: 0168-9002.

[19] S Beer et al. “Design and initial performance of PlanTIS: a high-resolution positron emission tomograph for plants”. In: *Physics in Medicine and Biology* 55.3 (Jan. 2010), pp. 635–646.

[20] V. De Schepper et al. “11C-PET imaging reveals transport dynamics and sectorial plasticity of oak phloem after girdling”. In: *Frontiers in Plant Physiology* 4.200 (2013), pp. 1–9. ISSN: 1664-462X.

[21] Ralf Metzner et al. “In vivo imaging and quantification of carbon tracer dynamics in nodulated root systems of pea plants”. In: *bioRxiv* (June 25, 2021). eprint: `https://www.biorxiv.org/content/early/2021/06/25/2021.06.23.449643.full.pdf`.

[22] Sina R. Schultes et al. “Does the maize rhizosphere microbialcommunity show spatial variation in response toroot carbon allocation?” In: *6th Joint Conference of DGBM & VAAM*. Leipzig, Mar. 10, 2020.

[23] Peter E. H. Minchin and Michael R. Thorpe. “Using the short-lived isotope ^{11}C in mechanistic studies of photosynthate transport”. In: *Functional Plant Biology* 30.8 (2003), pp. 831–841.

[24] J. Bühler et al. “Analytical model for long-distance tracer-transport in plants”. In: *Journal of theoretical biology* 270 (2011), pp. 70–79. ISSN: 0022-5193.

[25] Jonas Bühler, Eric von Lieres, and Gregor Huber. “Model-Based Design of Long-Distance Tracer Transport Experiments in Plants”. In: *Frontiers in Functional Plant Ecology* 9 (2018), p. 773. ISSN: 1664-462X.

[26] Hans Lambers, F. Stuart ChapinIII, and Thijs L. Pons. *Plant Physiological Ecology*. Springer, New York, NY, 2008. ISBN: 978-0-387-78341-3. eprint: `https://link.springer.com/book/10.1007%2F978-0-387-78341-3`.

[27] Bahi Bakeer et al. “On the characterisation of structure and properties of sorghum stalks”. In: *Ain Shams Engineering Journal* 4 (June 2013), pp. 265–271.

[28] G Skubisz, TI Kravtsova, and LP Velikanov. “Analysis of the strength properties of pea stems”. In: *International agrophysics* 21.2 (2007), p. 189.

[29] Siegfried Jahnke et al. “Distribution of photoassimilates in the pea plant: chronology of events in non-fertilized ovaries and effects of gibberellic acid”. In: *Planta* 180.1 (Dec. 1989), pp. 53–60. ISSN: 1432-2048.

[30] Edna L. Johnson. “SUSCEPTIBILITY OF SEVENTY SPECIES OF FLOWERING PLANTS TO X-RADIATION”. In: *Plant Physiology* 11.2 (1936), pp. 319–342. ISSN: 0032-0889. eprint: `http://www.plantphysiol.org/content/11/2/319.full.pdf`.

[31] F.A.L. Clowes and E.J. Hall. “The quiescent centre in root meristems of Vicia faba and its behaviour after acute x-irradiation and chronic gamma irradiation”. In: *Radiation Botany* 3.1 (1963), pp. 45–53. ISSN: 0033-7560.

[32] Sebastian R. G. A. Blaser, Steffen Schlüter, and Doris Vetterlein. “How much is too much?—Influence of X-ray dose on root growth of faba bean (Vicia faba) and barley (Hordeum vulgare)”. In: *PLOS ONE* 13.3 (Mar. 2018), pp. 1–18.

[33] Simon R. Cherry, James A. Sorenson, and Michael E. Phelps. *Physics in Nuclear Medicine*. Fourth Edition. Philadelphia: W.B. Saunders, 2012, pp. 481–488. ISBN: 978-1-4160-5198-5.

[34] Dale L Bailey et al. *Positron Emission Tomography*. Springer London, 2005. ISBN: 978-1-85233-798-8.

[35] Magnus Dahlborn Simon R. Cherry. *PET. Physics, Instrumentation, and Scanners*. Ed. by Michael E. Phelps. 1st ed. Springer-Verlag New York, 2006. ISBN: 978-0-387-34946-6.

[36] Demtröder, W. *Experimentalphysik 4: Kern-, Teilchen- und Astrophysik*. Wolfgang Demtröder. Springer, 2014. ISBN: 9783642214769.

[37] Robley D. Evans. *The Atomic Nucleus*. This massive book was written by an MIT professor for a 2-semester course in Nuclear Physics in 1955 and covers a great deal of material! Fla: TATA McGraw-Hill Publishing Company LTD., 1955.

[38] E. Fermi. “Versuch einer Theorie der β-Strahlen. I”. In: *Zeitschrift fur Physik* 88 (Mar. 1934), pp. 161–177.

[39] Knoll, G.F. *Radiation Detection and Measurement*. Fourth. John Wiley & Sons, 2010. ISBN: 9780470131480.

[40] M.J. Berger et al. *ESTAR, PSTAR, and ASTAR: Computer Programs for Calculating Stopping-Power and Range Tables for Electrons, Protons, and Helium Ions (version 2.0.1)*. National Institute of Standards and Technology, Gaithersburg, MD. July 31, 2017. URL: `http://physics.nist.gov/Star` (visited on 11/20/2020).

[41] B. Jasińska et al. “Human Tissues Investigation Using PALS Technique”. In: *Acta Physica Polonica B* 48.10 (2017), p. 1737. ISSN: 1509-5770.

[42] P Moskal et al. “Feasibility study of the positronium imaging with the J-PET tomograph”. In: *Physics in Medicine & Biology* 64.5 (Mar. 2019), p. 055017.

[43] M.J. Berger et al. *XCOM: Photon Cross Section Database (version 1.5)*. National Institute of Standards and Technology, Gaithersburg, MD. Nov. 30, 2010. URL: `http://physics.nist.gov/xcom` (visited on 11/20/2020).

[44] J H Hubbell. “Review of photon interaction cross section data in the medical and biological context”. In: *Physics in Medicine and Biology* 44.1 (Jan. 1999), R1–R22.

[45] Leonard I. Wiebe. “Radionuclides, radiotracers and radiopharmaceuticals for in vivo diagnosis”. In: *Radiation Physics and Chemistry (1977)* 24.3 (1984). Special Issue Radiation and Medicine, pp. 365–372. ISSN: 0146-5724.

[46] Laboratoire National Henri Becquerel. *Tables of Radionucleides* ^{11}C. Nov. 3, 2011. URL: `http://www.nucleide.org/DDEP_WG/Nuclides/C-11_tables.pdf` (visited on 07/22/2020).

[47] Laboratoire National Henri Becquerel. *Tables of Radionucleides* ^{18}F. Aug. 29, 2014. URL: `http://www.nucleide.org/DDEP_WG/Nuclides/F-18_tables.pdf` (visited on 07/22/2020).

[48] Laboratoire National Henri Becquerel. *Tables of Radionucleides* ^{68}Ge. Feb. 27, 2012. URL: `http://www.nucleide.org/DDEP_WG/Nuclides/Ge-68_tables.pdf` (visited on 09/03/2019).

[49] Laboratoire National Henri Becquerel. *Tables of Radionucleides* ^{68}Ga. July 4, 2012. URL: `http://www.nucleide.org/DDEP_WG/Nuclides/Ga-68_tables.pdf` (visited on 07/22/2020).

[50] M.S. Basunia. *Nuclear Data Sheets 107, 791.* 2006. URL: `https://www.nndc.bnl.gov/nudat2/`.

[51] Paul Lecoq, Alexander Gektin, and Mikhail Korzhik. *Inorganic Scintillators for Detector Systems.* Jan. 2017. ISBN: 978-3-319-45521-1.

[52] D. W. Cooke et al. “Crystal growth and optical characterization of cerium-doped Lu1.8Y0.2SiO5”. In: *Journal of Applied Physics* 88.12 (2000), pp. 7360–7362. eprint: `https://doi.org/10.1063/1.1328775`.

[53] T. Kimble, M. Chou, and B. H. T. Chai. “Scintillation properties of LYSO crystals”. In: *2002 IEEE Nuclear Science Symposium Conference Record.* Vol. 3. Nov. 2002, 1434–1437 vol.3.

[54] A. Nassalski et al. “Comparative Study of Scintillators for PET/CT Detectors”. In: *IEEE Transactions on Nuclear Science* 54.1 (Feb. 2007), pp. 3–10. ISSN: 1558-1578.

[55] K. Kobayashi A. Ghassemi K. Sato. *Technical Note: MPPC.* Tech. rep. Hamamatsu.

[56] K. G. McKay. “Avalanche Breakdown in Silicon”. In: *Phys. Rev.* 94 (4 May 1954), pp. 877–884.

[57] C. Y. Chang, S. S. Chiu, and L. P. Hsu. “Temperature dependence of breakdown voltage in silicon abrupt p-n junctions”. In: *IEEE Transactions on Electron Devices* 18.6 (1971), pp. 391–393.

[58] A. Kaplan. “Correction of SiPM temperature dependencies”. In: *Nuclear Instruments and Methods in Physics Research Section A: Accelerators, Spectrometers, Detectors and Associated Equipment* 610.1 (2009). New Developments In Photodetection NDIP08, pp. 114–117. ISSN: 0168-9002.

[59] F. Licciulli and C. Marzocca. “An Active Compensation System for the Temperature Dependence of SiPM Gain”. In: *IEEE Transactions on Nuclear Science* 62.1 (Feb. 2015), pp. 228–235. ISSN: 1558-1578.

[60] Philips Digital Photon Counting. *Digital Photon Counter Breakthrough in fully digital photon counting.* Ed. by Philips Digital Photon Counting.

[61] Philips Digital Photon Counting. *Module-TEK. User Manual.* 1.02. 2016.

[62] W. Bothe and W. Kolhörster. “Das Wesen der Höhenstrahlung”. In: *Zeitschrift fur Physik* 56.11-12 (Nov. 1929), pp. 751–777.

[63] Jared Strydhorst and Irène Buvat. “Redesign of the GATE PET coincidence sorter”. In: *Physics in Medicine & Biology* 61.18 (2016), N522.

[64] OpenGATE Collaboration. *GATE Documentation. Imaging Application: 3. Digitizer and Readout Parameters.* Nov. 27, 2019.

[65] N. Belcari et al. *NEMA NU 4 Performance Measurement of Small animal Positron Emission Tomographs.* National Electrical Manufacturers Association, 2008.

[66] Kenneth Lange, Richard Carson, et al. “EM reconstruction algorithms for emission and transmission tomography”. In: *J Comput Assist Tomogr* 8.2 (1984), pp. 306–16.

[67] L. A. Shepp and Y. Vardi. “Maximum Likelihood Reconstruction for Emission Tomography”. In: *IEEE Transactions on Medical Imaging* 1.2 (Oct. 1982), pp. 113–122. ISSN: 1558-254X.

[68] E. S. Chornoboy et al. “An evaluation of maximum likelihood reconstruction for SPECT”. In: *IEEE Transactions on Medical Imaging* 9.1 (Mar. 1990), pp. 99–110. ISSN: 1558-254X.

[69] Didier Benoit et al. “Optimized MLAA for quantitative non-TOF PET/MR of the brain”. In: *Physics in Medicine and Biology* 61.24 (Dec. 2016), pp. 8854–8874.

[70] Mehmet Yavuz and Jeffrey A. Fessler. “New statistical models for randoms-precorrected PET scans”. In: *Information Processing in Medical Imaging.* Ed. by James Duncan and Gene Gindi. Berlin, Heidelberg: Springer Berlin Heidelberg, 1997, pp. 190–203. ISBN: 978-3-540-69070-2.

[71] Dan J Kadrmas. “LOR-OSEM: statistical PET reconstruction from raw line-of-response histograms”. In: *Physics in Medicine and Biology* 49.20 (Sept. 2004), pp. 4731–4744.

[72] J. Nuyts et al. “Simultaneous maximum a posteriori reconstruction of attenuation and activity distributions from emission sinograms”. In: *IEEE Transactions on Medical Imaging* 18.5 (May 1999), pp. 393–403. ISSN: 1558-254X.

[73] A. Rezaei, M. Defrise, and J. Nuyts. “ML-Reconstruction for TOF-PET With Simultaneous Estimation of the Attenuation Factors”. In: *IEEE Transactions on Medical Imaging* 33.7 (2014), pp. 1563–1572.

[74] H. M. Hudson and R. S. Larkin. “Accelerated image reconstruction using ordered subsets of projection data”. In: *IEEE Transactions on Medical Imaging* 13.4 (Dec. 1994), pp. 601–609. ISSN: 1558-254X.

[75] V. J. Sank et al. “Performance Evaluation and Calibration of the Neuro-PET Scanner”. In: *IEEE Transactions on Nuclear Science* 30.1 (1983), pp. 636–639.

[76] B. E. Cooke et al. “Performance Figures and Images from the Therascan 3128 Positron Emission Tomograph”. In: *IEEE Transactions on Nuclear Science* 31.1 (1984), pp. 640–644.

[77] S. E. Derenzo et al. “The Donner 280-Crystal High Resolution Positron Tomograph”. In: *IEEE Transactions on Nuclear Science* 26.2 (Apr. 1979), pp. 2790–2793. ISSN: 1558-1578.

[78] C. W. Williams, M. C. Crabtree, and S. G. Burgiss. “Design and Performance Characteristics of a Positron Emission Computed Axial Tomograph–ECAT®-II”. In: *IEEE Transactions on Nuclear Science* 26.1 (1979), pp. 619–627.

[79] L. G. Byars et al. “Variance reduction on randoms from coincidence histograms for the HRRT”. In: *Proc. IEEE Nuclear Science Symp. Conf. Record.* Vol. 5. Oct. 2005, pp. 2622–2626.

[80] Ramsey Derek Badawi et al. “Randoms variance reduction in 3D PET.” In: *Physics in medicine and biology* 44 4 (1999), pp. 941–54.

[81] Michael E. Casey and Edward J. Hoffman. “Quantitation in Positron Emission Computed Tomography: 7. A Technique to Reduce Noise in Accidental Coincidence Measurements and Coincidence Efficiency Calibration”. In: *Journal of Computer Assisted Tomography* 10 (5 1986).

[82] Shoko KINOUCHI et al. “New Component-Based Normalization Method to Correct PET System Models”. In: *Medical Imaging Technology* 29.5 (2011), pp. 239–249.

[83] D. Hogg et al. “Maximum-likelihood estimation of normalisation factors for PET”. In: *Proc. IEEE Nuclear Science Symp. Conf. Record (Cat. No.01CH37310)*. Vol. 4. 2001, pp. 2065–2069.

[84] R D Badawi, M A Lodge, and P K Marsden. “Algorithms for calculating detector efficiency normalization coefficients for true coincidences in 3D PET”. In: *Physics in Medicine and Biology* 43.1 (1998), p. 189.

[85] R. D. Badawi and P. K. Marsden. “Developments in component-based normalization for 3D PET”. In: *Physics in Medicine and Biology* 44.2 (1999), p. 571.

[86] Shoaib Usman and Amol Patil. “Radiation detector deadtime and pile up: A review of the status of science”. In: *Nuclear Engineering and Technology* 50.7 (2018), pp. 1006–1016. ISSN: 1738-5733.

[87] Z. H. Cho et al. “Performance and Evaluation of the Circular Ring Transverse Axial Positron Camera (CRTAPC)”. In: *IEEE Transactions on Nuclear Science* 24.1 (Feb. 1977), pp. 532–543. ISSN: 1558-1578.

[88] T. Beyer et al. “The use of X-ray CT for attenuation correction of PET data”. In: *Proceedings of 1994 IEEE Nuclear Science Symposium - NSS’94*. Vol. 4. 1994, 1573–1577 vol.4.

[89] M Phelps et al. “Application of annihilation coincidence detection to transaxial reconstruction tomography.” In: *Journal of nuclear medicine : official publication, Society of Nuclear Medicine* 16 (Apr. 1975), pp. 210–24.

[90] S. E. Derenzo et al. “Imaging Properties of a Positron Tomograph with 280 Bgo Crystals”. In: *IEEE Transactions on Nuclear Science* 28.1 (1981), pp. 81–89.

[91] H. Iida et al. “Design and evaluation of HEADTOME-IV, a whole-body positron emission tomograph”. In: *IEEE Transactions on Nuclear Science* 36.1 (Feb. 1989), pp. 1006–1010. ISSN: 1558-1578.

[92] Ron Huesman et al. “Orbiting transmission source for positron tomography”. In: *Nuclear Science, IEEE Transactions on* 35 (Mar. 1988), pp. 735–739.

[93] J. A. Fessler. “Hybrid Poisson/polynomial objective functions for tomographic image reconstruction from transmission scans”. In: *IEEE Transactions on Image Processing* 4.10 (Oct. 1995), pp. 1439–1450. ISSN: 1941-0042.

[94] Elena Rota Kops et al. “Comparison of Template-Based Versus CT-Based Attenuation Correction for Hybrid MR/PET Scanners”. In: *Nuclear Science, IEEE Transactions on* 62 (Oct. 2015), pp. 2115–2121.

[95] J. S. Karp et al. “Continuous-slice PENN-PET: a positron tomograph with volume imaging capability”. In: *J Nucl Med* 31.5 (May 1990), pp. 617–627.

[96] S. R. Cherry and Sung-Cheng Huang. “Effects of scatter on model parameter estimates in 3D PET studies of the human brain”. In: *IEEE Transactions on Nuclear Science* 42.4 (1995), pp. 1174–1179.

[97] J. M. Ollinger and G. C. Johns. “Model-based Scatter Correction For Fully 3D PET”. In: *1993 IEEE Conference Record Nuclear Science Symposium and Medical Imaging Conference*. 1993, pp. 1264–1268.

[98] A. Werling et al. “Fast implementation of the single scatter simulation algorithm and its use in iterative image reconstruction of PET data”. In: *1999 IEEE Nuclear Science Symposium. Conference Record. 1999 Nuclear Science Symposium and Medical Imaging Conference (Cat. No.99CH37019)*. Vol. 3. Oct. 1999, 1158–1162 vol.3.

[99] C. C. Watson. “New, faster, image-based scatter correction for 3D PET”. In: *IEEE Transactions on Nuclear Science* 47.4 (Aug. 2000), pp. 1587–1594. ISSN: 1558-1578.

[100] C. C. Watson, J. Hu, and C. Zhou. “Extension of the SSS PET scatter correction algorithm to include double scatter”. In: *2018 IEEE Nuclear Science Symposium and Medical Imaging Conference Proceedings (NSS/MIC)*. Nov. 2018, pp. 1–4.

[101] Bo Ma et al. “Scatter Correction based on GPU-accelerated Full Monte Carlo Simulation for Brain PET/MRI”. In: *IEEE transactions on medical imaging* 39.1 (2020), pp. 140–151. ISSN: 1558-254X.

[102] C. S. Levin, M. Dahlbom, and E. J. Hoffman. “A Monte Carlo correction for the effect of Compton scattering in 3-D PET brain imaging”. In: *IEEE Transactions on Nuclear Science* 42.4 (Aug. 1995), pp. 1181–1185. ISSN: 1558-1578.

[103] C. H. Holdsworth et al. “Investigation of accelerated Monte Carlo techniques for PET simulation and 3D PET scatter correction”. In: *IEEE Transactions on Nuclear Science* 48.1 (Feb. 2001), pp. 74–81. ISSN: 1558-1578.

[104] C. H. Holdsworth et al. “Performance analysis of an improved 3-D PET Monte Carlo simulation and scatter correction”. In: *IEEE Transactions on Nuclear Science* 49.1 (Feb. 2002), pp. 83–89. ISSN: 1558-1578.

[105] J. Ye, X. Song, and Z. Hu. “Scatter correction with combined single-scatter simulation and Monte Carlo simulation for 3D PET”. In: *2014 IEEE Nuclear Science Symposium and Medical Imaging Conference (NSS/MIC)*. 2014, pp. 1–3.

[106] N. Kawachi et al. “Kinetic Analysis of Carbon-11-Labeled Carbon Dioxide for Studying Photosynthesis in a Leaf Using Positron Emitting Tracer Imaging System”. In: *IEEE Transactions on Nuclear Science* 53.5 (Oct. 2006), pp. 2991–2997. ISSN: 1558-1578.

[107] Jens Mincke et al. “Guide to Plant-PET Imaging Using 11CO2”. In: *Frontiers in Plant Science* 12 (2021), p. 997. ISSN: 1664-462X.

[108] X. Liang et al. “NEMA-2008 and In-Vivo Animal and Plant Imaging Performance of the Large FOV Preclinical Digital PET/CT System Discoverist 180”. In: *IEEE Transactions on Radiation and Plasma Medical Sciences* 4.5 (Sept. 2020), pp. 622–629. ISSN: 2469-7303.

[109] J. J. Scheins et al. “New Imaging Method of Positrons Leaving the Source Application for PET/MR hybrid Scanners -”. In: *2017 IEEE Nuclear Science Symposium and Medical Imaging Conference (NSS/MIC)*. Oct. 2017, pp. 1–2.

[110] Christoph Peter Weirich. “Quantitative PET Imaging with Hybrid MR-PET Scanners”. PhD thesis. RWTH Aachen University, 2014.

[111] Antonia Chlubek. “Setup of a gas exchange system for the application of radioactively labeled CO2 on plants”. Masterarbeit, FH Aachen, Campus Jülich, 2013. MA thesis. FH Aachen, Campus Jülich, 2013, 88 p.

[112] M. Streun et al. “PhenoPET: A dedicated PET scanner for plant research based on digital SiPMs (DPCs)”. In: *Proc. IEEE Nuclear Science Symp. and Medical Imaging Conf. (NSS/MIC).* Nov. 2014, pp. 1–3.

[113] Holger Nöldgen et al. “Read-out electronics for digital silicon photomultiplier modules”. In: 2013 IEEE Nuclear Science Symposium and Medical Imaging Conference (2013 NSS/MIC), Seoul (Korea (South)), 27 Oct 2013 - 2 Nov 2013. Oct. 27, 2013.

[114] M. Streun et al. “PhenoPET - results from the plant scanner”. In: *2016 IEEE Nuclear Science Symposium, Medical Imaging Conference and Room-Temperature Semiconductor Detector Workshop (NSS/MIC/RTSD).* Oct. 2016, pp. 1–2.

[115] Ben Zwaans. “PDPC Module Tile 2.0 architecture: Firmware”. Aug. 21, 2012.

[116] M. Streun et al. “Time Calibration of phenoPET based on the Lu-176 Background of LYSO”. In: *2017 IEEE Nuclear Science Symposium and Medical Imaging Conference (NSS/MIC).* Oct. 2017, pp. 1–2.

[117] Ben Zwaans. *PDPC RING SW manual manual.* Feb. 4, 2013.

[118] Michael Wagener. *phenoPET - Graphical User Interface.* Dec. 20, 2018.

[119] R. Brun and F. Rademakers. “ROOT: An object oriented data analysis framework”. In: *Nucl. Instrum. Meth. A* 389 (1997). Ed. by M. Werlen and D. Perret-Gallix. See also "ROOT" [software], Release v5.34/36, 05/04/2016, pp. 81–86.

[120] J. J. Scheins and H. Herzog. “PET Reconstruction Software Toolkit - PRESTO a novel, universal C++ library for fast, iterative, fully 3D PET image reconstruction using highly compressed, memory-resident system matrices”. In: *Proc. IEEE Nuclear Science Symp. Conf. Record.* Oct. 2008, pp. 4147–4150.

[121] J. J. Scheins, H. Herzog, and N. J. Shah. “Fully-3D PET Image Reconstruction Using Scanner-Independent, Adaptive Projection Data and Highly Rotation-Symmetric Voxel Assemblies”. In: *IEEE Transactions on Medical Imaging* 30.3 (Mar. 2011), pp. 879–892. ISSN: 0278-0062.

[122] J J Scheins et al. “High performance volume-of-intersection projectors for 3D-PET image reconstruction based on polar symmetries and SIMD vectorisation”. In: *Physics in Medicine and Biology* 60.24 (Nov. 2015), pp. 9349–9375.

[123] M. Streun et al. “PET scintillator arrangement on digital SiPMs”. In: *Proc. IEEE Nuclear Science Symp. and Medical Imaging Conf. (2013 NSS/MIC).* Oct. 2013, pp. 1–4.

[124] Jürgen Scheins. Private Correspondence, May. May 2020.

[125] Eder R. Moraes et al. “Towards component-based validation of GATE: Aspects of the coincidence processor”. In: *Physica Medica* 31.1 (2015), pp. 43–48. ISSN: 1120-1797.

[126] C. Hinz et al. “Count Rate Corrections for the Plant Dedicated PET System phenoPET”. In: *2018 IEEE Nuclear Science Symposium and Medical Imaging Conference Proceedings (NSS/MIC).* Nov. 2018, pp. 1–6.

[127] Gadagkar H Casey M E and Newport D. “A component based method for normalisation in volume PET”. In: *1995 International Meeting on Fully Three-Dimensional Image Reconstruction in Radiology and Nuclear Medicine.* July 4, 1995, pp. 67–71.

[128] B Bai et al. “Model-based normalization for iterative 3D PET image reconstruction”. In: *Physics in Medicine and Biology* 47.15 (2002), p. 2773.

[129] E Vicente et al. “Improved dead-time correction for PET scanners: application to small-animal PET”. In: *Physics in Medicine & Biology* 58.7 (2013), p. 2059.

[130] *Web Presence Laboratoire National Henri Becquerel.* `http://www.nucleide.org`. Last Access: Mai 2018.

[131] Julien Salvadori et al. “Monte Carlo simulation of digital photon counting PET”. In: *EJNMMI Physics* 7.1 (Apr. 2020), p. 23. ISSN: 2197-7364.

[132] Matteo Cacciari, Gavin P Salam, and Gregory Soyez. “The anti-ktjet clustering algorithm”. In: *Journal of High Energy Physics* 2008.04 (Apr. 2008), pp. 063–063.

[133] *Automatic TF1 Class Reference.* `https://root.cern.ch/doc/master/classTF1.html`, Sept. 1, 2020.

[134] Harold Rothfuss et al. “LSO background radiation as a transmission source using time of flight”. In: *Physics in Medicine and Biology* 59.18 (Aug. 2014), pp. 5483–5500.

[135] John Nuyts et al. “Iterative reconstruction for helical CT: a simulation study”. In: *Physics in Medicine and Biology* 43.4 (Apr. 1998), pp. 729–737.

[136] Katrien Van Slambrouck and Johan Nuyts. “Metal artifact reduction in computed tomography using local models in an image block-iterative scheme”. In: *Medical Physics* 39.11 (2012), pp. 7080–7093. eprint: `https://aapm.onlinelibrary.wiley.com/doi/pdf/10.1118/1.4762567`.

[137] K. Van Slambrouck and J. Nuyts. “Reconstruction Scheme for Accelerated Maximum Likelihood Reconstruction: The Patchwork Structure”. In: *IEEE Transactions on Nuclear Science* 61.1 (2014), pp. 173–181.

[138] Qingyang Wei. “Intrinsic Radiation in Lutetium Based PET Detector: Advantages and Disadvantages”. In: (Jan. 2015).

[139] J J Scheins et al. “High-throughput, accurate Monte Carlo simulation on CPU hardware for PET applications”. In: *Physics in Medicine & Biology* 66.18 (Nov. 2021), p. 185001.

[140] Jürgen Scheins. *Internal PRESTOlight Software Documentation.* Version 3.10. June 17, 2020.

[141] M. Streun et al. “phenoPET – Results from the Plant Scanner”. In: IEEE Medical Imaging Conference 2016, Strasbourg (France), 31 Oct 2016 - 5 Nov 2016. Oct. 31, 2016.

[142] S. Lee, A. G. Weisenberger, and M. F. Smith. “A method for characterization of PhytoPET in plant growth media”. In: *2013 IEEE Nuclear Science Symposium and Medical Imaging Conference (2013 NSS/MIC).* Oct. 2013, pp. 1–3.

[143] Landwirtschaftliche Untersuchungs und Forschungsanstalt Speyer. *Use of Standard Soils.* URL: `https://www.lufa-speyer.de/index.php/dienstleistungen/standardboeden/8-dienstleistungen/artikel/57-standard-soils` (visited on 08/20/2020).

[144] Ridha Boudiar et al. “Effects of Low Water Availability on Root Placement and Shoot Development in Landraces and Modern Barley Cultivars”. In: *Agronomy* 10.1 (2020). ISSN: 2073-4395.

[145] Esther Breuer. “Private Correspondence on humidity of Graberde, May”. Private Correspondence on humidity of Graberde, May. Apr. 14, 2020.

[146] Dagmar van Dusschoten et al. “Spatially Resolved Root Water Uptake Determination Using a Precise Soil Water Sensor”. In: *Plant physiology* 184.3 (2020), pp. 1221–1235. ISSN: 1532-2548.

[147] Stephen Strother, Michael Casey, and E.J. Hoffman. “Measuring PET scanner sensitivity: Relating countrates to image signal-to-noise ratios using noise equivalent counts”. In: *Nuclear Science, IEEE Transactions on* 37 (May 1990), pp. 783–788.

[148] “NEMA NU 2: Performance measurement of Positron Emission Tomographs”. In: ().

[149] Markus Michel. “Charakterisierung des hochauflösenden Positronen-Emissions-Tomographen, PlanTIS, nach dem neuen NEMA NU 4-2008 Standard”. MA thesis. Forschungszentrum Jülich GmbH,Zentralinstitut für Elektronik & Fachhochschule Koblenz, RheinAhrCampus Remagen, 2011.

[150] Patrick Hallen et al. “PET performance evaluation of the small-animal Hyperion IID-PET/MRI insert based on the NEMA NU-4 standard”. In: *Biomedical Physics & Engineering Express* 4.6 (Oct. 2018), p. 065027.

[151] M. Streun et al. ““PlanTIS: A positron emission tomograph for imaging 11C Transport in Plants””. In: *2007 IEEE Nuclear Science Symposium Conference Record*. Vol. 6. Oct. 2007, pp. 4110–4112.

[152] William W. Moses. “Fundamental Limits of Spatial Resolution in PET”. eng. In: *Nuclear instruments & methods in physics research. Section A, Accelerators, spectrometers, detectors and associated equipment* 648 Supplement 1 (Aug. 2011). 21804677[pmid], S236–S240. ISSN: 0168-9002.

[153] James, F. *Statistical Methods in Experimental Physics*. 2nd. World Scientific Publishing, 2006. ISBN: 981256795X.

[154] Luc Demortier and Louis Lyons. “Everything you always wanted to know aboutpulls”. Version 3. In: *CDF/ANAL/PUBLIC/5776* (Apr. 8, 2002).

[155] Rene Andrae, Tim Schulze-Hartung, and Peter Melchior. *Dos and don’ts of reduced chi-squared*. 2010. arXiv: `1012.3754 [astro-ph.IM]`.

[156] Jay Orear. “Least squares when both variables have uncertainties”. In: *American Journal of Physics* 50.10 (1982), pp. 912–916. eprint: `https://doi.org/10.1119/1.12972`.

Acronyms

2018 MIC 2018 IEEE Medical Imaging Conference.

API Application Programming Interface.

BMBF Bundesministerium für Bildung und Forschung.

BUW Bergische Universität Wuppertal.

CCB Concentrator Board, *Glossary:* Concentrator BoardconcentratorBoard.

CERN European Organization for Nuclear Research.

CPU Central Processing Unit.

CT Computer Tomography.

DCF dead time correction factor, *Glossary: DCF*.

DPC Digital Photon Counter, *Glossary:* Digital Photon Counter.

DPPN Deutsches Pflanzen Phänotypisierungsnetzwerk.

FOV Field-of-View.

FPGA field-programmable gate array.

FWHM Full Width at Half Maximum.

FZJ Forschungszentrum Jülich.

GPU Graphics Processing Unit.

GUI Graphical User Interface.

HDMI High Definition Multimedia Interface.

IBG-2 Institute of Bio- and Geosciences: Plant Sciences.

INM-1 Institute of Neuroscience and Medicine: Structural and functional organisation of the brain.

INM-4 Institute of Neuroscience and Medicine: Medical Imaging Physics.

INM-5 Institute of Neuroscience and Medicine: Nuclear Chemistry.

LED Light-emitting diode.

LOI Line-of-Intersection, *Glossary:* Length-of-Intersection.

LOR Line-of-Response, *Glossary:* Line-of-Responce.

LSO cerium-doped lutetium oxyorthosilicate, *Glossary:* LSO.

LYSO lutetium-yttrium oxyorthosilicate, *Glossary:* LYSO.

MLEM Maximum Likelihood Expectation-Maximization.

MLTR Maximum Likelihood for Transmission Reconstruction.

MRI Magnetic Resonance Imaging.

NECR noise-equivalent count rate.

NEMA National Electrical Manufacturers Association.

OP-MLEM Ordinary Poisson Maximum Likelihood Expectation-Maximization.

PDPC Philips Digital Photon Counting.

PET Positron Emission Tomography.

PMT Photo Multiplier Tube.

PRESTO PET Reconstruction Software Toolkiti, *Glossary:* PET Reconstruction Software Toolkit.

PVC Polyvinyl chloride.

RAID redundant array of independent disks, *Glossary:* redundant array of independent disks.

RAM Random-Access Memory.

RMS Root Mean Square.

ROI Region of Interest.

SiPM Silicon photomultiplier, *Glossary:* SiPM.

SPECT Single Positron Emission Computer Tomography.

SSS single scatter simulation.

TDC time to digital converter.

TOF Time of Flight.

TOR Tube-of-Response, *Glossary:* Tube-of-Responce.

VOI Volume-of-Intersection, *Glossary:* Volume-of-Intersection.

VRR Variance Reduced Randoms, *Glossary:* Variance Reduced Randoms.

XPS extruded polystyrene.

ZEA Central Institute of Engineering, Electronics and Analytics.

ZEA-1	Central Institute of Engineering, Electronics and Analytics (ZEA), Engineering and Technology.
ZEA-2	Central Institute of Engineering, Electronics and Analytics (ZEA), Electronic Systems.

Notation

AC activity concentration in a sample.

a_i attenuation of Line-of-Response (LOR) i by an object.

A_{ij} expected number of *true* coincidences for a LOR between crystals i and j for a model of the measurement. This is in particular used for the calculation of normalizations. The model is restricted to unscattered coincidences.

B blank data for a LOR. Blank data are a measurement for a transmission reconstruction without an object in the FOV .

CF calibration factor between the counts reconstructed by PET Reconstruction Software Toolkit (PRESTO) per time pcps=PRESTO Counts s^{-1} into $\mathrm{MBq\,ml}^{-1}$.

c_{ij} matrix element are used in iterative image reconstruction in Maximum Likelihood Expectation-Maximization (MLEM) based algorithms. c_{ij} describes the propability that an event in LOR i results from voxel j.

$coinDCF$ dead time correction factor for *trues* and *scattered* coincidences measured by all modules of *pheno*PET. An alternative version are $coinDCF_{n,m}$, which restricts to coincidences between the two modules n and m. *see also: DCF*.

DCF dead time correction factor (DCF) for *pheno*PET are defined as the ratio of ideal counts and measured counts.

ϵ sensetivity of a crystal as obtained from the component based normalization.

eT number of *estimated true* are *trues* plus the *scattered* coincidences. *Glossary: estimated true*.

f^{frames} correction factor for dropped and missing frames. f_n^{frames} for *singles* of module n and $f_{n,m}^{frames}$ for coincidences between module n and m.

g geometriy sensetivity of a LOR obtained from the component based normalization.

hat e.g. $\hat{p}$ the hat over a variable denotes an expected value. This is mainly used for the expected number of *prompts* $\hat{p}$.

λ amount of radioactivity activity of a source or activity concentration in a specific volume, e.g. a voxel or a Region of Interest (ROI).

λ decay constant to describe the exponential behavior of a radioactive decay.

M_{ij} expected number of measured events in a normalization measurement after considering the different sensitivities.

m_{ij} number of measured events between the crystals i and j in a normalization measurement.

μ attenuation coefficient. μ_i is the attenuation coefficient of voxel i.

overline e.g. $\overline{p}$ a line over a variable denotes the average of this value. In this example the average number of *prompts*.

p number of *prompt* coincidences. Those can either belong to a specific LOR or a larger number of LORs, like between two modules. See: *Glossary: prompt*.

ρ density, weight per volume, of a material.

S number of *singles*. See: *Glossary: single*.

s sensetivity. *Glossray:* sensitivity.

$sDCF$ dead time correction factor for *singles* measured by a module of *pheno*PET. *see also: DCF*.

s^{decay} correction factor for the decay of the radioactive source.

SE scatter estimates are used for the correction of *scattered* coincidences during the image reconstruction. *Glossary:* scatter estimate.

τ dead time caused by one event .

T_{coin} number of *trues*. See: *Glossary: true*.

t_{coin} The coincidence window t_{coin} is the maximum time difference between to *singles* to be sorted as a coincidence by the coincidence sorter.

VRR number of variance reduced randoms (VRR). See: *Glossary:* Variance Reduced Randoms *Acronyms:* VRRglos::VRR.

Glossary

attenuation correction correction for photons that are removed from LORs due to interaction with the material.

attenuation map voxelized image of the attenuation coefficients. Used for the attenuation correction and scatter correction in PET.

cell Avalanche photo diode operated in Geiger mode. A cell of a Digital Photon Counter (DPC) has a size of $59.4\,\mu m^2 \cdot 64\,\mu m^2$.

CINT C++ interpreter included in ROOT.

cluster Combination of several simultaneously detected hits on a tile. The combination process is called clustering..

clustering Process to combine several simultaneously detected hits on a tile. The crystal position is determined with a weighted mean of the pixel position with their energy depositions. The time stamp is the first of the contributing hits..

Concentrator Board This board is the interface between *pheno*PET and a measurement PC. It holds a FPGA to spread commands and collect the data from all modules.

count rate corrections correction of all effects that alter the count rates. *Glossary:* dead time, frame dropping & pile-up.

dead time is the reduction of the count rates as the detector is not sensitivity to a new event because already an event is being processed or not sensitive again.

die Region on a DPC. A die holds 2 × 2 pixels. Each die has a FPGA for processing and data acquisition..

Digital Photon Counter Digital silicon photo multiplier produced by Phillips. Each DPC has 16 dies..

DPCShell Command line program to control measurements with *pheno*PET.

estimated true are *trues* plus the *scattered* coincidences. Therefore, all events result at least from a real decay of an unstable nucleus. *estimated trues* are calculated as the difference between *prompts* and *random* coincidences.

frame Time interval defined by the fine clock on a DPC. Each clock tick is 19.5 ps long and a frame is 327.68 µs long. A complete frame has a package of each module..

frame dropping controlled dropping of frames by the Concentrator Board (CCB) of *pheno*PET.

GATE Geant4 application dedicated to the simulation of medical imaging and radiotherapy.

Geant4 C++ toolkit for Monte Carlo simulation of particle passing through matter.

hit Event on one DPC die. The raw data contain information about the die, energy deposition on each of the four pixel in triggered cells and a time stamp. Further processing calculates the deposited energy and the crystal position.

killAll Handling of multiple coincidences, that discards all *multiples*..

Length-of-Intersection Length of intersection between a line and a 3 object like a voxel.

Line-of-Responce Line between the two crystals detecting a coincidence.

LSO Anorganic scintillator with fast rise and decay constant of scintillation light, high light yield and high stopping power.

LYSO Anorganic scintillator with fast rise and decay constant of scintillation light, high light yield and high stopping power.

module Houses four DPCs and their crystal matrix. A FPGA processes the data.

module status package Status of for each module, if a valid package was transmitted in the current frame..

multiple A coincidence which is formed by more than two singles that are within an open coincidence window..

normalization correction for static sensitivities. Sensitivities are the mismatch between a model and the actual measurement. *Glossary:* sensitivity.

over long status package Status of for each module, if an over long package was transmitted to the CCB..

overlong package Package transmitted by a module as soon as the amount of data exceeds the memory of one data buffer. The CCB does not transmit these packages..

package Event data of a time frame of one module. Holds a header with general information and the hits of all dies of the four modules. The package header holds the current number of the frame which is in the range of 0 to 255 and wraps around..

PET Reconstruction Software Toolkit A software toolkit for iterative PET image reconstruction. For the reconstruction the geometry of the PET scanner is taken into account and no sinograms are required.

phenoGateSorter Coincidence sorter based on the GATE coincidence sorter but adopted the data structure provided by *pheno*PET.

***pheno*PET** A PET scanner dedicated for plants. Developed and constructed by Central Institute of Engineering, Electronics and Analytics (ZEA), Engineering and Technology (ZEA-1), ZEA-2 and Philips Digital Photon Counting (PDPC) for the Institute of Bio- and Geosciences: Plant Sciences (IBG-2).

phenosort Programm that reads in raw files and does preprocessing (clustering and calibrations) and provides a *phenoSorter* as coincidence sorter .

phenoSorter Coincidence sorter provided by the *phenosort* program. *Singles* are sorted into a buffer for each sector. Coincidences are search in the first *single* of each sector.

phenostore Programm to write the data stream provided by the CCB to disc.

photo assimilate photoassimilates are formed in the leafs from recently allocated CO_2. Photoassimilates are transported and allocated within the plant. $[^{11}C]CO_2$ can be used as radiotracer.

pile-up combination of two or more events in an integration interval. This can remove events out of the energy window or add events, that would have been discarded otherwise.

pixel Region on a DPC. Each pixel holds 3200 individual cells which are divided into four subpixel for triggering..

prompt Any coincidence detected by a coincidence sorter within the *single* events..

radiotracer radioactive isotopes that are used to visualize and quantify the flow and allocation of a molecule (e.g. sugar or CO_2) feeded to a plant, animal or human.

random Coincidences detected by a coincidence sorter as randoms. For this work in most cases a delayed coincidence window approach is applied.

redundant array of independent disks A computer providing a large amount of hard drive space. Often used for central storage of large anmount of data that are accessed by other computers.

ROOT C++ library developed at CERN for the analysis and visualization of large amounts of data.

scatter correction correction for *scattered* coincidences originating from other LORs.

scatter estimate A scatter estimate is an estimates for the expectation value for *scattered* coincidences in a LOR in a specific frame. For *pheno*PET scatter estimates are obtain from a Monte Carlo simulation and scaled to the number of events in a specific frame.

scatter iteration correction for *scattered* coincidences. A scatter iteration uses a reconstructed emission image to estimate the scatter distribution for the next emission reconstruction. The estimation of scatter coincidences is done with a Monte Carlo simulation for *pheno*PET.

scatter simulation a simulation to obtain the distribution of *scattered* coincidneces from an activity distribution and an attenuation map.

scattered Coincidence from a real decay but the directional information is lost due to compton scatter with the measured object or the detector, except the crystals.

sector The three modules at the same ring positions on top of each other.

sector board Three modules are mounted to one sector board. The sector board spreads the power supply and data transfer to the different modules.

sensitivity A sensitivity describes the fraction of events measured by a detector compared to the expected number of events from a model of the system.

single Candiate for a photon detected by a *tile*. The clustering is done by *phenosort*.

SiPM Solid state detector deivide in several cells. Each cell is an avalanche photodiode operated in Geiger mode.

takeAllGood Handling of multiple coincidences. This pairs all singles within a coincidence window to coincidences if they pass the geometric cuts and are within the coincidence time difference..

tile A DPC on a *pheno*PET module.

true Coincidences assumed to result from real decays, that did not interacted with the measured object and the system until the photons were detected.

Tube-of-Responce Tube between the two crystals detecting a coincidence.

Variance Reduced Randoms A method to estimate an expectation value for the number of randoms per LOR from a number of randoms obtained from a measurement.

Volume-of-Intersection Volume of the intersection between two 3D objects.

List of Figures

List of Tables

Acknowledgements

First of all I wish to thank Professor Uwe Pietrzyk (INM-4 & BUW) for the supervision of my thesis and Professor Markus Axer (INM-1 & BUW) for taking over my supervision after Professor Pietrzyk retired. In addition, I wish to thank my second assessor Professor Wolfgang Wagner (BUW). I am pleased, that Professor Reinhard Hentschke (BUW) and Professor Dirk Lützenkirchen-Hecht (BUW) agreed to be part of my board of examiners. At the IBG-2, a committee of supervisors guides each PhD student. I appreciate the work of my four supervisors, which contributed all with their desinct view on *pheno*PET. Jürgen Scheins (INM-4) is the developer of the reconstruction software PRESTO. Therefore, Jürgen provides valuable knowledge on image reconstruction and on the quantification of *pheno*PET. Matthias Streun (ZEA-2) worked on the construction of *pheno*PET and maintains the first generation scanner PlanTIS. Matthias is the first contact at the ZEA-2 and provides the required knowledge on the setup and the operation of *pheno*PET. Daniel Pflugfelder was my direct supervisor at the IBG-2. Daniel works on MRI measurements of plants. This includes the analysis of PET data in combination with MRI. In addition, Daniel supported me with the bureaucracy. Ralf Metzner is currently running and coordinating radiotracer experiments at the IBG-2. Ralf will apply *pheno*PET in plant research and therefore offers the unique view on the requirements for measurements. For me it is always fascinating to combine the different views on *pheno*PET and the consequences for the quantification of *pheno*PET and its application. The discussions on the data analysis, visualization and search for solutions of different issues were always interesting and challenging. Furthermore, I wish to thank my committee and supervisors for the corrections to my thesis.

I wish to thank Ulrich Schurr, head of IBG-2, for the support of my project together with the support of the radiotracer at the IBG-2 in general. The same is true for Siegfried Jahnke, the retired group leader of the Enabling Technologies. Siegfried has valuable experiences on the application of radiotracers to plants. For example, he used the PlanTIS system for first PET measurements of plants in Jülich and achieved the founding for the second generation system *pheno*PET as part of Deutsches Pflanzen Phänotypisierungsnetzwerk (DPPN). Therefore, Siegfried's work made a major contribution to the existence of *pheno*PET.

I also would like to thank the IBG-2 and especially the Enabling Technologies group for the interesting discussions and the insights into many different methods and aspects of plant science. Robert Koller, group leader of Enabling Technologies, always provides a good working environment and his enthusiasm for plant science and the application of PET is catching. I also have to thank Esther Breuer, Sarah Becker, Antonia Chlubeck and Marco Dautzenberg for their continuous support in the laboratory and their support during each measurement. In addition, Antonia does the planing of required components and coordinates the construction with the mechanical workshop of the IBG-2. Here, one important project was the moving of *pheno*PET into the new climate chamber. In addition, I wish to thank Thomas Hombach and Johannes Koch for their work on the electronics of the climate chamber and achieving a preliminary operation for my last experiments. Jonas Bühler and Gregor Huber develop the analysis of tracer flow and allocation in plants. Especially Jonas maintained the MeVisLab modules of the IBG-2. Andreas Fischbach develops the majority of control software for the climate chamber. Especially the software for the rotation systems was key for several experiments. Last but not least I wish to thank Sina Schultes for the possibility to provide reconstructed images. This gave fascinating insight into an actual application. It is always a great pleasure to discuss with all members of the Enabling Technologies group, either during a coffee break or while having barbecue as lunch.

The PhD program at the IBG-2 provides regular meetings for talks of each student. Furthermore, a yearly event is organized by the PhDs, which provides the opportunity to present the current research to the institute and discuss with the other scientists. It was always challenging to present physical topics to a broad audience with an ever growing number of backgrounds. It is always fascinating to see different approaches to plant science, which ranged from genetic analysis up to remote sensing to extract data for many plants with unmaned flying vehicles, planes or even satellites. Especially, I wish to thank Ingar Janzik. Ingar leads the PhD program and provided help for all processes regarding the Research Center Jülich. The IBG-2 also gave us PhD students the possibility to visit the University of Zurich and the ETH Zurich.

I would also like to thank all colleagues at the IBG-2. I had a large number of interesting discussions and attended to interesting presentations. A special thanks is required for the infrastructure provided by the institute, for example the IT team and the administrative done in the background. There are also voluntary jobs that need to be honored: the coffee team provides coffee and a clean machine while the snack box team provides snacks and drinks. In addition I want to thank the DPPN at the IBG-2 for the founding of *pheno*PET and the founding of my visit of the 2018 IEEE Medical Imaging Conference (2018 MIC).

I would also like to thank the ZEA-2 for their support and maintenance of *pheno*PET. The rework of the firmware was a major effort and I am unsure if any external company would have provided this amount of support. Here, I wish to thank especially Daniel Durini and Carsten Degenhardt, who lead the work resulting in the large improvement of *pheno*PET. At the ZEA-2 I had especially contact with Holger Nöldgen, Peter Wüstner and Michael Wagener. I want to thank all members of the ZEA-2 for their effort.

My experiments were also supported by colleagues from other institutes. The INM-5 produced the necessary short lived radiotracers (^{18}F, ^{11}C) for the experiments. Here, I want to thank Norbert Ponten, how provided us with the tracer and the operation team of the cyclotron. Lutz Tellmann from the INM-4 lent us further radioactive sources like the ^{68}Ge rod for the quantification and other test measurements. In addition, I have to thank Lutz for the interesting discussions on quantification in the daily clinical routine and the help during experiments.

Preparing and writing my thesis would not been possible without the support of my family and friends. Most important is the support of my wife Ronja over the years and especially during the writing. I also wish to thank my parents, Brigitte and Lothar, and my brother Volker for the support over the years. The same is true for my good friends Katja, Axel and Martina. A special thanks goes to Michael, who kindly read several chapters of my thesis and provided valuable linguistic corrections. Last but not least I have to thank my comrades in the disaster and civil protection unit of the German Red Cross in Jülich. This practical work is a relaxing contrast to the scientific work. In addition, the voluntary work provides unique experiences and several aspects can be applied in a daily work and life.

Appendix A

Quality of Fits: Residual Graphs and Pull Distributions

In the following section a brief overview on the general idea of a χ^2 fit and the evaluation of the quality of the fit is given. For the quality of the fit, residual graphs and pull distributions are presented. The focus is the application within this thesis. The aim of this section is a brief overview with a focus on the practical application. Much more details can be found in the literature, for example in [153, 154, 155].

A χ^2 fit can be used for the fitting of Gaussian distributed data. For simplicity we assume data pair of x and y which are described by a function with $y = f(x)$ with a number of parameters M. To obtain the parameters of the function $f(x)$ from N data points the relation

$$\chi^2 = \sum_{i=0}^{i<N} \left(\frac{y_i - f(x_i)}{\sigma(x_i)} \right)^2 \tag{A.1}$$

with $\sigma(x_i)$ the uncertainties on each value y_i. ROOT includes uncertainties on the x_i with the effective variance method [156]. This method combines the uncertainties on x, σ_x, and y, σ_y, with Gaussian error propagation

$$\sigma^2(x_i) = \sigma_{y,i}^2 + \left(\sigma_{x,i} \frac{\partial}{\partial x} f(x) \right)^2 . \tag{A.2}$$

The quality of a fit can be accessed by the χ^2 distribution. This requires the result of Equation (A.1) for a given fit and the degrees of freedom $N - M$. The latter one is the expectation value of the χ^2 distribution.

Residual Graphs are an additional tool to evaluate the quality of a fit. The residual r_i is calculated as the difference in Equation (A.1) with the uncertainties from Equation (A.2):

$$r_i = y_i - f(x_i). \tag{A.3}$$

This preserves the position of a point relative to the fit. Therefore, systematic deviations like peaks or drops can be identified. These deviations might not be visible in an evaluation of the χ^2 distribution.

Pull Distributions are a further tool to access the quality of a fit. The basic assumption of a χ^2 fit is a normal distribution of all measured parameters. This results in a normal distribution of the data points around the expected values. Therefore the pulls,

$$pull = \frac{y_i - f(x_i)}{\sigma(x_i)} \tag{A.4}$$

should follow a normal distribution with mean $\mu = 0$ and standard deviation $\sigma = 1$. The pulls are the quotients in Equation (A.1). The uncertainties on the x values should be included with Equation (A.2).

The pull distribution shows the overall distribution of the data points. This is usefull to identify deviations, like a skew distribution or a split into several peaks. It has to be noted that pull distribution requires a larger number of points. Afterwards it is a good tool to evaluate the overall distribution of the data around the fit. On the downside it loses position information of the residuals.

Appendix B

Convergence of Transmission Reconstruction

The reconstruction of attenuation map with the Maximum Likelihood for Transmission Reconstruction (MLTR) has three parameters that influence the convergence of the reconstructed images. Here, the relaxation parameter α_{relax} and the number of iterations are handed over to the algorithm. These two parameters are investigated with a synthetic attenuation map. The third parameter is the number of events in the transmission measurement. This is investigated with the reconstruction of measurements with different durations.

B.1 Relaxation Parameter and Number of Iterations

The MLTR implemented in PET Reconstruction Software Toolkit (PRESTO) is presented in Section 7.1.1. Here, the relaxation parameter α_{relax} and the number of iterations need to be set. A parameter range for α_{relax} has been found by a trial and error approach. Several values within this region are studied systematically with synthetic data. This is combined with an investigation of the number of iterations to identify a suitable point of operation. Therefore, a reconstruction should combine a fast and stable processing with a low noise.

B.1.1 Method

The blank data for MLTR (see Section 7.1.2) are used to model the measurement of a synthetic cylinder with $\mu_{syn} = 0.1\,\mathrm{cm}^{-1}$. This cylinder has a radius of 40 mm and a height of 163 mm. The cylinder is placed outside of the center of the Field-of-View (FOV) at $x = 8.1\,\mathrm{mm}$, $y = 27\,\mathrm{mm}$ and $z = -18\,\mathrm{mm}$. This gives synthetic attenuation data a_i as the Line-of-Intersection (LOI) between each Line-of-Response (LOR) i and the cylinder. The synthetic *prompts* p_i^s and Variance Reduced Randoms VRR_i^s are calculated from the blank scan (p_i^B & VRR_i^B) according to

$$\begin{aligned}
p_i^s &= a_i \cdot \left(p_i^B - VRR_i^B\right) + VRR_i^B \\
a_i &= \exp\left(-\mu_{syn} \cdot LOI\right) \\
VRR_i^s &= VRR_B^i \\
B_i &= p_i^B - VRR_i^B \text{ with } B_i \geq 0.
\end{aligned}$$

The resulting synthetic and blank data are reconstructed with different α_{relax}. The attenuation maps after different iteration steps are saved with a maximum of 210 iterations. The mean attenuation coefficient in the cylinder is calculated to investigate the convergence of the reconstruction. The Root Mean Square (RMS) is calculated to study the noise within the reconstructed images.

B.1.2 Results and Discussion

The overview on the mean attenuation is given in Figure B.1. A $\alpha_{relax} < 0.05$ result in a slow convergence. Here, the mean starts to approach the expectation values after over 30 iterations. Additional 100 iterations are required to achieve values close to those of larger α_{relax}. On the other hand for $\alpha_{relax} > 0.15$ the mean oscillates for odd and even iteration steps before the mean converges. For $\alpha_{relax} = 0.2$ the oscillations continue even for over 200 iterations, as visible by the last two values, iterations 200 and 209.

The best convergence reach a mean of about 0.095 cm^{-1}. This is about 5 % below the expectation of 0.1 cm^{-1}. A quite large bias results from the boarders of the cylinder. Therefore, the results show a lower bias of about 1.5 % if the mean is calculated in a Region of Interest (ROI) with a reduced radius of 35 mm instead of the full 40 mm of the cylinder.

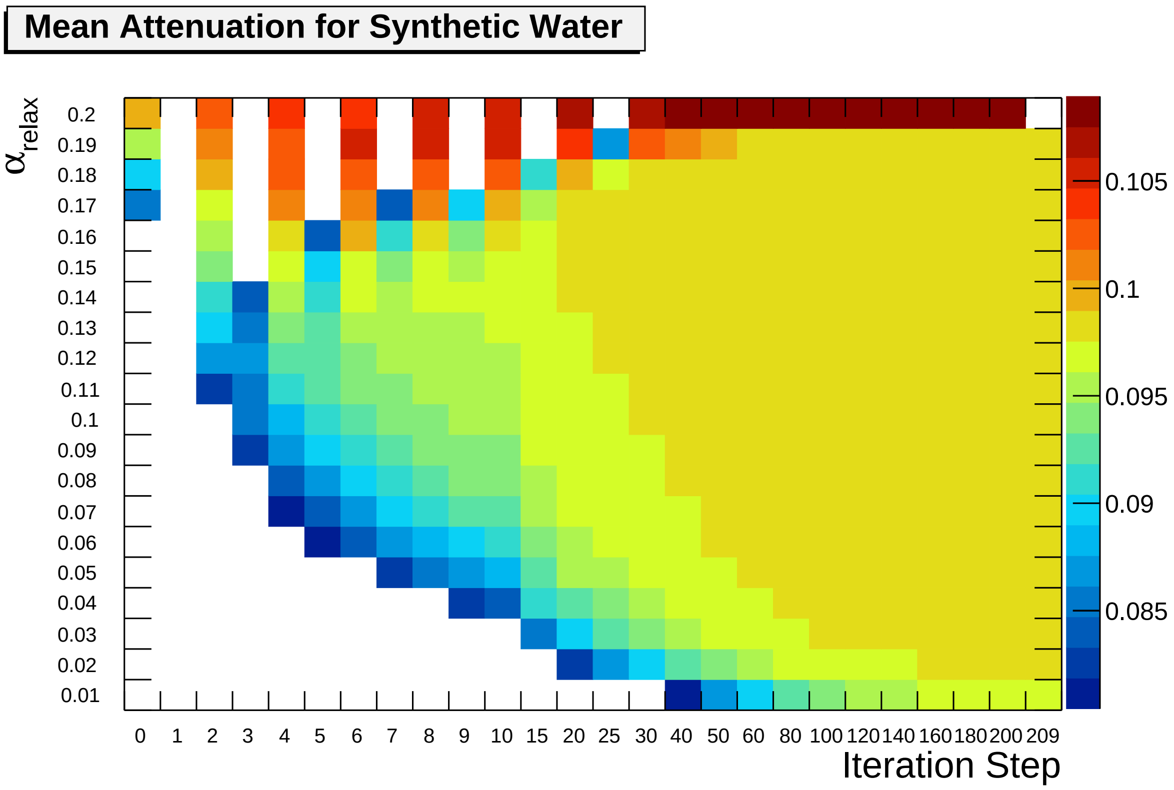

Figure B.1: Overview on the mean attenuation coefficients from the synthetic cylinder with μ_{syn}=0.1 cm^{-1}. The values are zoomed around the expected value. White values are below the color scale. None of the reconstructions converges to the expected values.

The different RMS are presented in Figure B.2. A valley of minimum RMS is found for iteration numbers between 15 and 50 iterations for α_{relax} between 0.1 and 0.17. Similar RMS are found for the lower α_{relax} for more than 140 iterations. For $\alpha_{relax} = 0.2$ a oszillation of the RMS similar to the mean value is observed.

A practical application requires a short computation time, low noise and a stable convergence. Low α_{relax} are to slow. Larger α_{relax} in the range of 0.1 and 0.17 reach similar RMS and convergence for fewer iterations and are therefore more suitable for a routine application. The oscillations for $\alpha_{relax} > 0.13$ do not look desirable for a routine application, especially for low number of iterations. For the further investigations $\alpha_{relax} = 0.1$ is used. The maximum number of iterations is restricted to 30 due to the minimum RMS.

B.2 Duration of Transmission Measurements

The previous section investigated the convergence under ideal conditions. In this section I investigate, how many events are required in the transmission measurement for a good reconstruction. Again the dependency of the reconstructed images on the number of iterations is addressed for up to 30 iterations.

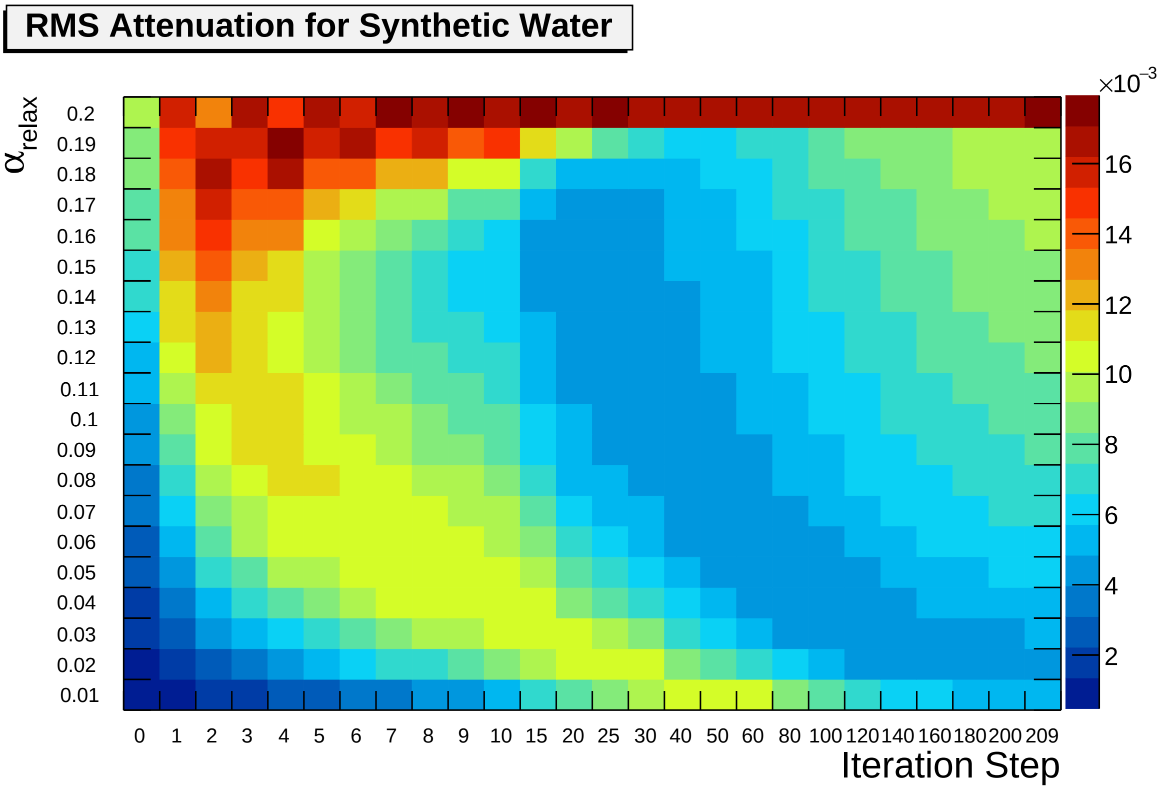

Figure B.2: Overview on the RMS from the transmission reconstruction of the synthetic cylinder. A valley of minimum RMS is visible around $\alpha_{relax} = 0.1$ and 30 iterations.

For a routine operation a short transmission measurement is desired. On the other hand the attenuation map is later included into the scatter simulation and thus a low noise is desirable.

B.2.1 Method

A 15 h long transmission measurement of a water filled cylinder phantom is acquired. The cylinder has an outer diameter of 80 mm, a height of 163 mm and a fillable volume of about 0.5 L. It is placed on a Polyvinyl chloride (PVC) socket and the top of the cylinder is close to the upper border of the FOV. The ^{68}Ge rod source had an activity of about 2 MBq during the measurement.

Transmission reconstruction is done with different fractions of the measurement. The reconstructed images are analyzed after different iteration steps by comparing the mean and RMS of a ROI. The ROI has a radius of 35 mm and a height of 143 mm to cover the water within the phantom.

B.2.2 Results and Discussion

The mean attenuations in Figure B.3a converge to values of about 0.06 cm^{-1} due to the missing scatter correction (see Section 7.3). In general the mean converges earlier compared to the 30 iterations required for the synthetic data in Section B.1. For shorter measurement durations the convergence is slower.

The RMS in Figure B.3b increases with the number of iterations. This is in contrast to the synthetic data in Figure B.2 the RMS increase with the number of iterations. Furthermore do

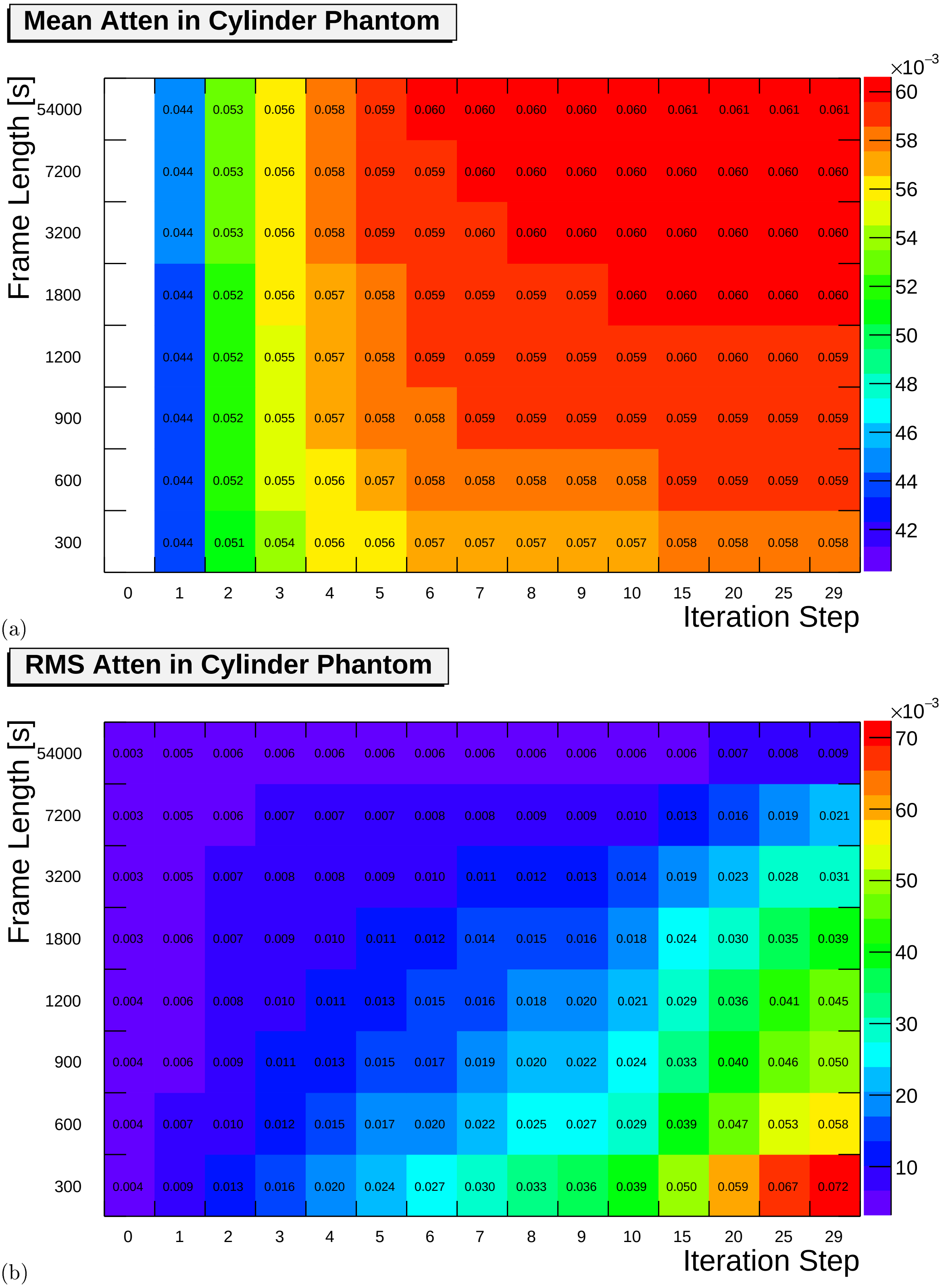

Mean Atten in Cylinder Phantom

Frame Length [s]	0	1	2	3	4	5	6	7	8	9	10	15	20	25	29
54000		0.044	0.053	0.056	0.058	0.059	0.060	0.060	0.060	0.060	0.060	0.061	0.061	0.061	0.061
7200		0.044	0.053	0.056	0.058	0.059	0.059	0.060	0.060	0.060	0.060	0.060	0.060	0.060	0.060
3200		0.044	0.053	0.056	0.058	0.059	0.059	0.060	0.060	0.060	0.060	0.060	0.060	0.060	0.060
1800		0.044	0.052	0.056	0.057	0.058	0.059	0.059	0.059	0.059	0.060	0.060	0.060	0.060	0.060
1200		0.044	0.052	0.055	0.057	0.058	0.059	0.059	0.059	0.059	0.059	0.060	0.060	0.060	0.059
900		0.044	0.052	0.055	0.057	0.058	0.058	0.059	0.059	0.059	0.059	0.059	0.059	0.059	0.059
600		0.044	0.052	0.055	0.056	0.057	0.058	0.058	0.058	0.058	0.058	0.059	0.059	0.059	0.059
300		0.044	0.051	0.054	0.056	0.056	0.057	0.057	0.057	0.057	0.057	0.058	0.058	0.058	0.058

(a)

RMS Atten in Cylinder Phantom

Frame Length [s]	0	1	2	3	4	5	6	7	8	9	10	15	20	25	29
54000	0.003	0.005	0.006	0.006	0.006	0.006	0.006	0.006	0.006	0.006	0.006	0.006	0.007	0.008	0.009
7200	0.003	0.005	0.006	0.007	0.007	0.007	0.008	0.008	0.009	0.009	0.010	0.013	0.016	0.019	0.021
3200	0.003	0.005	0.007	0.008	0.008	0.009	0.010	0.011	0.012	0.013	0.014	0.019	0.023	0.028	0.031
1800	0.003	0.006	0.007	0.009	0.010	0.011	0.012	0.014	0.015	0.016	0.018	0.024	0.030	0.035	0.039
1200	0.004	0.006	0.008	0.010	0.011	0.013	0.015	0.016	0.018	0.020	0.021	0.029	0.036	0.041	0.045
900	0.004	0.006	0.009	0.011	0.013	0.015	0.017	0.019	0.020	0.022	0.024	0.033	0.040	0.046	0.050
600	0.004	0.007	0.010	0.012	0.015	0.017	0.020	0.022	0.025	0.027	0.029	0.039	0.047	0.053	0.058
300	0.004	0.009	0.013	0.016	0.020	0.024	0.027	0.030	0.033	0.036	0.039	0.050	0.059	0.067	0.072

(b)

Figure B.3: Comparison of the mean and RMS after iteration steps and for different measurement duration. The convergence depends on the measurement duration. Furthermore, the RMS increase with higher iteration steps. The numbering of the iteration steps starts with zero.

the RMS do not reach a minimum. This might be a result of the missing scatter correction. For shorter measurements larger RMS are visible. This is expected due to the smaller number of events in these short measurements.

The scatter correction for the transmission reconstruction uses an object depending scaling factor. Therefore, a full convergence of the attenuation map is not necessary. This allows to accept small deviations for a reduced RMS of the attenuation coefficients. In this thesis for example measurements with 54 000 s=15 h are reconstructed with 30 iterations. Here, the images converge to (0.60 ± 0.09) a.u. (mean ± RMS). A convergence to (0.059 ± 0.012) a.u. is achieved for a 1800 s long measurement with seven iterations. This is fast enough for a routine application and has a quite low noise compared to shorter measurements or more iterations.

B.3 Outlook

The investigations with the synthetic data reveals a large number of possible combinations of α_{relax} and the number of iterations for the reconstruction with MLTR. Here, a region with a good convergence and a low noise can be identified. The reconstructions with measured data and without a scatter correction is more challenging. The noise increases with the number of iterations and also for shorter measurements. Here, the duration of the measurement is a measure for the number of decays during the measurement. A overall larger activity of the transmission source can reduce the duration and lead to comparable results.

The missing scatter correction is a further challenge. A systematic study with a data driven scatter correction for each measurement duration would be desirable. These attenuation maps should be used for the scatter and attenuation correction for emission reconstructions. The image quality of these emission images needs to be evaluate. This would allow to address the best trade-off between quality and effort for the measurement and reconstruction. It has to be noted that the scatter correction for MLTR is a limiting factor due to its duration. Therefore, improvements of the simulation have a higher priority than reducing the duration of transmission measurements. Furthermore, investigations of the dynamic effects over a day can help to reduce the number of required transmission scans and therefore speed up the overall measurement duration.